

REPORT DOCUMENTATION PAGE

AFRL-SR-BL-TR-98-

Public reporting burden for this collection of information is estimated to average 1 hour per response, including the time and maintaining the data needed, and completing and reviewing the collection of information. Send comments regarding this information, including suggestions for reducing this burden, to Washington Headquarters Services, Directorate for Information Operations and Reports, 1204, Arlington, VA 22202-4302, and to the Office of Management and Budget, Paperwork Reduction Project (0704-0188).

1. AGENCY USE ONLY (Leave Blank)	2. REPORT DATE	3. REPORT TYPE AND DATES	
	August, 1990	Final	
4. TITLE AND SUBTITLE Alfven Waves and Static Fields in Magnetosphere/Ionosphere Coupling: In-Situ Measurements and a Numerical Model		5. FUNDING NUMBERS	
6. AUTHORS David J. Knudsen			
7. PERFORMING ORGANIZATION NAME(S) AND ADDRESS(ES) Cornell University		8. PERFORMING ORGANIZATION REPORT NUMBER	
9. SPONSORING/MONITORING AGENCY NAME(S) AND ADDRESS(ES) AFOSR/NI 4040 Fairfax Dr, Suite 500 Arlington, VA 22203-1613		10. SPONSORING/MONITORING AGENCY REPORT NUMBER	
11. SUPPLEMENTARY NOTES			
12a. DISTRIBUTION AVAILABILITY STATEMENT Approved for Public Release		12b. DISTRIBUTION CODE	
13. ABSTRACT (Maximum 200 words) See Attachment			
14. SUBJECT TERMS		15. NUMBER OF PAGES	
		16. PRICE CODE	
17. SECURITY CLASSIFICATION OF REPORT Unclassified	18. SECURITY CLASSIFICATION OF THIS PAGE Unclassified	19. SECURITY CLASSIFICATION OF ABSTRACT Unclassified	20. LIMITATION OF ABSTRACT UL

DTIC QUALITY INSPECTED 3

**ALFVÉN WAVES AND STATIC FIELDS IN
MAGNETOSPHERE/IONOSPHERE COUPLING: *IN-SITU*
MEASUREMENTS AND A NUMERICAL MODEL**

**A Dissertation
Presented to the Faculty of the Graduate School
of Cornell University
in Partial Fulfillment of the Requirements for the Degree of
Doctor of Philosophy**

by

David J. Knudsen

August, 1990

© David J. Knudsen 1990
ALL RIGHTS RESERVED

19981202 053

ALFVÉN WAVES AND STATIC FIELDS IN
MAGNETOSPHERE/IONOSPHERE COUPLING: *IN-SITU*
MEASUREMENTS AND A NUMERICAL MODEL

David J. Knudsen, Ph.D.

Cornell University 1990

Perturbation electric and magnetic fields carry in excess of 10^{10} to 10^{12} W of electrical power between the magnetosphere and high-latitude ionosphere. Most of this power is generated by the solar wind. The ionosphere at large spatial and temporal scales acts as a dissipative slab which can be characterized by its height-integrated Pedersen conductivity Σ_p , so that the power flux into the ionosphere due to a quasi-static electric field E is given by $\Sigma_p E^2$.

The energy transferred to the ionosphere by time-varying electromagnetic fields in the form of Alfvén waves is more difficult to calculate because density and conductivity gradients can reflect energy. Thus, field resonances and standing wave patterns affect the magnitude and altitude distribution of electrical energy dissipation. We use a numerical model to calculate the frequency-dependent electric field reflection coefficient of the ionosphere and show that the ionosphere does not behave as a simple resistive slab for electric field time scales less than a few seconds.

Time variation of spacecraft-measured high-latitude electric and perturbation magnetic fields is difficult to distinguish from spatial

structuring that has been Doppler-shifted to a non-zero frequency in the spacecraft frame. However, by calculating the frequency-dependent amplitude and phase relations between fluctuating electric and magnetic fields we are able to show that low frequency fields (< 1 Hz) measured by an auroral sounding rocket traveling parallel to the auroral oval are due to standing Alfvén waves rather than quasi-static structures. Comparing the field fluctuations with electron energy measurements indicates that the waves occur near auroral arcs.

We include satellite data in our study as well. The amplitude relations between electric and magnetic field measurements taken by the HILAT satellite (traveling perpendicular to the auroral oval at an altitude of 800 km) show that the field fluctuations are due largely to Doppler-shifted quasi-static structures, but in some cases standing Alfvén waves also contribute.

Biographical Sketch

David J. Knudsen was born in Rapid City, South Dakota on 24 April, 1963. He attended elementary school in Wichita, Kansas, and junior high and high schools in Fort Dodge, Iowa. He graduated from Fort Dodge Senior High School in 1981. He then entered the electrical engineering program at Iowa State University. While he was an undergraduate, David held a summer internship at the Ford Aerospace and Communications Corp. in Newport Beach, California, and he worked as a student engineer at WOI Television in Ames, Iowa. He graduated with the B. S. degree in May, 1985. Since June, 1985 he has worked with the Space Plasma Physics Group at Cornell University.

The author married Ellen S. Miller in June, 1986, and they have a son, Aaron, who was born on 21 September, 1989.

To Ellen, Aaron,
and our families,
for making this project seem
like an adventure
rather than an ordeal.

Acknowledgments

It is my pleasure to extend my sincere thanks to Prof. M. C. Kelley for serving as chairman of my special committee. Despite an amazing number of other projects, Mike is always willing to spend an hour or two in lively discussions about Poynting flux or auroral physics. I also appreciate the effort he put forth in introducing me to the space physics community, and in helping me find post-doctoral employment.

I would also like to thank the other members of my committee: Prof. D. Hammer and Prof. D. T. Farley, whose excellent classroom instruction and careful attention to this project are much appreciated, and Dr. J. F. Vickrey. I have very much enjoyed working with Dr. Vickrey, who has been extremely helpful during the entire duration of my graduate program. Jim has supplied a huge amount of experimental data and many good ideas for interpreting it.

Thanks are due to Prof. C. E. Seyler for the interest and time he has devoted to this project. I have also enjoyed working with Prof. P. M. Kintner, Prof. W. E. Swartz, Dr. Jason Providakes, and Prof. N. Otani.

Dr. Greg Earle, Dr. Wayne Scales, Prof. James LaBelle, Dr. Robert Pfaff, Dr. Carl Siefring, and Dr. Charles Cornish deserve thanks for helping me to define my research program in the early stages, and for many good insights into graduate student life. I am indebted to Dr. John Sahr and Dr. James Providakes for allowing me to remain mostly computer-illiterate by offering lots of computer help, and also for being good office mates and friends from my first days at Cornell. Many thanks to Phil Erickson and Dr. Joe Pingree, who did most of the

calculations in Chapter 6, and who were, along with Richard Brittain, Chuck Swenson, and Glenn Berg, very generous with computer advice over the years. I've also very much enjoyed working with Tim Hall, Brett Isham, Robert Green, Steve Powell, Tim Wheeler, Cho-Hoi Hui, Dave Hysell, Jorge Vago, John Cho, Marian Silberstein, and Jian Ding. I gratefully acknowledge the friendly competence of Laurie Shelton, Sally Bird, and Susan Swartz in keeping our research group running smoothly.

Terri Dabbs, Nancy Walker, Mary McCready, Craig Heinzelman, and Denise Rust of SRI International have been very helpful in supplying and processing HILAT satellite and Sondrestrom radar data. Thanks are also due to Dr. M. Boehm, Dr. B. McFadden, and Prof. C. Carlson of the University of California at Berkeley for providing the sounding rocket data presented in Chapters 3 and 5.

I am grateful to Dr. H. Carlson and Dr. E. Weber of the Air Force Geophysics Laboratory for helping me apply for and obtain an Air Force Office of Scientific Research Graduate Laboratory Fellowship, which I have held for the past two years.

Finally, I would like to acknowledge the support of close friends and family. Grant Heffelfinger is responsible in large part for my coming to Cornell. Paul Bay, Gretta Anderson, Sam Otter, and Caverlee Cary deserve much of the credit for my staying here. And most importantly, I would like to express my deep love and gratitude to Ellen, Aaron, Mom, Dad, and the rest of our families, to whom this dissertation is dedicated.

Table of Contents

Biographical Sketch	iii
Dedication	iv
Acknowledgments	v
Table of Contents	vii
List of Tables	ix
List of Figures	x
1. INTRODUCTION	1
1.1 Background	1
1.2 Purpose and Organization of This Work	4
2. BACKGROUND AND REVIEW	9
2.1 The Solar Wind and Magnetosphere	9
2.2 The Aurora	13
2.3 Linear Theory of Alfvén Waves	15
2.4 Oblique Propagation of Alfvén Waves	21
2.5 Kinetic Alfvén Waves and Parallel Electric Fields	25
2.6 Alfvén Waves and Magnetosphere-Ionosphere Coupling	29
3. MEASURING ENERGY COUPLING BETWEEN THE MAGNETOSPHERE AND HIGH-LATITUDE IONOSPHERE	32
3.1 Introduction	32
3.2 Techniques for Measuring Electromagnetic Energy Input to the Ionosphere	35
3.3 The Effect of Neutral Winds on Energy Flow Measurements	41
3.4 Satellite Observations of Kinetic Energy and Poynting Flux	50
3.5 Sounding Rocket Observations	64
3.6 Time-Domain Measurements of Auroral Field Impedances	67
4. A NUMERICAL MODEL OF ALFVÉN WAVES INTERACTING WITH THE HIGH-LATITUDE IONOSPHERE	74
4.1 Introduction	74
4.2 Derivation	76
4.3 Boundary Conditions	79
4.4 Model Input	81
4.5 Quasi-Static Fields in the Ionosphere	91
4.6 A 1 Hz Alfvén Wave in the Ionosphere	98
4.7 Reflection of Alfvén Waves from Different Ionospheric Density Profiles	101
4.8 The Effect of Collisions on $\Gamma(f)$	106
4.9 $\Gamma(\lambda_x)$	108

5. ROCKET AND SATELLITE MEASUREMENTS OF ALFVÉN WAVES	110
5.1 Introduction	110
5.2 The Impedance Function	113
5.3 The Normalized Cross-Spectrum	117
5.4 Greenland II Rocket Data	120
5.5 HILAT Satellite Data	126
5.6 A Quantitative Estimate of the Amount of Alfvén Wave Energy in Electromagnetic Field Data	148
5.7 Discussion	150
6. THE EFFECT OF ALFVÉN WAVES ON INCOHERENT SCATTER RADAR MEASUREMENTS	155
6.1 Introduction	155
6.2 Incoherent Scatter Spectra with Time-Varying Drifts	157
6.3 Conclusions	164
7. CONCLUSIONS AND SUGGESTIONS FOR FUTURE RESEARCH	165
7.1 Summary of Results	165
7.2 Future Research: Quasi-Static Fields and Neutral Winds	171
7.3 Future Research: Spacecraft Measurements of Alfvén Waves	178
7.4 Future Research: Incoherent Scatter Radar Measurements of the Aurora	180
APPENDIX A. POYNTING'S THEOREM	183
APPENDIX B. STATIC MAGNETIC FIELDS FROM AN IDEALIZED AURORAL ARC	185
REFERENCES	189

List of Tables

4.1	Density model input parameters as defined in Equations 4.10 and 4.11.	88
5.1	Ensemble average of the frequency-averaged coherency $ C_{12} $ calculated from twenty different time series consisting of Gaussian white noise.	120
5.2	HILAT passes searched for 100 s intervals with a frequency averaged $E-\delta B$ coherency exceeding 0.5. Passes with an asterisk satisfy this criterion.	127

List of Figures

2.1	Possible sources of magnetospheric Alfvén waves which propagate to the ionosphere: I. Kelvin-Helmholtz instability. II. Tail reconnection and associated substorms. III. A "gusty" solar wind can generate a time-varying electric field.	10
2.2	Applying a static electric field \mathbf{E} perpendicular to \mathbf{B}_0 causes a dielectric response in the plasma by displacing charges relative to each other in the direction of \mathbf{E} .	17
2.3	The two Alfvén wave modes as defined by Stix [1962]. For typical auroral parameters the fast mode is evanescent, causing the meridional electric field E_x to dominate.	23
3.1	S_1 is the surface through which magnetospheric Poynting flux \mathbf{S} enters the upper atmosphere. S_2 is the Earth's surface, which is a good conductor and therefore requires $E_\perp = 0$ and hence $\mathbf{S} = 0$. Assuming that the magnetic field lines are straight and vertical, and the fair weather electric field is vertical implies that $\mathbf{S} \cdot \hat{\mathbf{n}}_3 \equiv 0$ where $\hat{\mathbf{n}}_3$ is a unit vector normal to the surface S_3 .	40
3.2	Cross-section in the meridional plane of a simplified model illustrating the effect of neutral winds on ionospheric dissipation of magnetospherically applied electric field energy.	43
3.3	Cross-section in the meridional plane of a simplified model illustrating the interaction of neutral wind dynamos in conjugate hemispheres.	46
3.4a	Meridional and zonal magnetic field perturbations for two HILAT passes. The 40 second variation in the Day 164 data and the longer period variation in the Day 122 data are due to attitude oscillations of the satellite. Superimposed on these are clear signatures of large-scale field-aligned currents.	52
3.4b	Meridional and zonal electric fields for the two HILAT passes shown in Figure 3.4a.	54
3.5	Comparison of electromagnetic and particle energy inputs into the ionosphere and the large-scale field-aligned current structure for a summer noon descending pass.	55

3.6	Comparison of the Joule heating rate and Poynting flux for the HILAT pass shown in Figure 3.5.	59
3.7	Comparison of electromagnetic and particle energy inputs into the ionosphere and the large-scale field-aligned current structure for a HILAT pass through the afternoon sector.	61
3.8	Expanded view of a two minute interval during the HILAT pass on Day 122, 1984 during which upward Poynting flux was observed.	62
3.9	Comparison of the Joule heating rate and Poynting flux for the HILAT pass shown in Figure 3.7.	63
3.10	Data taken from a Black Brant X sounding rocket launched from Sondrestrom, Greenland on 23 January, 1985. The rocket traveled eastward along the auroral oval. (Data are courtesy of C. Carlson, B. McFadden, and M. Boehm at the University of California, Berkeley.)	65
3.11	Electromagnetic field impedance as a function of time calculated from the Day 164, 1984 data. The impedances in the lower panel are normalized to Σp^{-1} .	69
3.12	Electromagnetic field impedance as a function of time calculated from the Day 122, 1984 data. The impedances in the lower panel are normalized to Σp^{-1} .	70
3.13	Electric field during a short event measured by HILAT on Day 164, 1984, plotted at the full time resolution of the instrument (16 s^{-1} or 32 s^{-1}). The coherent nature of the burst is indicative of time variation (i.e. an Alfvén wave) rather than spatial structuring.	72
3.14	Electromagnetic field impedance as a function of time calculated from the sounding rocket data shown in Figure 3.10. The impedances are normalized to a constant value of $\Sigma p^{-1} = (3 \text{ mhos})^{-1}$.	73
4.1	Schematic representation of the five independent solutions which are combined into a single solution for the electromagnetic fields between 0 and 1000 km.	82
4.2	a) A typical electron density profile and the associated b) direct, c) Pedersen and d) Hall conductivity profiles for a sunlit, daytime ionosphere.	84
4.3	a) A typical electron density profile and the associated b) direct, c) Pedersen and d) Hall conductivity profiles for a post-sunset ionosphere with an F region only.	85

4.4	a) A typical electron density profile and the associated b) direct, c) Pedersen and d) Hall conductivity profiles for a nighttime ionosphere caused by relatively energetic electron precipitation.	86
4.5	a-c) Electron and ion collision frequency profiles for the density profiles shown in Figures 4.2-4.4. d) Relative concentration of O ⁺ and NO ⁺ as a function of altitude used for input to the numerical model.	90
4.6a,b	a) Meridional and b) zonal electric field profiles in the quasi-static limit.	93
4.6c,d	c) Meridional and d) zonal perturbation magnetic field profiles in the quasi-static limit.	96
4.7	a) Meridional electric, b) zonal electric, c) meridional magnetic, and d) zonal magnetic field profiles due to a 1 Hz Alfvén wave reflecting from the ionosphere.	99
4.8a	Surface plot showing the variation of the magnitude of the meridional electric field $ E_x $ as a function of frequency and altitude.	102
4.8b	Surface plot showing the variation of the magnitude of the zonal electric field $ E_y $ as a function of frequency and altitude.	103
4.9	a) Magnitude and b) phase of the complex electric field reflection coefficient Γ at 1000 km altitude for the three ionospheric density profiles shown in Figures 4.2-4.4.	104
4.10	Illustration of the effects that changes in ion collision frequencies (upper panel) and electron collision frequencies (lower panel) can have on the magnitude of $ \Gamma $.	107
4.11	Reflection coefficient magnitude, $ \Gamma $, as a function of inverse horizontal spatial scale λ_x^{-1} .	109
5.1	Data taken from a Black Brant X sounding rocket launched from Sondrestrom, Greenland on 23 January, 1985. The rocket traveled eastward along the auroral oval. (Data are courtesy of C. Carlson, B. McFadden, and M. Boehm at the University of California, Berkeley.)	121
5.2	Numerical results compared with sounding rocket data averaged over the entire interval shown in Figure 5.1. Averages were formed from 21 sub-intervals of 32 points each.	123

5.3	Electron density profile used as model input for the curves in Figure 5.2. This profile approximates the density profile taken on board a Terrier-Malemute rocket launched nearly simultaneously and in the same direction as the Black Brant [see <i>Earle, 1988</i>].	124
5.4	Distribution of frequency-averaged coherency spectra from a) HILAT data, and b) Gaussian white noise. Each coherency spectrum was formed from 11 electric and magnetic field spectra, which were in turn formed from 32 data points each.	129
5.5	Smoothed and unsmoothed density profiles taken by the Sondrestrom radar on 10 December, 1983 and averaged in latitude (left), taken at the same time as the HILAT electric and perturbation magnetic field data shown at right.	132
5.6	Comparison of numerical model and experimental results using the smoothed density profile and electric and magnetic fields shown in Figure 5.5. Ensemble averages were formed from 11 separate 32 point (16 s) intervals overlapping by 16 points each. Boxes indicate a coherency exceeding 0.5.	133
5.7	Smoothed and unsmoothed density profiles taken by the Sondrestrom radar on 3 March, 1984, and averaged in latitude (left), taken at the same time as the HILAT electric and perturbation magnetic field data shown at right.	134
5.8	Comparison of numerical model and experimental results using the smoothed density profile and electric and magnetic fields shown in Figure 5.7. Ensemble averages were formed from 11 separate 32 point (16 s) intervals overlapping by 16 points each. Boxes indicate a coherency exceeding 0.5.	135
5.9	Smoothed and unsmoothed density profiles taken by the Sondrestrom radar on 5 April, 1984, and averaged in latitude (left), taken at the same time as the HILAT electric and perturbation magnetic field data shown at right.	136
5.10	Comparison of numerical model and experimental results using the smoothed density profile and electric and magnetic fields shown in Figure 5.9. Ensemble averages were formed from 11 separate 32 point (16 s) intervals overlapping by 16 points each. Boxes indicate a coherency exceeding 0.5.	137

5.11	Smoothed and unsmoothed density profiles taken by the Sondrestrom radar on 27 June, 1984, and averaged in latitude (left), taken at the same time as the HILAT electric and perturbation magnetic field data shown at right.	138
5.12	Comparison of numerical model and experimental results using the smoothed density profile and electric and magnetic fields shown in Figure 5.11. Ensemble averages were formed from 11 separate 32 point (16 s) intervals overlapping by 16 points each. Boxes indicate a coherency exceeding 0.5.	139
5.13	Smoothed and unsmoothed density profiles taken by the Sondrestrom radar on 17 September, 1984, and averaged in latitude (left), taken at the same time as the HILAT electric and perturbation magnetic field data shown at right.	140
5.14	Comparison of numerical model and experimental results using the smoothed density profile and electric and magnetic fields shown in Figure 5.13. Ensemble averages were formed from 11 separate 32 point (16 s) intervals overlapping by 16 points each. Boxes indicate a coherency exceeding 0.5.	141
5.15	Smoothed and unsmoothed density profiles taken by the Sondrestrom radar on 4 October, 1985, and averaged in latitude (left), taken at the same time as the HILAT electric and perturbation magnetic field data shown at right.	142
5.16	Comparison of numerical model and experimental results using the smoothed density profile and electric and magnetic fields shown in Figure 5.13. Ensemble averages were formed from 11 separate 32 point (16 s) intervals overlapping by 16 points each. Boxes indicate a coherency exceeding 0.5.	143
5.17	Model meridional electric field profiles for two Alfvén waves illustrating the fact that higher frequency waves reflect from lower altitudes.	146
6.1	Theoretical ion-line spectra at 1290 MHz assuming an O ⁺ plasma with two different densities.	158
6.2	Spectra which would result from smearing the spectra in Figure 6.1 with a 750 m/s amplitude sinusoidal drift velocity which has a period less than the radar integration time.	160

6.3	Electron an ion temperature fits to ideal 1290 MHz ion-line spectra which have been smeared with a drift velocity of the form $V_d = V_{d,max} \sin(2\pi t/T)$, where T is less than the radar integration time.	161
6.4	Electron an ion temperatures fits to ideal 933 MHz ion-line spectra which have been smeared with a drift velocity of the form $V_d = V_{d,max} \sin(2\pi t/T)$, where T is less than the radar integration time.	162
7.1	a) Zonal magnetic field perturbation due to a 100 m/s neutral wind which is constant in altitude. b-d) Magnetic perturbations due to zonal neutral winds of the form $U_y(z) = 100 \cos(2\pi(z - 100 \text{ km})/\lambda_z)$. All four profiles were calculated using Profile "EF" shown in Figure 4.2, and the upper boundary condition demands that $E_x/\delta B_y = V_A$.	177
B1	Geometry used to calculate magnetic fields due to an idea auroral arc which produces no Hall current and which has an infinitely thin Pedersen current layer at $z = 0$.	186

CHAPTER 1

INTRODUCTION

1.1 Background

Eighteenth century scientists might have been satisfied with the idea of an infinite void, save for a relative few heavenly bodies, extending outward from somewhere above the cloud tops had it not been for the tantalizing geophysical clues provided by nature. In the early 1700s the Earth's magnetic field was well understood, static and predictable enough to use as a navigational tool, but why did G. Graham's finer measurements in 1722 reveal fluctuations? Balfour Stewart was able to show in 1882 that the magnetic fluctuations were due to electrical currents above the Earth. Of course this finding was probably stranger than the B-field fluctuations themselves, but Marconi's trans-Atlantic radio broadcast in 1901 corroborated the idea of a conducting layer high in the atmosphere.

The origin of the auroras borealis and australis had to be and still is one of the more interesting puzzles posed to those fortunate enough to view them, especially after the turn of the century when triangulation measurements placed the displays between 100 and 1000 km above the Earth's surface. The electrical nature of the aurora was known from the magnetic perturbations measured at ground level and associated with individual auroral arcs, but not until spacecraft flights through auroras in the 1960s was it known with certainty that energetic electrons (many

keV) crashing into the neutral atmosphere from above were responsible for the optical fluorescence.

Two discoveries in the 1950s pushed the envelope containing the known part of the Earth's environment well beyond the 1000 km upper boundary of the visible aurora. The first was that whistlers, the descending tone, audio-frequency electromagnetic waves known since World War I, were due to lightning discharges. More importantly, their dispersion was found to be the result of propagation through charged particles permeating space tens of thousands of km above the Earth's surface. Secondly, satellite measurements in this same region led to the discovery of the very high energy particles comprising the Van Allen radiation belts.

The present view is that the Earth's near space environment must be viewed as a complete system which includes the Sun's outermost atmosphere. One of the main goals of present day research is to construct a self-consistent model of that system's energy source (which is to say the Sun itself), the means of energy transmission (photons and the particles and magnetic fields of the solar wind), and the energy deposition in and associated dynamics of the Earth's magnetosphere, ionosphere, and neutral atmosphere. We might separate the effort to construct this model into two parts: 1) a detailed study of all the separate constituents of the system, and 2) an examination of how these constituents are interconnected. By and large this dissertation falls into the "connecting" category, where the two pieces we are trying to fit together are the magnetosphere and ionosphere.

The magnetosphere extends from about ten to hundreds of Earth radii away (depending on whether you are "upwind" or "downwind"

from the Earth) down to the ionosphere starting at roughly 1000 km in altitude, where collisions with the neutral atmosphere begin to take control of the charged particle dynamics. The study of magnetosphere-ionosphere coupling pertains mostly to high latitudes because that is where geomagnetic field lines extend from the ionosphere deep into the magnetosphere. At lower latitudes magnetic field lines are shorter and do not extend as far from the Earth.

Energy is exchanged between the magnetosphere and ionosphere in two main ways, via kinetic energy of charged particles which we will consider briefly in Chapter 3, and by quasi-static and wave related electric and magnetic fields, which we will emphasize throughout. Each of these energy sources can at certain times and places dominate the other, but the total power carried by each of them is roughly 10^{10} to 10^{12} W. Although this is 5 to 7 orders of magnitude smaller than the energy flux into the sunlit polar cap from solar photons, most of the solar flux goes directly into the neutral atmosphere at relatively low altitudes, leaving magnetosphere-ionosphere energy exchange to determine a significant part of the ionospheric plasma (and high-altitude neutral atmosphere) dynamics at high latitudes. Of course much of the ionospheric plasma is produced by photoionization in the first place, but its bulk motions, structuring, and instabilities are due in large part to particle precipitation and electric fields. In the polar winter, these sources dominate the energetics and dynamics of the upper atmosphere. Interactions with the neutral atmosphere (e.g. from gravity waves) and chemical processes also play a role.

On average the ionosphere acts as a dissipative load attached to the magnetospheric energy source, which in turn is driven by the interaction

between the magnetosphere and the solar wind. The situation can be quite complex because magnetospheric electric fields driving currents in the ionosphere are often accompanied by beams of energetic particles, which modify the conductivity of the ionosphere. This change in the load can affect the ionospheric electric fields and conceivably the particle precipitation itself, creating a feedback effect which is not yet fully understood and which we will not attempt to address. Other complications arise when neutral winds drive the ionospheric plasma, creating dynamo electric fields and switching the role of the magnetosphere from source to load.

1.2 Purpose and Organization of This Work

The central topic we address in this dissertation is the interpretation of spacecraft measurements of low frequency (less than 1 Hz) electric and perturbation magnetic fluctuations above the high-latitude ionosphere. As mentioned in the previous section, magnetic perturbations have been measured on the ground for centuries. *Birkeland* [1908] noted that these perturbations were especially strong under auroral arcs, and suggested they were caused by electric currents flowing along geomagnetic field lines associated with the aurora. The discovery of the Alfvén wave [*Alfvén*, 1950] allowed for the interpretation that B-field fluctuations measured on the ground were due to Alfvén wave resonances in the Earth's dipole field. Early satellite measurements [see *Zmuda et al.*, 1966] showed magnetic fluctuations in the polar region, and these also were interpreted predominantly in terms of Alfvén waves. *Cummings and Dessler* [1967] called into question the Alfvén wave interpretation by arguing that it was not possible for Alfvén waves to be localized as

satellite measurements had shown, and they again proposed, as Birkeland had, that quasi-static field-aligned currents were primarily responsible for the magnetic fluctuations.

Despite their arguments that quasi-static currents could explain spacecraft magnetic field measurements, Cummings and Dessler acknowledged the possibility that localized Alfvén waves are possible when accompanied by field-aligned currents. Nonetheless, the static model was generally accepted following the publication of *Cummings and Dessler* [1967]. In the last decade, the validity of the static field model has been re-examined. Obliquely propagating Alfvén waves known as "shear" or "slow" mode waves [Stix, 1962] carry field-aligned currents, and it is now known that these waves are indeed very important in magnetospheric electrodynamics. We argue in this dissertation that the static field model alone does not adequately describe high-latitude electromagnetic fields, and that it is appropriate to include the effect of shear Alfvén waves in studies of high-latitude and auroral dynamics.

In some sense the static Birkeland current model is a limiting case of the shear Alfvén wave model. However, there are important differences between the static and wave models because time-varying fields allow for reflections, resonances, and interference. It is difficult to discern from measurements on board a spacecraft if electric and magnetic field fluctuations are due to waves or to localized static disturbances which are Doppler-shifted to a finite frequency in the spacecraft frame. *Sugiura et al.*, [1982] used the Dynamics Explorer satellite to show that the electric and magnetic field fluctuations above the auroral zone are often highly correlated, and they used a novel approach to distinguish between the wave and static field cases by

calculating the ratio of the r.m.s. field amplitudes $\mu_0 E_{rms}/\delta B_{rms}$. They found the value of this ratio to be equal to the inverse of the height-integrated Pedersen conductivity of the ionosphere Σ_P^{-1} , and we will show in Chapter 3 that this is expected from static electric fields and associated Birkeland currents.

A problem with the analysis of Sugiura *et al.* [1982] is that E and δB power spectra are usually monotonically decreasing with frequency, so the lowest frequencies are emphasized in a correlation analysis. In Chapter 5 we remedy this problem by calculating the ratio of electric and magnetic field amplitudes *as a function of frequency*. We will also study the frequency-dependent phase relation between E and δB . In so doing we find that Alfvén wave dynamics play an important role in electrodynamic coupling between the magnetosphere and ionosphere for time scales less than about 10 s. We also show that, in at least one sounding rocket experiment, most of the Alfvén wave energy lies near regions of auroral precipitation.

The Alfvén wave model can be sub-divided into two categories: traveling waves and standing waves. This distinction is important because standing waves are indicative of reflections, and an understanding of these reflections is crucial in determining the fraction of electrical energy incident from the magnetosphere that is dissipated in the ionosphere. Our analysis in Chapter 5 shows that standing waves are present in both the satellite and rocket data (taken at 800 km and near 600 km, respectively).

The reflection characteristics of the ionosphere are complicated and change with wave frequency as a result of the strong altitude dependence of the plasma density and collision frequencies, and of the fact that the

thickness of the ionospheric "load" is on the order of an Alfvén wavelength. In order to accurately compute the amplitude and phase relations between E and δB fields due to Alfvén waves reflecting from the ionosphere, one must in general use a numerical model. We devote Chapter 4 to the development and general results of such a model. The model we choose was originally used by *Hughes* [1974] to predict properties of ground-based magnetometer measurements.

The electric field reflection coefficient of the ionosphere is often estimated by treating the ionosphere as a slab reflector with height-integrated Pedersen conductivity Σ_P , and the region above the ionosphere as a homogeneous "transmission line" with characteristic impedance $Z_A = \mu_0 V_A$ where V_A is the Alfvén velocity. The E-field reflection coefficient of the ionosphere is then given by $(\Sigma_P^{-1} - Z_A)/(\Sigma_P^{-1} + Z_A)$ [see for example *Paul and Nassar*, 1987]. As one of the main results of Chapter 4 we show that this approximation is not valid for time scales less than a few seconds, and we present plots of the reflection coefficient for small time scales and for different ionospheric density profiles.

While Chapters 4 and 5 treat time-varying electric and magnetic fields, Chapter 3 is devoted to interpretation of satellite and sounding rocket estimates of ionospheric Joule heating and Poynting flux into and out of the ionosphere in the DC limit. The Poynting flux method has not been used extensively, but it has several advantages over other electromagnetic energy measurements and we discuss those in detail. There are several factors which complicate all energy measurements; neutral winds and temporal variations are particularly important. We treat the topic of neutral winds in Chapter 3.

Having established in Chapter 5 the importance of Alfvén waves in the high-latitude ionosphere, we turn in Chapter 6 to a brief study of the effects that large amplitude waves can have on the interpretation of incoherent scatter radar data. But first we will review the literature and some of the physical concepts pertaining to Alfvén waves, in Chapter 2.

CHAPTER 2

BACKGROUND AND REVIEW

2.1 The Solar Wind and Magnetosphere

Much of the previous work in magnetosphere-ionosphere coupling has emphasized the region extending from the top of the ionosphere up to several thousand km. The ionosphere itself is often modeled simply as a conducting slab characterized by its height-integrated Pedersen conductivity (see references in Section 2.6). We will take the opposite approach by thinking of the magnetosphere only as an "upper boundary condition" which supplies electric fields, currents, and particles to the ionosphere and treating in detail the interaction between those energy sources and the ionosphere. In Chapter 4 we will use a detailed model of the ionosphere as input to a numerical model, so we will save a review of the ionosphere's morphology until then and concentrate now on the magnetosphere and some of the ways it can produce Alfvén waves -- the magnetosphere-ionosphere coupling mode which will receive most of the attention in this thesis.

Figure 2.1 shows a cross section of the magnetosphere in the noon-midnight meridian plane when the z component of the interplanetary magnetic field (IMF) is southward, which allows the IMF to penetrate to the magnetopause and connect with the Earth's magnetic field. The solar wind impinging from the left is comprised mostly of protons and electrons ($\approx 5 \text{ cm}^{-3}$, $T_i \approx T_e \approx 10 \text{ eV}$) traveling at about 500 km/s. The kinetic energy flux from this bulk flow is thus $\approx 5 \times 10^{-4} \text{ W/m}^2$. Assuming

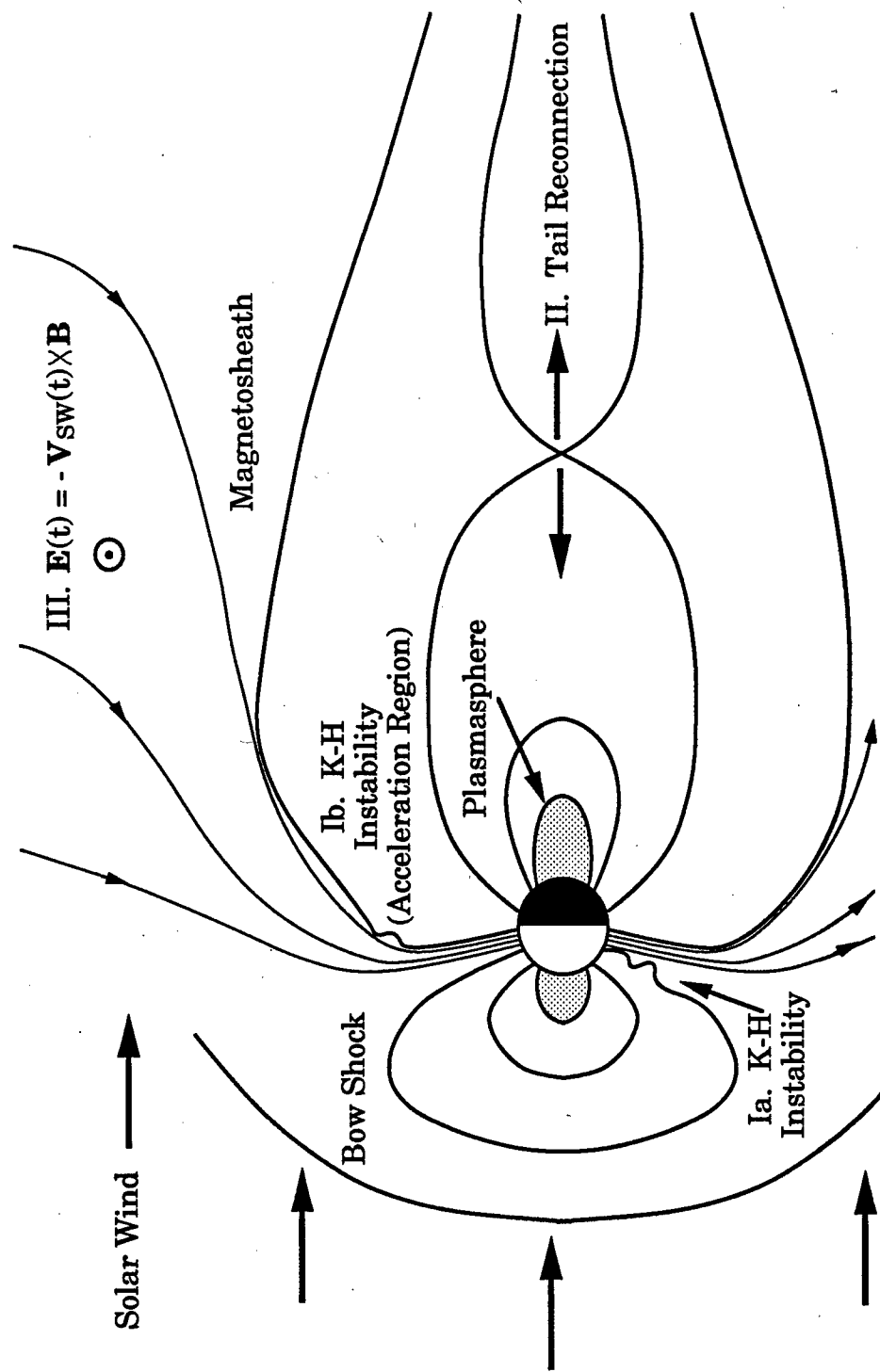


Figure 2.1 Possible sources of magnetospheric Alfvén waves which propagate to the ionosphere: I. Kelvin-Helmholtz instability. II. Tail reconnection and associated substorms. III. A "grusty" solar wind can generate a time-varying electric field.

that the magnetosphere has a cross section of $\pi \times (10 R_{\text{Earth}})^2$ leaves on the order of 10^{13} W of available solar wind power. Solar photons carry more than 10^6 times more energy flux (1400 W/m^2), but the "capture area" is 100 times less since it is the Earth rather than the magnetosphere which intercepts the energy. The solar wind has a magnetic field of about 5 nT which means it can carry energy in the form of Alfvén waves in addition to the kinetic energy.

Although energy input from the solar wind to the Earth is usually 4-5 orders of magnitude smaller than from solar photon flux, solar wind energy is also much more variable and can have important effects on industry, electrical power systems, communications, and space operations and astronaut safety. This point is illustrated nicely by the huge solar flare and subsequent geomagnetic storm during the weeks following March 6, 1989 [Allen *et al.*, 1989]. The aurora, normally visible over the northern U. S. and Canada, was seen clearly in Georgia, Texas, and New Mexico. HF communications and navigation systems (< 50 MHz) which rely on reflection from the ionosphere were useless. Most of Quebec Province experienced a power blackout for up to 9 hours, large voltage swings appeared on undersea cables, and huge currents induced in pipelines caused concerns about corrosion. In a particularly bizarre event a Navy ship had to go to a backup shore-based radio system, causing automatic garage door openers in a California coastal suburb to start opening and closing.

When the solar wind has a velocity component perpendicular to magnetospheric field lines, electric fields are created and the process is called an "MHD dynamo" (see Figure 2.1). Magnetic field lines in collisionless plasmas are equipotentials, thus the dynamo electric fields

are mapped throughout the magnetosphere where they create a large scale plasma convection pattern (see *Stern* [1977] and references therein). If the solar wind is uniform and constant the convection pattern can remain in a steady state. But changes in the solar wind affect the entire convection pattern, and the new equilibrium is found after different parts of the system exchange energy in the form of Alfvén waves. Magnetic field lines which have fixed ends (e.g. at the Earth) can set up standing Alfvén waves which oscillate at resonant frequencies. The resulting magnetic perturbations can be measured with ground-based magnetometers, and the phenomenon has traditionally been studied under the name "micropulsations."

The solar wind is certainly not the only source of changes in the magnetosphere, and is not necessarily the most important. A leading explanation for the origin of micropulsations is the Kelvin-Helmholtz instability, which causes waves on the boundary between two fluids in relative motion. Examples are waves on lakes and flags flapping in the breeze. See *Melrose* [1986] for a more detailed discussion of the K-H instability.

Magnetospheric substorms are another source of Alfvén waves. Over a period of hours or days the magnetosphere can store energy in the form of magnetic fields in its tail. This is thought to take place through the process of dayside reconnection of geomagnetic field lines with the IMF and subsequent deposition in the magnetotail. At some point the tail thins and field lines there reconnect, sweeping part of the tail downstream in the solar wind and snapping the remaining part back towards the Earth. The result is a huge flux of particle and Alfvén wave energy towards the polar caps, accompanied by increases in auroral

displays, electrojet currents, and more. (See the review paper on substorms by *McPherron* [1979].)

There are other proposed sources of magnetospheric Alfvén waves for which references can be found in the review paper by *Hughes* [1982]. There one can also find a good review of micropulsation observations from spacecraft.

The observations presented in this thesis are taken within the auroral oval because that is where much of the magnetospheric energy is deposited. It is this energy, not the aurora itself, with which we are primarily concerned, but the aurora is an important part of the environment we study and we will devote the next section to a brief overview.

2.2 The Aurora

A large part of the study of both space and laboratory plasmas is devoted to the instruments used to make diagnostic measurements. Only after a huge amount of work can one piece together the measured fields, potentials, drifts, etc., into a coherent picture of some physical phenomenon. The aurora is one of the few examples of a plasma physics experiment that can be observed simply by looking upward at the right latitude, and the results are displayed in 3-D and brilliant color across the entire sky. Unfortunately, even this dynamic display did not provide enough information for early researchers to understand the cause of the aurora, and today after thousands of satellite passes above auroral displays, dozens of rocket flights through them, and countless hours of ground-based radar observations, there are many remaining questions.

The auroral oval is actually more of a torus centered near the magnetic pole with representative boundaries extending from 65°-75° in magnetic latitude. The oval thickens and extends equatorward during magnetic activity. Within the oval are smaller "curtains" or "arcs" extended in the zonal (E-W) direction for hundreds or thousands of km and ranging from 1-100 km in latitudinal thickness. The arcs in turn have twists, folds, and intensity enhancements which race along the edge, and which have been found to be due to the Kelvin-Helmholtz instability [*Hallinan and Davis, 1970*]. The morphology of the aurora is quite a large subject in itself, but a nice overview with color photographs is given by *Eather [1980]*.

The term "aurora" encompasses many different phenomena which in general are characterized by light emitted in the upper atmosphere (100-1000 km) due to electrons incident from above and colliding with neutral atoms. The resulting fluorescence extends from infrared to ultraviolet and beyond, but the visible aurora is due to electrons with a kinetic energy of 1-10 keV directed along the geomagnetic field. In the early 1970s these electron beams were measured by satellites and rockets, and their energy spectra were found to be roughly monoenergetic. This and other measurements led to the discovery that the electrons were accelerated by a quasi-static potential drop maintained from 1-2 Earth radii above the surface (see *Akasofu, [1981]* and references therein).

Since the plasma in the acceleration zone is collisionless, it is hard to explain the existence of electric fields parallel to **B** that last for tens of minutes. The origin of this energization is still under debate, and is possibly the strongest motivator behind current auroral research. The leading theories for the potential drop associated with small scale intense

arcs involve anomalous resistivity, double layers, and kinetic Alfvén waves.

Plasma wave turbulence can arise from the intense field-aligned currents which are known to exist over the aurora. The turbulence can in some cases mimic the effects of collisions, allowing a finite conductivity along field lines. This effect is termed "anomalous resistivity" and is thought to play a role in sustaining the kV potentials through which auroral electrons are accelerated.

Double layers are small structures (several Debye lengths long) which are driven by field-aligned currents and, most importantly, support a net potential drop across themselves. The potential difference is on the order of the electron temperature, which is only about 1 eV. As small as these structures are, they have been observed by the S3-3 and Viking satellites [*Temerin et al.*, 1982; *Boström et al.*, 1988; *Koskinen et al.*, 1989], and if thousands of them occur on a single field line they might possibly explain the electron acceleration.

A third contender in explaining auroral electron energies is the kinetic Alfvén wave theory. Since we will deal with Alfvén waves throughout much of this thesis, we will spend the next few sections reviewing their linear theory, and in the process we will talk a little about Alfvén waves as a possible auroral acceleration mechanism.

2.3 Linear Theory of Alfvén Waves

Without a static magnetic field, electromagnetic waves cannot propagate below the electron plasma frequency. Alfvén waves are electromagnetic waves which exist in a magnetized plasma at frequencies below all of the cyclotron frequencies. They propagate as

perturbations along the static \mathbf{B} -field in the plasma. A useful intuitive picture of Alfvén waves comes from thinking of \mathbf{B} -field lines as taut strings which propagate perturbations when plucked. The linear dispersion relation for Alfvén waves is derived in most plasma theory textbooks from the equations of magnetohydrodynamics. We will instead stress the physical picture of the mechanism underlying Alfvén waves, and by examining the motions of single particles in the presence of low frequency electric fields we will find the dielectric response of a plasma to low frequency perturbations.

In Figure 2.2 an ion and an electron are shown (schematically) in the presence of a z - directed static magnetic field \mathbf{B}_0 . Both particles are initially on the line $y = 0$, but when a static electric field $E_y \hat{y}$ is applied they begin to $\mathbf{E} \times \mathbf{B}$ drift in the x direction. Since this drift is the same for electrons and ions, there is no current in the x direction. Notice however that the *average* positions of the particles have separated in \hat{y} , i.e. in the direction of the electric field.

We can draw an analogy between this situation and the polarization of a dielectric solid. Applying an electric field to a slab of dielectric material causes the individual atoms in the dielectric to polarize, which gives them a dipole moment $e\mathbf{d}$ where e is the fundamental unit of charge and \mathbf{d} is an effective separation of positive and negative charges. The dipole moment per unit volume is known as the polarization $\mathbf{P} = ned$ where n is the density of atoms. The electric flux density vector is the sum of the "free space" flux density plus the polarization of the material, i.e. $\mathbf{D} = \epsilon_0 \mathbf{E} + \mathbf{P}$. Finally, the dielectric constant of the material ϵ is defined by $\mathbf{D} = \epsilon \mathbf{E}$, thus

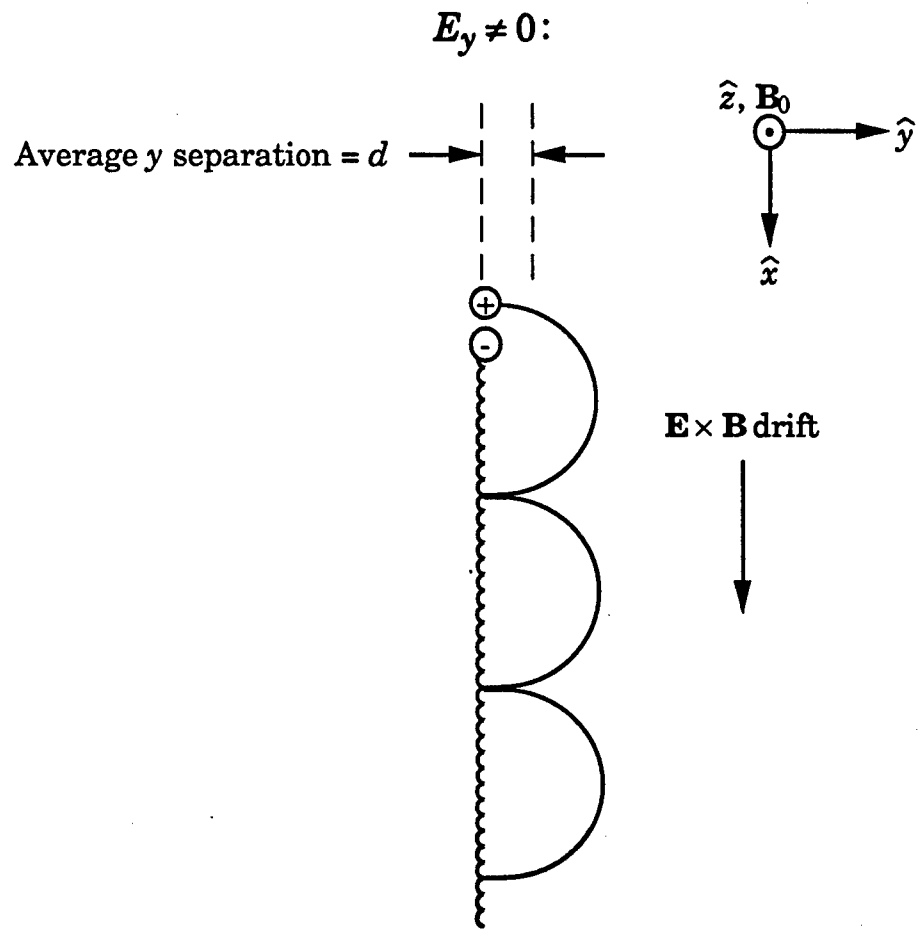


Figure 2.2 Applying a static electric field \mathbf{E} perpendicular to \mathbf{B}_0 causes a dielectric response in the plasma by displacing charges relative to each other in the direction of \mathbf{E} .

$$\epsilon = \epsilon_0 + ne|\mathbf{d}|/|\mathbf{E}| \quad (2.1)$$

This type of analysis is commonly used in introductory electromagnetics texts [e.g. *Paul and Nasar*, 1987] to explain the dielectric behavior of solids, and the picture is useful over a wide band of frequencies. The model breaks down at high frequencies, where the dielectric "constant" becomes frequency dependent.

In plasmas, the dielectric response is very dependent on frequency due to the various fundamental frequencies in the plasma such as the plasma and cyclotron frequencies. It follows then that plasma textbooks do not use the polarization model reviewed above to find the dielectric function for plasmas. As we will show, it turns out that the analogy with dielectric solids *does* predict the dielectric response of a magnetized plasma at frequencies well below the plasma and cyclotron frequencies, in the regime of Alfvén waves. We choose this approach since it is not commonly used in the literature and it does provide some useful insights.

Our main job now in finding the low frequency polarizability of a magnetized plasma is to find the average total displacement (labeled d in Figure 2.2) between ions and electrons after an electric field is imposed. To do this we can solve the equations of motion for a single ion in the presence of static magnetic and electric fields. Using the field directions shown in Figure 2.2,

$$\frac{dv_x}{dt} = \frac{q_i}{m_i} B_0 v_y \quad (2.2a)$$

and

$$\frac{dv_y}{dt} = \frac{q_i}{m_i} (E_y - B_0 v_x) \quad (2.2b)$$

Eliminating v_y gives a second-order equation for v_x :

$$\frac{d^2v_x}{dt^2} = \Omega_i^2 \left(\frac{E_y}{B_0} - v_x \right) \quad (2.3)$$

Equation 2.3 has the general solution

$$v_x(t) = A \sin(\Omega_i t) + B \cos(\Omega_i t) + (E_y/B_0) \quad (2.4)$$

This may now be substituted into (2.2a) to find $v_y(t)$:

$$v_y(t) = A \cos(\Omega_i t) - B \sin(\Omega_i t) \quad (2.5)$$

If we require $v_x(0) = v_y(0) = 0$ then $A = 0$, $B = -E_y/B_0$. Finally, we can integrate the velocities and impose $x(0) = y(0) = 0$ to obtain:

$$x(t) = \frac{E_y}{B_0} \left(t - \frac{1}{\Omega_i} \sin(\Omega_i t) \right) \quad (2.6a)$$

$$y(t) = \frac{E_y}{B_0} \cdot \frac{1}{\Omega_i} (1 - \cos(\Omega_i t)) \quad (2.6b)$$

Equation 2.6a shows that the ion gyrates at the cyclotron frequency Ω_i with a radius $\rho = E_y/(B_0 \Omega_i)$. Notice that this is the "usual" gyroradius with the thermal velocity v_{th} replaced by the $\mathbf{E} \times \mathbf{B}$ drift velocity. Superimposed on the gyro motion is the $\mathbf{E} \times \mathbf{B}$ drift, represented by the first term in Equation 2.6a. Our main interest is in the first term in Equation 2.6b. That is the term which remains after averaging over the fast cyclotron motion, leaving an offset in the \hat{y} direction equal to one "E×B gyro radius." This offset is proportional to E_y , and is the polarization effect we are looking for. We can now substitute $|d| = E_y/(B_0 \Omega_i)$ into Equation 2.1 to obtain:

$$\epsilon = \epsilon_0 + nm_i/B_0^2 \quad (2.7)$$

It is important to remember that (2.7) was derived assuming that the applied electric field is perpendicular to \mathbf{B}_0 . Our simple analogy with dielectric solids breaks down for electric fields parallel to \mathbf{B}_0 , although we can correct this problem, as we will show later. We have neglected the \hat{y} displacement of the electrons because it is smaller than the ion displacement by m_e/m_i , as is evident from Equation 2.6b.

Now consider an electromagnetic plane wave propagating along B_{0z} with a \hat{y} -directed electric field and a perturbation magnetic field associated with the wave in the $-\hat{x}$ direction. What is the phase velocity of such a wave? In this case we can use the simple relation

$$v_{ph} = \frac{c}{\sqrt{\epsilon/\epsilon_0}} \quad (2.8)$$

Combining (2.7) and (2.8) shows that electromagnetic waves propagating along \mathbf{B}_0 travel at the Alfvén velocity, i.e. $v_{ph} = V_A$, where

$$V_A = \frac{B_0}{\sqrt{\mu_0 n m_i}} \quad (2.9)$$

We have assumed that $V_A^2 \ll c^2$, which is true in the ionosphere.

To summarize, a low frequency electromagnetic wave traveling along the background magnetic field in a plasma polarizes the plasma by displacing the ion gyro orbits in the direction of the wave electric field. This interaction leads to a high refractive index $n = c/V_A$. In the ionosphere, n is typically several hundred. Some plasma textbooks treat Alfvén waves by solving for the *current* caused by the changing centers of gyration of the ions. This current is known as the polarization current J_{pol} and can be found using $J_{pol} = ne\dot{y}$. However, we cannot use $\dot{y} = v_y$ from (2.5) because we assumed that E_y was constant in time, leaving only motions at the cyclotron frequency in the \hat{y} direction. That is, (2.5) is

accurate only to zeroth order in ω . It turns out that the polarization drift can be found from (2.6b) when one takes the time derivative of the "constant" of (the spatial) integration, $E_y/(B_0\Omega_i)$, yielding

$$J_{pol} = (\partial E_y / \partial t) / (\mu_0 V_A^2) \quad (2.10)$$

In effect this is a perturbation solution good to first order in ω/Ω_i . A somewhat more rigorous derivation of the polarization drift can be found in various plasma textbooks, e.g. *Nicholson* [1983].

2.4 Oblique Propagation of Alfvén Waves

Now that we have established the basic mechanism underlying Alfvén waves, we are ready to add another detail: propagation directions with a component perpendicular to \mathbf{B}_0 . This is important for use in subsequent chapters because the Alfvén waves we will study are confined in at least one spatial direction perpendicular to \mathbf{B}_0 , either by the auroral oval or by individual auroral arcs.

To begin we assume a homogeneous plasma with a background magnetic field $\mathbf{B}_0 = B_0\hat{z}$. We allow the propagation vector to have along- \mathbf{B}_0 and off- \mathbf{B}_0 components: $\mathbf{k} = k_x\hat{x} + k_z\hat{z}$. Thus we may assume that all field quantities vary as $\exp(i\omega t - ik_x x - ik_z z)$. In this case, Maxwell's wave equation

$$\nabla \times \nabla \times \mathbf{E} + \mu_0 \frac{\partial \mathbf{J}}{\partial t} + \frac{1}{c^2} \frac{\partial^2 \mathbf{E}}{\partial t^2} = 0 \quad (2.11)$$

can be expressed in component form as follows:

$$x: k_z^2 E_x - k_x k_z E_z + i \omega \mu_0 J_x - \frac{\omega^2}{c^2} E_x = 0 \quad (2.12a)$$

$$y: (k_x^2 + k_z^2) E_y + i \omega \mu_0 J_y - \frac{\omega^2}{c^2} E_y = 0 \quad (2.12b)$$

$$z: k_x^2 E_z - k_x k_z E_x + i \omega \mu_0 J_z - \frac{\omega^2}{c^2} E_z = 0 \quad (2.12c)$$

To solve for the Alfvén wave dispersion relations, we need to express the currents J_x , J_y , and J_z in terms of the electric field components. For the two currents perpendicular to \mathbf{B}_0 , J_x and J_y , we can use the expression for the polarization current from Equation (2.10). The polarization current cannot operate parallel to \mathbf{B}_0 , so we need to refer to the particle equations of motion to find the current:

$$\frac{dv_{j,z}}{dt} = \frac{q_j}{m_j} E_z \quad (2.13)$$

The subscript j is a species index. Using $J_z = nev_z$, we obtain (neglecting $m_e \ll m_i$)

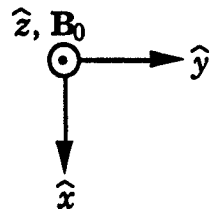
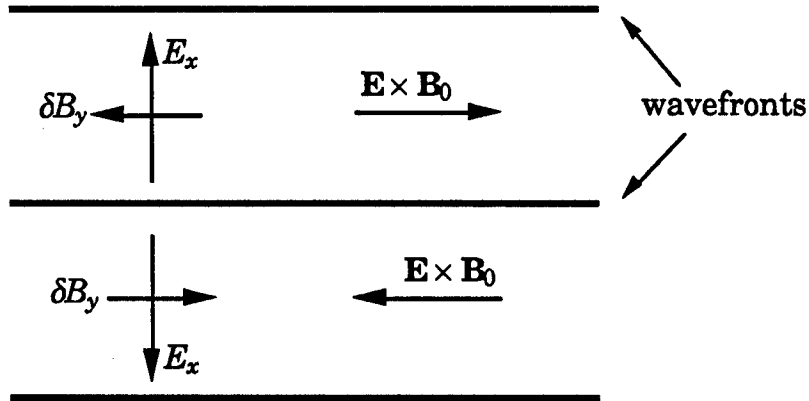
$$J_z = \frac{\omega_{pe}^2}{i\omega} \epsilon_0 E_z \quad (2.14)$$

Notice that since E_x and E_y are decoupled in Equations 2.12, the two resulting wave modes are linearly polarized. We are now ready to eliminate E_x and E_z from (2.12a) and (2.12c) to find the dispersion relation for Alfvén waves with the perpendicular electric field E_x in the same direction as the across- \mathbf{B}_0 component of the propagation vector, k_x . The geometry of this case is illustrated in the top part of Figure 2.3, and the corresponding dispersion relation is

$$k_z^2 = \frac{\omega^2}{V_A^2} \left(1 + k_x^2 c^2 / \omega_{pe}^2 \right) \text{ (slow mode)} \quad (2.15)$$

Oblique Propagation of Alfvén Waves
 $\mathbf{k} = k_x \hat{x} + k_z \hat{z}$

Slow Mode: $k_z^2 = \omega^2/V_A^2$



Fast Mode: $k_z^2 = \omega^2/V_A^2 - k_x^2$

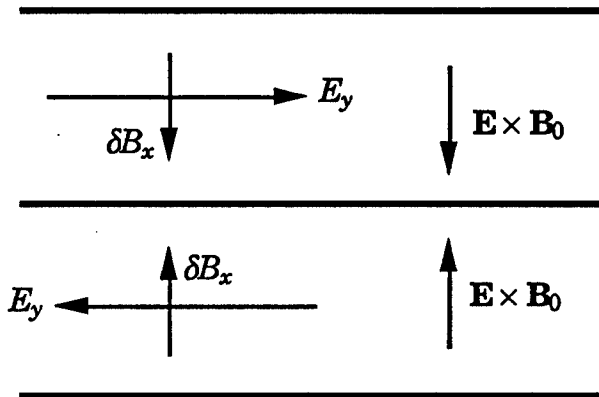


Figure 2.3 The two Alfvén wave modes as defined by Stix [1962]. For typical auroral parameters the fast mode is evanescent, causing the meridional electric field E_x to dominate.

This mode is referred to in the literature either as the "slow mode" or the "shear mode" Alfvén wave [Stix, 1962]. The term "slow mode" comes from the fact that (neglecting for convenience $k_x^2 c^2 / \omega_{pe}^2 \ll 1$) (2.15) can be re-written $\omega/k = V_A \cos(\theta)$, where θ is the angle between \mathbf{k} and \mathbf{z} . The phase velocity ω/k becomes arbitrarily small as the propagation direction becomes perpendicular to \mathbf{B}_0 . Note however that the projection of the phase velocity *along* \mathbf{B}_0 is always V_A . The reason for the term "shear mode" can be seen in Figure 2.3. Since the perpendicular electric field is along \mathbf{x} , the plasma will $\mathbf{E} \times \mathbf{B}$ drift along \mathbf{y} . But the direction of the drift reverses in alternating phases of the wave as one moves along \mathbf{x} , causing the $\mathbf{E} \times \mathbf{B}$ drift to be sheared.

When the electric field is in the \mathbf{y} direction, the $\mathbf{E} \times \mathbf{B}$ drift is along \mathbf{x} , and from the bottom part of Figure 2.3 one can see that there is a non-zero divergence or *compression* in the $\mathbf{E} \times \mathbf{B}$ drift. For this case the Alfvén wave is referred to as "compressional" or "fast." We will use the latter term. The dispersion relation follows directly from (2.12b):

$$k_z^2 = \frac{\omega^2}{V_A^2} - k_x^2 \quad (\text{fast mode}) \quad (2.16)$$

The interesting thing about (2.16) is that if k_x is larger than ω/V_A , k_z becomes imaginary. Thus the fast mode is evanescent at low frequencies, much as an electromagnetic wave in a waveguide cannot propagate below the cutoff frequency. This phenomenon lends insight to the auroral ionosphere. Structuring in the aurora is usually in the N-S (or meridional) direction, with the arcs and associated electric potentials elongated in the zonal (E-W) direction. To a first approximation we can ignore zonal variations and choose $\lambda_x = 2\pi/k_x$ to be between 1 km (roughly the minimum meridional thickness of an auroral arc) and 1000 km (the

width of the auroral oval). Using typical ion densities in the ionosphere, we find that Alfvén waves contained in the auroral oval are below the fast mode cutoff for $f = \omega/2\pi$ less than 1 Hz. In other words, if we assume that the wave properties do not vary in the zonal direction, the result is that the normal mode with a zonal electric field cannot propagate, leaving only the meridional electric field in the slow mode. Spacecraft measurements confirm that the meridional electric field is dominant in the aurora, although to be sure most studies assume that this field is quasi-static. One of our goals is to find the relative importance of static versus Alfvénic electric fields. We will find in Chapter 4 that if we include the effect of collisions, the slow and fast modes are coupled, and slow mode Alfvén waves propagating into the auroral ionosphere from above will drive the fast mode in the E-region, giving a non-zero zonal electric field (but which is still much smaller than the meridional electric field).

2.5 Kinetic Alfvén Waves and Parallel Electric Fields

There has been quite a bit of interest in the slow mode Alfvén wave (2.15) because it has associated with it an electric field parallel to \mathbf{B}_0 . As mentioned in Section 2.2, parallel electric fields are known to play an important role in one of the still unsettled problems concerning the aurora: the acceleration of auroral electrons through a large potential drop, often as much as 10 kV or more. Since ideally the conductivity parallel to \mathbf{B}_0 is infinite in a collisionless plasma, it is difficult to explain the presence of such a large potential drop for *tens of minutes*, which is roughly the lifetime of auroral arcs. Alfvén waves have been considered as a source of parallel electric fields because a finite parallel conductivity

is not required to maintain a parallel electric field. E_z is created as a result of the inertia of the electrons which carry the current J_z . This can be shown from the z component of Ampere's Law, using (2.14) to eliminate J_z in favor of E_z :

$$k_x B_y = \frac{\omega_{pe}^2}{c^2} \cdot \frac{E_z}{\omega} \quad (2.17)$$

The electron mass and therefore the inertial effect is contained in the electron plasma frequency ω_{pe} . The term "kinetic Alfvén wave" is used to describe waves for which k_x is large enough so that electron dynamics along B_0 affect the phase velocity of the slow mode, and allow for finite E_z as indicated in (2.17). Unfortunately, if we assume $\omega = 2\pi/(10$ minutes) as a representative auroral arc frequency, then inserting even "optimistic" values into (2.17) will not yield nearly enough of a parallel electric field to explain electron acceleration in auroral arcs. However, C. Seyler [personal communication, 1990] has suggested that the electrons associated with an arc drifting in the meridional direction with velocity V_d will experience an effective frequency $\omega = k_x V_d$. The electromagnetic skin depth c/ω_{pe} is representative of the smallest horizontal scales associated with auroral arcs (~ 1 km) so setting $\lambda_x = c/\omega_{pe}$ allows us to estimate an upper limit for E_z using (2.17),

$$E_z = V_d B_y \quad (2.18)$$

A typical arc drift in the ionosphere is a few hundred m/s, and when mapped up to the electron acceleration region it is near 1 km/s. Spacecraft routinely measure zonal magnetic fields of a few hundred nT. Thus a hundred μ V/m parallel electric field is possible in a drifting arc. This electric field must be maintained over at least 10,000 km to obtain kV

potential drops, which is possible. At present the debate over the auroral acceleration mechanism is continuing, and the importance of Alfvén waves versus other mechanisms has yet to be established.

So far in this review of Alfvén waves we have assumed that the electrons are cold. However, this assumption breaks down when the thermal velocity of electrons v_{th} is fast enough so the electrons can shield parallel potential variations. This requires that $v_{th} \gg V_A$, or equivalently $\beta \gg m_e/m_i$. (β is the ratio of the electron pressure nkT_e to the magnetic field pressure $B_0^2/2\mu_0$.) When this is satisfied the electrons will adjust to the wave potential ϕ according to a Boltzmann distribution:

$$n_e = n_0 \exp(e\phi/kT_e) \quad (2.19)$$

For small ϕ we can expand this and differentiate with respect to z to obtain

$$\frac{\partial n_e}{\partial z} = -n_0 e E_z / kT_e \quad (2.20)$$

We're interested in small horizontal scales (as we will see in the result), so we can neglect $k_z \ll k_x$ in the equation of current continuity

$$\nabla \cdot \mathbf{J} + \frac{\partial \rho_c}{\partial t} = 0 \quad (2.21)$$

which results in

$$-ik_x J_x = i\omega(\delta n_e)e \quad (2.22)$$

We can use the polarization current from (2.10) to eliminate J_x , and (2.20) to substitute E_z for δn_e , which gives

$$E_z = -k_x k_z \rho_i^2 E_x \quad (2.23)$$

where $\rho_i = c_s / \Omega_i$ is the ion gyro radius. Finally, this combined with (2.12a) gives the dispersion relation for kinetic Alfvén waves with $\beta \gg m_e/m_i$:

$$\frac{\omega^2}{k_z^2} = V_A^2 (1 + k_x^2 \rho_i^2) \quad (2.24)$$

This dispersion relation was derived by *Hasegawa* [1977] and was applied to the aurora by *Goertz and Boswell* [1979]. Notice the similarity to the cold plasma dispersion relation in (2.15), with the ion gyro radius ρ_i replacing the electromagnetic skin depth c/ω_{pe} as the horizontal length scale at which the phase velocity is significantly different from the plane Alfvén wave case, and also the scale at which the parallel electric field becomes important. However, a large k_x causes an increase in the phase velocity ω/k_z in (2.24), but a decrease in (2.15).

To estimate the electric field let $k_x \rho_i = 1$ in (2.23), which corresponds to Alfvén waves with horizontal scales on the order of 1 km. In this case $E_z/E_x = k_z/k_x$. If we assume as before a drifting arc which generates in the arc frame a frequency $\omega = k_x V_d$ then $E_z/E_x = V_d/\sqrt{2} V_A$. Perpendicular electric fields of hundreds of mV/m, arc drifts of hundreds of m/s, and Alfvén velocities appropriate for a low density ($n_e \sim 100$) hydrogen plasma can produce parallel electric fields on the order of 100 μ V/m, just as in the cold plasma case. If Alfvén waves associated with drifting arcs are responsible for auroral electron acceleration, then the mechanism should be able to operate over a range of temperatures. In particular, we have shown that the cases $\beta = 0$ and $\beta \gg m_e/m_i$ can generate similar parallel electric fields. However, in obtaining this

result we have assumed in the cold plasma case that $\lambda_x = c/\omega_{pe}$, and in the warm case that $\lambda_x = \rho_i$. (The cold approximation is probably more relevant for auroral acceleration.) For nominal parameters the proton gyroradius in the acceleration region is roughly a factor of 10 smaller than c/ω_{pe} , and one can compare (2.23) and (2.17) with the aid of the appropriate dispersion relations (2.15 and 2.24) to find $E_{z,cold}/E_{z,warm} \approx c^2/\omega_{pe}^2 \rho_i^2$. Thus for a fixed horizontal scale the electric field in the cold plasma case is larger. We have not treated the intermediate case $0 < \beta < m_e/m_i$, but it is reasonable to assume that the magnitude of parallel electric fields from waves in this regime would fall somewhere between the cases we have studied.

2.6 Alfvén Waves and Magnetosphere-Ionosphere Coupling

The simplest (and often entirely sufficient) approach to M-I coupling comes from thinking of a voltage generator in the magnetosphere (e.g. the MHD generator from the solar wind-magnetosphere interaction) applying an electric field \mathbf{E}_\perp which maps to the ionosphere and drives a Pedersen current in the ionosphere $\mathbf{J}_\perp = \sigma_p \mathbf{E}_\perp$ where σ_p is the Pedersen conductivity. (These relationships will be discussed in more detail in the next chapter). Any horizontal divergence of this current in the ionosphere must be closed by field-aligned currents to and from the magnetosphere as required by current continuity (see Section 3.6).

This simple model breaks down for many reasons. Vickrey *et al.* [1986] found that at horizontal scales between 3 and 80 km the magnetosphere acts more like a current source than a voltage source. This has important consequences concerning the boundary conditions appropriate for simulations of M-I coupling, as discussed by Lysak [1986].

Weimer et al. [1985] simultaneously measured electric fields at two altitudes with the DE 1 and 2 spacecraft and found that even for static electric fields, field line mapping in the collisionless region above the ionosphere is ineffective for horizontal scales below 100 km. This result stems from the presence of the parallel electric fields and the requirement that static electric fields must be curl-free. In this thesis we will discuss other complications in the simple coupling model above which result from neutral winds in the ionosphere and time varying electric fields.

Mallinckrodt and Carlson [1978] were among the first to realize that any changes in either the magnetospheric generator or ionospheric load must be communicated along magnetic field lines by Alfvén waves. They modeled the wave as it propagated towards the ionosphere through the changing refractive index which results from the Earth's dipole magnetic field and the increasing plasma density. The ionosphere is treated as a slab of conducting material characterized by its integrated conductivity Σ_p that causes a reflected wave resulting from the mismatch between Σ_p and the intrinsic impedance of Alfvén waves above the ionosphere. They also pointed out that incident and reflected Alfvén waves with small horizontal scales will only interfere close to the ionosphere, because plasma convection will carry the reflected wave away from the incident part.

Goertz and Boswell [1979] looked in detail at the front edge of an electric field pulse applied suddenly in the magnetosphere. They showed that such a pulse will propagate at the Alfvén velocity and that a parallel fringing field will exist at the leading edge of the pulse. If the pulse reflects enough times between the ionosphere and magnetosphere it can

repeatedly accelerate electrons. *Lysak and Carlson* [1981] showed that for Alfvén wave pulses with typical parameters, electrostatic ion cyclotron wave turbulence can cause large effective collision frequencies along \mathbf{B} in the magnetosphere. *Lysak and Dum* [1983] included the effects of this turbulence in a time-dependent MHD simulation of Alfvén wave propagation and found that a magnetospheric region of wave turbulence can support parallel electric fields and decouple the magnetospheric generator from an ionospheric load. This decoupling may be a useful idea in explaining the fact that arcs are often found to drift at a velocity not equal to the $\mathbf{E} \times \mathbf{B}$ drift velocity in the ionosphere. *Lysak* [1986] further improved on these MHD simulations by dynamically changing the conductivity of the ionosphere as a result of energetic electrons incident from above, creating a feedback effect between the magnetosphere and ionosphere.

Tests of these competing and complimentary theories are suffering from an absence of experimental data pertaining to the relative importance of quasi-static and electromagnetic coupling. One of the primary goals of this thesis is to fill this experimental gap.

CHAPTER 3

MEASURING ENERGY COUPLING BETWEEN THE MAGNETOSPHERE AND HIGH-LATITUDE IONOSPHERE

3.1 Introduction

Energy is efficiently transferred between the solar wind-magnetosphere system and high-latitude ionosphere because of the geomagnetic field $\mathbf{B}_0 = B_0 \hat{z}$. The magnetic field facilitates energy exchange in two ways. First, in the absence of electric fields perpendicular to \mathbf{B}_0 the field lines constrain charged particle motion to the \hat{z} direction, and in this chapter we will show, in agreement with previous work (e.g. *Foster et al.* [1983]), that the resulting field-aligned flux of kinetic energy integrated over the high-latitude region can exceed 10^{10} W. The second mode of energy transfer is electrical. Magnetic field lines act as "wires" that carry electrical current to the ionosphere, where Joule heating in the dense, partially ionized medium dissipates the incident energy. *Vickrey et al.* [1982] showed that although the daily averages of the energy flux from particles and Joule heating are comparable in the auroral oval, there is a tendency for the two to be anticorrelated. Based on Chatanika incoherent scatter radar measurements, those authors found the morning sector (westward electrojet) particle energy deposition rate to be generally larger than that in the pre-midnight sector eastward electrojet. The Joule heating rate has the opposite asymmetry about midnight.

This tendency for anticorrelation has one straightforward explanation. Where the particle flux is relatively energetic, as it is in the morning sector as compared to the evening sector, ionization is produced at lower altitudes. At these altitudes the conductivity tensor is such that electric fields and associated currents are mostly perpendicular to each other, which limits the Joule dissipation $\mathbf{J} \cdot \mathbf{E}$. (We will discuss the conductivity tensor in detail in the next section.) When precipitating electrons are less energetic, they increase the plasma density at somewhat higher altitudes, where \mathbf{J} and \mathbf{E} are more nearly parallel. Thus, less kinetic energy deposition leads to more Joule dissipation [Kelley *et al.*, 1990].

This interrelationship is likely more than coincidental. It is reasonable to expect that the ionosphere/magnetosphere system operates in a feedback mode. For example, Joule heating requires field-aligned currents, and when these currents exceed a certain threshold various plasma waves can become destabilized. The waves may then convert electrical to kinetic energy through wave/particle interactions, which might explain the anticorrelation between kinetic and electrical energy deposition rates in the ionosphere.

The possibility for such an important interrelationship between electrical and kinetic energy input to the ionosphere is one of the reasons for the study we have conducted. In addition, on a global scale Joule heating is thought to be larger than particle energy deposition because it is spread over a wider range of latitudes. In the summer polar cap, for example, when B_z is southward, considerable Joule heating occurs while any particles that precipitate are generally soft. It is crucial therefore to

develop remote sensing techniques to determine the Joule heat input to the upper atmosphere.

Sensing of particle precipitation is straightforward and is regularly performed by polar orbiting spacecraft. The electromagnetic input, on the other hand, is not routinely monitored and its estimation usually requires severe approximations such as neglect (or very simplistic modeling) of the atmospheric wind; e.g. *Vickrey et al.* [1982]. In this chapter we show that the electromagnetic energy flux into the atmosphere can be reliably measured remotely by polar orbiting spacecraft at altitudes in the range 400-1000 km using the vertical component of the Poynting flux, and we present examples of its measurement using both the HILAT satellite and a sounding rocket. Since this measurement is of a local quantity, no assumptions are required concerning the relative orientation of the spacecraft velocity and current sheets such as are needed in determination of Birkeland currents. Moreover, knowledge of the ionospheric conductivity and conductivity gradients are not necessary for the measurement of the energy input.

The concept of the Poynting flux as a diagnostic tool in the study of time-varying electromagnetic waves is well established. As discussed by *Feynman et al.* [1964], under certain circumstances the Poynting flux provides a valid conceptual measure of energy flow even for steady or DC electric and magnetic fields. In Section 3.2 we give a brief derivation and a discussion of the concept as applied to geophysical systems. We show that a local measurement of $(\delta E_{\perp} \times \delta B_{\perp})/\mu_0$ at typical ionospheric satellite altitudes yields the local electromagnetic power input to the Earth's atmosphere. It is important to note that no geometric assumptions are

necessary to find this quantity, unlike those required to determine, say, J_z from magnetic field measurements along a trajectory. That is, although $\mu_0 J_z$ can in principle be found from $\partial B_y / \partial x - \partial B_x / \partial y$, one must in practice neglect the y derivative for a satellite moving in the x direction. The Poynting flux technique can also be used to detect energy flow *out* of the Earth's ionosphere, which can occur where a neutral wind dynamo is present.

While measurements of kinetic and electrical energy flow between the magnetosphere and ionosphere are not new, the various methods used have their own advantages and problems which until recently have not been carefully compared. In this chapter, Sections 3.3 and 3.4 are devoted to a discussion of two methods for measuring the electrical energy flux at high latitudes. Later in the chapter we will present energy flow calculations using data from the HILAT satellite and from a sounding rocket. Our purpose will not be to present an exhaustive survey of energy flow measurements from spacecraft, but rather we will develop and compare techniques for doing so. We begin with a discussion of the theory behind these methods.

3.2 Techniques for Measuring Electromagnetic Energy Flow Between the Ionosphere and Magnetosphere

A satellite such as HILAT, with the capability to measure electric and magnetic fields simultaneously, can be a very useful tool to monitor the rate of electromagnetic energy flow into or out of the ionosphere at the magnetosphere-ionosphere interface. However, as with any measurement of a physical parameter, the process is imperfect and we must anticipate the various complications and errors which will arise.

We will begin with a simple model of the magnetosphere/ionosphere energy exchange. We limit our discussion to high latitudes, so we can assume that the geomagnetic field \mathbf{B}_0 is vertical. In this chapter we will assume that the energy sources are constant in time, but we will relax this requirement in Chapter 4. And we will first treat the case in which there is no neutral wind.

In the static case, the amount of electromagnetic energy generated or dissipated in some volume V is the Joule dissipation:

$$W = \iiint_V \mathbf{J} \cdot \mathbf{E} \, dV \quad (3.1)$$

The plasma fluid equations allow us to relate the current density \mathbf{J} and electric field \mathbf{E} through the conductivity tensor σ :

$$\mathbf{J} = \sigma \cdot \mathbf{E} \quad (3.2)$$

where

$$\sigma = \begin{pmatrix} \sigma_P & \sigma_H & 0 \\ -\sigma_H & \sigma_P & 0 \\ 0 & 0 & \sigma_0 \end{pmatrix} \quad (3.3)$$

and

$$\sigma_0 = \varepsilon_0 \sum_j \frac{\omega_{pj}^2}{v_j} \quad (3.4a)$$

$$\sigma_P = \varepsilon_0 \sum_j \frac{v_j \omega_{pj}^2}{v_j^2 + \Omega_j^2} \quad (3.4b)$$

$$\sigma_H = \varepsilon_0 \sum_j \frac{\Omega_j \omega_{pj}^2}{v_j^2 + \Omega_j^2} \quad (3.4c)$$

j is a species index and σ_0 , σ_P , and σ_H are known as the direct (or specific), Pedersen, and Hall conductivities respectively. We will derive a generalized version of σ in Chapter 4 which allows for time variation of field quantities.

Although σ_0 is generally much larger than σ_P or σ_H , the field-aligned electric field E_z is much smaller than E_x and E_y for the range of physical parameters that are of interest to us, and we can safely neglect the dissipation term $J_z E_z$. One consequence of the small electric field parallel to \mathbf{B}_0 is that the perpendicular fields are approximately constant along \mathbf{B}_0 . This allows us to carry out the z integration in (3.1) to obtain

$$W = \iint_A \Sigma_p (E_x^2 + E_y^2) dx dy \quad (3.5)$$

where

$$\Sigma_p = \int_{ionosphere} \sigma_p dz \quad (3.6)$$

Equation (3.5) can be used to estimate the energy dissipated in the ionosphere. Since the electric field maps along \mathbf{B}_0 , it can be measured either by satellites or sounding rockets in or above the ionosphere, or by high altitude balloons since the electric field maps into the lower atmosphere [Mozer and Serlin, 1969]. Σ_p is more difficult to determine since it requires altitude profiles of the plasma and neutral atmosphere densities. Ionospheric plasma at high latitudes can be produced by electron precipitation from the magnetosphere in an unpredictable and time dependent manner, and once produced the plasma can quickly convect away. Thus without a direct measurement from an incoherent

scatter radar, for example, estimates of Σ_P are limited by poor knowledge of the plasma density.

Poynting's theorem can be used to eliminate the need for a Σ_P estimate in ionospheric energy deposition measurements as long as the magnetic field can be measured at the same time as the electric field. We give a formal derivation of Poynting's theorem and an example of its application to energy dissipation in a simple resistor in Appendix A. Poynting's theorem states that

$$W = \iint_A \mathbf{S} \cdot d\hat{s} = \iiint_V \left(\mathbf{J} \cdot \mathbf{E} + \mathbf{E} \cdot \frac{\partial \mathbf{D}}{\partial t} + \mathbf{H} \cdot \frac{\partial \mathbf{B}}{\partial t} \right) dV \quad (3.7a)$$

where $\mathbf{S} = (\mathbf{E} \times \mathbf{B})/\mu_0$, the vector $d\hat{s}$ is normal to an element of surface area and points into the volume V everywhere, \mathbf{D} is the electric flux density, and \mathbf{H} is the magnetic field intensity. In the case of DC energy flow, $\partial/\partial t = 0$ and thus

$$W = \iint_A \mathbf{S} \cdot d\hat{s} = \iiint_V \mathbf{J} \cdot \mathbf{E} dV \quad (3.7b)$$

For our application to the problem of magnetosphere-ionosphere coupling, we first consider the volume enclosed by the surface of the Earth and a "cap" covering all latitudes above say 50 degrees. The cap is located at an altitude that is not crucial but which is between 400 and 1000 km. (Below, we assume that it is the HILAT satellite's orbital altitude of 800 km.) This height is chosen to be high enough that particle collisions are rare but below any region of significant field-aligned electric fields associated with the aurora.

We assume that the zonal component of the perpendicular electric field goes smoothly to zero at the boundary of this region, that the magnetic field lines are everywhere vertical, and we ignore curvature of the magnetic field lines over this height range. The volume of interest, shown in Figure 3.1, is then bounded by the high altitude cap, S_1 , the surface of the Earth, S_2 , and the surface S_3 linking the cap and the Earth. Since the Earth is a good conductor the electric field vanishes on S_2 and the Poynting flux is zero across it. If no thunderstorms are located near the boundary then we can assume that the fair weather electric field is vertical and the Poynting flux across S_3 is also zero. This implies that the entire electromagnetic power dissipated in the volume may be found by integrating the Poynting flux across S_1 . Since S_1 is perpendicular to \mathbf{B}_0 , the power input to the Earth's atmosphere in the high latitude zone is given by

$$W = \frac{1}{\mu_0} \iint_{S_1} (\mathbf{E}_\perp \times \delta\mathbf{B}_\perp) \cdot d\hat{s} \quad (3.8)$$

where \mathbf{E}_\perp is the perpendicular electric field on S_1 and $\delta\mathbf{B}_\perp$ is the deviation of the total magnetic field from the undisturbed value in the plane perpendicular to \mathbf{B}_0 .

We now argue that the cross product of these two quantities gives the local value of the energy flow rate into the atmosphere. Consider an infinitesimal element of the surface S_1 and the volume it subtends between S_1 and the Earth. The contribution at the Earth vanishes as before. Since we know that the flow in the high altitude ionosphere is incompressible, it follows that the integral of $(\mathbf{E}_\perp \times \delta\mathbf{B}_\perp) \cdot d\hat{s}$ over the sides of the volume vanishes there. Furthermore, since large scale DC electric fields map without distortion along field lines into and through the E

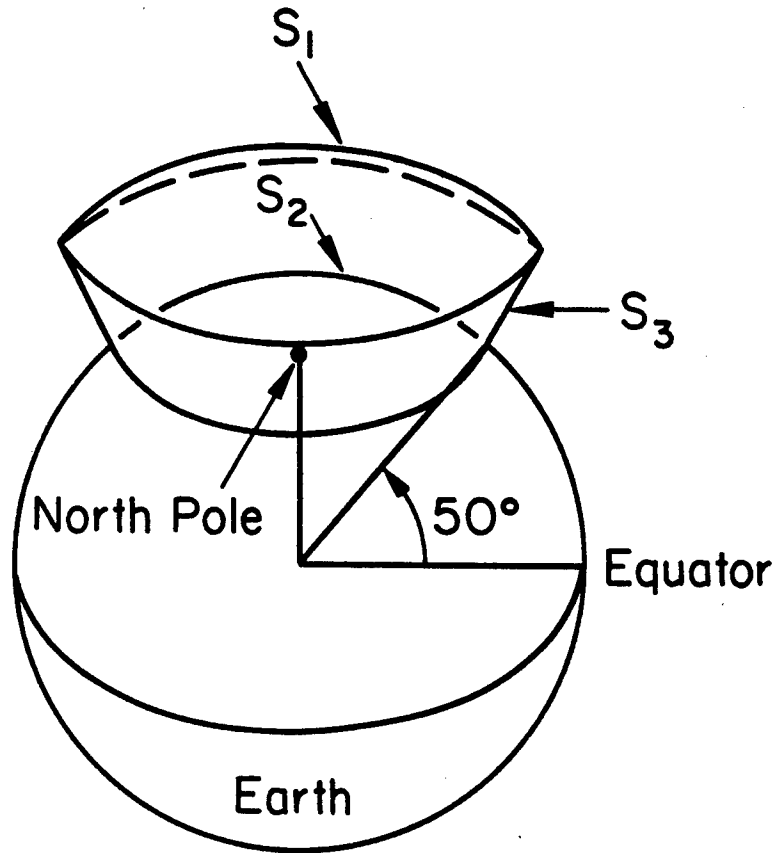


Figure 3.1 S_1 is the surface through which magnetospheric Poynting flux \mathbf{S} enters the upper atmosphere. S_2 is the Earth's surface, which is a good conductor and therefore requires $E_\perp = 0$ and hence $\mathbf{S} = 0$. Assuming that the magnetic field lines are straight and vertical, and the fair weather electric field is vertical implies that $\mathbf{S} \cdot \mathbf{n}_3 \equiv 0$ where \mathbf{n}_3 is a unit vector normal to the surface S_3 .

region and vertically deep into the atmosphere [Mozer and Serlin, 1969], where they go smoothly to zero near the Earth's surface, the integral of $(\mathbf{E}_\perp \times \delta \mathbf{B}_\perp) \cdot d\mathbf{s}$ vanishes on these edges as well.

This discussion of the amount of Poynting flow across various surfaces of the volume in Figure 3.1 is necessary because we need to establish that by integrating the Poynting flux across the high altitude surface S_1 we are actually measuring a *divergence* in the Poynting flux -- i.e. Poynting flux is entering the ionosphere from above, but it can't "escape" from the sides (S_2) or through the Earth's surface (S_3). A single measurement of Poynting flux alone can be meaningless. For example, imagine placing a net electrical charge on the surface of the Earth, which would cause a radial electric field. At the magnetic equator the Earth's dipole field \mathbf{B}_0 crossed into the radial electric field gives a non-zero Poynting vector \mathbf{S} . However, if we integrate \mathbf{S} over any closed surface we find no divergence and therefore no net dissipation or generation of electrical power, as we can see from the definition of \mathbf{S} with the aid of a vector identity:

$$\mu_0 \nabla \cdot \mathbf{S} \equiv \nabla \cdot (\mathbf{E} \times \mathbf{B}_0) = \mathbf{B}_0 \cdot (\nabla \times \mathbf{E}) - \mathbf{E} \cdot (\nabla \times \mathbf{B}_0) \quad (3.9)$$

In the case at hand $\nabla \times \mathbf{E} = 0$, $\nabla \times \mathbf{B}_0 = \mu_0 \mathbf{J} = 0$, and $\nabla \cdot \mathbf{S} = 0$. Only when there is a non-zero current \mathbf{J} can there be a net divergence of Poynting flux for a steady state system. We will show with a specific example in Section 3.6 that Poynting flux into the ionosphere is associated with Birkeland (field-aligned) currents that close as Pedersen currents.

3.3 The Role of the Neutral Winds in Energy Flow

Thus far we have assumed that all of our measurements are made in the Earth-fixed reference frame and that the neutral wind is zero. We

have presupposed an externally applied electric field and studied the energy dissipated in a conducting ionosphere. If the neutral atmosphere is in motion however, it can also be a source of electric current and Poynting flux. In fact if we examine the case with an external medium acting as a passive load with an effective height-integrated conductivity Σ_E , a wind generated current source yields an upward Poynting flux above the ionosphere, and the integral of $(\mathbf{E} \times \delta\mathbf{B}) \cdot d\mathbf{s}$ over the surface of the external load is equal to the volume integral of $\mathbf{J} \cdot \mathbf{E}$ within the load. In this case $\mathbf{J} \cdot \mathbf{E} < 0$ in the ionosphere, indicating that the neutral wind in the ionosphere is acting as a generator and supplying electrical energy to the external load. Even when the ionosphere is acting as a load, the neutral wind affects its interaction with any external energy sources. We will look at two examples of an ionospheric load with a neutral wind.

For the first example consider an external generator which applies an electric field E_G across geomagnetic field lines. The generator is not ideal and has associated with it an internal conductance which we model as a thin strip extended in y characterized by σ_G (mho/m) such that the potential across it and current density through it are related by $V\sigma_G = I$ (A/m), as shown in Figure 3.2. Magnetic field lines connect the generator to an ionospheric load region with height-integrated conductivity Σ_P and constant neutral wind U_y . We will treat the ionosphere as a simple slab, with $\Sigma_P = 0$ outside of the gray region. The current density in the \hat{x} direction is given by $J_x = \sigma_P(E_x + U_y B_0)$ (A/m²) in the ionosphere, and in the generator by $(E_x - E_G)d\sigma_G$ (A/m) where d is the width of the system in the \hat{x} direction. Current continuity requires

$$I = |\mathbf{I}| = \Sigma_P(E_x + U_y B_0) = (E_G - E_x)d\sigma_G \quad (\text{A/m}) \quad (3.10)$$

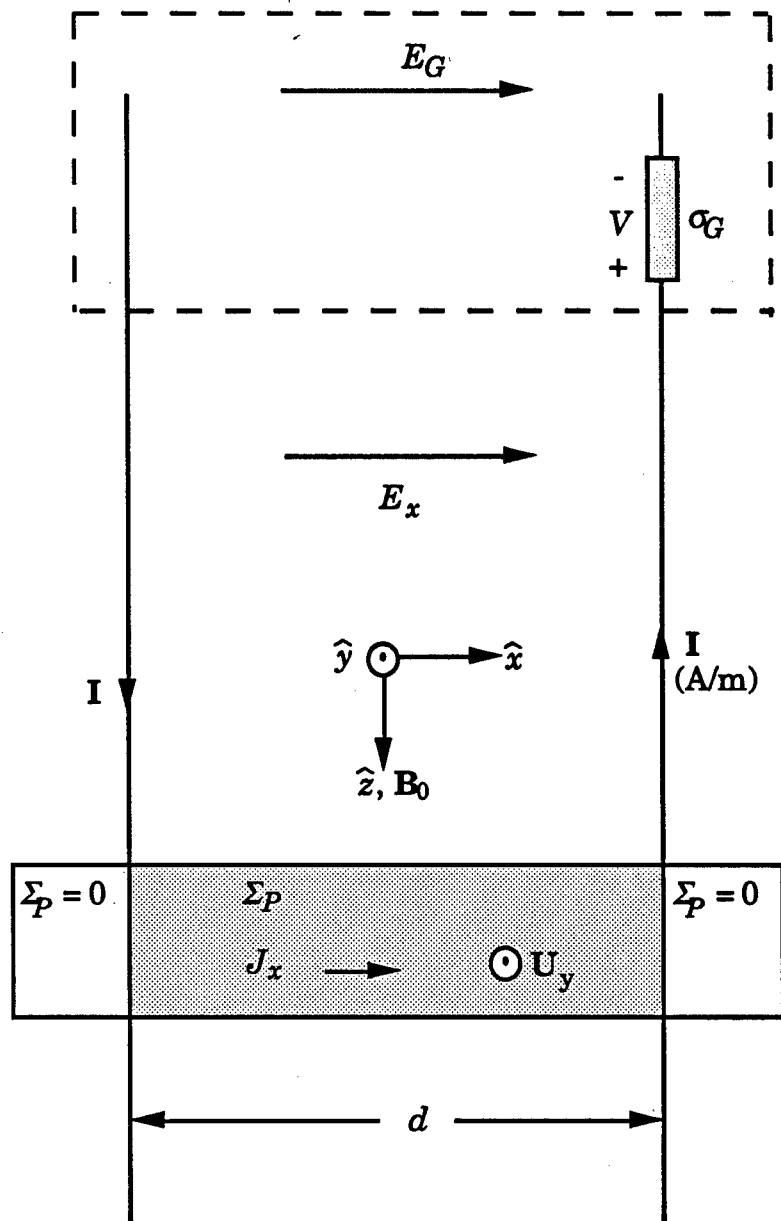


Figure 3.2 Cross-section in the meridional plane of a simplified model illustrating the effect of neutral winds on ionospheric dissipation of magnetospherically applied electric field energy.

with the direction of \mathbf{I} shown in the figure. The perturbation magnetic field at the center of the diagram, which is assumed to be very far from the cross field currents at either end, is $\delta\mathbf{B} = \mu_0 I_y$. The Poynting flux measured in the Earth-fixed frame is thus $\mathbf{S} = \mathbf{E} \times \delta\mathbf{B}/\mu_0 = \Sigma_P E_x (E_x + U_y B_0) \hat{z}$.

With (3.10) we can solve for $E_x = (dE_G \sigma_G - U_y B_0 \Sigma_P)/(\Sigma_P + d\sigma_G)$ which allows us to write the Poynting vector as

$$\mathbf{S} = \hat{z} \left(\frac{d\sigma_G \Sigma_P}{d\sigma_G + \Sigma_P} \right)^2 \left(\frac{E_G}{\Sigma_P} - \frac{U_y B_0}{d\sigma_G} \right) (E_G + U_y B_0) \quad (3.11)$$

Clearly for large σ_G the external source will dominate and the Poynting flux will be downward. Likewise for $E_G = 0$, electrical energy generated by the neutral wind will flow upward.

The \hat{z} component of the Poynting vector is equal to the height-integrated value of $\mathbf{J} \cdot \mathbf{E}$ in the ionosphere

$$\int_{ionosphere} \mathbf{J} \cdot \mathbf{E} dz = \Sigma_P E_x (E_x + U_y B_0) \quad (3.12)$$

$\mathbf{J} \cdot \mathbf{E}$ is the Joule dissipation when measured in the frame of the neutral wind, but in the present case we have written the electrodynamic quantities in a frame with a non-zero wind. We will now discuss the meaning of the quantity $\mathbf{J} \cdot \mathbf{E}$ in the presence of a neutral wind.

As long as the wind velocity is non-relativistic, the frame in which the magnetic field is measured does not matter. This can be seen from the equations which transform electric and magnetic fields from the neutral wind frame (primed coordinates) to the Earth-fixed frame (not primed), where the neutral wind velocity is \mathbf{U} :

$$\mathbf{E}' = \mathbf{E} + \mathbf{U} \times \mathbf{B} \quad (3.13a)$$

$$\mathbf{B}' = \mathbf{B} \quad (3.13b)$$

We have neglected $\mathbf{U} \times \mathbf{E}/c^2 \ll \mathbf{B}$. A discussion of these transformations can be found in Chapter 2 of *Kelley [1989]*. Equation (3.13b) implies that $\mathbf{J}' = \mathbf{J}$. With these transformations we can write the Joule dissipation $\mathbf{J}' \cdot \mathbf{E}'$ in the Earth-fixed frame as $\mathbf{J} \cdot (\mathbf{E} + \mathbf{U} \times \mathbf{B}_0)$. A vector identity allows us to write this as

$$\mathbf{J} \cdot \mathbf{E} = \mathbf{J}' \cdot \mathbf{E}' + \mathbf{U} \cdot (\mathbf{J} \times \mathbf{B}_0) \quad (3.14)$$

hence in a frame where the neutral wind is non-zero $\mathbf{J} \cdot \mathbf{E}$ can be interpreted as the Joule heat plus the work done on the neutral wind by the $\mathbf{J} \times \mathbf{B}$ force.

To summarize, in the presence of a neutral wind the Poynting flux measured by a satellite can determine the amount of energy flowing into or out of the ionosphere. If the neutral wind is acting as a generator, some of the energy will be dissipated by the ionosphere and the Poynting flux will measure only the net outward energy flow. Nonetheless, it is this very exchange of energy which is crucial in the study of magnetosphere-ionosphere coupling.

A potentially confusing aspect of Poynting flux measurements is the fact that their value depends on the reference frame in which they are measured. From Equations (3.13) we can see that the magnetic field does not change with reference frame but the electric field depends on the velocity of the measuring platform. We will consider one additional example which will help to clarify the reason for this.

Consider two ionospheres in conjugate hemispheres connected by the geomagnetic field \mathbf{B}_0 . Figure 3.3 shows the configuration with the

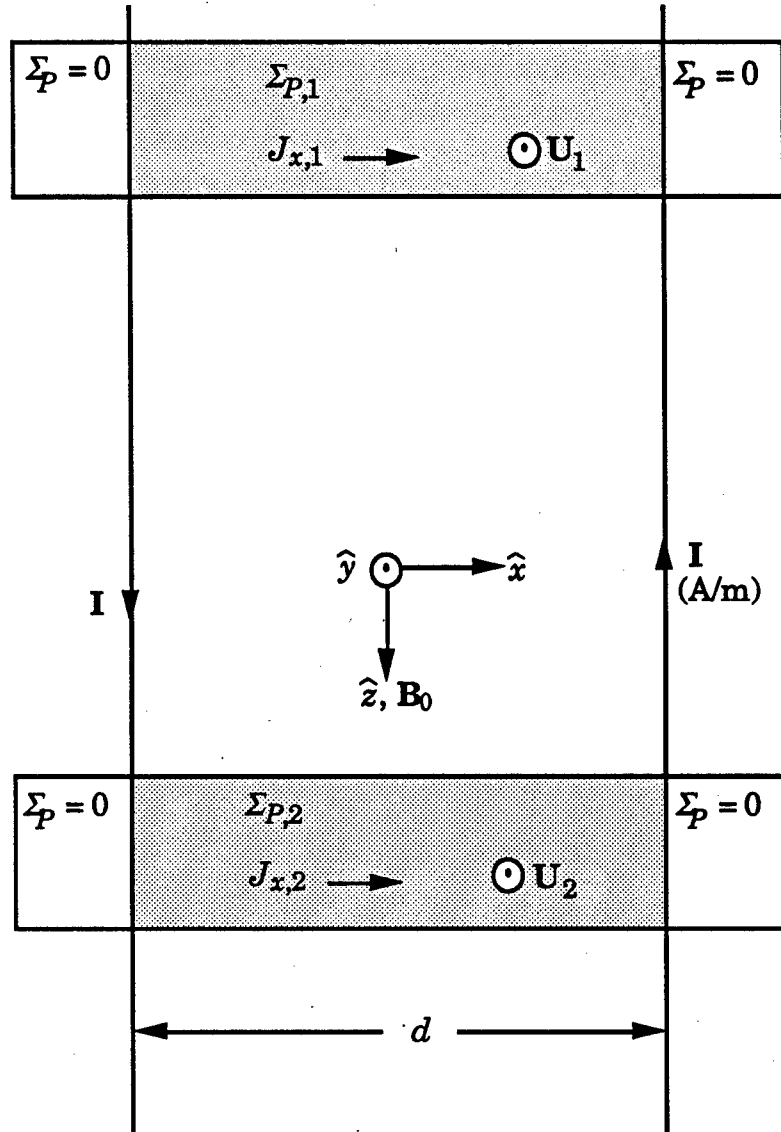


Figure 3.3 Cross-section in the meridional plane of a simplified model illustrating the interaction of neutral wind dynamos in conjugate hemispheres.

field lines straightened into a rectangular geometry. The two ionospheres are labeled "1" and "2" and each has its own height-integrated Pedersen conductivity $\Sigma_{P,j}$ and neutral wind $U_{y,j}$ where j indexes the ionospheres. The conducting region is limited in the x direction to a width d , and outside of this region we assume zero conductivity. All quantities extend infinitely in the y direction as before.

The neutral winds will carry plasma across geomagnetic field lines and in general will create some electric field E_x which will in turn drive currents in both ionospheres given respectively by

$$J_{x,j} = \sigma_{P,j} (E_x + U_{y,j} B_0) \quad (3.15)$$

Current continuity at the edges of the conducting troughs requires two infinite sheet currents

$$\mathbf{I} = -\Sigma_{P,1}(E_x + U_{y,1}B_0)\hat{z} = \Sigma_{P,2}(E_x + U_{y,2}B_0)\hat{z} \quad (3.16)$$

where again \mathbf{I} has units of A/m. This allows us to calculate the electric field as a function of the U_y :

$$E_x = -\frac{(\Sigma_{P,1}U_{y,1} + \Sigma_{P,2}U_{y,2})B_0}{\Sigma_{P,1} + \Sigma_{P,2}} \quad (3.17)$$

Using this with (3.16) allows us to solve for magnitude of the sheet currents:

$$|\mathbf{I}| = \frac{\Sigma_{P,1}\Sigma_{P,2}}{\Sigma_{P,1} + \Sigma_{P,2}} (U_{y,2} - U_{y,1}) B_0 \quad (3.18)$$

Electric fields and winds cause the ionospheric plasma to collide with neutral atmosphere particles which results both in increased temperature and changes in the bulk velocity of the neutral wind. The electromagnetic coupling between the two ionospheres will act to cause

the neutral winds to be equal eventually. If enough time passes so that they become equal, no current will flow between the two hemispheres, as we can see from (3.17).

In the case for which $U_{y,1} = 0$, the E_x generated by $U_{y,2}$ will act to accelerate the neutral wind in ionosphere "1" and the resulting drag on $U_{y,2}$ will slow it down. In the Earth-fixed frame it is natural to think of "2" as a generator and "1" as a load. Of course this is entirely dependent upon reference frame. If we happen to be traveling along with the neutral wind in "2" then the now non-zero wind in "1" will cause $U_{y,2}$ to accelerate, and the role of generator and load are reversed.

We will now calculate the Poynting flux that would be measured by a spacecraft flying between the two ionospheres. The magnetic perturbation caused by the current sheets is $\delta\mathbf{B} = \mu_0 I \hat{\mathbf{y}}$ and thus (assuming $\Sigma_{P,1} = \Sigma_{P,2}$ for simplicity) the resulting Poynting vector $E_x \delta H_{y,2}$ can be written

$$\mathbf{S} = \frac{\Sigma_P (U_{y,1}^2 - U_{y,2}^2) B_0^2}{4} \hat{\mathbf{z}} \quad (3.19)$$

Equation (3.19) tells us that if one of the ionospheres has zero neutral wind then the Poynting vector is directed towards it. This is consistent with the fact that a zero velocity neutral wind also has zero bulk kinetic energy. Thus any plasma motion driven by electric fields must increase the kinetic energy of the neutrals, and the neutral atmosphere acts as a load. The neutral wind in the conjugate hemisphere acts as a generator and the bulk kinetic energy of the neutral wind there decreases.

Of course in the case of an ionospheric load not all of the Poynting flux energy increases the bulk velocity of the neutrals, and likewise in a neutral wind generator not all of the kinetic energy supplied by the wind

appears as Poynting flux. In both cases the neutral gas and the plasma are heated. This leads us to interpret the Poynting vector measured above the ionosphere in the Earth-fixed frame as the rate at which electromagnetic energy from the magnetosphere is causing the neutral wind in the ionosphere (also measured in the Earth-fixed frame) to change its kinetic energy per unit area plus the rate at which that energy is heating the atmosphere:

$$\frac{1}{\mu_0} (\mathbf{E}_\perp \times \delta \mathbf{B}_\perp) = \frac{\partial}{\partial t} \left[\int_{ionosphere} \frac{\rho U^2}{2} dz + \Delta Q \right] \quad (3.20)$$

where ΔQ is the heat per unit volume supplied to the atmosphere and ρ is the mass density of the neutrals. We are neglecting the kinetic energy of the plasma since its density is many orders of magnitude less than the neutral density in the ionosphere. The Poynting vector is positive when directed towards the ionosphere.

The conclusion we can draw from the above discussion is that the Poynting vector $\mathbf{E}_\perp \times \delta \mathbf{B}_\perp / \mu_0$ measured in the Earth-fixed frame can be used to detect whether the neutral atmosphere below the measurement platform is gaining energy (i.e. is load-like) or losing energy (generator-like) *in the Earth-fixed frame*. Since the kinetic energy of the neutral wind depends on the velocity squared, its time rate of change depends on the neutral wind velocity, thus the time derivative of the kinetic energy and the Poynting vector are frame-dependent.

There are two situations which can cause $\mathbf{S} = 0$, namely $\mathbf{E}_\perp = 0$ and $\delta \mathbf{B}_\perp = 0$. In the first case there is still energy exchange between the ionosphere and a conjugate ionosphere or the magnetosphere if we move to a different frame. If $\delta \mathbf{B}_\perp = 0$ there is no energy exchange in *any* frame.

In this sense magnetic perturbations associated with field-aligned currents are more indicative of energy coupling to the ionosphere than are electric fields.

A disadvantage that Poynting flux measurements have is that the perturbation magnetic field $\delta\mathbf{B}_\perp$ is usually found by subtracting a model of the geomagnetic field \mathbf{B}_0 from the total field \mathbf{B} measured by the satellite magnetometer. Since \mathbf{B}_0 is roughly 40,000 nT and perturbations from field-aligned currents are typically several hundred nT, small errors in the model can greatly affect $\delta\mathbf{B}_\perp$ measurements. However, model errors manifest themselves as DC (or low frequency) offsets in $\delta\mathbf{B}_\perp$, thus in the following section we will ignore the Poynting flux from low-frequency fields by high-pass filtering the data.

3.4 Satellite Observations of Kinetic Energy and Poynting Flux

In this section we present examples of Poynting flux measurements in the high latitude ionosphere. The instruments used were not optimized for measurement of this parameter and yet the results are quite reasonable. We believe that when interpreted as discussed in the previous section that these examples support the idea that Poynting flux is a useful diagnostic quantity, and we hope that other researchers pursue this concept with more sensitive instruments and better behaved measurement platforms. Since the electric fields detected are considerably larger than UB_0 in the high latitude E region we will ignore neutral wind effects.

The first two examples come from the HILAT satellite. HILAT is a polar-orbiting, real-time satellite which means it cannot store data on board. Thus measurements are available only when the satellite is in

view of a ground receiving station. The data we will present were recorded at the station in Sondrestrom, Greenland (67° N), so each pass is centered about this geographic latitude. HILAT orbits at about 800 km with a velocity of 7.4 km/s, and it is in view of a ground station for about 10 minutes per pass, depending on its elevation angle at closest approach.

HILAT measures the vector magnetic field using a fluxgate magnetometer sampled at 20 s^{-1} and deduces the electric field from a cross-track ion drift meter switching between 16 and 32 s^{-1} . We have averaged the data to 1.5 s^{-1} . These and other instruments on HILAT are described in detail elsewhere [Potemra *et al.*, 1984; Rich *et al.*, 1984]. Since the satellite is in a high-inclination orbit (81°), its orbital velocity (defined to be in the x direction) is mostly meridional. z is taken to be downward, and y completes the right-hand system in HILAT coordinates. The cross-track ion drift allows one to calculate the meridional electric field. The in-track drift component yields the cross-track (zonal) electric field but is only available once per second since it requires a sweep of the retarding potential analyzer. In the auroral zone, the zonal electric field is generally much smaller than E_x and adds only a small correction to the Poynting flux found from the meridional electric field alone.

The spacecraft is gravity gradient stabilized but suffers attitude perturbations from thermal stress. Examples of the magnetic field data which we have used in the two satellite orbits presented here are given in Figure 3.4a and show the attitude problem very clearly. The upper panel shows magnetic field data obtained on Day 164, 1984. The sinusoidal modulation of the signal is due to one of the unfortunate attitude

HILAT Magnetic Field Data

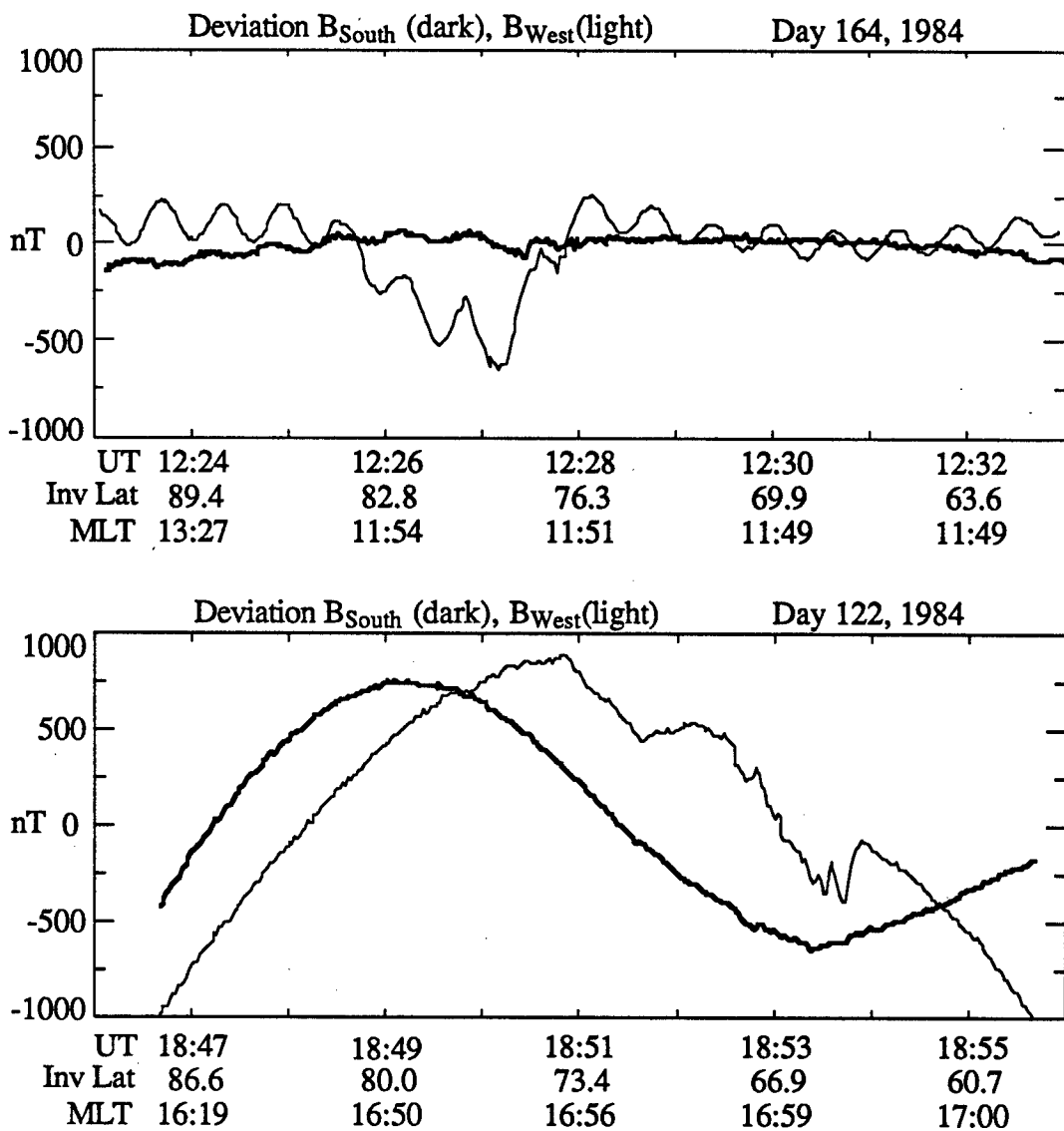


Figure 3.4a Meridional and zonal magnetic field perturbations for two HILAT passes. The 40 second variation in the Day 164 data and the longer period variation in the Day 122 data are due to attitude oscillations of the satellite. Superimposed on these are clear signatures of large-scale field-aligned currents.

oscillation modes of the spacecraft. Another mode is clearly seen in the second panel using data obtained on Day 122 of the same year. Here a very long period attitude oscillation is seen in the signal.

It is clear from both satellite passes that signals of geophysical significance are present. On both days the spacecraft passes through large scale regions of field-aligned current as ascertained from the derivative of the magnetometer signal, ignoring the sinusoidal oscillations of the satellite. In the analysis below we have filtered the signals to remove these perturbing influences. A notch filter (order 20 digital Butterworth) with a center frequency of .0286 Hz and a bandwidth of 0.01 Hz was used for Day 164; a high pass filter allowing only frequencies above 0.0029 Hz to contribute was used for both days. This necessary filtering precludes measurement of the largest scale size Poynting flux input to the high latitude system.

We will see that even after filtering out the lowest frequencies in the HILAT data, the Poynting flux is still mostly downward, which is what we would expect for an ionospheric load. One reason that filtering does not destroy the Poynting flux measurement is that the satellite is above the auroral oval for only a fraction of the entire pass, therefore perturbations associated with the auroral oval (and which represent most of the Poynting flux) are above the filter cutoff. The fractional orbit acquisitions from a real time satellite system such as HILAT are not suited for fully global measurements, and we are therefore restricted to studies such as auroral oval crossings. The electric field after filtering for these two passes is presented in Figure 3.4b.

The Poynting flux measured on Day 164 is presented in Figure 3.5a along with the field-aligned current and precipitating electrons in two

HILAT Electric Field from Ion Drift

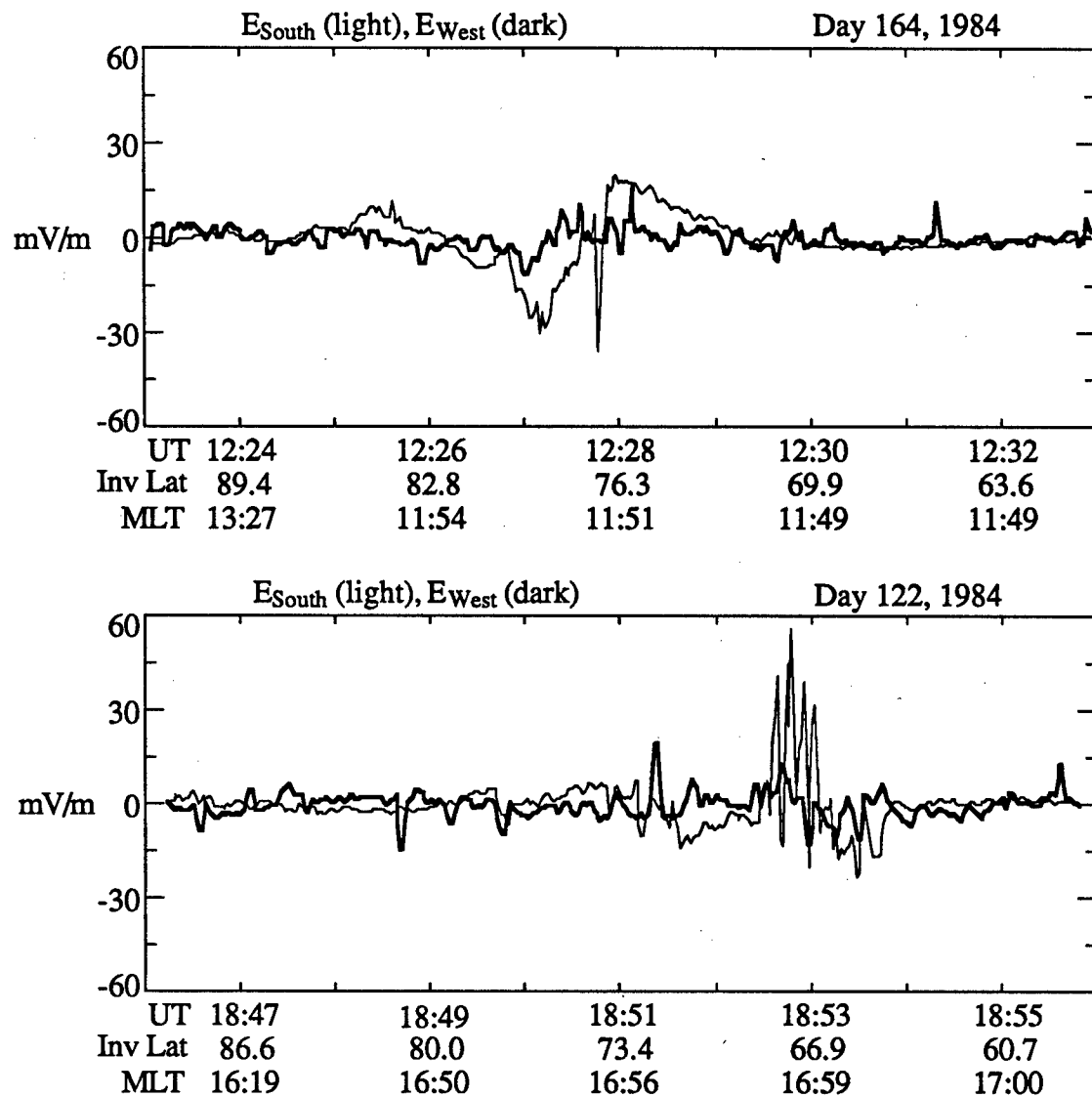


Figure 3.4b Meridional and zonal electric fields for the two HILAT passes shown in Figure 3.4a.

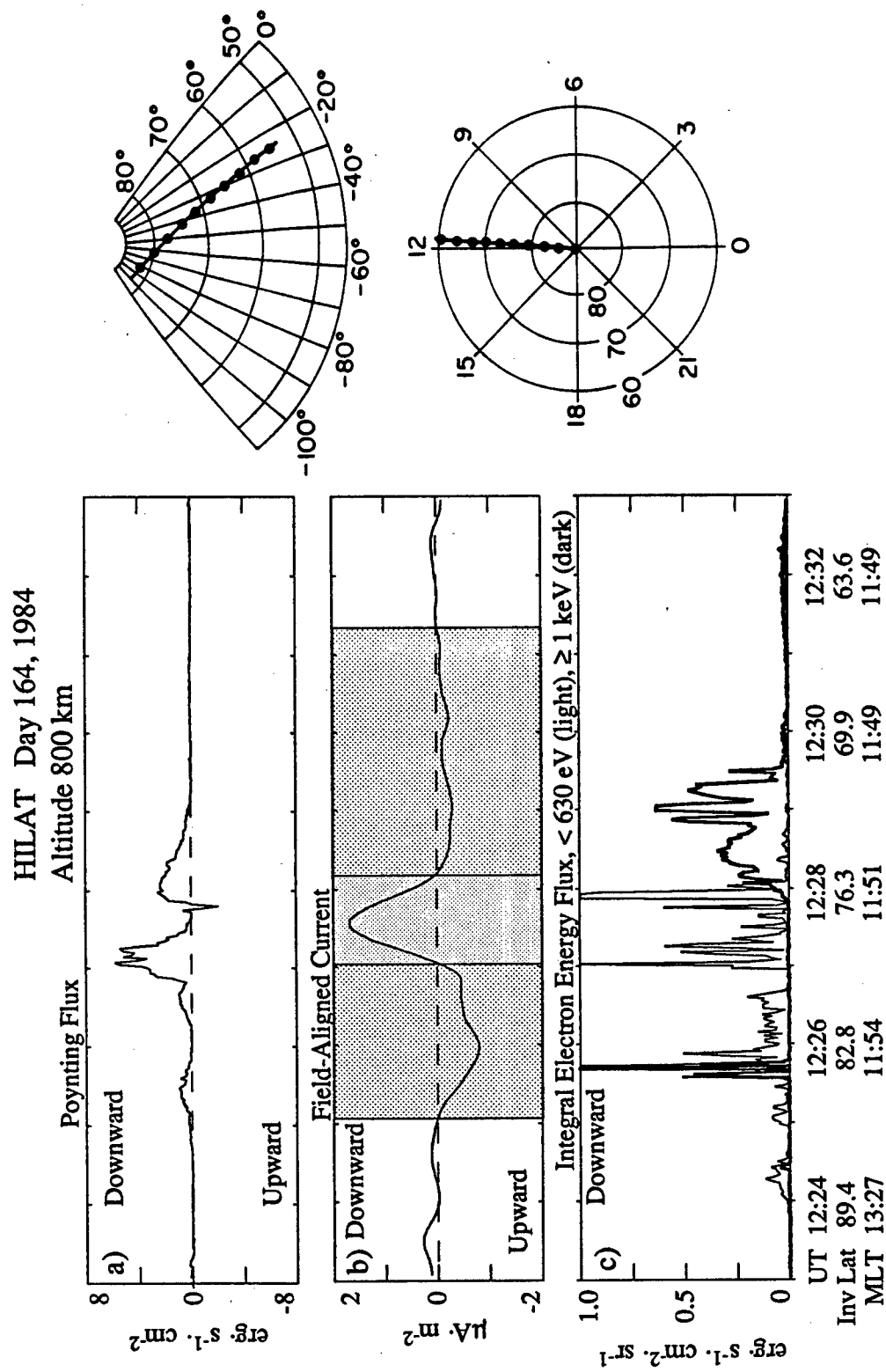


Figure 3.5 Comparison of electromagnetic and particle energy inputs into the ionosphere and the large-scale field-aligned current structure for a summer noon descending pass.

energy bands. The latter are plotted positive for downward energy flow since the detector looks upward. The inset shows the pass in a magnetic local time invariant-latitude format. The satellite was acquired in the polar cap and passed over the dayside auroral oval just before local noon.

We have plotted the Poynting flux in ergs/(cm²s) to conform to the usual notation in presenting particle fluxes in the aurora. The power flux is almost entirely downward throughout the pass, with the single exception of a brief burst of upward flux near 12:28 UT. The average vertical electrical power flux during the pass is equal to 0.45 ergs/(cm²s) (or 0.45 mW/m²) downward, while an upper limit for the average kinetic power flux due to the electrons was 0.70 ergs/(cm²s). To obtain this value a distribution of downgoing electrons isotropic over 2π steradians was assumed. Comparison of the 45° and vertical electron sensors (not shown here) indicate this is a reasonable assumption. Integrating along the trajectory yields 2100 W/m (electromagnetic) and 3300 W/m (kinetic energy). To give some perspective we can estimate the total power from both sources into the entire auroral oval region by assuming that the energy input is independent of local time. This yields 7.9×10^{10} W. This value is a lower limit since we cannot determine the Poynting flux at the largest scales.

Figure 3.5b is the field-aligned current derived from $\partial B_y / \partial x = \mu_0 J_z$ assuming that variation in the \hat{y} direction is unimportant. Because a derivative is required some smoothing has been necessary. We restrict attention to the three shaded current sheets in the center of the figure and not the small variations outside this region as they may be due to the filter. The existence of three sheets is quite common in the noon sector [Iijima and Potemra, 1976]. The upward current sheet at invariant

latitudes below about 72° is co-located with fairly hard electron precipitation, as shown in Figure 3.5c, as well as convection toward the noon meridian. The Poynting flux near the central (downward) current sheet was greater than the precipitating electron energy flux, even assuming that the down-going particle energies are distributed over 2π steradians.

It is interesting to note that the flux of soft electrons in the region of downward current is anticorrelated with the measured current density. Furthermore the precipitating electrons carry current of the opposite sign to that measured. A lower limit to the current carried by the soft electrons can be estimated by assuming that the perpendicular energy of the electrons is small so that they all fall within the aperture of the detector (6° by 4° , or 7.3×10^{-3} sr). The current nev_e due to a 1 erg/(cm²s·sr) flux can be found by multiplying by the angular area of the aperture and dividing by the estimated average energy of the electrons. The current caused by, say, 10 eV electrons is $0.7 \mu\text{A}/\text{m}^2$. The implication is that the upward thermal electron flux must have been fairly large or a considerable ion precipitation was occurring to counter the upward current from the soft electron precipitation.

The Day 164, 1984 orbit was such that the ionosphere was sunlit over the entire trajectory. By taking into account the solar depression angle, the electron density and the conductivity of the E region can be determined [Robinson and Vondrak, 1984]. Although it is not particularly important in this case, we have also estimated the contribution of particle precipitation to the conductivity by assuming that the observed electron flux has been present long enough for a steady state electron density profile to be reached. With this estimate for Σ_p and the

observed electric field from the ion drift meter we can estimate the Joule heating in the ionosphere and compare it to the Poynting flux as shown in Figure 3.6. The ratio of the Joule heating rate to Poynting flux magnitude in Figure 3.6c shows that the two quantities coincide roughly within a factor of two. The Joule dissipation estimate relies on a model for the neutral atmosphere to compute collision frequencies. This model in turn uses an estimate of the thermospheric temperature, but in general this parameter is difficult to determine, and this uncertainty is one possible explanation for the deviation from unity of the Poynting Flux to Joule heat ratio.

The ratio is "spiky" in places, which is to be expected when dividing two noisy quantities, but we will show in Section 3.6 that the spike near 12:27:45 UT coincides with a burst of temporally varying fields, which invalidates one of the assumptions allowing us to use the Joule dissipation in Equation 3.5. Poynting flux, on the other hand, is a valid way to measure energy fluxes in electromagnetic waves. It is important to note that in this case the Poynting flux is upwards, which means that the ionosphere is either reflecting or generating instead of dissipating energy, and this is not discernable from the Joule heating calculation alone. (Since we cannot measure Poynting flux on the largest scales it is possible that the measured upward Poynting flux is actually an upward perturbation on a large scale downward flux.) For these reasons and those discussed in Section 3.3 we argue that Poynting flux as a tool is superior to Joule heating estimates. However, we must qualify this statement for HILAT satellite measurements since the magnetometer resolution is about 15 nT. For small signal levels the quantization noise

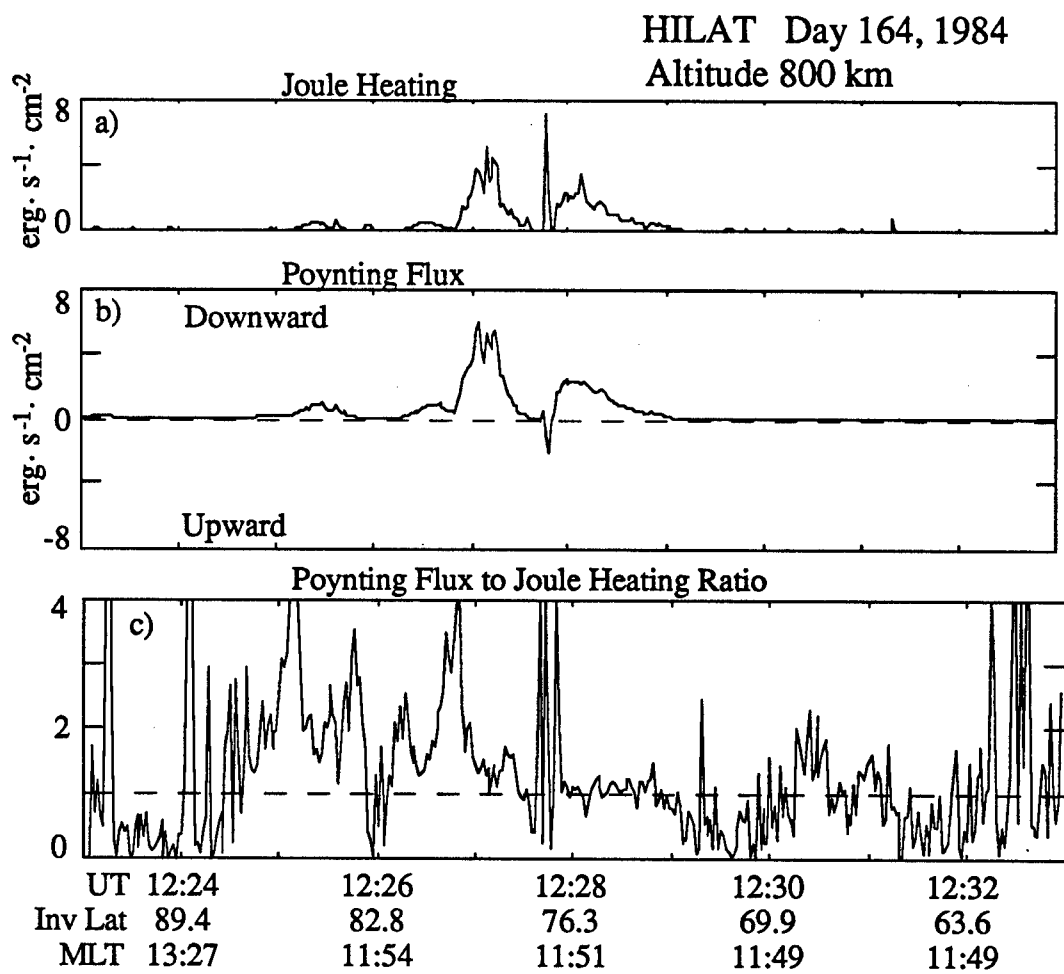


Figure 3.6 Comparison of the Joule heating rate and Poynting flux for the HILAT pass shown in Figure 3.5.

can cause an anomalously large magnetic field (and therefore Poynting flux) estimate.

Data from the second event are presented in Figure 3.7 in a format nearly identical to that used in Figure 3.5. As can be seen in the raw data in Figure 3.4a and in the smoothed Birkeland currents in the second panel, several current sheets were detected during this dusk pass through the auroral oval. This is unusual, at least as far as the literature indicates. All significant upward currents are co-located with a burst of electron precipitation and anti-sunward convection while downward current regions were associated with sunward flow and no precipitation. There was still significant Poynting flux in regions where the particle input was low and the Birkeland currents downward. In the central downward current sheet, regions of both upward and downward Poynting flux were found. Figure 3.8 shows this effect in an expanded plot of the meridional electric field, the Poynting flux, and the electron energy flux for the period 18:52-18:54 UT. The magnitude of the average electromagnetic power density over the entire pass was 0.22 ergs/(cm²s); the rate of kinetic energy input was 2.0 ergs/(cm²s). The integrated values over the pass are 980 W/m and 8900 W/m. Again we assumed an angular spread of 2π steradians in the kinetic energy based on vertical and 45° electron energy measurements. Assuming no variation of energy input with local time in this case gives 1.5×10^{11} W for the total electrical and mechanical power input into the auroral oval.

In Figure 3.9 we plot the Joule heating rate, the Poynting flux, and the ratio of the two quantities for Day 122, 1984. There appears to be good agreement except near 18:53 UT, where the Joule heating estimate is much larger than the Poynting flux. For the periods in which magnetic

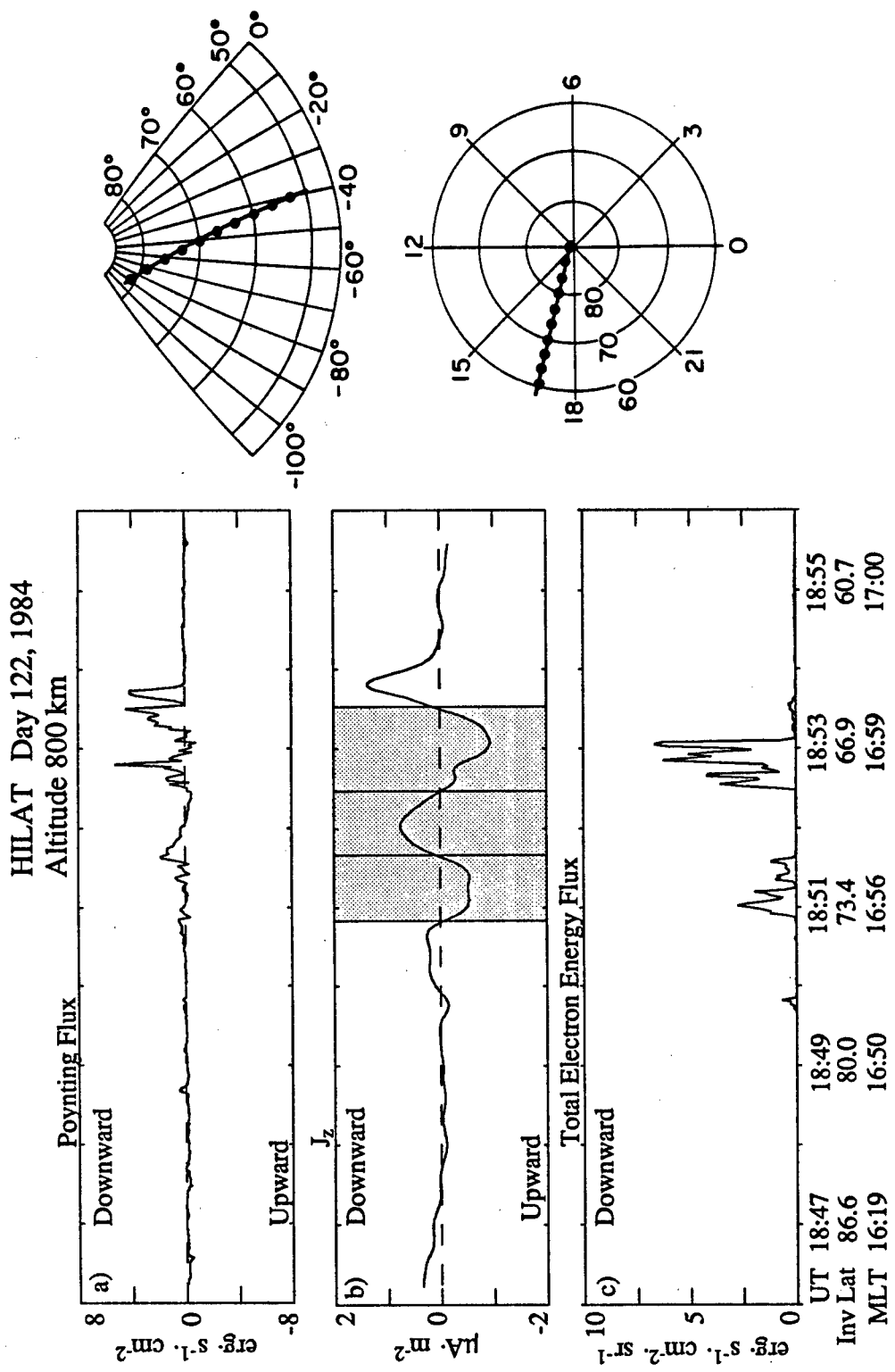


Figure 3.7 Comparison of electromagnetic and particle energy inputs into the ionosphere and the large-scale field-aligned current structure for a HILAT pass through the afternoon sector.

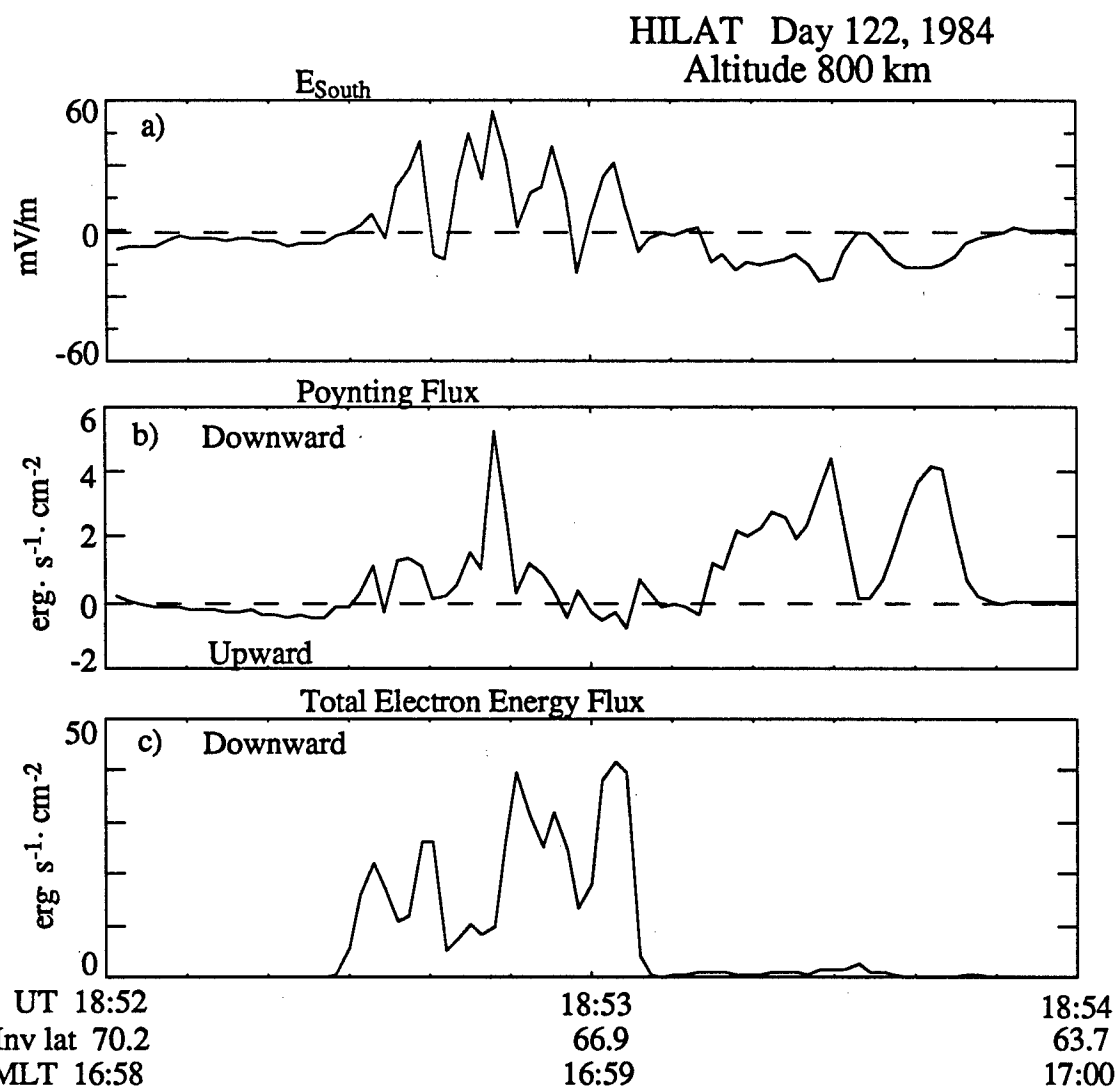


Figure 3.8 Expanded view of a two minute interval during the HILAT pass on Day 122, 1984 during which upward Poynting flux was observed.

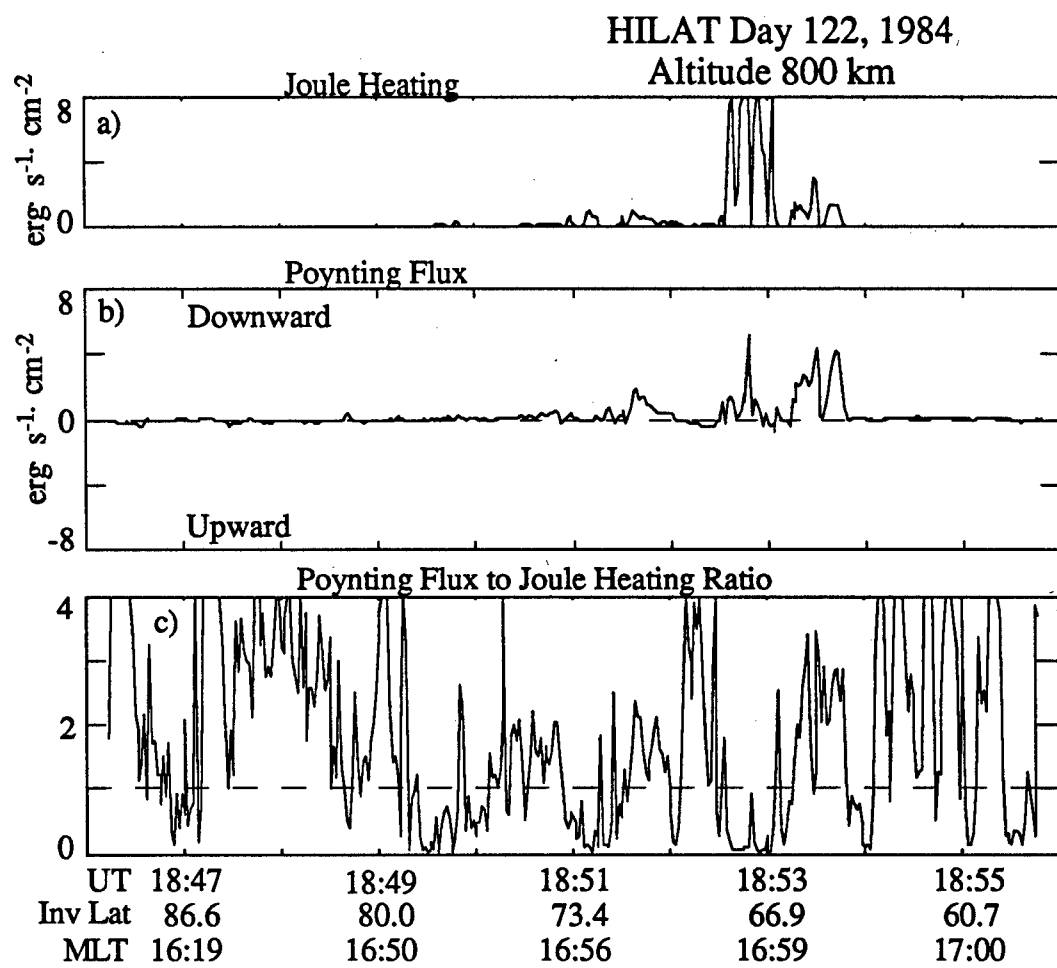


Figure 3.9 Comparison of the Joule heating rate and Poynting flux for the HILAT pass shown in Figure 3.7.

field fluctuations exceed the minimum resolution of the magnetometer, we attribute the disagreement between the two measurements mainly to errors in the conductivity estimate from the particle flux and hence in the Joule heating estimate.

3.5 Sounding Rocket Observations

As part of the 1985 NASA Greenland I campaign a Black Brant X sounding rocket was launched from Sondrestrom eastward into the dayside auroral oval and remained inside the oval for the entire upleg. Other results from that flight have been published by *Boehm et al.* [1990]. The measurements we present were taken during the upleg of the rocket flight at altitudes between 400 and 770 km. Electric fields perpendicular to \mathbf{B}_0 were measured with perpendicular 3 m electric field booms, and magnetic measurements were taken with a fluxgate magnetometer. To obtain electric fields below the rocket spin frequency, electric field measurements were fit to a sine wave at the spin frequency, then averaged to obtain two measurements per rocket spin period. The resulting sample period is 0.887 s. The measured $\delta\mathbf{E}$ and $\delta\mathbf{B}$ fields perpendicular to \mathbf{B}_0 for the ascending half of the flight are shown in the top two panels of Figure 3.10.

To illustrate the amount of electromagnetic power flowing between the magnetosphere and ionosphere during the flight we plot the field-aligned component of the Poynting vector in Figure 3.10c. We must be especially wary of the Poynting flux estimate in this case because 1) small errors in the geomagnetic field model can cause large errors in estimates of the perturbation magnetic fields used in the Poynting flux calculations, and 2) we cannot distinguish magnetic field perturbations

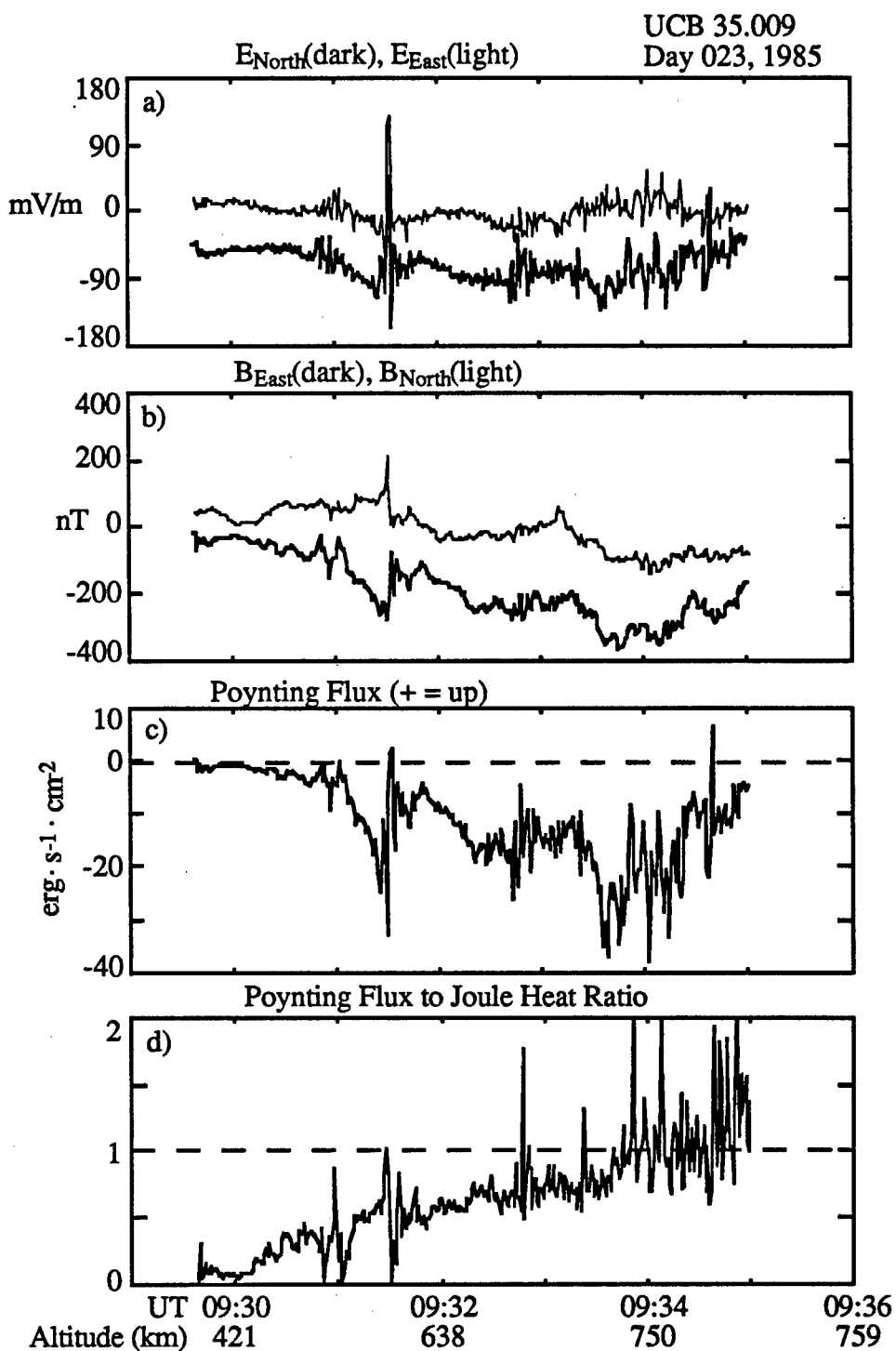


Figure 3.10 Data taken from a Black Brant X sounding rocket launched from Sondrestrom, Greenland on 23 January, 1985. The rocket traveled eastward along the auroral oval. (Data are courtesy of C. Carlson, B. McFadden, and M. Boehm at the University of California, Berkeley.)

due to large scale current systems from an error in the zero order magnetic field model. We can detect the associated electric field however since there is no zero order electric field. This effect almost certainly explains the large difference between the Poynting flux and $\Sigma_p E_{\perp}^2$ early in the flight where $\mathbf{E} \neq 0$ but the model subtraction yields $\delta\mathbf{B} \approx 0$. The high-pass filter technique we used for the satellite data does not work in this case, because the data are taken completely within the auroral oval. Recall that in the satellite case the auroral oval crossing was only a fraction of the total duration of the pass, causing it to lie in the filter passband. We still have some confidence in the validity of the rocket-measured Poynting flux, however, because it agrees reasonably well with $\Sigma_p E_{\perp}^2$ as we can see from the Poynting flux to Joule heat ratio shown in Figure 3.10d. The slow trend causing this ratio to increase over the course of the flight could be due to an error in the perturbation magnetic field estimate, or to the fact that we used a constant value of $\Sigma_p = 3$ mhos throughout the flight. The rocket flew eastward into regions of increasing sunlight, which would cause Σ_p to increase throughout the flight. But due to the general agreement between the two power flow estimates we will assume that the perturbation magnetic fields are not too contaminated by low frequency field model errors. Notice that the magnitude of the Poynting flux is consistently tens of ergs/(cm²s), which is several times larger than the peak power fluxes from the two satellite passes discussed in the previous section.

The Poynting flux is predominantly downward except for 2 short intervals, near 09:30:30 and 09:34:40 U.T. In Chapter 5 we will show that much of the electric field energy during the flight is dominated by standing Alfvén waves. Standing waves can produce both upward and

downward Poynting flux during different phases of their cycle, and this could possibly account for the observed upward Poynting flux.

3.6 Time-Domain Measurements of Auroral Field Impedances

We have shown that Joule dissipation in the ionosphere implies electric and perturbation magnetic fields perpendicular to \mathbf{B}_0 above the ionosphere. In order to understand the origin of the perturbation fields it is helpful to consider a simple model of current closure through the ionosphere. In this model we assume that fields and ionospheric parameters such as density and collision frequencies vary in the meridional (x) direction only. As we will show in the next chapter, no variation in the zonal (y) direction implies that the zonal electric field E_y is much smaller in magnitude than the meridional field E_x , and we will therefore neglect it. If we apply a meridional electric field $E_x(x)\hat{x}$ above the ionosphere, that field will map into the ionosphere and drive a current $\mathbf{J} = J_x\hat{x} + J_y\hat{y}$. Since $\partial/\partial y = 0$ the current continuity equation $\nabla \cdot \mathbf{J} = 0$ can be written

$$J_z = \frac{\partial}{\partial x} \int_{ionosphere} J_x dz \quad (3.21)$$

where J_z is the field-aligned current above the ionosphere. Ampere's law in the region above the ionosphere is $\mu_0 J_z = \partial B_y / \partial x$, which we can apply to (3.21) to obtain

$$S_z = E_x B_y / \mu_0 = \int_{ionosphere} J_x E_x dz \quad (3.22)$$

We have assumed E_x is constant in altitude, and the constant of integration over x is taken to be zero to ensure that $S_z = 0$ in the absence of

Joule dissipation. As we might expect, the z component of the Poynting vector gives the height-integrated Joule dissipation per unit area in the ionosphere. The point we wish to make with this example is that a Poynting vector measured *above* the ionosphere correctly measures the Joule dissipation *in* the ionosphere because the zonal perturbation magnetic field B_y is caused by field-aligned currents which close through the ionosphere.

In addition to Joule dissipation in the ionosphere, the electromagnetic fields above the ionosphere can be used to predict another useful quantity. Replacing J_x in (3.22) with $\Sigma_P E_x$ gives the following result:

$$\frac{E_x}{B_y} = \frac{1}{\mu_0 \Sigma_P} \quad (3.23)$$

This allows us to remotely estimate the height-integrated Pedersen conductivity of the ionosphere directly below the spacecraft. Again, we have assumed no variation in the zonal (y) direction, negligible E_y , quasi-static fields, and no neutral winds.

Notice that we were able to eliminate the x derivative in (3.21), which means that no assumptions are necessary concerning the scale length of variations in x . Whether we measure fields associated with an auroral arc or with the entire auroral oval, (3.23) holds. However, we will show in the next chapter with the aid of a numerical model that (3.23) is violated at scales less than a few km, due to the fact the small scale electric fields do not map without attenuation along the geomagnetic field.

In Figures 3.11 and 3.12 we plot $\mu_0 |E_x/B_y|$ along with those same values multiplied by Σ_P as a function of time for the two satellite passes

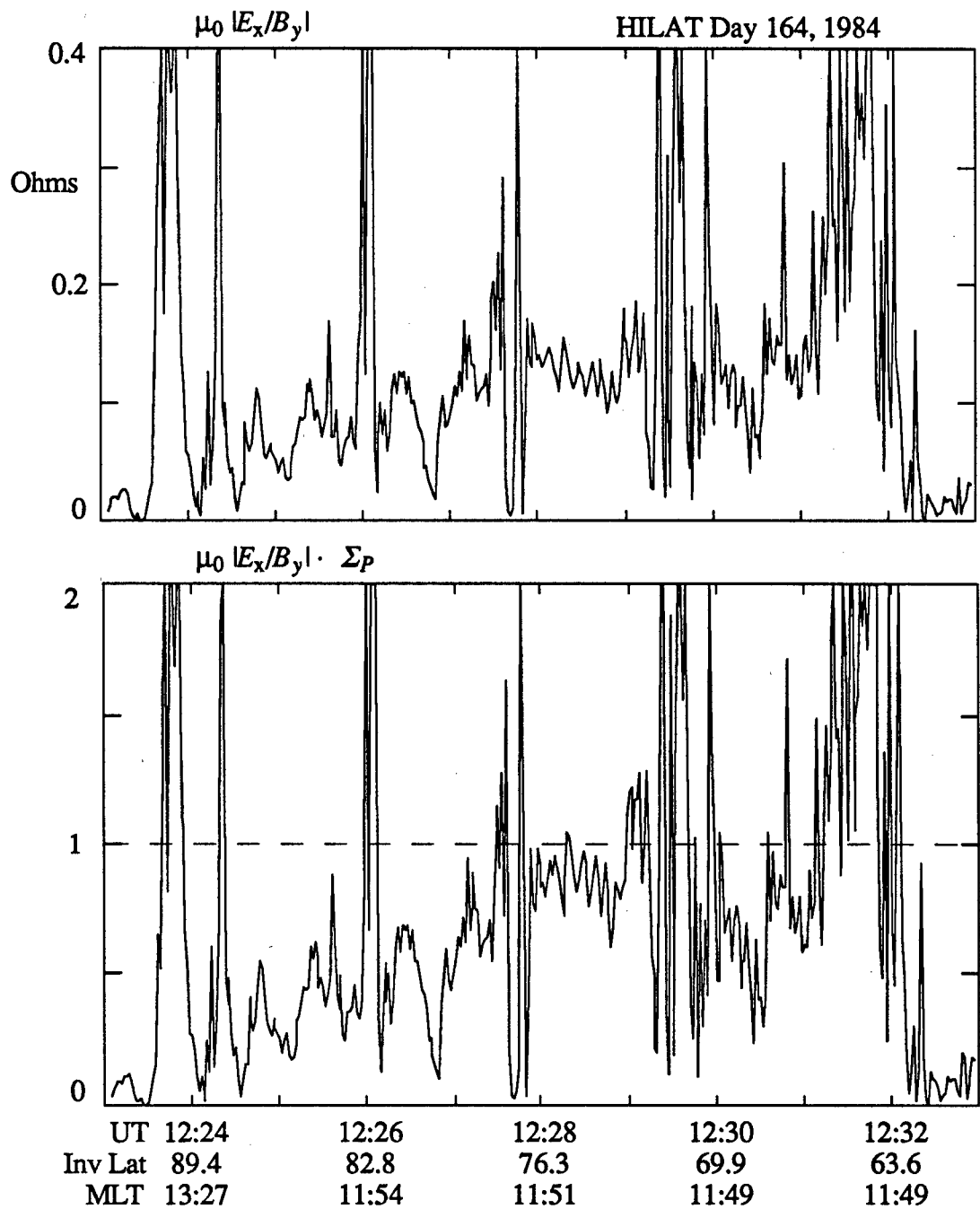


Figure 3.11 Electromagnetic field impedance as a function of time calculated from the Day 164, 1984 data. The impedances in the lower panel are normalized to Σ_P^{-1} .

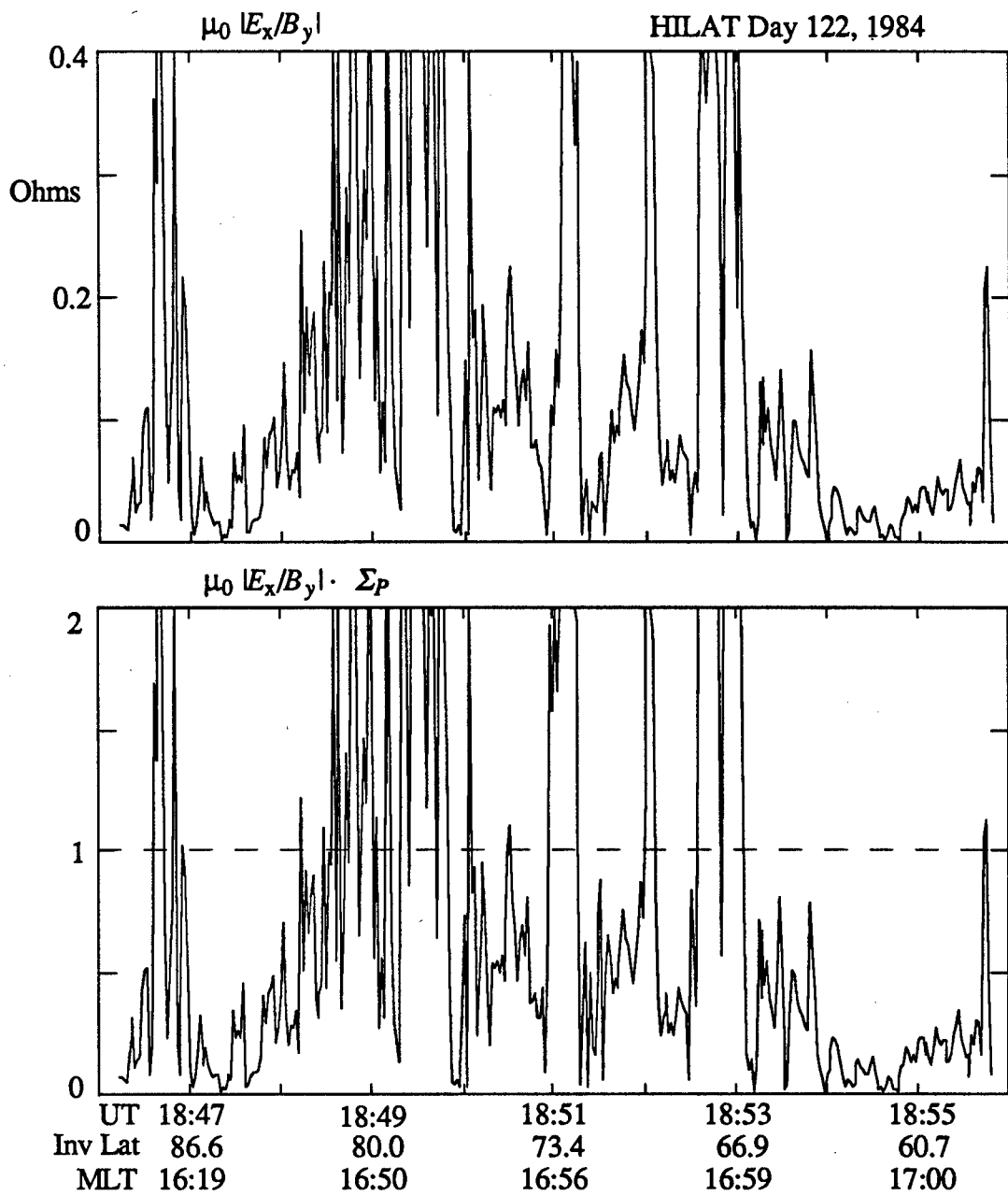


Figure 3.12 Electromagnetic field impedance as a function of time calculated from the Day 122, 1984 data. The impedances in the lower panel are normalized to Σ_P^{-1} .

discussed in the previous section. Deviations from unity in Figures 3.11b and 3.12b indicate either that our Σ_p estimates are in error, that one or more of the assumptions leading to Equation (3.23) are violated, or that the magnetic field fluctuations are below the resolution of the instrument. In one of the cases we can identify the exact cause of the deviation. Figure 3.13 shows the meridional electric field plotted at the full time resolution of the instrument for the time period near 12:27:45 UT on Day 164, 1984. The electric field shows a wave-like burst with a peak amplitude of over 100 mV/m. The coherent nature of the burst is indicative of temporal variation. Thus the spike in Figure 3.11b just before 12:28 UT can be attributed to a breakdown in our assumption of static fields.

A similar increase in $\mu_0 |E_x/B_y|$ over Σ_p^{-1} occurs in the sounding rocket data, shown in Figure 3.14. As in Figure 3.10d, the slow trend is probably due to our inadequate estimate of Σ_p or to errors in the geomagnetic field model. The electromagnetic fields associated with the huge deviation near 09:31:30 UT have been identified as an Alfvén wave by *Boehm et al. [1990]*. Thus in at least two cases, one measured from a satellite and one from a sounding rocket, a substantial increase in $\mu_0 |E_x/B_y|$ over Σ_p coincides with temporally varying fields. In Chapter 5 we will develop a technique which can help to determine the importance of time varying fields (i.e. Alfvén waves) in time series data for which no coherent wave structures are evident. But first we will investigate the details of the interaction of Alfvén waves with the ionosphere, which is the topic of Chapter 4.

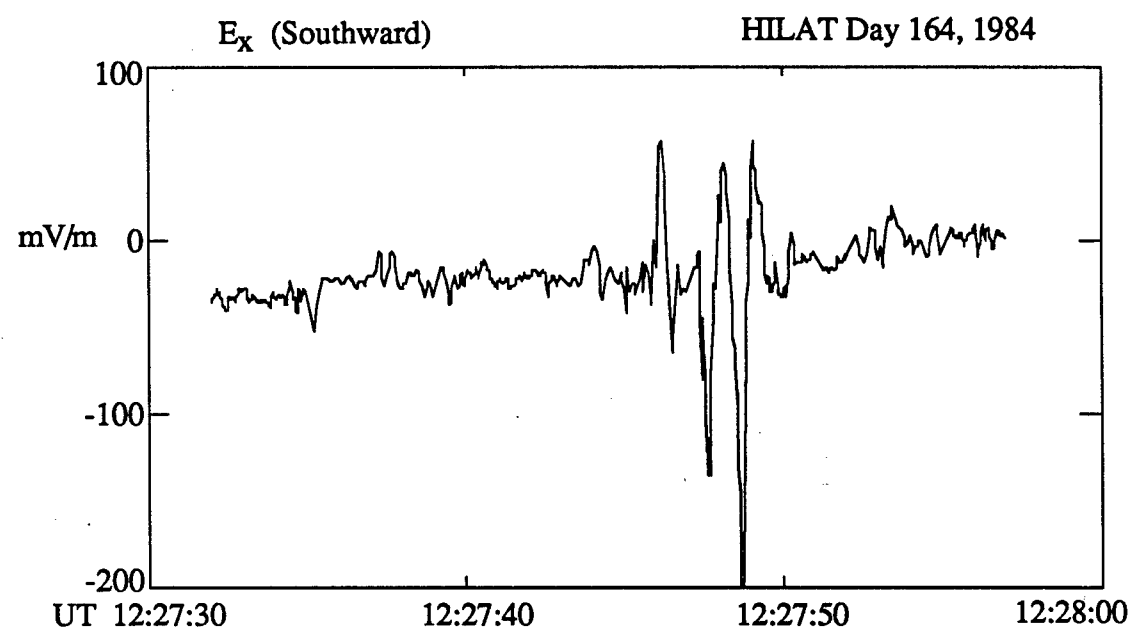


Figure 3.13 Electric field during a short event measured by HILAT on Day 164, 1984, plotted at the full time resolution of the instrument (16 s^{-1} or 32 s^{-1}). The coherent nature of the burst is indicative of time variation (i.e. an Alfvén wave) rather than spatial structuring.

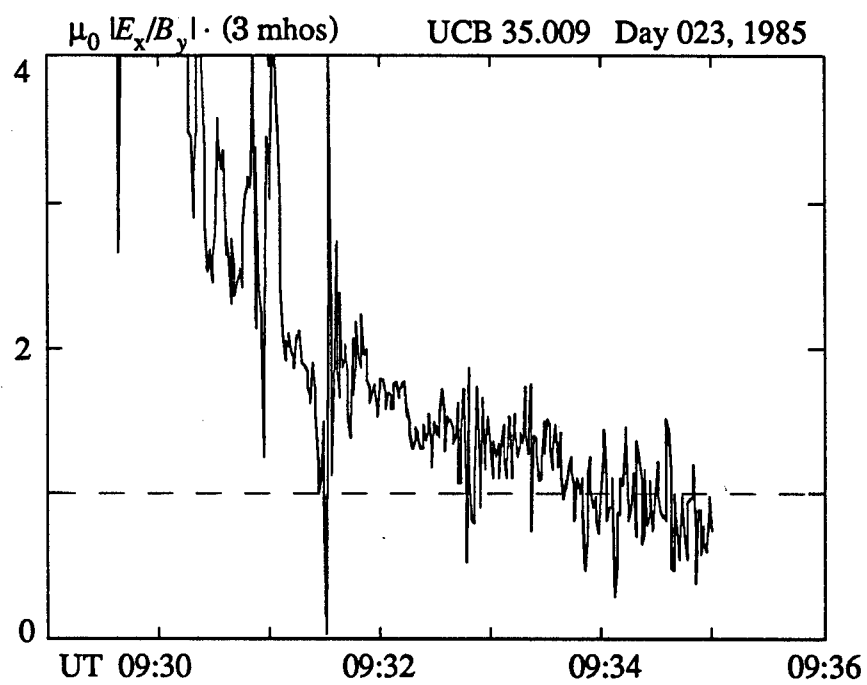


Figure 3.14 Electromagnetic field impedance as a function of time calculated from the sounding rocket data shown in Figure 3.10. The impedances are normalized to a constant value of $\Sigma p^{-1} = (3 \text{ mhos})^{-1}$.

CHAPTER 4

A NUMERICAL MODEL OF ALFVÉN WAVES INTERACTING WITH THE HIGH-LATITUDE IONOSPHERE

4.1 Introduction

If the electric and magnetic fields carrying energy from the solar wind and magnetosphere to the high-latitude ionosphere do not vary in time, we can assume that for the most part magnetic field lines are equipotentials, and the energy dissipated in the ionosphere is $\Sigma p E^2$ (neglecting neutral winds), as we discussed in the last chapter. Now consider time varying fields, but with frequencies less than, say, 10 Hz. In the magnetosphere and ionosphere these waves fall in the Alfvén wave regime, and we have to consider wave-related behaviors like reflections, interference, and particle inertial effects.

As an Alfvén wave propagates towards the ionosphere, it encounters a steeply changing refractive index due to variations in density, composition, and collision frequency. The plasma density varies over several orders of magnitude between 1000 km and the Earth's surface, and at low frequencies this distance can be much less than an Alfvén wavelength. Ion and electron collisions begin to play an important role below a few hundred kilometers, and below a certain altitude (which we will calculate later in the chapter) they control the charged particles to such an extent that what once was an Alfvén wave above the ionosphere cannot now interact with the charged particles, and the wave travels towards the Earth's surface as a "light wave", i.e. $\omega/k = c$. Finally, since

the surface of the Earth is a good conductor, it reflects most of the wave energy. The point to be taken from this description is that the amplitude and phase of an Alfvén wave at one point depend strongly on the plasma characteristics at other points, and those characteristics change rapidly with altitude. Thus in general we need a numerical model to accurately describe Alfvén wave propagation through the ionosphere.

As discussed in Section 2.6, there have been many numerical simulations of Alfvén waves traveling through the density gradient within a few Earth radii of the auroral ionosphere. All of these models treat various phenomena in the collisionless region between the source of Alfvén waves and the ionosphere, but they treat the ionosphere as a single slab characterized by its height-integrated conductivity. In contrast, we will ignore the region above the ionosphere except to treat it as a source of Alfvén waves. We will then model the details of the interaction between these incident Alfvén waves and the ionosphere, with realistic density and collision frequency profiles. We will also find the conditions under which the ionosphere can be modeled as a conducting slab, and our results can be used to provide more realistic boundary conditions for simulations like those mentioned in Chapter 2.

Turning from simulations of Alfvén waves above the ionosphere to waves *in* the ionosphere, we find an enormous amount of literature on the subject. *Budden* [1985] is a good general reference. One of the first computer solutions of Alfvén waves propagating through the ionosphere was carried out by *Francis and Karplus* [1960], who calculated the amount of ionospheric heating by Alfvén waves at 45° latitude for frequencies less than 4 Hz. *Prince and Bostick* [1964] found the amount of attenuation for waves below 10 Hz as they propagate between the

magnetopause and the Earth's surface. These works used relatively coarse models of the ionospheric profile, and treated only vertically incident plane waves. *Greifinger* [1972], *Hughes* [1974], and *Hughes and Southwood* [1976] allowed for obliquely propagating waves and found field amplitude profiles and reflection coefficients for waves incident from the magnetosphere onto the ionosphere for a variety of ionospheric conditions.

The numerical model that we develop in this chapter is nearly identical to that presented by *Hughes* [1974] and *Hughes and Southwood* [1976], although those authors dealt with wave periods of many minutes, while we emphasize periods of several seconds. Our main purpose for developing the model is to carefully compare its predictions with satellite measurements, which we present in Chapter 5 and which are treated by none of the above references. While developing the model we hope to emphasize an understanding of the physical reasons behind different features in the modeled Alfvén waves.

4.2 Derivation

The propagation of electric and magnetic fields \mathbf{E} and \mathbf{B} with frequency ω is described by Maxwell's curl equations

$$\nabla \times \mathbf{E} = -i\omega \mathbf{B} \quad (4.1a)$$

$$\nabla \times \mathbf{B} = \mu_0 \sigma \mathbf{E} + \frac{i\omega}{c^2} \mathbf{E} \quad (4.1b)$$

$\sigma = \sigma(\omega)$ is the frequency-dependent conductivity, which for our needs can be derived from the linearized fluid equations of motion

$$i\omega \mathbf{v}_j = \frac{q_j}{m_j} (\mathbf{E} + \mathbf{v}_j \times \mathbf{B}_0) - v_j \mathbf{v}_j \quad (4.2)$$

where j is a species index. The usual theory of cold plasma waves (see for example Stix [1962]) is also derived from the fluid equations of motion, but without the collision term. Notice that collisions can be thought of as creating an effective wave frequency $\omega' = \omega - iv$. We take \mathbf{B}_0 to be in the \hat{z} direction, solve for the \mathbf{v}_j terms and substitute into the definition of conductivity:

$$\mathbf{J} = \sum_j n_j q_j \mathbf{v}_j = \sigma \cdot \mathbf{E} \quad (4.3)$$

The resulting σ has the following form:

$$\sigma = \begin{pmatrix} \sigma_1 & \sigma_2 & 0 \\ -\sigma_2 & \sigma_1 & 0 \\ 0 & 0 & \sigma_0 \end{pmatrix} \quad (4.4)$$

where

$$\sigma_0 = \epsilon_0 \sum_j \frac{\omega_{pj}^2}{(i\omega + v_j)} \quad (4.5a)$$

$$\sigma_1 = \epsilon_0 \sum_j \frac{(i\omega + v_j) \omega_{pj}^2}{[(i\omega + v_j)^2 + \Omega_j^2]} \quad (4.5b)$$

$$\sigma_2 = \epsilon_0 \sum_j \frac{\Omega_j \omega_{pj}^2}{[(i\omega + v_j)^2 + \Omega_j^2]} \quad (4.5c)$$

σ_0 describes the relation between \mathbf{J} and \mathbf{E} when they are both parallel to each other, and to \mathbf{B}_0 . For $\omega = 0$ it is known as the "direct" conductivity. In the small ω limit σ_1 is the Pedersen conductivity (Equation 3.4b), and describes dissipative currents ($\mathbf{J} \cdot \mathbf{E} > 0$) which are perpendicular to \mathbf{B}_0 . If we neglect $\omega \ll \Omega_i$ in the denominator and let $v = 0$ we find $\sigma_1 = \epsilon_0 i \omega \omega_{pe}^2 / \Omega_i^2 = i \omega / \mu_0 V_A^2$, where V_A is the Alfvén velocity. Thus σ_1 carries

the information allowing us to model Alfvén waves while σ_2 is the generalization of the Hall conductivity ($\mathbf{J} \perp \mathbf{E} \perp \mathbf{B}_0$) for $\omega \neq 0$. We have written (4.5c) in such a way that Ω carries the sign of the charge, so that it is negative for electrons.

To solve Equations 4.1 we assume a flat Earth surface, upward z , periodic variation of the fields in the \hat{x} direction, and no variation in the \hat{y} direction. The ambient magnetic field \mathbf{B}_0 is vertical, and σ is assumed to be homogeneous in x and y . Under these conditions we can eliminate E_z and B_z by substituting the z component of Equation (4.1b) ($-ik_x B_y = (\mu_0 \sigma_0 + i\omega/c^2) E_z$) into the \hat{y} component of (4.1a), and the z component of (4.1a) ($\omega B_z = k_x E_y$) into the \hat{y} component of (4.1b). The result is 4 equations in 4 unknowns:

$$\frac{\partial E_x}{\partial z} = - \left(\frac{k_x^2}{\mu_0 \sigma_0 + i\omega/c^2} + i\omega \right) B_y \quad (4.6a)$$

$$\frac{\partial E_y}{\partial z} = i\omega B_x \quad (4.6b)$$

$$\frac{\partial B_x}{\partial z} = -\mu_0 \sigma_2 E_x + \left(\mu_0 \sigma_1 + \frac{i\omega}{c^2} - \frac{ik_x^2}{\omega} \right) E_y \quad (4.6c)$$

$$\frac{\partial B_y}{\partial z} = - \left(\mu_0 \sigma_1 + \frac{i\omega}{c^2} \right) E_x - \mu_0 \sigma_2 E_y \quad (4.6d)$$

The integration in z is necessary because all of the conductivities vary with altitude. *Hughes* [1974] solved for E_z and B_z explicitly by integrating $\nabla \cdot \mathbf{B} = 0$ and the current continuity equation $\nabla \cdot \mathbf{J} + \partial \rho_c / \partial t = 0$ along with Equations (4.1), which makes a total of six equations to integrate. The price we pay for integrating two fewer equations is that we must apply the additional constraint $\omega \neq 0$, as is obvious from the term proportional to ω^{-1} in (4.6c). The physical reason for this constraint is

that Equations (4.6) satisfy $\nabla \cdot \mathbf{B} = 0$ identically as long as $\omega \neq 0$, which can be seen by taking the divergence of (4.1a). Thus there is no need to solve $\nabla \cdot \mathbf{B} = 0$ explicitly. In a similar way it can be shown that (4.1b) satisfies the current continuity equation for $\omega \neq 0$. We can still treat "DC" fields by making ω very small. We solve Equations (4.6) using an adaptive step size, 4th order Runge-Kutta ODE solver [Press et al, 1986].

4.3 Boundary Conditions

At the upper boundary of the modeled region (1000 km) we can neglect σ_2 as long as $\omega \gg v_i$ and $\omega \ll \Omega_i$ (recall that Ω_i is a signed quantity). Equations (4.6a) and (4.6d) then decouple from (4.6b) and (4.6c), and if we assume no variation in σ_0 and σ_1 with z above the upper boundary we find solutions for E_x and B_y varying as $\exp(ik_{z,s}z)$ where

$$k_{z,s} = \sqrt{-\left(\frac{k_x^2}{\mu_0\sigma_0 + i\omega/c^2} + i\omega\right)(\mu_0\sigma_1 + i\omega/c^2)} \quad (4.7)$$

In the MHD limit ($v \ll \omega \ll \Omega_i$) we can take $\sigma_0 \rightarrow \infty$ and $\sigma_1 = i\omega/(\mu_0 V_A^2)$ where V_A is the Alfvén velocity. Neglecting $1/c^2 \ll 1/V_A^2$ results in $k_{z,s}^2 = \omega^2/V_A^2$, which is the dispersion relation for the slow Alfvén mode [Stix, 1962]. By replacing $\partial/\partial z$ with $ik_{z,s}$ in Equation (4.6d) we obtain a relation between E_x and B_y which serves as the upper boundary for the slow mode.

Turning to E_y and B_x we find from (4.6b) and 4.(6c) that they vary as $\exp(ik_{z,f}z)$ where

$$k_{z,f} = \sqrt{-\left(i\omega\mu_0\sigma_1 - \omega^2/c^2 + k_x^2\right)} \quad (4.8)$$

Taking the MHD limit this time gives $k_{z,f}^2 = \omega^2/V_A^2 - k_x^2$, which is the Alfvén fast mode. The fast mode is evanescent for $\omega^2/V_A^2 < k_x^2$, which is

satisfied for the range of parameters that we will use at the top of the model region. The source of fast mode energy is in the ionosphere where $\sigma_2 \neq 0$, so we choose boundary conditions at the top of the model region such that the fast mode attenuates with increasing altitude. Substituting $k_{z,f}$ for $\partial/\partial z$ in (4.6d) determines B_x for arbitrary starting values of E_y .

At the bottom of the model region we find two independent solutions to Equations (4.6) by first setting $B_x = 0$, then $B_y = 0$. The electric field is also zero at the perfectly conducting surface. The two solutions are integrated up to about 200 km, where they are matched to the upward and downward propagating slow mode waves and the upwardly evanescent fast mode wave, which have been integrated downward. The reason for matching the solutions at 200 km altitude is that the field amplitudes maximize there, and numerical integration of second order differential equations is most stable in the direction that the solution increases. After the 4 independent solutions have been found, a linear combination is found that allows for a downward-propagating slow wave which has a unit amplitude at 1000 km. The coefficients a_j used to take the linear combination of solutions are found from

$$\begin{pmatrix} E_{x,g1} & E_{x,g2} & -E_{x,s,up} & -E_{x,f} \\ E_{y,g1} & E_{y,g2} & -E_{y,s,up} & -E_{y,f} \\ B_{x,g1} & B_{x,g2} & -B_{x,s,up} & -B_{x,f} \\ B_{y,g1} & B_{y,g2} & -B_{y,s,up} & -B_{y,f} \end{pmatrix} \cdot \begin{pmatrix} a_1 \\ a_2 \\ a_3 \\ a_4 \end{pmatrix} = \begin{pmatrix} E_{x,s,down} \\ E_{y,s,down} \\ B_{x,s,down} \\ B_{y,s,down} \end{pmatrix} \quad (4.9)$$

where subscripts "g1" and "g2" denote the two solutions starting from the ground, "S" and "F" are the slow and fast modes, and "down" and "up" indicate propagation direction. The field values are all taken at the solution matching altitude.

Figure 4.1 summarizes the boundary conditions. At the top of the simulation region we impose a unit amplitude slow wave ($\omega^2 = k_z^2 V_A^2$) propagating downward. This wave is also the reference for zero phase angle in the system. While this mode has $E_y = B_x = 0$ at 1000 km, these field components become non-zero as the wave propagates into regions where $\sigma_2 \neq 0$, which explains why they cannot be neglected at the solution matching altitude and thus appear in the column vector on the right side of (4.9). There is also an upward-propagating slow wave which has an amplitude at 1000 km a_3 , given by Equation 4.9. Since the downward slow wave has unit amplitude, a_3 is the "voltage reflection coefficient" ($E_{\text{reflected}}/E_{\text{incident}}$) at 1000 km for slow mode Alfvén waves incident on the ionosphere.

In addition to the incident and reflected slow waves, there is the evanescent fast wave which is driven due to coupling of energy from the slow wave in the E region where the conductivity σ_2 is non-negligible. Since the energy source for this mode is below 1000 km in altitude, we choose the solution which decays with increasing altitude. After finding the two modes below 200 km shown in Figure 4.1, they are matched to the 3 upper solutions using Equation 4.9.

4.4 Model Input

The physical description of the atmosphere and ionosphere is contained in the conductivities in Equation 4.5. To find the conductivities we need altitude profiles from 0 to 1000 km of electron density, ion composition, collision frequencies, and the geomagnetic field.

We simplify the geomagnetic field model by restricting our attention to high latitudes, where we can assume that B_0 is vertical. In the next

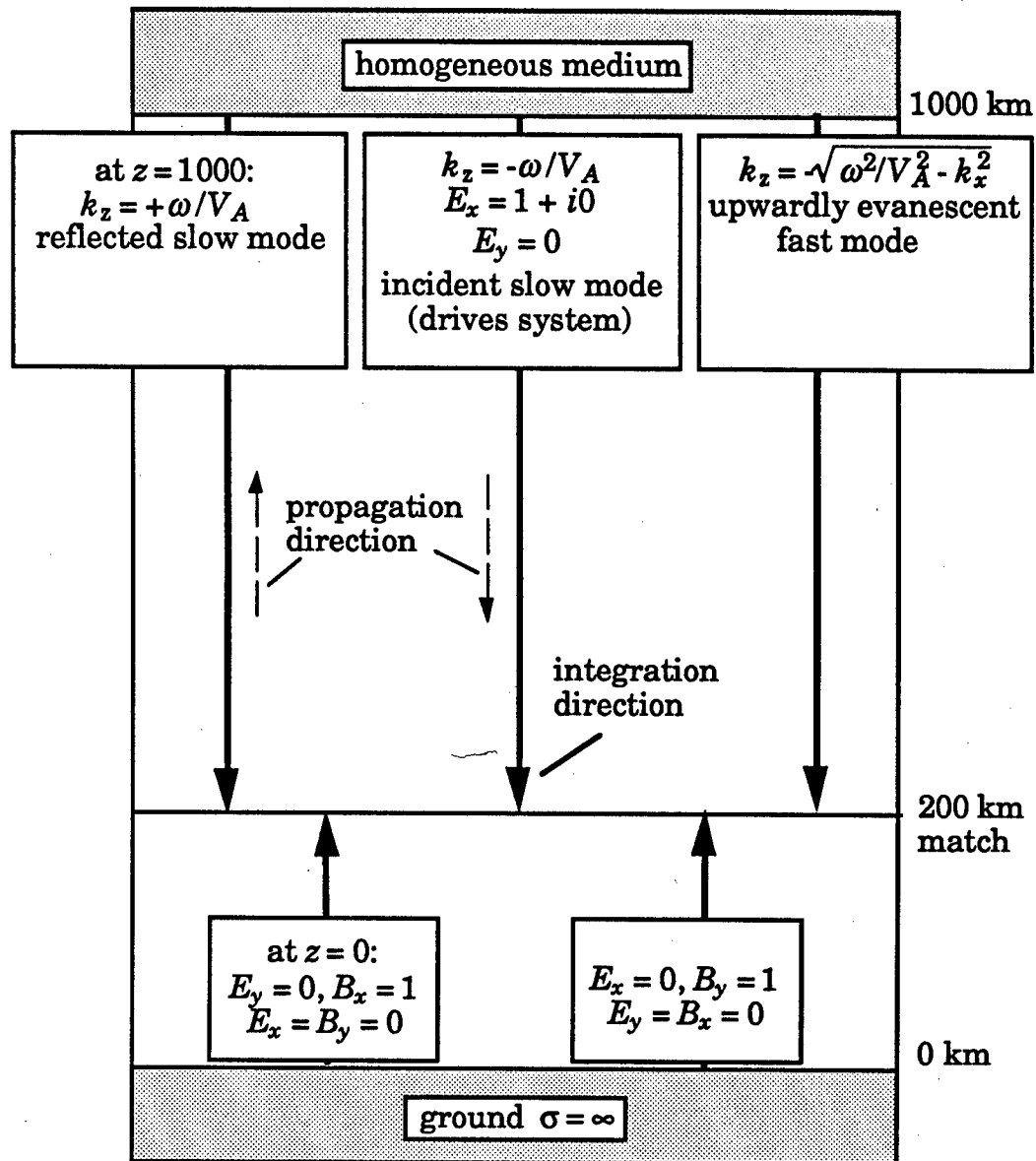


Figure 4.1 Schematic representation of the five independent solutions which are combined into a single solution for the electromagnetic fields between 0 and 1000 km.

chapter we will compare the result of the model with experiments carried out above Sondrestrom, Greenland, so in our model we use Sondrestrom's surface magnetic field of 0.56×10^{-4} T (downward). In a dipole field, $B_0 \propto r^{-3}$, and we let our model magnetic field fall off accordingly with altitude.

The most important input into our model is the plasma density profile above 95 km. At high latitudes this is very difficult to model. The plasma density profile created by photoionization can be predicted by a Chapman production function, but this plasma can have a very long lifetime in the F region, and it can convect far away from its point of production. In addition to photoionization, precipitation of energetic electrons produces a significant amount of the high latitude plasma, but in an unpredictable manner. Later, when we compare the model results with experimental measurements, we will use measurements of the electron density profile from the Sondrestrom Incoherent Scatter Radar. Our purpose in this chapter is to see how the interaction of Alfvén waves with the ionosphere changes with various inputs, so we will use each of the 3 different model electron density profiles shown in Figures 4.2 - 4.4. With each of the profiles is plotted the conductivities σ_0 , σ_1 , and σ_2 with $\omega = 0$. The profile in Figure 4.2a, labeled "EF", is a typical daytime profile with both an E and F region. The "F" profile in Figure 4.3a lacks an E region, and therefore has associated with it a low Pedersen conductivity. This profile could occur, for example, after sunset when the E region quickly recombines leaving an F region only. The "E" profile in Figure 4.4a could occur in darkness with electron precipitation leading to the ionization bump below 200 km. The E-region ionization in the "E" and "EF" profiles is modeled with a Gaussian:

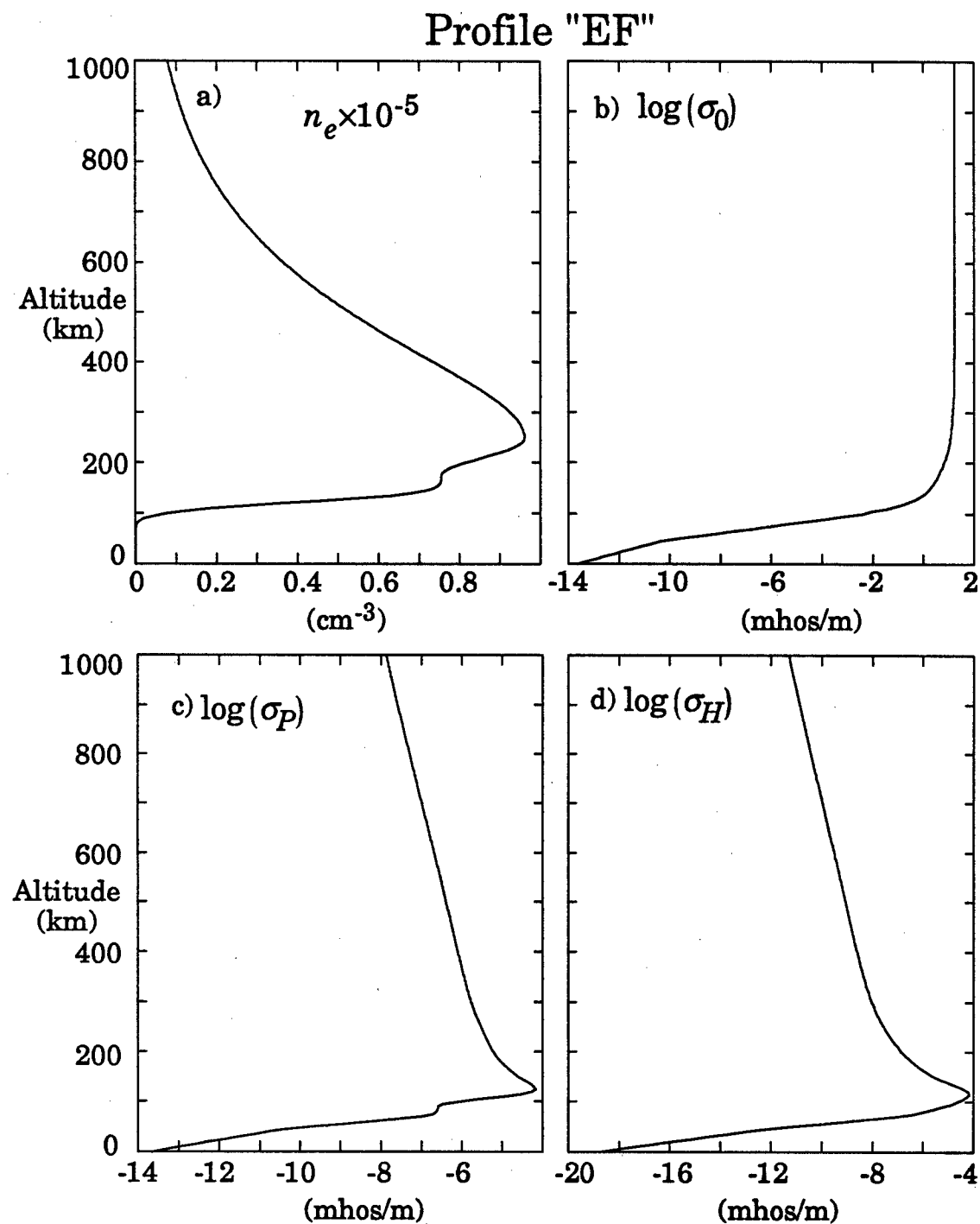


Figure 4.2 a) A typical electron density profile and the associated b) direct, c) Pedersen and d) Hall conductivity profiles for a sunlit, daytime ionosphere.

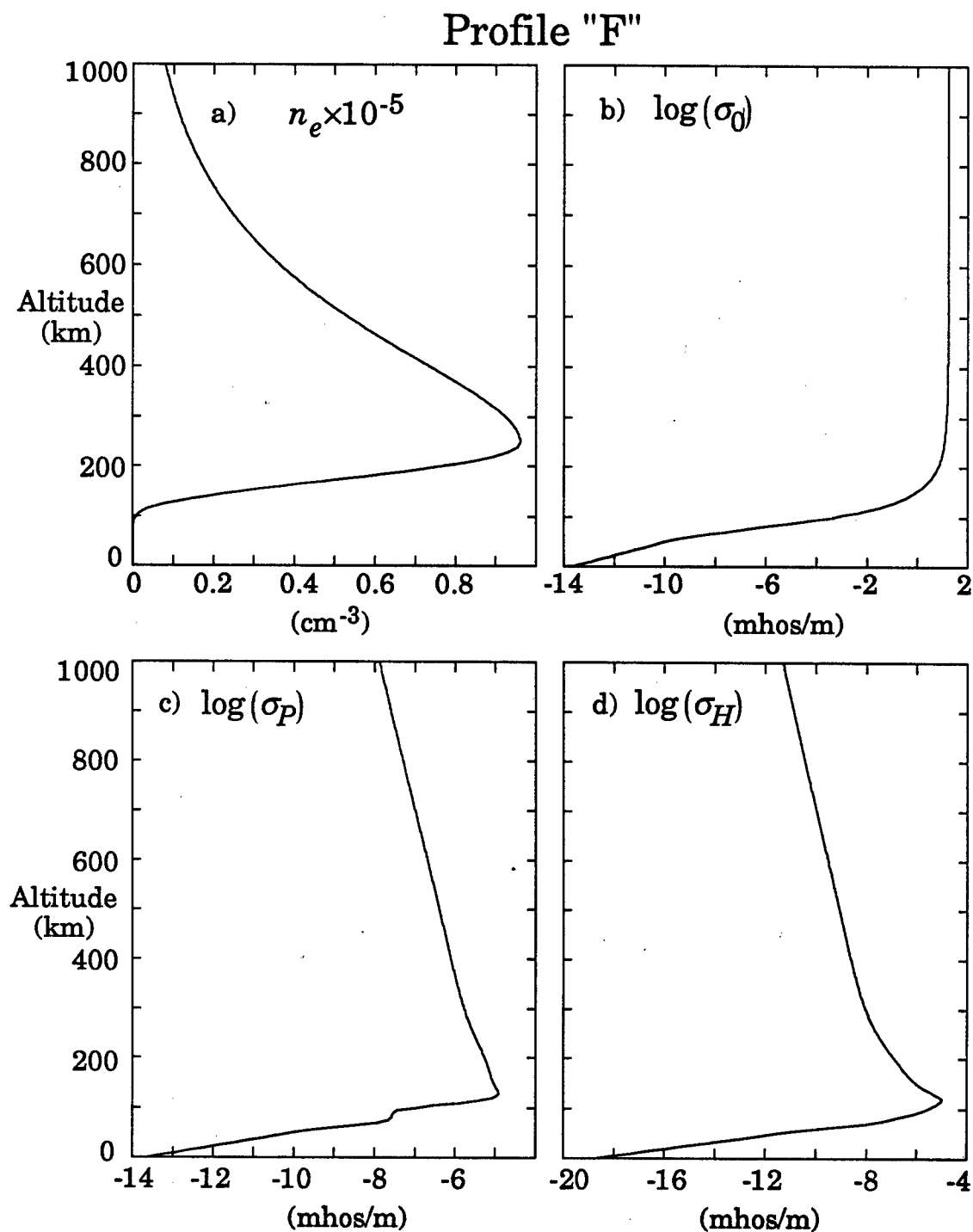


Figure 4.3 a) A typical electron density profile and the associated b) direct, c) Pedersen and d) Hall conductivity profiles for a post-sunset ionosphere with an F region only.

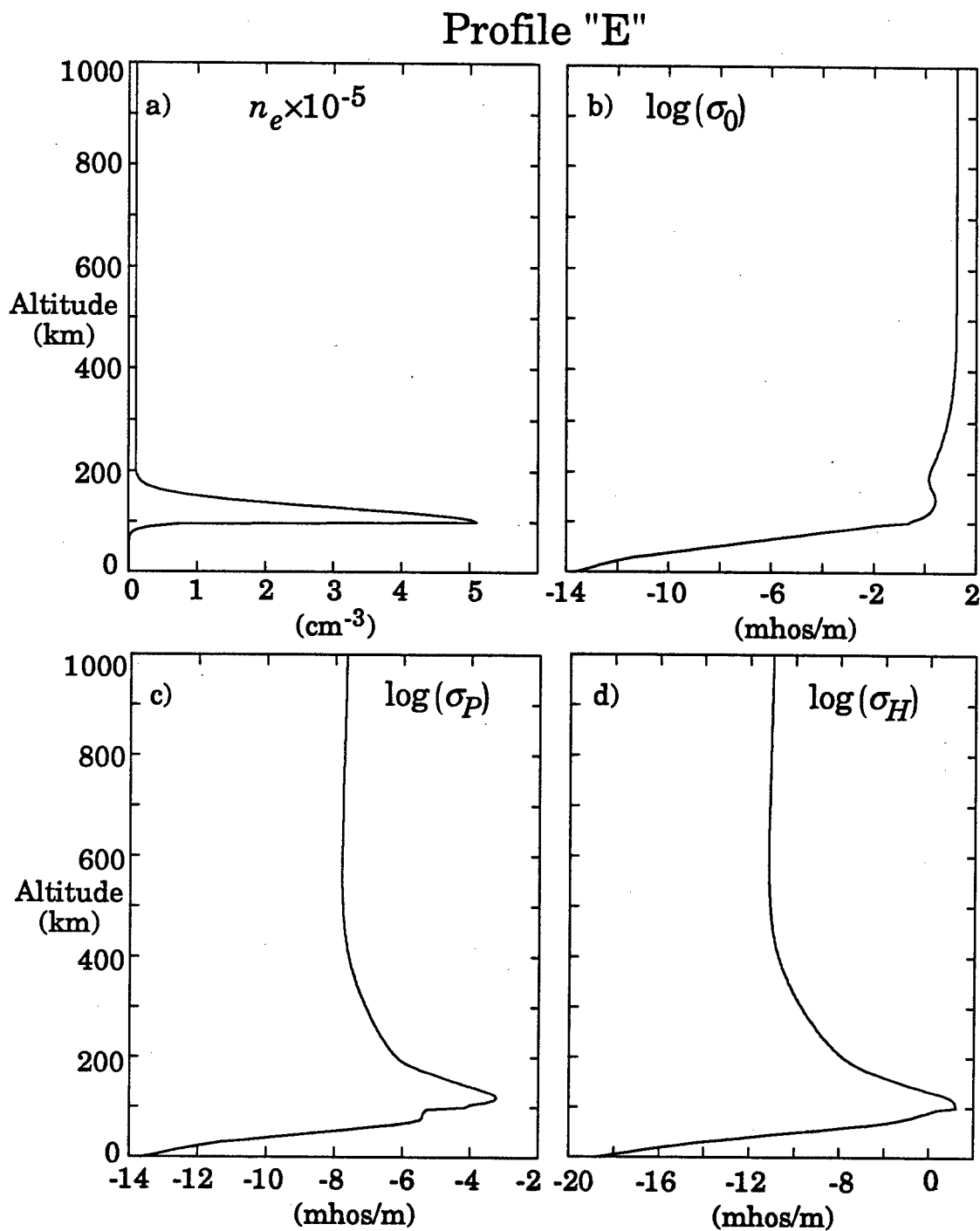


Figure 4.4 a) A typical electron density profile and the associated b) direct, c) Pedersen and d) Hall conductivity profiles for a nighttime ionosphere caused by relatively energetic electron precipitation.

$$n_{e,E}(z) = N_E \exp(-z^2/a^2) \quad (4.10)$$

The F-region ionization is from a Chapman profile [*Banks and Kockarts, 1973*],

$$n_{e,F}(z) = N_F \exp(0.5(1 - z' \cdot \exp(-z') \sec\chi)) \quad (4.11)$$

where $z' = (z - z_{max})/H$, z_{max} is the altitude of maximum ionization density, H is the scale height of the neutral atmosphere, and χ is the angle between the local zenith and the sun. For the model density profiles we have used $\sec(\chi) = 1$, and we adjust the value of H to give a "reasonable" profile based on the measured profiles we will present in the next chapter. We found that to mimic the experimental data, different scale heights above and below the F-region peak altitude were sometimes necessary. The various parameters used to create the model profiles are given in Table 4.1.

We calculate ion-neutral collision frequencies using the formulas in the appendix of *Schunk and Walker [1973]* in conjunction with the *Jacchia [1971]* neutral atmosphere model. The neutral atmosphere model uses an assumed thermospheric temperature as input, and although this parameter can vary widely we use 1000 K throughout this chapter and the next. *Banks and Kockarts [1973]* supply expressions for electron-neutral and electron-ion collision rates. We add these two quantities to obtain an effective electron collision frequency, i.e. $\nu_e = \nu_{en} + \nu_{ei}$. Strictly speaking, this is incorrect because the collisional drag term in the fluid equations is proportional to the velocity difference of the colliding species, and we have written (4.3) in a way that assumes that charged particles are colliding with particles at rest. The term ν_{ei} represents electron collisions with ions that are not necessarily at rest, although at altitudes where ν_{en} is not the dominant source of collisions it

Table 4.1. Density model input paramters as defined in Equations 4.10 and 4.11.

	<u>Profile E</u>	<u>Profile F</u>	<u>Profile EF</u>
N_E (cm $^{-3}$)	5×10^5	0	5×10^4
E-region topside, scale, a_{top} (km)	40		40
E-region bottomside scale, a_{bottom} (km)	5		40
E-region z_{max} (km)	100		140
N_F (cm $^{-3}$)		9.5×10^4	9.5×10^4
F-region topside scale, H_{top} (km)		120	120
F-region bottomside scale, H_{bottom} (km)		60	60
F-region z_{max} (km)		250	250
Background density (cm $^{-3}$)	10^4	10^3	10^3
Σ_P (mhos)	14	0.93	2.6

is reasonable to neglect the ion velocity. We also neglect collisions between ions of different species.

Below 95 km we increase collision frequencies and decrease charged particle densities exponentially with a scale height of 6 km, corresponding to the scale height of the neutral atmosphere. However, we do not allow the electron density to decrease below 1 cm^{-3} in order to make conductivities within 10 km of the ground consistent with Figure 20.3 of *Sagalyn and Burke [1985]*. Varying the density and collision frequencies in the lower atmosphere has little effect on the Alfvén wave electromagnetic fields above the ionosphere. Figures 4.5a-c show the electron and ion collision frequencies between 0 and 1000 km altitude for the 3 model profiles in Figures 4.2-4.4. The gross features of the profiles are quite similar, although v_e in the "E" profile does not decrease with decreasing altitude above 500 km as in the "EF" and "F" profiles. This is because electron-ion collisions dominate at the highest altitudes, and the high altitude ion density is constant in altitude for profile "E".

We use 2 ion species in our model. Far above 180 km we assume that O⁺ is the only constituent, and it changes smoothly to NO⁺ over about 40 km (centered at 180 km) as shown in Figure 4.5d. Of course there can be many other positively and negatively charged ions in the D and E regions of the ionosphere. *Hughes [1974]* chose to incorporate negative ions into his numerical model, but his purpose was to find Alfvén wave fields on the Earth's surface, so he needed an accurate measure of the attenuation of waves in the D region. In our case we will be comparing the model to data taken at several hundred km in altitude, and from working with the model we found that for our purposes the exact composition of the D region was unimportant.

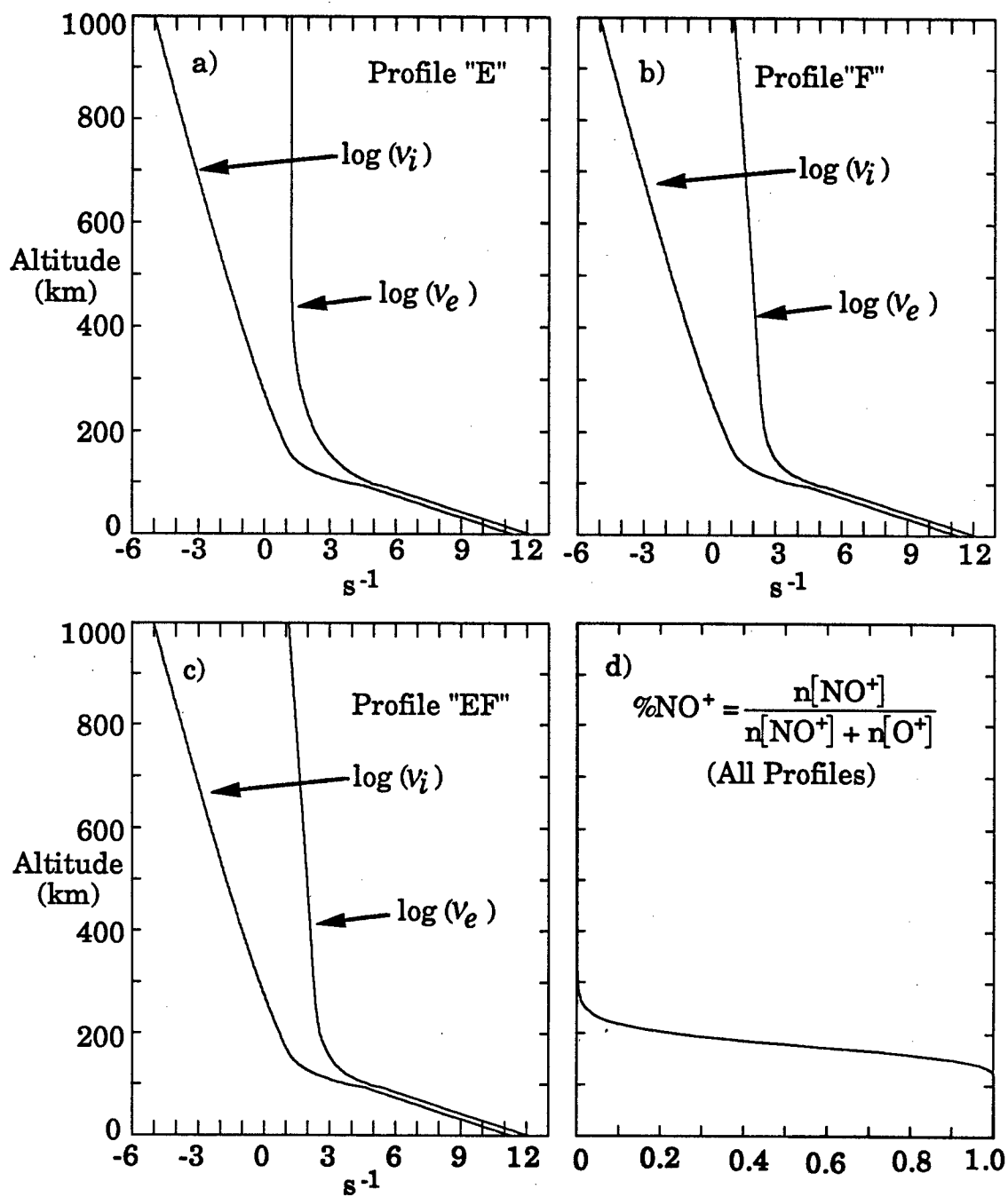


Figure 4.5 a-c) Electron and ion collision frequency profiles for the density profiles shown in Figures 4.2-4.4. d) Relative concentration of O^+ and NO^+ as a function of altitude used for input to the numerical model.

Charged molecular oxygen, O_2^+ , can be important in the E region, but its molecular mass (32 a.m.u.) is very close to that of NO^+ (30 a.m.u.), causing only a small change in the gyrofrequency and Alfvén velocity. The collision frequency for O_2^+ is different than that of NO^+ , but not enough to significantly change the results of the model. Later we will use the model to illustrate that small changes in collision frequencies have only a minor effect on the fields above the ionosphere.

Our purpose in this chapter is to illustrate with the numerical model the effects of various ionospheric features on Alfvén waves incident from the magnetosphere. One of the main subjects we will investigate will be the Alfvén wave reflection coefficient (a_3 in Equation 4.9) as a function of frequency for various ionospheric models. But first we will try in the next 2 sections to provide a general idea of some the phenomena associated with the Alfvén wave/ionosphere interaction by examining altitude profiles of the electric and magnetic field amplitudes at two different frequencies.

4.5 Quasi-Static Fields in the Ionosphere

Before we present output from the numerical model, we must make a few comments concerning our plotting conventions. We plot altitude profiles of the fields with 3 different curves. The first is the real part of the field, to give an idea of the number of wavelengths contained in each plot. We also plot both the amplitude of the field and the negative of the amplitude, which creates a wave "envelope". We do this because if we plot only the real part of the wave and the (positive) amplitude, it is often difficult to distinguish between the two.

A second convention we use is to plot all magnetic flux densities after multiplying them by the speed of light c . This means that magnetic and electric fields are plotted in the same units (V/m). Furthermore, since the incident slow mode electric field has a unit amplitude, cB_y is related to the refractive index of the slow mode. It is equal to the refractive index of the slow mode in the special case of no reflections.

Our model is constrained to non-zero frequencies, but we can make the frequency small enough to study the behavior of fields which are effectively "DC" in the ionosphere and lower atmosphere. It turns out that $f = 10^{-3}$ Hz is sufficiently low because at that frequency the spatial extent of the ionosphere is a very small fraction of an Alfvén wavelength. We have calculated the electric and magnetic field profiles with the "EF" density profile (Figure 4.2) for $f = 10^{-3}$ Hz and a horizontal spatial scale $\lambda_x = 1000$ km.

Turning to Figure 4.6a, we see that the meridional electric field E_x is constant at a value of about $E_x = 0.25$ until very close to $z = 0$, where it suddenly falls to zero as it must since we assume a perfectly conducting ground. At high altitudes the constant electric field E_x can be explained by referring to Equation 4.6a. When the neutral density becomes small, so do the collision frequencies, thus σ_0 becomes large. Since we have used a very small ω , Equation 4.6a reduces to

$$\partial E_x / \partial z \approx 0 \quad (4.12)$$

Equation 4.12 is equivalent to the statement that "large scale static electric fields map along field lines". We can see from the plot of the zonal electric field E_y in Figure 4.6b that σ_0 is not infinite, because it is evident that E_y does not map along field lines. Note that E_y is two orders

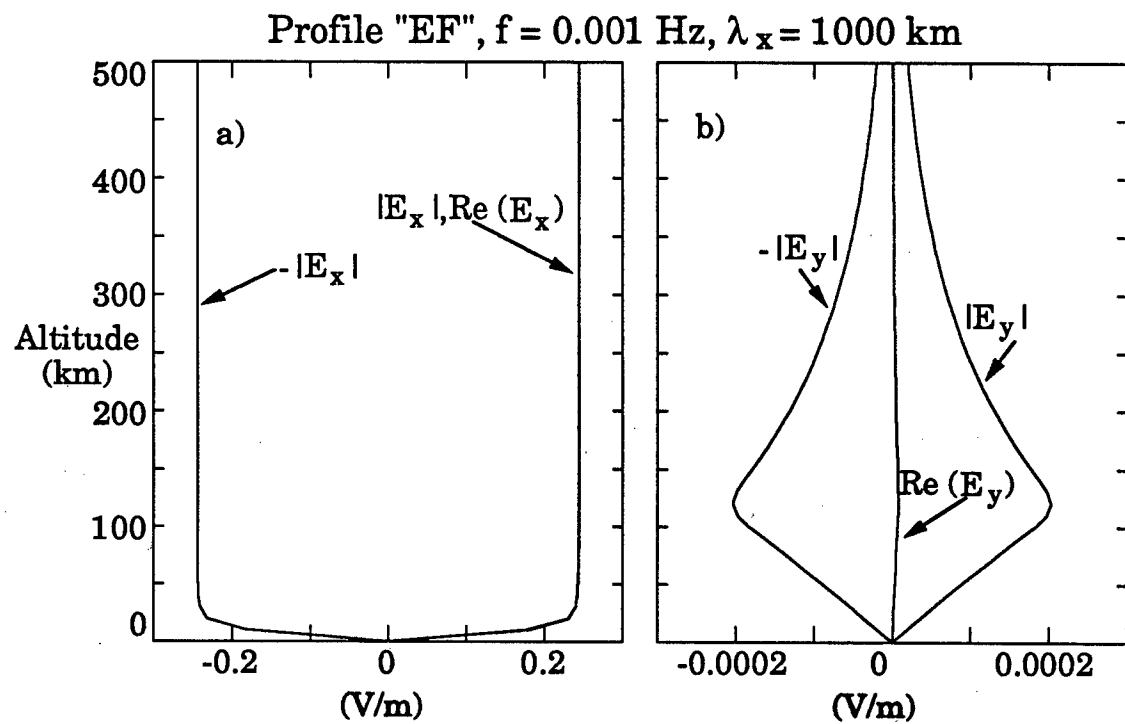


Figure 4.6 a) Meridional and b) zonal electric field profiles in the quasi-static limit.

of magnitude smaller than E_x . The reason for the different behaviors of the meridional and zonal electric fields is that we have assumed no variation in the \hat{y} direction, thus there can be no divergence in E_y . This means that the E_y is not sustained by electric charge concentrations building up along magnetic field lines, which is the case for E_x . Instead, we can think of E_y as a sort of "fringing field" which decreases with distance from its source in the E region, where σ_2 is large. At such a low frequency the electric fields must be essentially curl-free, so the change in E_y with altitude implies a non-zero parallel electric field E_z , which is only possible in our DC approximation for non-zero σ_0 . Both the zonal and parallel electric fields have very small amplitudes compared to the meridional electric field.

It is instructive to derive an expression for E_x near the Earth's surface in the DC approximation. At low altitudes we may safely neglect $\Omega \ll v$ (i.e. the medium is completely collision dominated), which from Equations 4.5 means that $\sigma_0 \approx \sigma_1$. We may also neglect σ_2 because it decreases as v^{-2} , while σ_0 and σ_1 decrease as v^{-1} . If we assume that the charged particle density near the ground is constant and $v_e \propto \exp(-z/H)$ where H is the neutral atmosphere scale height, we may write

$$\sigma_0, \sigma_1 \approx S_0 \exp(z/H) \quad (4.13)$$

If we neglect ω as unimportant and use (4.13) then (4.6a) and (4.6d) can be written

$$E'_x = -\frac{k_x^2}{\mu_0 S_0} e^{-z/H} B_y \quad (4.14a)$$

$$B'_y = -\mu_0 S_0 e^{z/H} E_x \quad (4.14b)$$

A prime denotes differentiation by z . If we multiply Equation (4.14a) by $e^{(z/2H)}$, (4.14b) by $e^{-(z/2H)}$, and recognize that $(e^{(z/2H)}E_x)' = (e^{(z/2H)}E_x)' - (2H) \cdot 1 e^{(z/2H)}E_x$, we can solve for $E_x(z)$:

$$E_x(z) = A e^{-z/2H} \sinh(z\sqrt{(2H)^2 + k_x^2}) \quad (4.15)$$

We have eliminated a "cosh" term from (4.15) to satisfy $E_x(0) = 0$. In the limit $H \ll \lambda_x$, (4.15) reduces to $E_x(z) = A(1 - e^{-z/H})$. Thus, in agreement with Figure 4.7a, we see that the DC meridional electric field maps from the magnetosphere through the lower atmosphere, and to within H of the Earth's surface.

One final detail concerning the DC meridional electric field is the magnitude of the field, or "A" in (4.15). The value in Figure 4.6a of 0.25 comes from the fact that we are applying an incident field of unit magnitude far from the ionosphere, but our model includes wave reflections. We can infer then that a reflected wave of amplitude -0.75 is interfering with the incident wave, and therefore the low frequency electric field reflection coefficient for the "EF" profile we have used is also -0.75. A simple way to check this is to treat the ionosphere as a conducting slab with $\Sigma_p = 2.6$ mhos for profile "EF" and the region above the ionosphere as a transmission line with characteristic impedance $Z_A = \mu_0 V_A = 2.8 \Omega$ at 1000 km for profile "EF". The resulting electric field reflection coefficient is then $(\Sigma_p^{-1} - Z_A)/(\Sigma_p^{-1} + Z_A) = -0.76$.

We turn now to the quasi-DC zonal magnetic field cB_y shown in Figure 4.6d. As with the meridional electric field E_x , cB_y "maps" along B_0 at high altitudes, but it does not penetrate into the lower atmosphere as does E_x . The reason for this is that at low frequencies and high altitudes, cB_y is created by field-aligned currents. Around a couple of

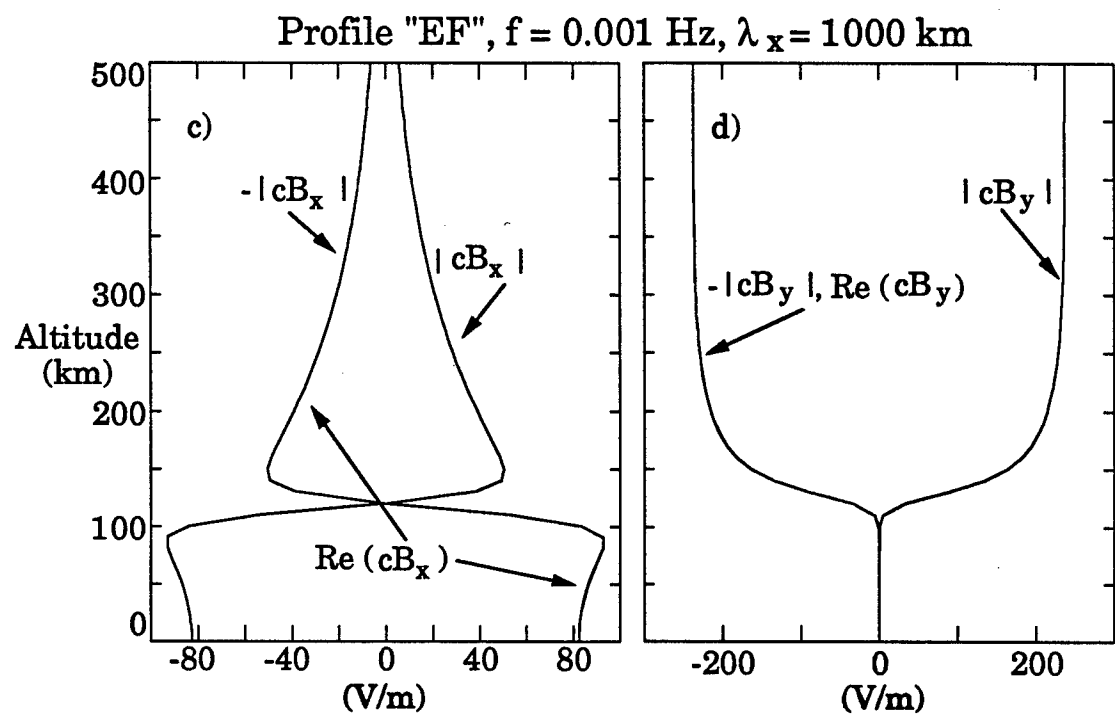


Figure 4.6 c) Meridional and d) zonal perturbation magnetic field profiles in the quasi-static limit.

hundred km altitude the field-aligned currents begin to close horizontally as the Pedersen conductivity becomes important. By the bottom of the ionosphere (around 100 km) the field-aligned currents have been completely closed by the Pedersen currents.

The absence of field-aligned currents alone does not explain the lack of any magnetic field cB_y below 90 km. That is, even though the field-aligned current sheets end at about 100 km, one might expect the magnetic field due to them to extend below 100 km. It turns out that the magnetic perturbation from the Pedersen current layer exactly cancels the field-aligned current contribution below the current system, so that no zonal magnetic field can "leak out" into the lower atmosphere. This is similar to the case of the magnetic field outside an infinitely long solenoid, which is identically zero everywhere. In Appendix B we prove that the magnetic field is zero outside of an idealized auroral arc consisting of two semi-infinite field-aligned current sheets which are connected by a thin Pedersen current layer. The Hall current in an auroral arc creates a magnetic field B_x that does have a magnetic signature on the ground.

The fact that the zonal magnetic field cB_y disappears below the E region is consistent with the fact that almost no Alfvén wave energy is dissipated in the lower atmosphere. This can be seen from the Poynting vector $\mathbf{E} \times \mathbf{H}$. Since $cB_y = 0$ in the lower atmosphere, the component $E_x \times H_y$ is also zero. The other part of the vertical component of the Poynting vector is also zero because even though the fast mode fields E_y and cB_x are both non-zero in the lower atmosphere, they are 90° out-of-phase, thus the time average of their product is zero. For example, at an altitude of 50 km, $E_y = 8.79 \times 10^{-5} \angle 87.9^\circ$ V/m and $cB_x = 86.7 \angle -2.1^\circ$ V/m. Electric fields

measured with balloons were compared to ground-based magnetic field measurements by *Mozer and Manka* [1971], who showed \mathbf{E}_\perp and $\delta\mathbf{B}_\perp$ were parallel, thus it follows that the vertical component of the Poynting vector was zero in the lower atmosphere.

The fast mode fields E_y and cB_x (Figures 4.6b and c) maximize near their source in the E region, and they fall off with a scale length roughly equal to the horizontal scale λ_x . This can be seen from the zero frequency limit of the fast mode dispersion relation in Equation (2.15), i.e. $k_z^2 = -k_x^2$. The narrow null in cB_x (Figure 4.6c) is due to the fact that there is a zonal Hall current driven by the meridional electric field E_x . One would expect cB_x to have opposite signs above and below the Hall current layer, thus the field must go through zero within the current sheet. Notice that unlike the zonal field cB_y , cB_x is non-zero at the ground.

4.6 A 1 Hz Alfvén Wave in the Ionosphere

At 1 Hz the wave nature of electromagnetic fields in the ionosphere is very evident. Another way of saying this is that the thickness of the lower atmosphere/ionosphere system is on the order of an Alfvén wavelength for frequencies on the order of 1 Hz. Thus static electric field mapping ideas are not applicable. This is evident in Figures 4.7a-d, where we plot the four horizontal field components at 1 Hz, using the same "EF" density profile (Figure 4.2a) as in the previous section.

Referring first to the meridional electric field E_x we see that at higher altitudes the magnitude of the field is much greater than in the quasi-static case, and it is not constant with altitude. This is because we are seeing the standing wave pattern caused by the interfering incident and reflected slow mode Alfvén waves. It appears from Figure 4.7a that

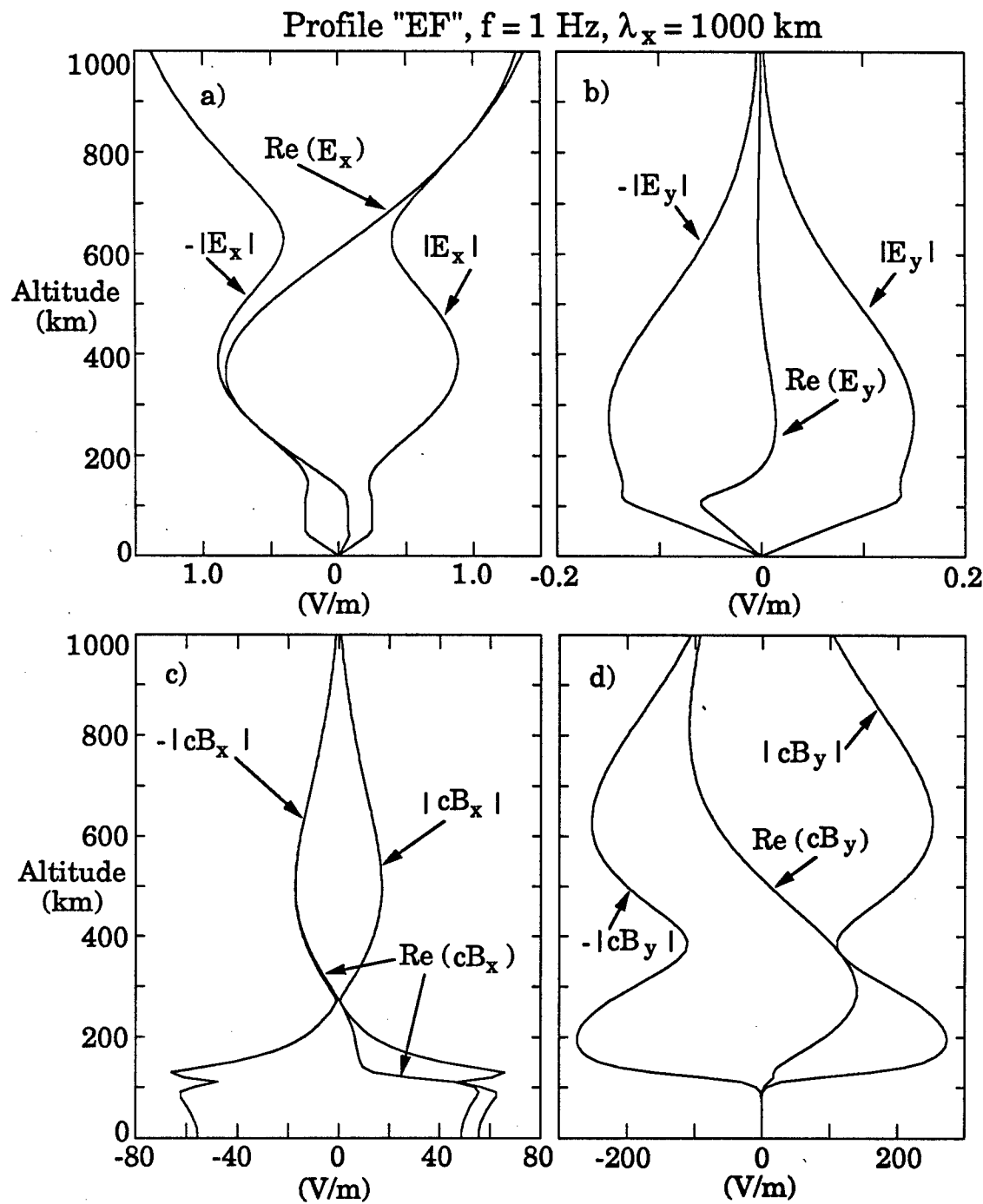


Figure 4.7 a) Meridional electric, b) zonal electric, c) meridional magnetic, and d) zonal magnetic field profiles due to a 1 Hz Alfvén wave reflecting from the ionosphere.

most of the reflection takes place at or above 100 km, and at 1000 km constructive interference leads to an amplitude greater than the incident wave amplitude (unity). The reflection coefficient at 1 Hz for this density profile is -0.4, so we expect a peak amplitude of 1.4 at half-wavelength intervals above 1000 km.

Below 100 km E_x is constant until about 40 km, then it begins to drop off, reaching zero at the ground. The zonal magnetic field cB_y in Figure 4.7b is similar to the quasi-static case except for the standing wave pattern above 100 km. As before, there is no zonal magnetic perturbation at the ground.

There are two notable differences between the 1 Hz and quasi-static fast mode fields E_y and cB_x (Figures 4.7c and d). First, E_y at 1 Hz is 2-3 orders of magnitude greater than in the quasi-static case, and secondly there is a "bulge" in the 1 Hz field amplitudes above 200 km. This is due to the fact that the 1 Hz Alfvén wavelength in the F region peak is about 690 km, which makes it less than the horizontal spatial scale λ_x of 1000 km. From Equation 2.16 this makes k_z real. Thus the fast mode Alfvén wave is not evanescent in the F region. As the density decreases above the F region, k_z again becomes imaginary. If we decrease λ_x to be less than 690 km the bulge in the field amplitudes disappears, but the fields in the E region and below do not change much.

As in the quasi-static case, the vertical component of the Poynting vector for a 1 Hz wave in the lower atmosphere is zero because $cBy = 0$ and E_y and cB_x are almost 90° out-of-phase. For example, at an altitude of 50 km, $E_y = 5.9 \times 10^{-2} \angle 119.8^\circ$ V/m and $cB_x = 58.3 \angle 28.9^\circ$ V/m. The phase difference is thus 90.9° . Again, this is consistent with the fact that almost no Alfvén wave energy is dissipated below the E region.

To provide a qualitative picture of the variation in electric field profiles versus frequency and altitude we have plotted surface contours of the meridional and zonal electric fields in Figures 4.8a and 4.8b. We have used $\lambda_x = 1000$ km. As the frequency exceeds 1 Hz the zonal field suddenly "turns on" and resonates in the F-region cavity. This resonance is driven at the expense of meridional electric field energy, as is evident from the slight decrease in the meridional field amplitude near 1.2 Hz.

At this point we are ready to study the effects of varying ionospheric parameters on Alfvén waves. We want to investigate the Alfvén wave/ionosphere interaction at many different frequencies; hence, the field amplitude profiles shown in the last two sections are not the most useful format for comparing numerical results. Instead we will use the frequency-dependent complex reflection coefficient for the slow mode Alfvén wave.

4.7 Reflection of Alfvén Waves from Different Ionospheric Density Profiles

The complex reflection coefficient Γ for the slow mode Alfvén wave is defined by

$$\Gamma = E_{x,up}(z = 1000)/E_{x,down}(z = 1000) \quad (4.16)$$

where the subscripts "up" and "down" refer to propagation direction, and the electric fields are evaluated at 1000 km. In our model we impose $E_{x,down}(z = 1000) = 1 + i0$, thus $\Gamma = E_{x,up}(z = 1000) = a_3$, where a_3 is found from Equation 4.9. Figures 4.9 a and b show the magnitude and phase of

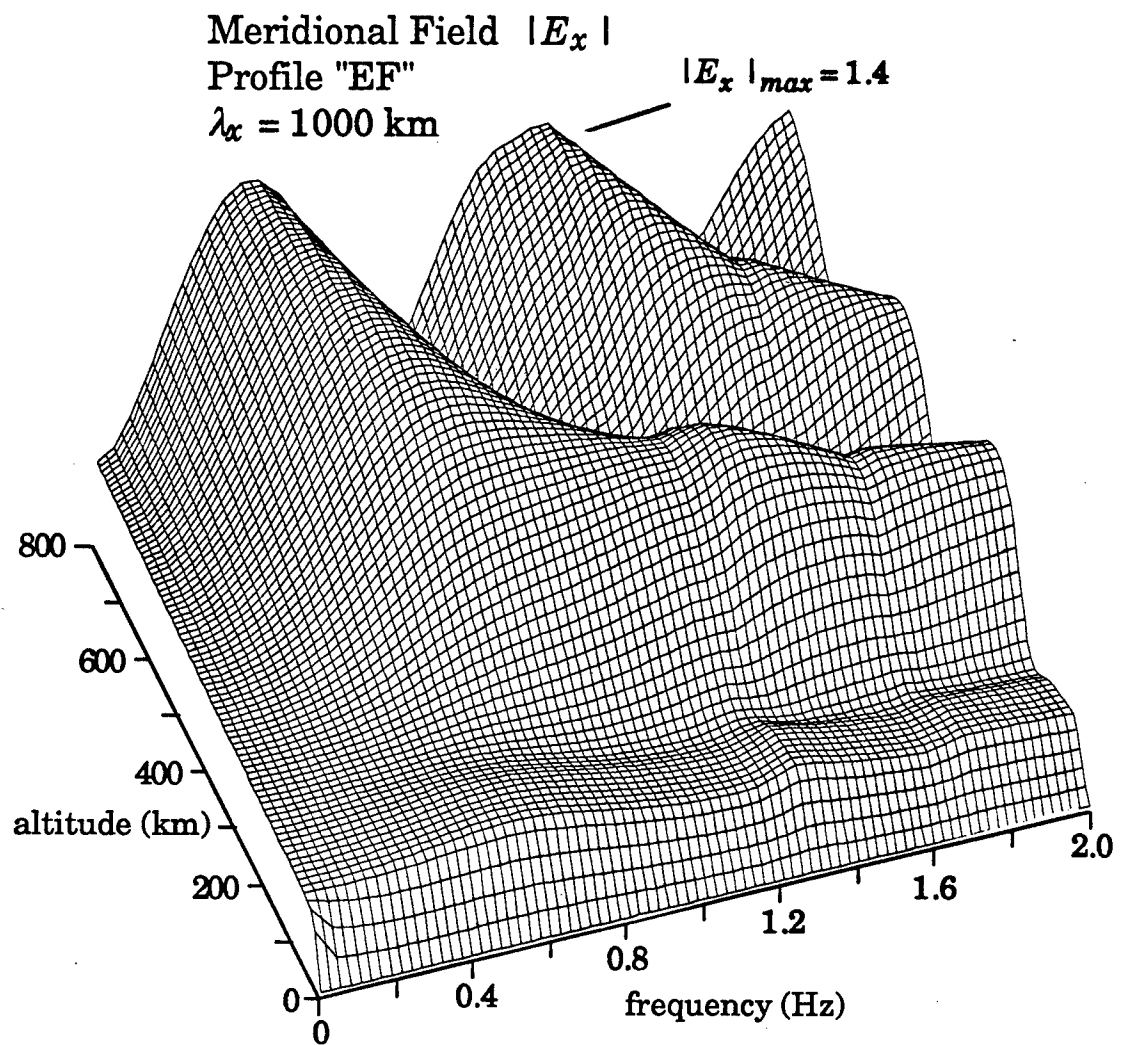


Figure 4.8a Surface plot showing the variation of the magnitude of the meridional electric field $|E_x|$ as a function of frequency and altitude.

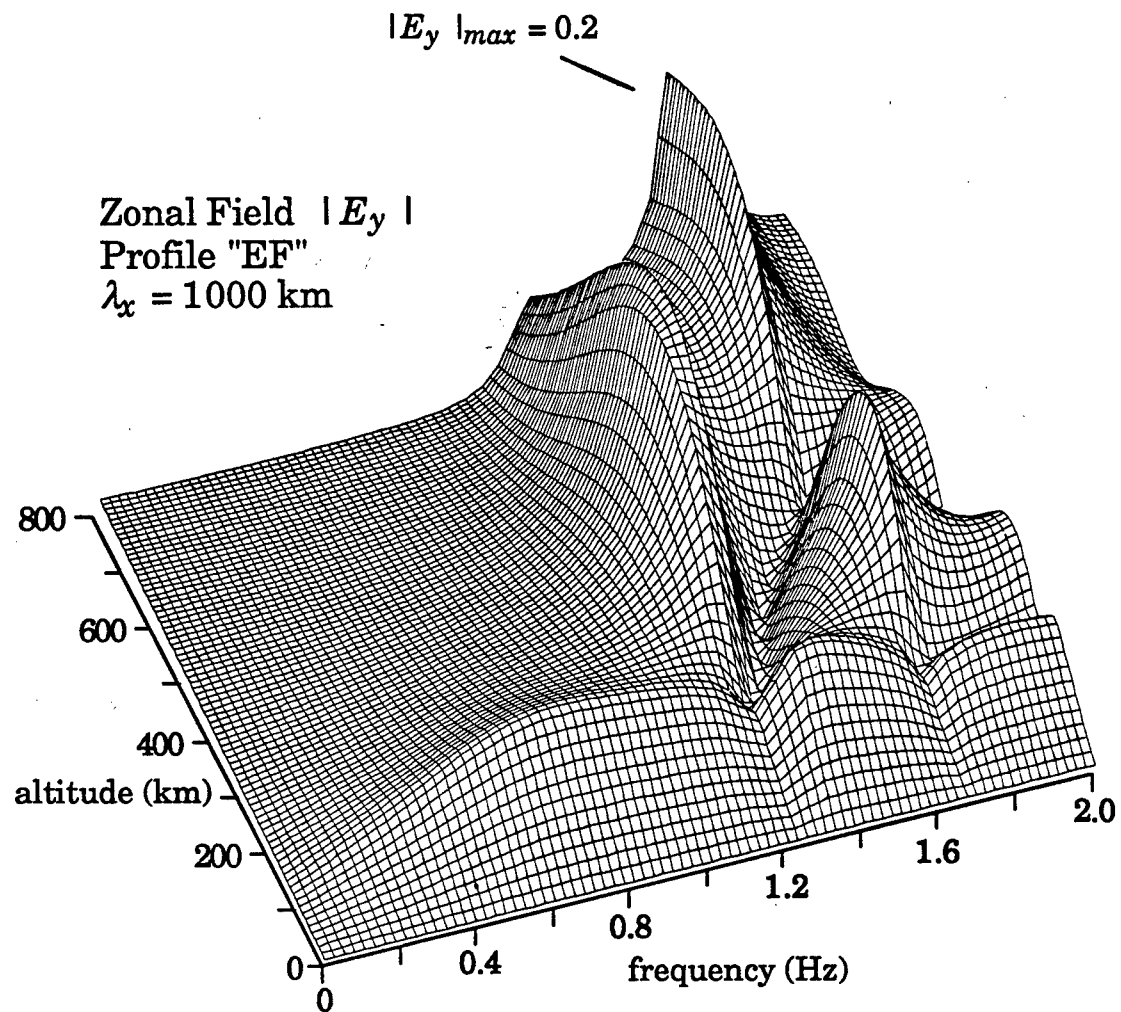


Figure 4.8b Surface plot showing the variation of the magnitude of the zonal electric field $|E_y|$ as a function of frequency and altitude.

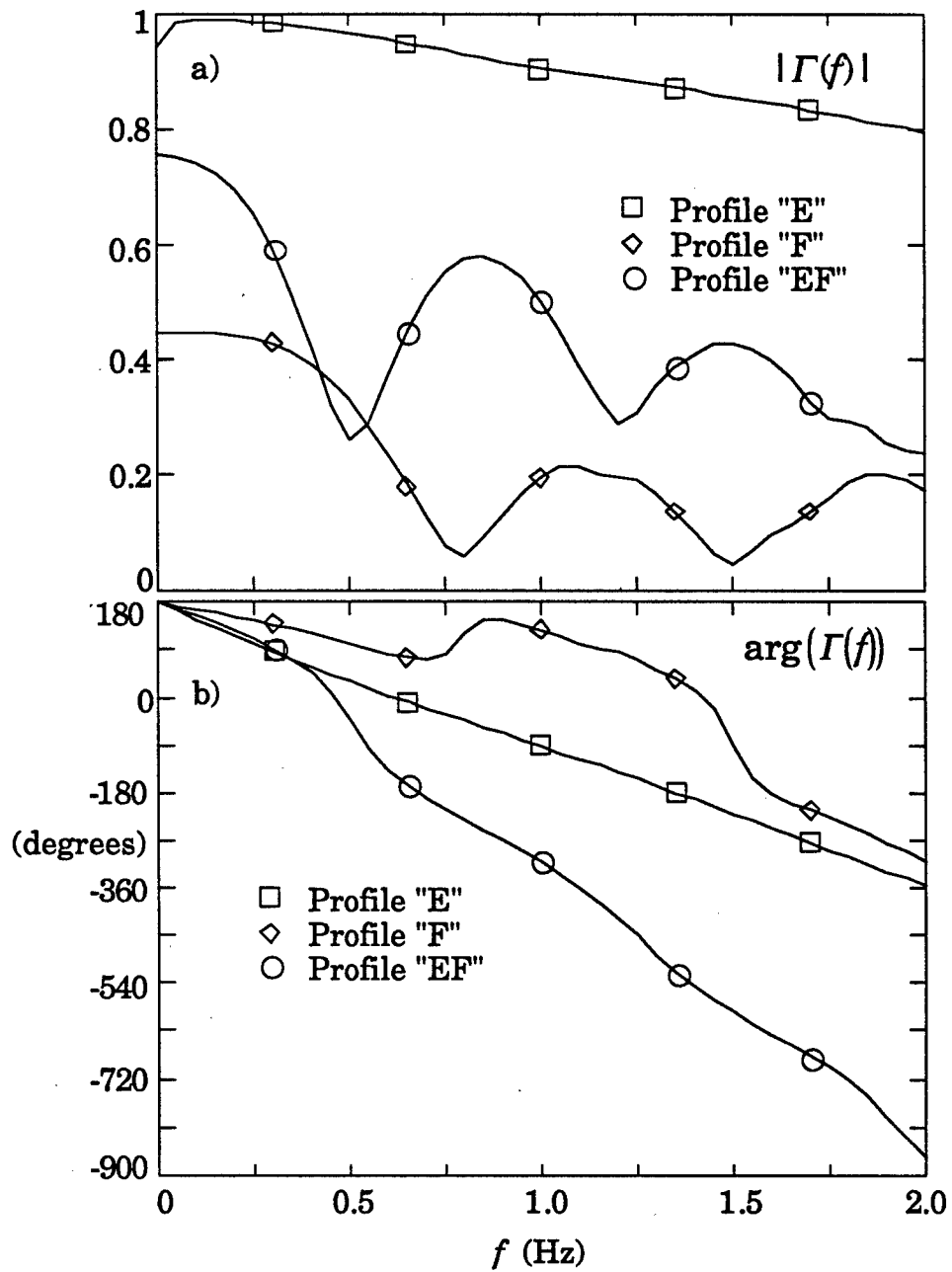


Figure 4.9 a) Magnitude and b) phase of the complex electric field reflection coefficient Γ at 1000 km altitude for the three ionospheric density profiles shown in Figures 4.2-4.4.

Γ as a function of frequency for each of the three density profiles in Figures 4.2 - 4.4. We use $\lambda_x = 1000$ km for these calculations.

In the low frequency limit for all three profiles the reflection coefficient Γ can be predicted with the transmission line analogy discussed in Section 4.5 by $(\Sigma_P^{-1} - Z_A)/(\Sigma_P^{-1} + Z_A)$ where again $Z_A = \mu_0 V_A$. The height-integrated Pedersen conductivities in each case are given in Table 4.1. As the frequency increases the "E" and "EF" profile reflection coefficients go through pronounced dips. This is a result of the fact that the ionosphere is a distributed load, thus the slab reflection model is not appropriate above roughly 0.1 Hz. A lower reflection coefficient Γ is a result of an increase in Joule dissipation given by $(E_x^2 + E_y^2)\Re(\sigma_1) + E_z^2\Re(\sigma_0)$. The real parts of the conductivities (denoted by the symbol \Re) are mostly unaffected by changes in frequency. Thus the increase in Joule dissipation is due to an increase in electric field magnitudes within the conducting layer. At the minimum Γ frequencies in Figure 4.9a the electric field standing wave pattern is such that E_x is increased in the E region. This increase in E_x can be seen in the surface plot in Figure 4.8a.

Superimposed on the dips in Γ in the "EF" and "F" curves is a general trend towards smaller reflection coefficients at higher frequencies. This is the propagation loss which increases as the electrical length of propagation increases. In a homogeneous medium this loss increases exponentially with electrical length. A second energy sink at higher frequencies is the zonal electric field, which increases because it is no longer evanescent, at least in regions of high density.

Figure 4.9b shows the phase angle in degrees of $\Gamma(f)$. If we again use a transmission line/load analogy, the overall negative slope in $\Gamma(f)$ gives an effective reflection altitude for the Alfvén waves. If we let d denote the

distance from 1000 km to the reflection point, then the phase angle ϕ between the upward and downward propagating slow Alfvén waves at 1000 km is given by $\phi = 2(360^\circ)d/\lambda$, thus $d\phi/df = 720^\circ d/V_A$. Applying this to the curve for the "E" profile in Figure 4.9b gives $d = 820$ km, or a reflection altitude of 180 km, which corresponds to the steep conductivity gradient on the top side of the E region.

In all 3 density profiles we have examined, the lower atmosphere plasma density profile was the same, namely an exponential decrease in charge density with decreasing altitude below 95 km. We have chosen a 6 km scale height for this decrease. We found that doubling the scale height to 12 km had no discernable effect on the 0-2 Hz reflection coefficient for the "EF" density profile, hence we conclude that accurate modeling of charge density in the lower atmosphere is unimportant for our purposes.

4.8 The Effect of Collisions on $\Gamma(f)$

Small reflection coefficients are due to efficient dissipation of electrical energy in the form of Joule heat, which is the result of particle collisions. If both electron and ion collisions are absent, then $\Gamma(f) \approx 1$. To determine the relative importance of the two types of collisions, we again calculated $\Gamma(f)$ for the "EF" density profile in Figure 4.2a, but we multiplied and divided the ion collision frequency ν_i by 3 at all altitudes, as shown in Figure 4.10. We have re-plotted the original $\Gamma(f)$ from Figure 4.9a for reference. At low frequencies, more ion collisions increase Σ_p and consequently the reflection coefficient. The behavior is not as intuitively predictable above 1 Hz.

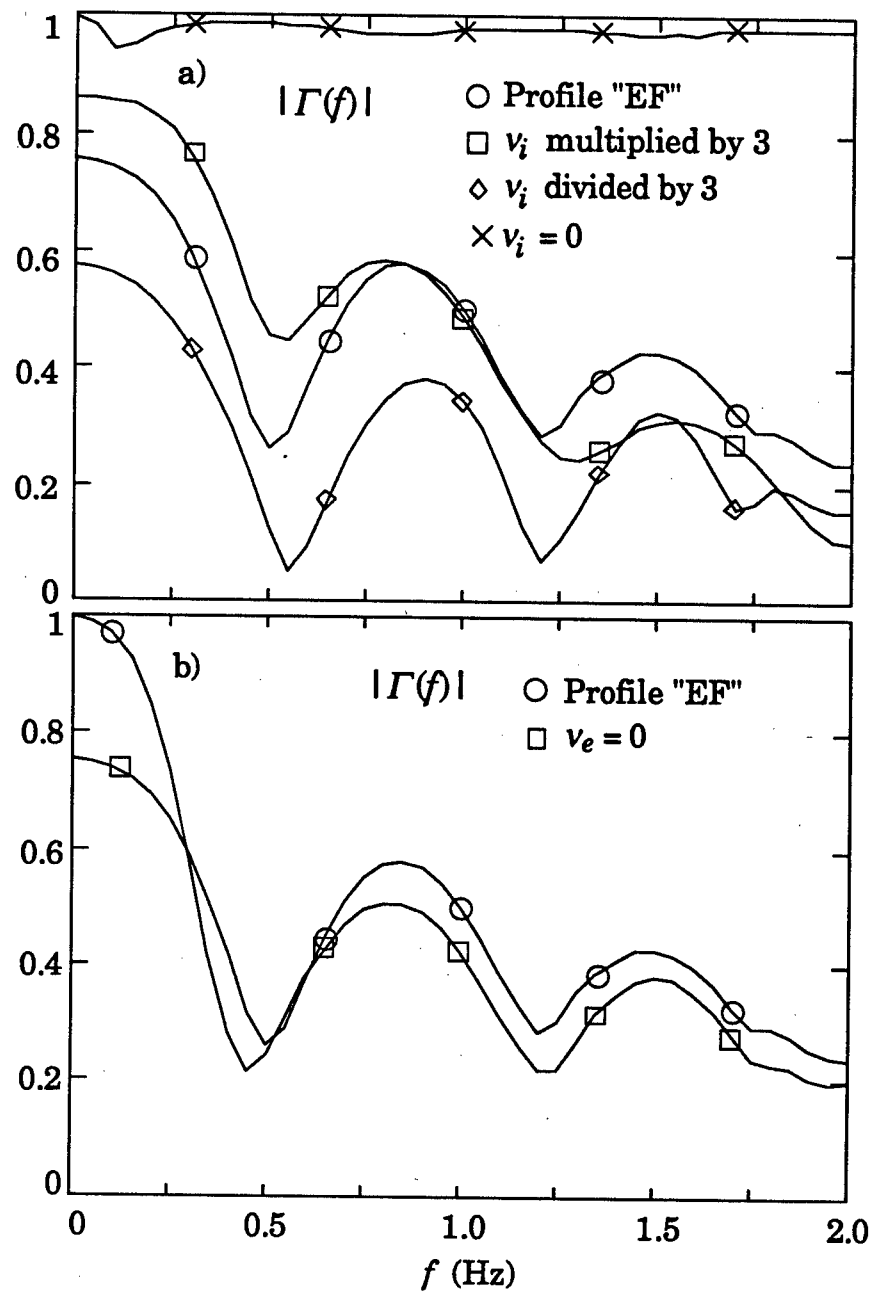


Figure 4.10 Illustration of the effects that changes in ion collision frequencies (upper panel) and electron collision frequencies (lower panel) can have on the magnitude of $|\Gamma|$.

The Γ curve resulting from $v_i = 0$ in Figure 4.10a shows that electron collisions account for only a small part of the energy absorption, allowing most of the incident wave to reflect. Figure 4.10b also illustrates the slight effect of electron collisions by comparing the original $\Gamma(f)$ along with the curve for $v_e = 0$. Above 0.2 Hz the two curves differ by only a few percent. We can conclude that ion collisions are mainly responsible for the dissipation of Alfvén wave energy.

Notice in Figure 4.10a that decreasing the ion collision frequency by a factor of three reduces $|\Gamma|$, but eliminating v_i completely increases $|\Gamma|$ to near unity. This seemingly contradictory behavior is a result of the fact that ion collisions play two distinct roles -- they both reflect and absorb energy. Dividing v_i by three decreases Σ_P and allows for a better impedance match to the region above the ionosphere. As a result, electric fields penetrate deeper into the E region, and more energy is dissipated. But at some point, decreasing v_i will limit the amount of E-region attenuation and the wave will simply reflect off of the Earth's surface and back into the magnetosphere.

4.9 $\Gamma(\lambda_x)$

In previous sections we have varied ionospheric parameters but assumed a constant horizontal spatial scale λ_x of 1000 km. The reflection coefficient for the slow mode Alfvén wave is mostly unaffected as long as $\lambda_x > 10$ km. To investigate smaller scales with the numerical model we have to neglect the fast mode completely because the fast mode at x scales near 10 km is very evanescent, and over the 1000 km simulation region the code must integrate through hundreds of e-folds in amplitude, which is computationally prohibitive. Neglecting the fast mode probably doesn't

cause significant errors in our results because its amplitude is quite small for small λ_x . Figure 4.11 shows $|\Gamma(\lambda_x)|$ between 10 and 1 km for quasi-DC fields, and although the dependence is not strong, a clear trend towards smaller Γ below 2.0 km scales is evident. A possible reason for this decrease is that electric fields with horizontal spatial scales less than a few km map poorly through the E region. This scale-size dependence of electric field mapping is well known [see for example Farley, 1960]. A consequence of this poor mapping is that the electric field "sees" less of the conductivity in the E region, so the effective height-integrated conductivity is less. This in turn means the ionospheric impedance is more nearly matched to the Alfvén impedance above the ionosphere, and an impedance match implies a smaller reflection coefficient.

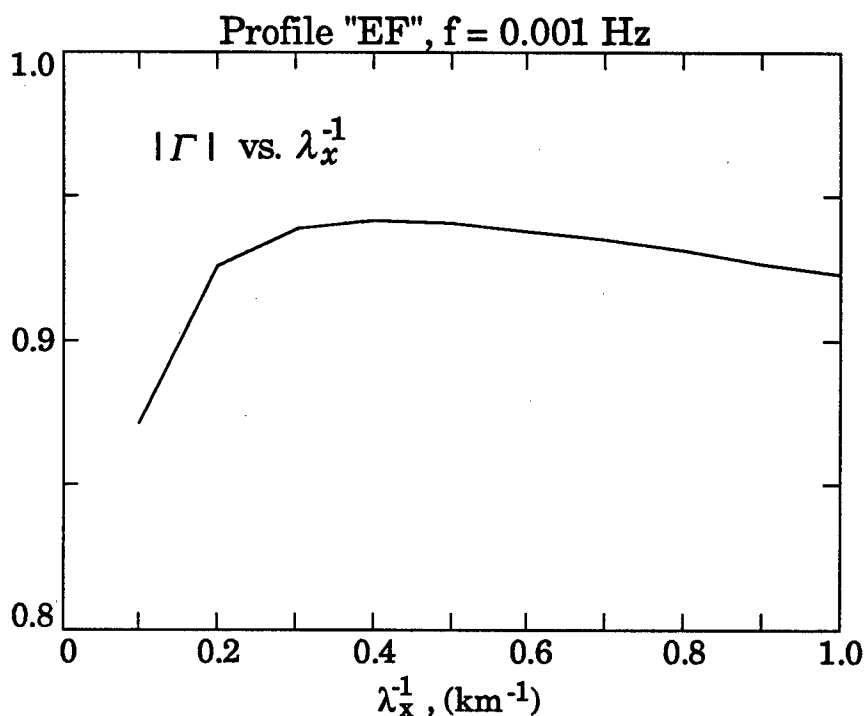


Figure 4.11 Reflection coefficient magnitude, $|\Gamma|$, as a function of inverse horizontal spatial scale λ_x^{-1} .

CHAPTER 5

ROCKET AND SATELLITE MEASUREMENTS OF ALFVÉN WAVES ASSOCIATED WITH THE DISCRETE AURORA

5.1 Introduction

The connection between Alfvén waves and auroral arcs has been discussed by many authors [*Hasegawa, 1976; Goertz and Boswell 1979; Haerendel 1983; Seyler 1988*], mainly because Alfvén waves are a possible mechanism for auroral electron acceleration. One of the purposes of this chapter is to establish experimentally (at least in a few examples) that Alfvén waves occur near auroral arcs. Our main goal is more general, however. We will develop and apply techniques to analyze auroral electric and perturbation magnetic field data and extract information concerning the source, propagation, dissipation, and relative amounts of spatial and temporal structuring of those fields.

Zmuda et al. [1966] were among the first to measure magnetic fluctuations with a satellite. The measurements were taken at 1100 km with the 1963 38C satellite and the authors interpreted the fluctuations as Alfvén waves. Many authors have identified Alfvén waves in satellite measurements taken at altitudes of several Earth radii, most recently *Erlandson et al. [1990]*, who measured very coherent burst of elliptically polarized waves below 1 Hz with the Viking satellite. *Iyemori and Hayashi [1989]* also found coherent bursts of Alfvén waves with the Magsat satellite orbiting at 400 km, but purposefully neglected latitudes

above 65° "because of the difficulty in distinguishing the waves from the small-scale field-aligned current structures."

Sugiura et al. [1982], *Sugiura* [1984], and *Smiddy et al.* [1984] measured electric and magnetic fields perpendicular to \mathbf{B}_0 with the DE-2 satellite near the ionosphere (< 1000 km) at auroral latitudes and found them to be highly correlated but not coherent as in the above studies. Furthermore, they found that the ratio $Z = \mu_0 E_{rms} / \delta B_{rms}$ was not equal to $\mu_0 V_A$ as one would expect from Alfvén waves but instead $Z = \Sigma p^{-1}$. As we discussed at the end of Chapter 3, this can be explained by a static electric field/Birkeland current model with fluctuations arising from the motion of the spacecraft through spatial structures with scale sizes from hundreds of meters to hundreds of km. Since the spectrum of fluctuating fields measured by a spacecraft traversing the auroral oval is generally a monotonically decreasing function of frequency, the bulk of the spectral energy lies at low frequencies. A correlation analysis of electromagnetic field fluctuations measured in the oval will therefore emphasize the largest scales in the system.

Rather than forming a single r.m.s. measure of field fluctuations, we will relate the amplitudes and phases of electric and magnetic fields as a function of frequency, which allows us to investigate spatial and/or temporal scales that are smaller than those considered in previous studies of auroral fields and closer to the regime associated with discrete auroral arcs and Alfvén waves.

There are several ways to detect Alfvén waves in the ionosphere. The most direct is to look for coherent electromagnetic field oscillations in the time-domain data. We have already seen an example of this in HILAT satellite data in Chapter 3 (Figure 3.13). Recently *Boehm et al.*

[1990] found Alfvén waves in the time-domain data from a Black Brant X sounding rocket launched into the morning auroral oval (see Section 3.5). One can also detect Alfvén waves by forming frequency-time sonograms and looking for narrow-band enhancements in the electric and magnetic field spectra. For example *Erlandson et al.* [1990] used this technique with Viking satellite data.

The frequencies at which spectral enhancements occur provide information pertaining to the source and propagation of Alfvén waves which has to date not been fully exploited. The peaks may represent the frequency of the source supplying the Alfvén waves, or properties of the medium through which they have traveled. For example *Lysak* [1988] showed that the exponential density decrease thousands of km above the ionosphere can give rise to resonant excitations in the ionosphere. Another cause for structuring in frequency is interference between waves incident from the magnetosphere and reflected from the ionosphere, i.e. standing waves. One way to distinguish between these possibilities is to form the quotient of the electric and magnetic field spectra. Spectral enhancements due to the source of Alfvén waves will appear in both the electric and magnetic field spectra. Dividing the spectra gives what we call the "impedance function" $Z(f)$, and we will show in the next section that any structuring it has in frequency must be due to standing Alfvén waves. In this chapter we will also examine the frequency-dependent phase relation between the meridional electric and zonal magnetic fields E_x and δB_y , and show that this can also be used to identify standing wave patterns. These techniques have the advantage that in some cases they can detect Alfvén waves when their presence in time-domain or spectral data alone is not obvious.

5.2 The Impedance Function

Let $\tilde{E}_x(f)$ and $\delta\tilde{B}_y(f)$ be the complex Fourier transforms of the meridional electric and zonal magnetic fields measured in the frame of a moving satellite or sounding rocket. The complex impedance $\tilde{Z}(f)$ is defined by

$$\tilde{Z}(f) = \mu_0 \tilde{E}_x(f) / \delta\tilde{B}_y(f) \quad (5.1)$$

We will use $Z(f)$ to denote the magnitude of $\tilde{Z}(f)$, and this is what we will call the "impedance function". In practice we find the impedance function from $\mu_0(P_E/P_B)^{1/2}$ where P_E and P_B are the electric and magnetic field power spectra of $E_x(t)$ and $\delta B_y(t)$.

We will compare $Z(f)$ from spacecraft-measured electromagnetic fields above the aurora with the predictions of three ideal models: 1) Structured static fields and Birkeland currents, 2) traveling Alfvén waves with no horizontal structure, and 3) standing Alfvén waves with no horizontal structure.

In the static field model the frequency f measured in the spacecraft frame is due entirely to the motion of the spacecraft through spatial structures with scale size λ_x . If the spacecraft velocity in the \hat{x} direction is V_s , then $f\lambda_x = V_s$. In this case $Z(f) = \Sigma_P^{-1}$ for all spatial scales greater than a few km. This is violated at small scales because the electric fields do not map completely through the E region, thus the height-integrated Pedersen current decreases.

A traveling Alfvén plane wave will have an impedance function which is constant in frequency and which is equal to the characteristic impedance of Alfvén waves, $Z_A = \mu_0 V_A$. As we mentioned in the introduction, $Z(f)$ is constant in this case even when the Alfvén wave

source supplies waves at preferred frequencies because spectral enhancements occur in both P_B and P_E and therefore divide out. Obliquely propagating traveling waves have a modified impedance when the horizontal wavelength λ_x approaches the electromagnetic skin depth c/ω_{pe} , and this can cause $Z(f)$ to vary with frequency. We will consider this possibility in more detail in the discussion section at the end of this chapter.

Previous authors have measured the ratio of electric and magnetic field spectra and have found values between Z_A and ΣP^{-1} . One of the first to do this was *Gurnett et al.* [1984] who used the Dynamics Explorer 1 satellite to measure the refractive index cB/E (proportional to $Z^{-1}(f)$) between 1.78 and 31.1 Hz. These authors pointed out that a static field-aligned current model was not sufficient at all frequencies. *Berthelier et al.* [1989] also calculated the refractive index versus f using the AUREOL-3 satellite and found a refractive index that was structured in frequency but again was larger than could be expected from Alfvén waves. They concluded that the fields must have been due to Doppler-shifted static fields. As we will see, both the structuring in frequency and the seemingly high refractive index are consistent with the standing Alfvén wave model.

Near a boundary such as the ionosphere, an Alfvén wave will be partially reflected due to the high conductivity, and the incident and reflected waves will form a standing wave pattern. In this case the impedance function will vary with distance from the reflection point.

The vertically changing field impedances in a standing wave pattern are essentially impossible to detect directly in the Earth's auroral zone since satellite trajectories are horizontal, and rockets cannot make a

vertical cut through a distance of several times $\lambda/4$ quickly enough to unambiguously separate temporal and spatial variations. (Future satellite or space shuttle experiments with tethered probes may make a direct measurement of a standing wave pattern possible.) This is not true in the case of whistler mode waves which have much shorter wavelengths. For example *Siefring et al.* [1990] have reported standing VLF waves at two frequencies below a sporadic E layer. In this case the transmitters were on the ground and at a fixed frequency so the analysis was straightforward. Here we must cope with a geophysical source of unknown character which co-exists with a spatially turbulent convection electric field, and in which are imbedded field-aligned current sources. Furthermore, in our case the reflecting surface is almost certainly structured at scales which in the satellite frame generate frequencies in the Alfvén wave regime. Despite these difficulties, evidence for standing Alfvén waves can be found from the impedance function because different frequencies correspond to different electrical lengths above the ionosphere; that is, higher frequencies in $Z(f)$ correspond to larger electrical distances above the ionosphere.

For a uniform reflecting sheet of integrated conductivity Σ_P in contact with a uniform medium characterized by a constant impedance Z_A the electric and magnetic fields due to an Alfvén wave can be written

$$\tilde{E}(z, t) = \tilde{E}_{\text{incident}}(e^{i(\omega t + k_z z)} + \Gamma e^{i(\omega t - k_z z)}) \quad (5.2a)$$

$$\tilde{B}(z, t) = \tilde{B}_{\text{incident}}(e^{i(\omega t + k_z z)} - \Gamma e^{i(\omega t - k_z z)}) \quad (5.2b)$$

where a tilde denotes a complex quantity, $\omega/k_z = V_A$ and Γ is the electric field reflection coefficient $(\Sigma_P^{-1} - Z_A)/(\Sigma_P^{-1} + Z_A)$. (See for example *Ramo, Whinnery, and Van Duzer* [1965] or other texts on plane wave

propagation or transmission lines.) The ratio of (5.2a) to (5.2b) gives the complex impedance function

$$\tilde{Z}(\omega) = \mu_0 V_A \left[\frac{1 + \Gamma e^{-2i\omega z / V_A}}{1 - \Gamma e^{-2i\omega z / V_A}} \right] \quad (5.3)$$

The magnitude of the impedance function $Z(f)$ varies between Z_A/S and $Z_A S$ where S is the standing wave ratio given by $S = (1 + |\Gamma|)/(1 - |\Gamma|)$. For ionospheric reflections with $Z_A > \Sigma_p^{-1}$ the minimum and maximum impedances above the ionosphere are Σ_p^{-1} and $Z_A^2 \Sigma_p$ and are separated by a distance $\lambda_z/4$ where $\lambda_z = V_A/f$.

Of course the ionosphere above the reflecting E region is not homogeneous as we have assumed above, and later in the chapter we will attempt to predict the behavior of measured impedance spectra using the numerical model of Chapter 4. However, a simple and reasonable estimate of the frequency f_{max} of the first peak in $Z(f)$ can be found by neglecting partial reflections off of F-region density gradients and assuming a single reflection from the top of the E region (at z_{min}). (This assumption is valid under a WKB approximation.) The result is

$$\frac{1}{f_{max}} = 4 \int_{z_{min}}^{z_{max}} \frac{dz}{V_A(z)} \quad (5.4)$$

which reduces to $f_{max} = V_A/[4(z_{max} - z_{min})]$ for constant V_A . Here z_{max} is the height at which the fields are measured.

Knudsen et al. [1990] showed in two examples, one from a sounding rocket and one from the HILAT satellite, in which measured peaks in the impedance functions were predicted by (5.4). We will present some of those results along with new data later in the chapter. When calculating impedance spectra from sounding rocket and satellite data, large fluctuations due to noise arise when dividing the electric and magnetic

field spectra. To reduce the amount of statistical variation in the measured impedance spectra, we split the time series data into several 32 point sub-intervals overlapping by 16 points. The electric and magnetic field spectra from each sub-interval are averaged before dividing to find $\tilde{Z}(f)$. Before calculating the individual spectra we subtract a linear least-squares fit from the time-domain data and multiply by a Hanning window [Press *et al.*, 1986].

5.3 The Normalized Cross-Spectrum

Standing Alfvén waves can be distinguished from traveling waves or static fields not only by the magnitude of the complex impedance function as discussed above, but by its phase as well. In a pure standing electromagnetic wave (i.e. with $\Gamma = \pm 1$) the electric and magnetic fields are shifted by $\pm 90^\circ$, according to (5.3). Dubinin *et al.* [1985] measured this effect with the *Intercosmos-Bulgaria-1300* satellite by calculating the phase shift between each Fourier component of E and δB field fluctuations. If the standing wave ratio is finite, $|\arg(\tilde{Z}(f))|$ is less than 90° and varies along the propagation direction. For traveling Alfvén waves ($\Gamma = 0$), E_x and δB_y are in phase. This is also true for static fields as one can see by letting $\omega = 0$ in Equation 5.3.

For Alfvén waves reflecting from a complicated medium such as the ionosphere, we can use the numerical model in Chapter 4 to predict the phase angle of $\tilde{Z}(f)$ in order to compare with measurements. An experimental measure of the phase angle of $\tilde{Z}(f)$ is given by the normalized cross-spectrum defined in general by

$$\tilde{C}_{12} = \frac{\langle \tilde{S}_1(f) \tilde{S}_2^*(f) \rangle}{\langle |\tilde{S}_1(f)|^2 \rangle^{1/2} \langle |\tilde{S}_2(f)|^2 \rangle^{1/2}} \quad (5.5)$$

where \tilde{S}_1 and \tilde{S}_2 are the Fourier transforms of the two time series to be compared, brackets denote ensemble averages, and the asterisk signifies the complex conjugate. \tilde{C}_{12} will provide us not only with a phase relation between E_x and δB_y but also with a measure of the validity of that estimate. General discussions of the cross-spectrum and applications can be found in signal processing textbooks, e.g. *Papoulis* [1965] or *Jenkins and Watts* [1968].

The cross-spectrum has been used in a variety of geophysical experiments. For example, in coherent backscatter radar work \tilde{S}_1 and \tilde{S}_2 are the Fourier transforms of the received signals from spatially separated antennas, thus the phase angle $\arg(\tilde{C}_{12}(f))$ (known as the "phase spectrum") can be used to estimate the source location of scatterers and the magnitude $|\tilde{C}_{12}(f)|$ (the "coherency spectrum") contains information both on the signal-to-noise ratio and the spatial extent of the scatterer [Farley *et al.*, 1981; Kudeki, 1983; Providakes, 1985; Sahr, 1990]. Labelle [1985] used the cross-spectrum to measure plasma wave vectors by correlating the signals from spatially separated density probes on board a sounding rocket.

In our case we will take \tilde{S}_1 and \tilde{S}_2 to be the Fourier transforms of the meridional electric and zonal magnetic fields E_x and δB_y , respectively. The phase angle given by the cross-spectrum measures the difference of the phase angles of the Fourier components of E_x and δB_y , which of course is the phase angle of $\tilde{Z}(f)$. If a constant phase relation between E_x and δB_y is maintained throughout the time series and the signal is not noisy, then the coherency $|\tilde{C}_{12}(f)|$ will be close to unity. Smaller values

can be due either to a small signal-to-noise ratio or to an E_x - δB_y phase shift which changes throughout the time series. In choosing the duration of our time series we must balance these two effects. Increasing the length of the time series will increase the number of averages contributing to the cross-spectrum and therefore reduce the statistical fluctuations, but the probability of the measured process maintaining a coherent phase throughout the series decreases.

A typical data set which we will analyze in this chapter has two data points per second and is 100 s long. We separate the series into segments of 32 points which overlap by 16 points, yielding 11 segments. The data are then prepared in the same way as described in the previous section: we subtract a least-squares linear fit from each segment, multiply by a Hanning window, and Fourier transform. We then operate on the resulting transforms as indicated in (5.5).

Since our cross-spectra have a relatively small number of individual time series which contribute to the ensemble average, we can expect that statistical fluctuations might cause the coherency at a given frequency to be large even in the presence of uncorrelated data. Also, overlapping data segments by $N/2$ points can lead to an artificially enhanced coherency. To arrive at a criterion for selecting statistically significant data we processed time series of mock E and δB data made up of Gaussian white noise. We then took ensemble averages of 5, 10, and 15 individual cross-spectra formed from 32 data points each, overlapping the data used to create each spectrum by 16 points. We repeated the process 20 times using different random data each time to obtain an idea of the range of coherencies that a random signal source can generate. The results are given in Table 5.1. Thus if we choose to average 10

spectra, we expect noise-generated coherencies (averaged over frequency) to fall between 0.27 and 0.37.

Table 5.1. Ensemble average of the frequency-averaged coherency calculated from 20 different time series consisting of Gaussian white noise.

<u># of individual spectra averaged for each cross-spectrum</u>	<u>$\langle C_{12} \rangle$</u>	<u>std. dev.</u>
5	0.453	0.058
10	0.323	0.049
15	0.285	0.035

5.4 Greenland I Rocket Data

In Section 3.5 we found the DC Poynting flux for the upleg of a Black Brant X sounding rocket flight made during the Greenland I campaign. The rocket was launched eastward into the morning auroral oval from Sondrestrom, and it remained in the auroral oval during the entire upleg. When plotted at high resolution, coherent Alfvén waves can be identified in the time domain data [Boehm *et al.*, 1990]. Since we know Alfvén waves are present in the field data, this data set is ideal for testing the impedance spectrum and normalized cross-spectrum as diagnostic tools in low frequency electromagnetic field studies.

To form $Z(f)$ and $\tilde{C}_{12}(f)$ for the rocket data we split the entire E_x (northward) and δB_y (eastward) time series plotted in Figure 5.1 into 32 point segments overlapping by 16 points, giving a total of 21 power

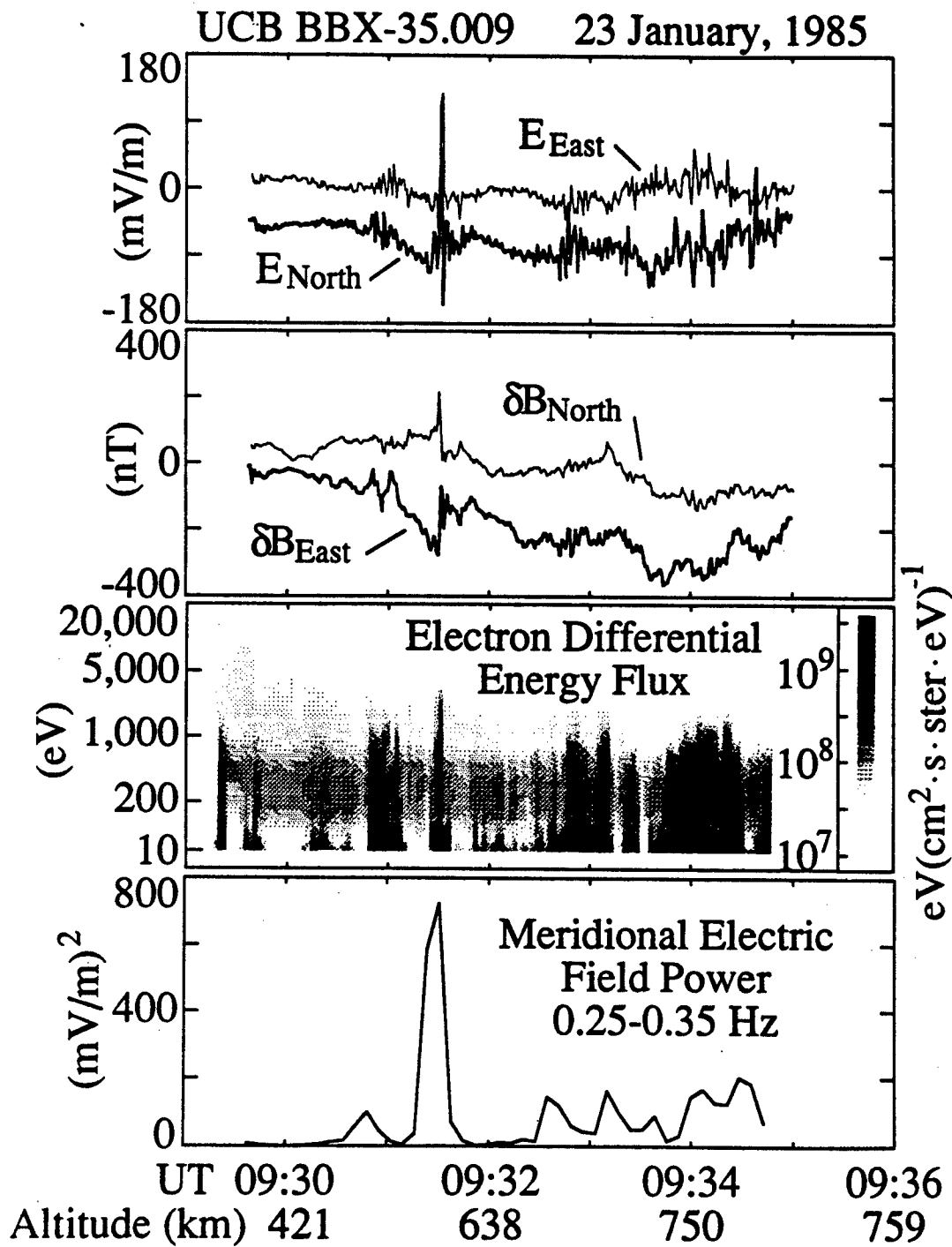


Figure 5.1 Data taken from a Black Brant X sounding rocket launched from Sondrestrom, Greenland on 23 January, 1985. The rocket traveled eastward along the auroral oval. (Data are courtesy of C. Carlson, B. McFadden, and M. Boehm at the University of California, Berkeley.)

spectra. The electric fields perpendicular to B_0 were measured with perpendicular 3 m electric field booms, and magnetic measurements were taken with a fluxgate magnetometer. To obtain electric fields below the rocket spin frequency, electric field measurements were fit to a sine wave over time intervals of one spin period, resulting in a sampling period of 0.887 s. The impedance and phase spectra are shown in Figure 5.2. Also shown in Figure 5.2 are the predicted phase and impedance spectra from the numerical model (Chapter 4) assuming a constant measurement altitude of 600 km and a horizontal spatial scale λ_x of 1000 km. The density profile used as input to the model is shown in Figure 5.3 and was parameterized from a profile measured with a Langmuir probe on board a Terrier-Malemute rocket launched nearly simultaneously with the Black Brant X [Earle, 1988]. For reference we have plotted Σ_P^{-1} in Figure 5.2 as deduced from measurements made by the Sondrestrom radar during the rocket flight.

The data curve in the bottom panel of Figure 5.2 clearly shows that the phase between E_x and δB_y varies with frequency. In either the static model or the traveling Alfvén wave model, electric and perturbation magnetic fields are shifted by 0° or 180° . In the coordinate system we are using, a 180° phase indicates a downward-directed Poynting vector, which is the case in the zero frequency limit of Figure 5.2 for both theory and experiment. At higher frequencies the measured phase increases to a maximum of nearly 260° at 0.4 Hz. Fields such as these which are nearly out of phase are exactly what is expected in standing Alfvén waves, as shown by the theoretical curve plotted with the data. Thus with the phase spectrum in this case we are able not only to

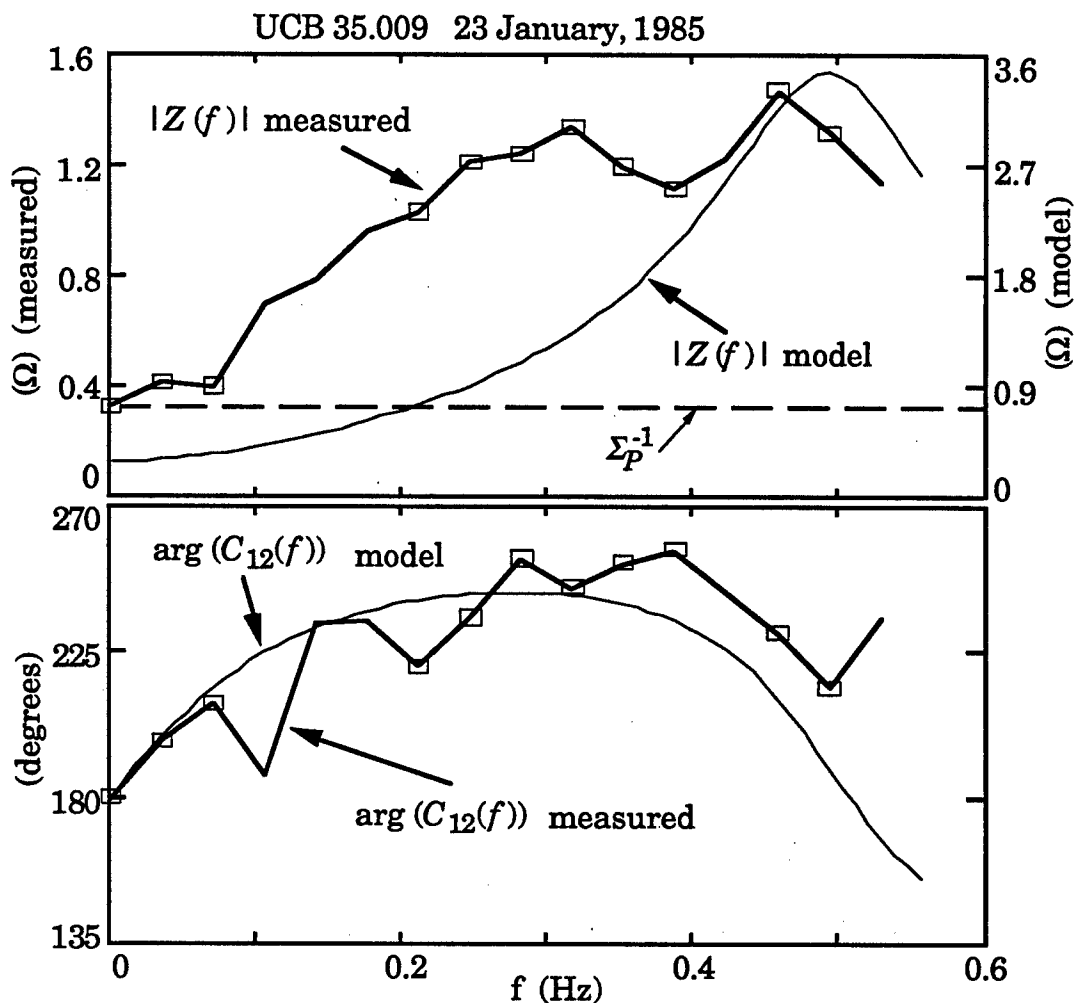


Figure 5.2 Numerical results compared with sounding rocket data averaged over the entire interval shown in Figure 5.1. Averages were formed from 21 sub-intervals of 32 points each.

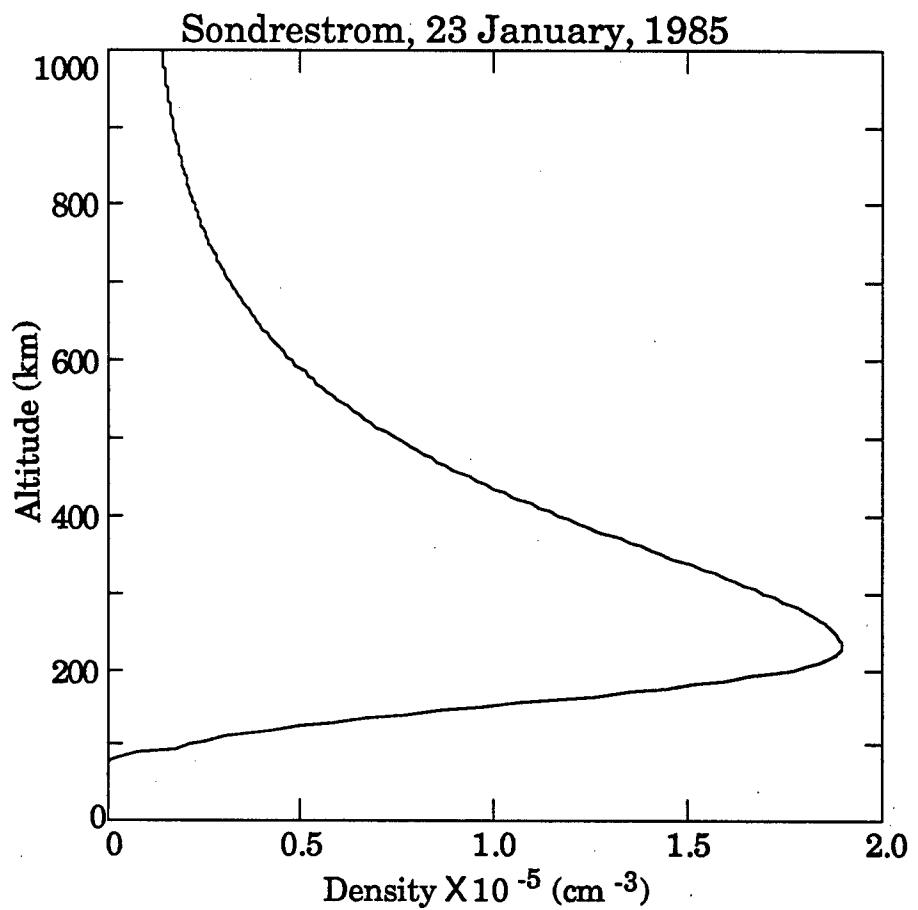


Figure 5.3 Electron density profile used as model input for the curves in Figure 5.2. This profile approximates the density profile taken on board a Terrier-Malemute rocket launched nearly simultaneously and in the same direction as the Black Brant [see Earle, 1988].

detect the presence of Alfvén waves, but we can determine that both incident and reflected components are present.

The impedance spectrum in Figure 5.2 is also consistent with the standing wave model. A trend toward increasing impedance at higher frequencies is clearly visible. The static field model predicts $Z(f) = \Sigma_p^{-1}$ for all Doppler-shifted frequencies. As shown in Figure 5.2, the standing Alfvén wave model predicts a peak in the impedance spectrum at 0.5 Hz.

Qualitatively, the theoretical and experimental impedance curves match well. However, the latter is less peaked, and the peak is much lower (1.5 vs. 3.5Ω) than the theory curve. There are at least four possible reasons for this: 1) The model assumes uniform ionospheric density, collision frequencies, etc. in the horizontal direction, which is not the case in the auroral oval. Ionospheric structure will tend to smear the peaked nature of the electric and magnetic field spectra, which will in turn broaden the impedance spectrum and decrease its peak value. 2) If static fields are present in addition to Alfvén waves, the mixture of these two will tend to make the impedance fall somewhere between the pure standing wave impedance and Σ_p^{-1} . 3) The measured spectral power at a single frequency is actually an average of the power in a frequency range Δf . Thus any spectral peaks will be reduced by averaging with neighboring values. Finally, 4) we have assumed a constant measurement altitude for the numerical model's predictions, but in fact the rocket altitude varies between 400 and 770 km during the interval we have analyzed. The altitude dependence of the standing wave impedance will thus lead to smearing in $Z(f)$. However, while the rocket actually traverses about 350 km in altitude during the time interval we are interested in, over half of the data are taken in the upper 100 km due to

the parabolic time dependence of the rocket altitude. Running the numerical model for a 700 km rather 600 km measurement altitude decreases the frequency of the impedance peak only by about 5%, therefore we suspect that the altitude variation of the sounding rocket is not the primary cause of small measured impedance values.

The bottom two panels of Figure 5.1 allow us to compare the fluctuating electric field power integrated between 0.25-0.35 Hz with electron precipitation. The two quantities are well correlated and we may conclude that much of the Alfvén wave energy in this frequency band is spatially coincident with auroral arcs. The sounding rocket was traveling eastward, nearly parallel to auroral structures. This allowed the rocket to dwell in the vicinity of arcs and enhanced Alfvén wave activity. Polar-orbiting satellites fly perpendicular to the auroral oval, and as a consequence they traverse auroral arcs very quickly. We will see in the next section that this limits the amount of Alfvén wave energy one can measure from the HILAT satellite.

We have used the impedance and cross-spectrum to verify the presence of Alfvén waves in sounding rocket data, and also to show that incident and reflected wave components are interfering as a result of the highly conducting, and therefore reflecting, ionosphere. We will now turn to HILAT measurements of $Z(f)$ and $\tilde{C}_{12}(f)$ to search for evidence of Alfvén waves which are not obvious in the time domain data alone.

5.5 HILAT Satellite Data

In order to find HILAT data with a significant correlation between E_x and δB_y we studied the 26 different HILAT passes listed in Table 5.2. (In the HILAT coordinate system, \hat{x} is the direction of the

Table 5.2. HILAT passes searched for 100 s intervals with a frequency-averaged $E\text{-}\delta B$ coherency exceeding 0.5. Passes with an asterisk satisfy this criterion.

<u>Year</u>	<u>Day</u>	<u>Start Time (UT)</u>	<u>MLT at 60°</u>	<u>Solar Zenith Angle (deg)</u>
1983	344*	13:05	11:00	85
1984	019	09:19	05:45	115
1984	023	09:21	05:15	120
1984	047	18:55	16:30	70
1984	058	17:33	14:15	65
1984	063*	17:04	13:30	60
1984	067	02:05	00:00	130
1984	075	15:16	12:00	55
1984	096*	11:16	11:15	60
1984	122	18:45	18:45	60
1984	164*	12:23	11:45	35
1984	179*	10:58	10:00	45
1984	217*	04:37	05:15	90
1984	242*	03:56	01:45	110
1984	245	04:19	04:30	120
1984	261*	15:43	12:30	50
1984	318*	19:54	16:00	85
1984	329	16:48	17:00	80
1984	345	14:56	12:45	75
1984	346	14:30	12:45	75
1985	052	20:09	16:45	80
1985	089	00:59	23:00	115
1985	112	12:42	12:45	55
1985	148	17:30	17:45	45
1985	265	17:06	13:45	50
1985	277*	15:15	12:15	55

satellite's velocity, z is downward, and y completes the right-hand system.) Each pass contains roughly 10 minutes of data taken in the northern hemisphere auroral oval and polar cap. The HILAT magnetometer samples at 20 s^{-1} and the electric field is derived from ion drift measurements taken either at 16 or 32 s^{-1} . Since for our purposes we are only interested in the frequency components below 1 Hz we averaged the field quantities to 2 samples/s, or one measurement every 3.7 km. We did not filter out the lowest frequency magnetic field variations due to mechanical oscillations of the satellite as we did in Chapter 3 because those variations are well below the range of frequencies we will consider here. The magnetometer resolution is about $\pm 6.7 \text{ nT}$, but averaging gives an effective resolution somewhat lower than this.

We separated the data from the 26 passes in Table 5.2 into 284 data segments of 100 s each and found the coherency spectrum from 11 sub-segments as described in Section 5.3. The resulting coherency from each 100 s interval we then averaged over frequency to obtain a single measure of the E_x - δB_y correlation. By averaging the coherency spectrum over all frequencies as a test to find meaningful correlations, we allow for the possibility of low correlation near DC but high correlation at higher frequencies.

Figure 5.4a shows the distribution of frequency-averaged coherencies $\overline{C_{12}}$ for the 288 100 s intervals obtained from the HILAT data survey. Figure 5.4b shows for comparison the distribution of coherencies for 284 100s intervals consisting of Gaussian white noise. The 3 intervals with values of $\overline{C_{12}}$ exceeding 0.8 are from Day 217, 1984 and occur during periods of extremely small electric and magnetic fields. Using straight

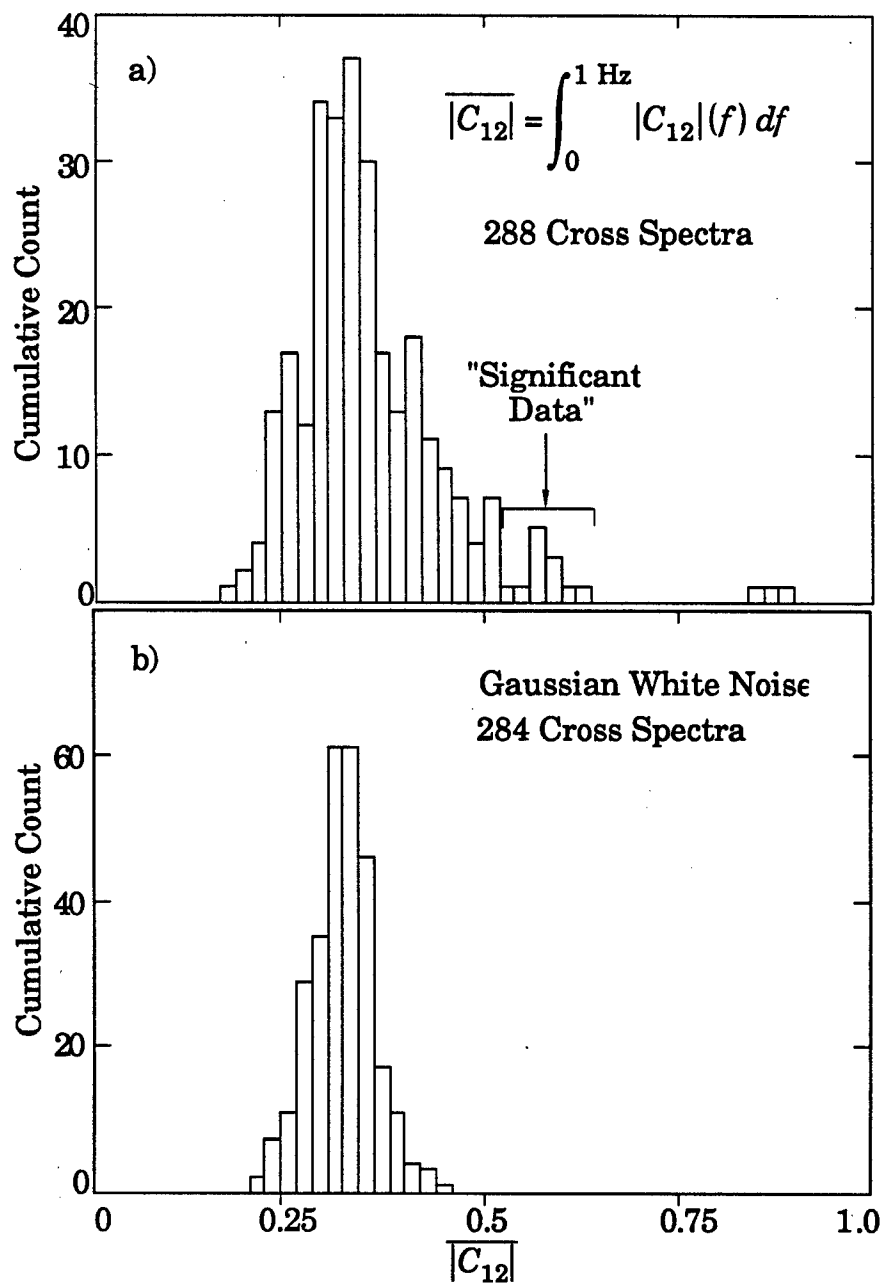


Figure 5.4 Distribution of frequency-averaged coherency spectra from a) HILAT data, and b) Gaussian white noise. Each coherency spectrum was formed from 11 electric and magnetic field spectra, which were in turn formed from 32 data points each.

lines (i.e. $E(t) = a_1 t + c_1$, $\delta B(t) = a_2 t + b_2$) alone as input to the analysis routines yields coherencies of unity, and we suspect that the Day 217 coherencies are high for this same reason. That is, any segment of the magnetic field data has a low-order trend due to the oscillation of the satellite, and when no geophysical signals are present, the time series resulting from this trend can generate anomalously high coherencies. The passes of most interest to us are those with a noticeable amount of signal energy present and with \bar{C}_{12} above 0.5, indicated by the arrow in Figure 5.4a.

Notice from Figure 5.4b that even though the noise used to calculate the cross-spectra has a coherence of zero, the apparent coherence is near 0.3. This is due to the small number of data segments contributing to the ensemble average (i.e. $N = 11$). The average coherency in Figure 5.4b will decrease with increasing N , roughly as $N^{-1/2}$. In fact, it is easy to verify that the average coherencies in Table 5.1 fall quite close to $N^{-1/2}$ in magnitude.

Having now identified several promising data intervals we will analyze in detail six examples which were taken when the Sondrestrom Incoherent Scatter Radar was scanning more or less along the N-S meridian. The radar measured ionospheric density profiles up to 850 km altitude and over a 800 km range in latitude (depending on the measurement altitude). The density profiles were averaged over latitude to obtain a single altitude profile [M. McCready and J. F. Vickrey, personal communication, 1990]. Since the density profiles are averaged in latitude, some of the apparent structure in altitude may actually be due to horizontal structuring in plasma density.

Often the upper range gates of the radar data are corrupted either by a poor signal-to-noise ratio or by echoes from man-made satellites. When this appears to be the case we replace the top portion of the radar-measured profile with an exponentially decreasing density to use as input to our numerical model. We also smooth the radar profiles, and we extrapolate the profile below 95 km using a 6 km exponential scale height. The high-coherency HILAT data in each case were not necessarily taken in the same region that the radar measured.

In Figures 5.5-5.16 we show in chronological order the radar density profiles (both measured and smoothed), $E_x(f)$ and $\delta B_y(f)$ for the 100 s intervals of interest, and measured and modeled cross-spectra and impedance spectra for each of the six HILAT passes. While we present only the high-coherency data intervals, it is evident from the complete data sets that in each pass the large coherencies are found within the auroral oval, as indicated by large scale magnetic perturbations from the Region 1/Region 2 current systems. Unfortunately, unlike the sounding rocket example of the previous section, in all six HILAT passes it appears that the measured phase spectra have very large variances, and a comparison between measured and modeled curves is unconvincing. All cases do show a 180° phase shift between E_x and δB_y , at DC however, which indicates a downward-directed Poynting vector for quasi-static fields.

The measured and modeled impedance spectra are in better agreement than the measured and modeled phase spectra. On Day 096, 1984 (Figure 5.10), Day 179, 1984 (Figure 5.12), and Day 277, 1985 (Figure 5.16), the density profiles are somewhat similar and the numerical model predicts a single impedance peak in the 0.3-0.6 Hz range. In all three of

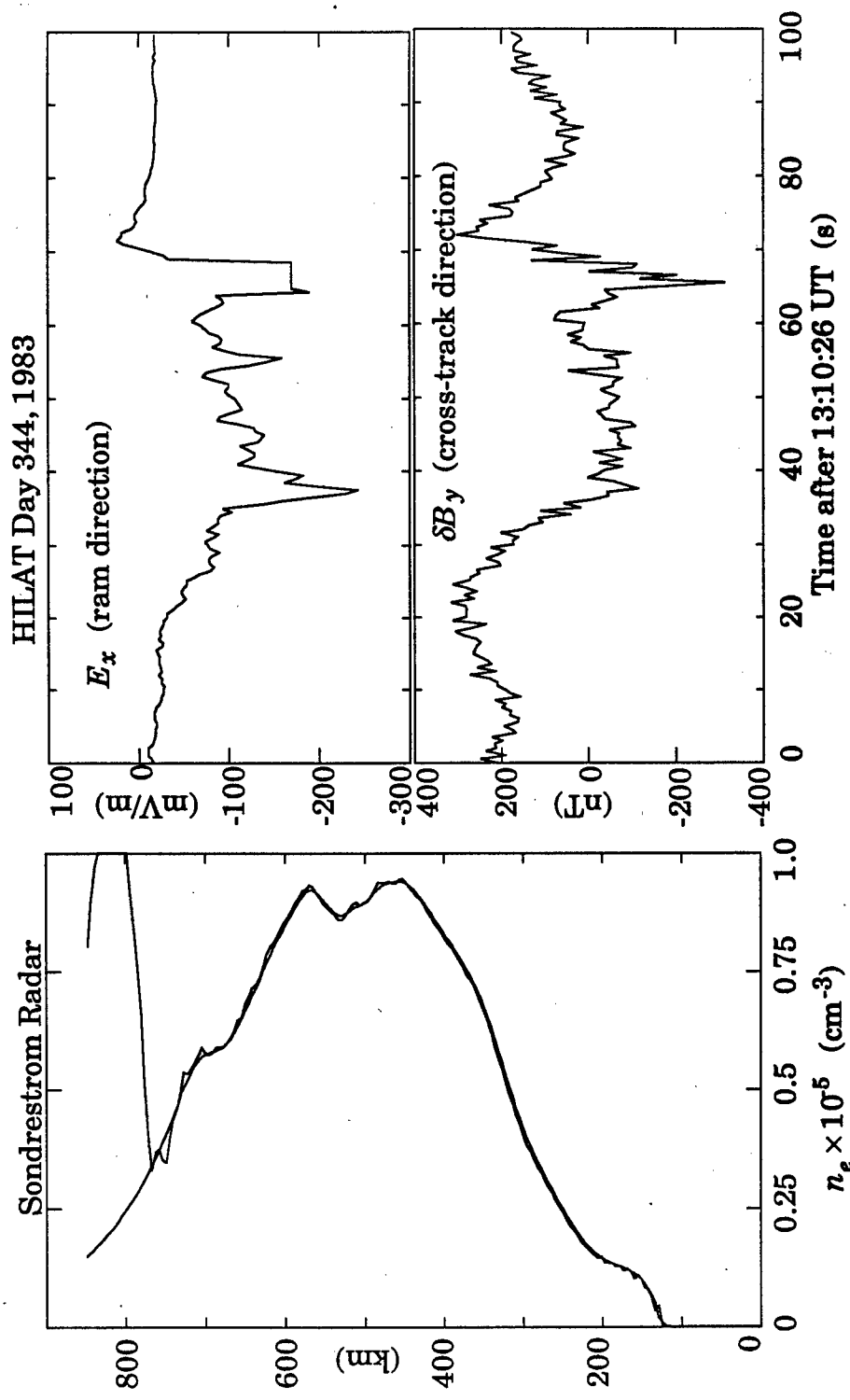


Figure 5.5 Smoothed and unsmoothed density profiles taken by the Sondrestrom radar on 10 December, 1983 and averaged in latitude (left), taken at the same time as the HILAT electric and perturbation magnetic field data shown at right.

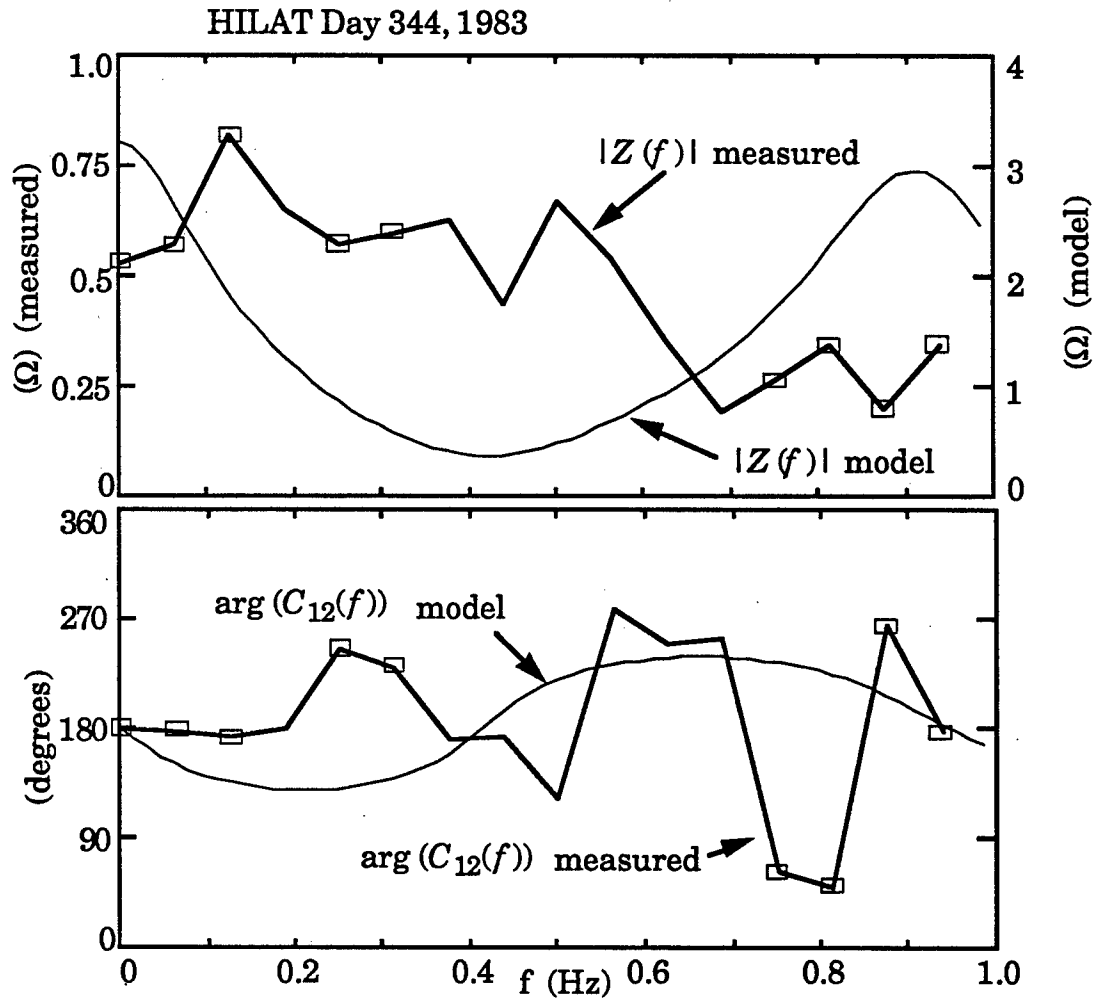


Figure 5.6 Comparison of numerical model and experimental results using the smoothed density profile and electric and magnetic fields shown in Figure 5.5. Ensemble averages were formed from 11 separate 32 point (16 s) intervals overlapping by 16 points each. Boxes indicate a coherency exceeding 0.5.

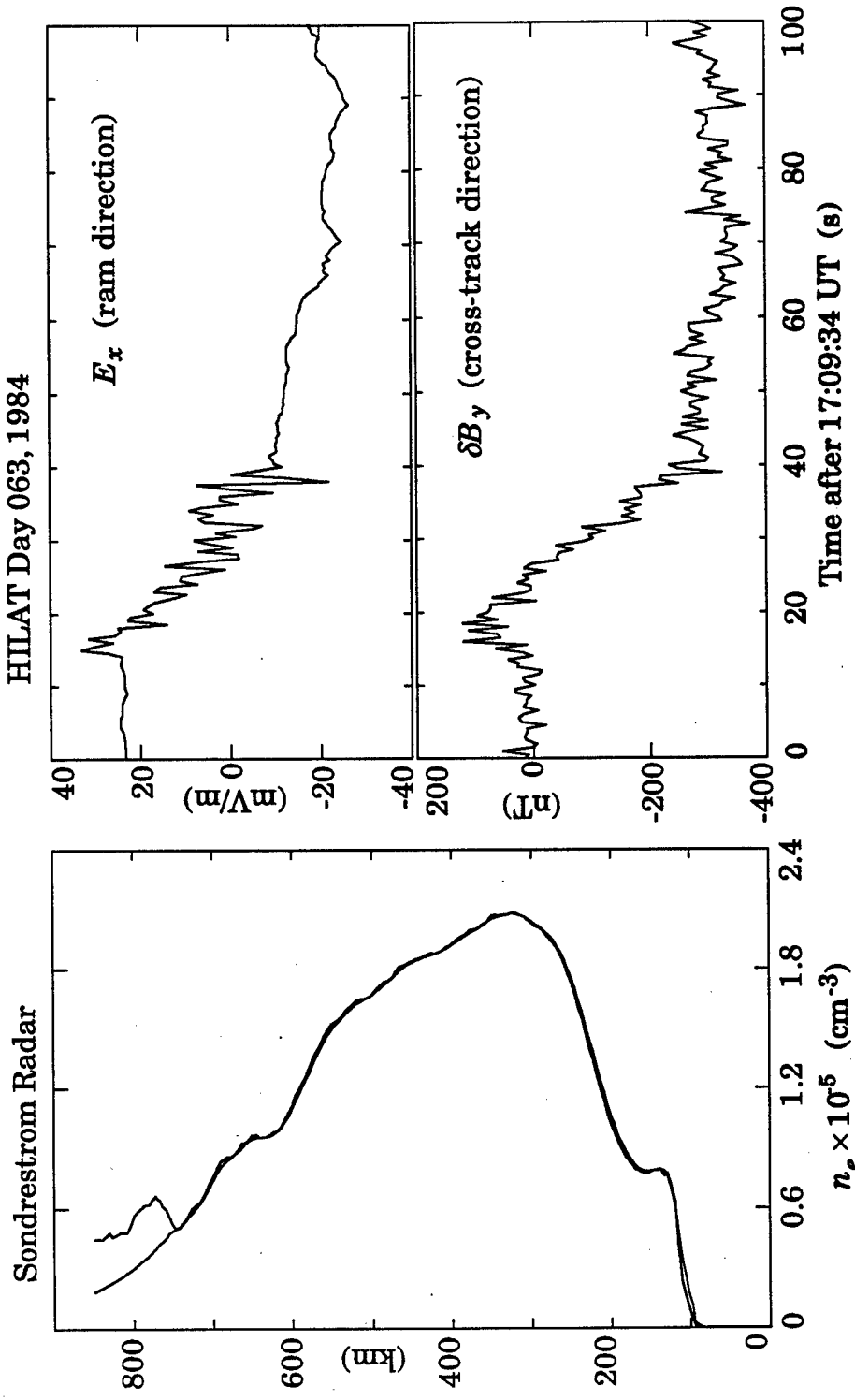


Figure 5.7 Smoothed and unsmoothed density profiles taken by the Sondrestrom radar on 3 March, 1984, and averaged in latitude (left), taken at the same time as the HILAT electric and perturbation magnetic field data shown at right.

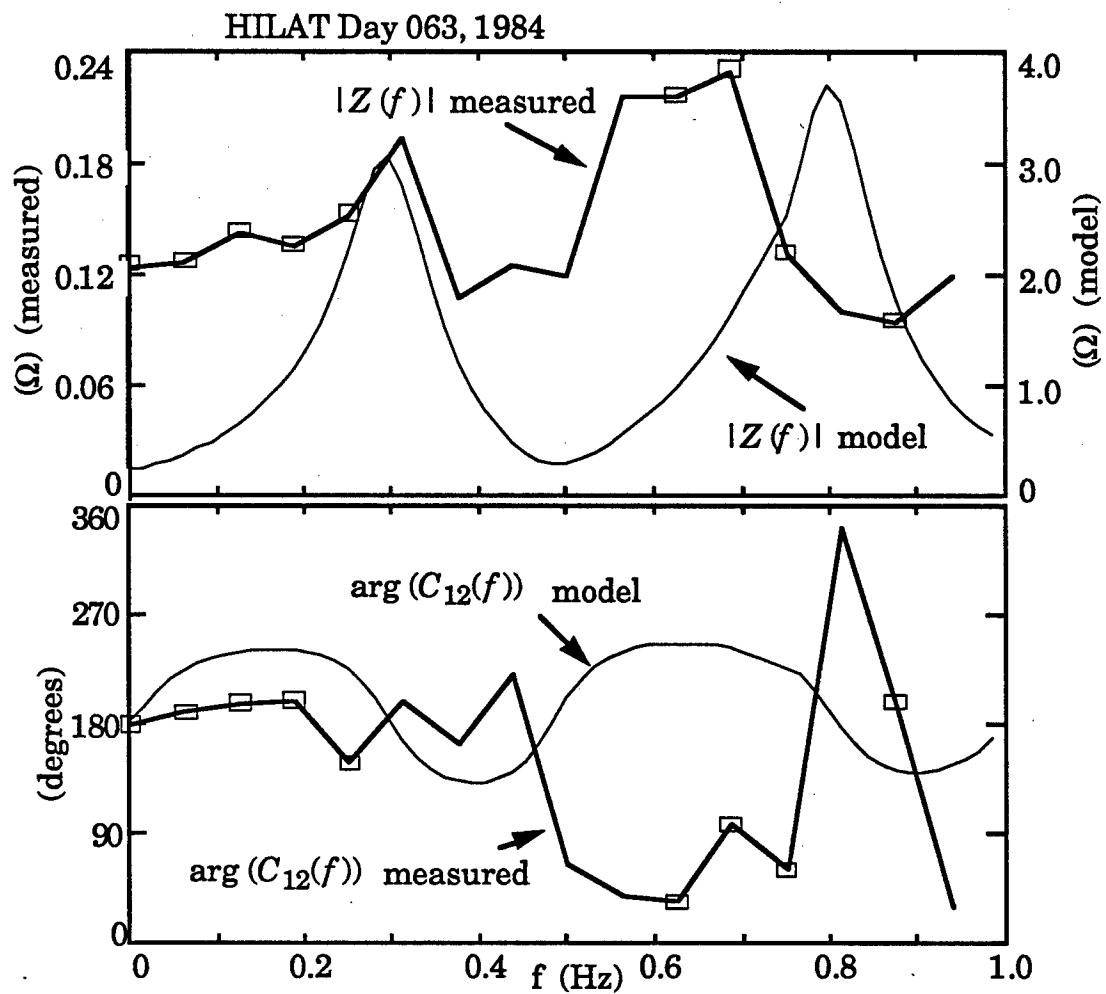


Figure 5.8 Comparison of numerical model and experimental results using the smoothed density profile and electric and magnetic fields shown in Figure 5.7. Ensemble averages were formed from 11 separate 32 point (16 s) intervals overlapping by 16 points each. Boxes indicate a coherency exceeding 0.5.

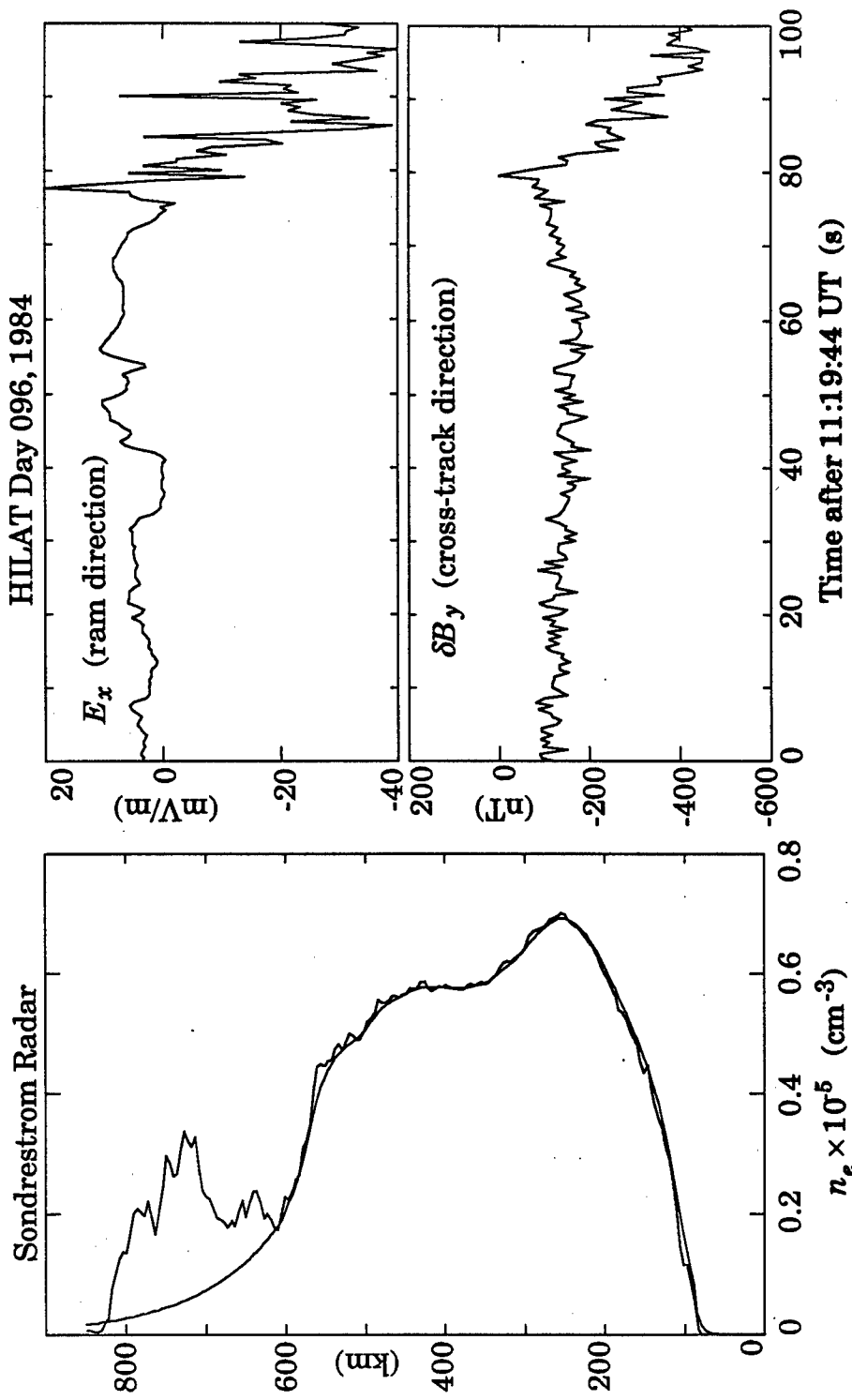


Figure 5.9 Smoothed and unsmoothed density profiles taken by the Sondrestrom radar on 5 April, 1984, and averaged in latitude (left), taken at the same time as the HILLAT electric and perturbation magnetic field data shown at right.

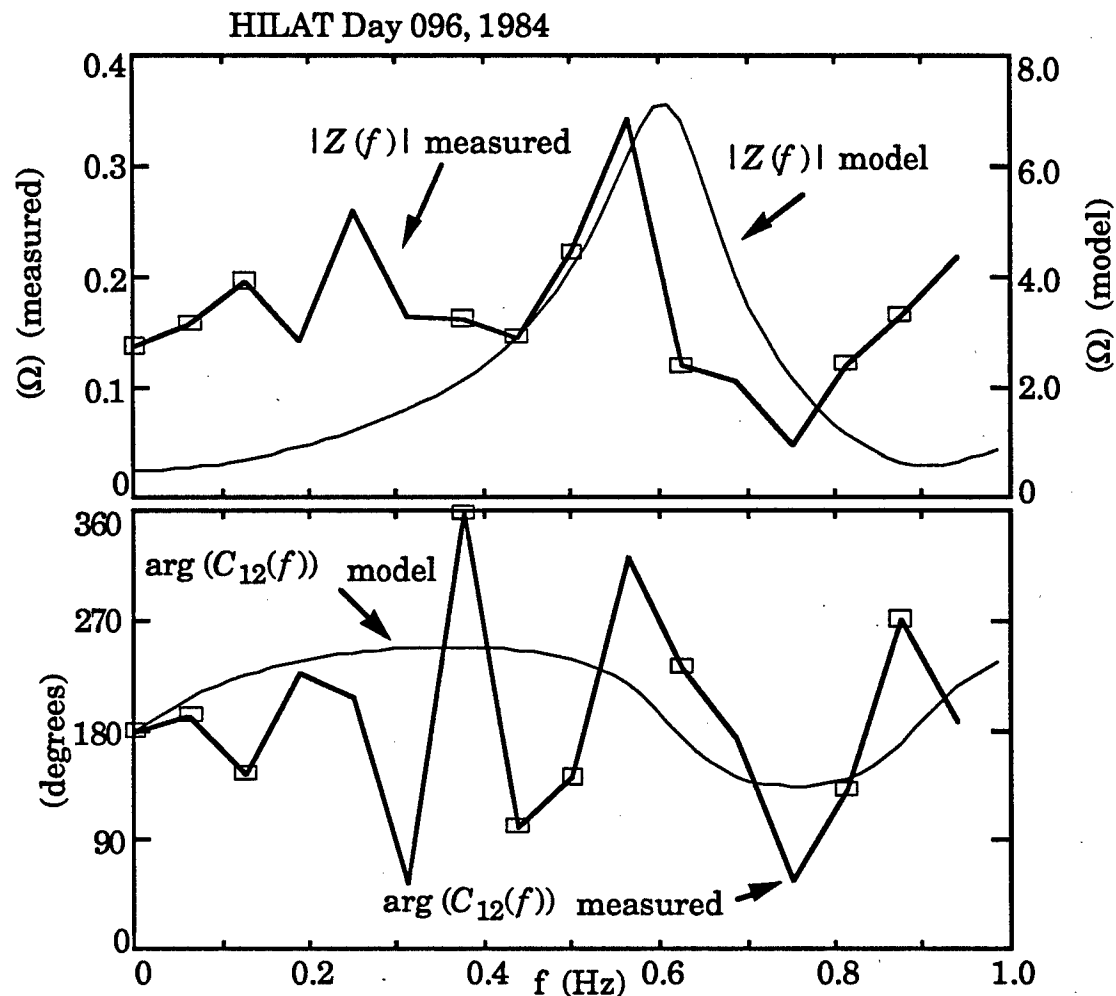


Figure 5.10 Comparison of numerical model and experimental results using the smoothed density profile and electric and magnetic fields shown in Figure 5.9. Ensemble averages were formed from 11 separate 32 point (16 s) intervals overlapping by 16 points each. Boxes indicate a coherency exceeding 0.5.

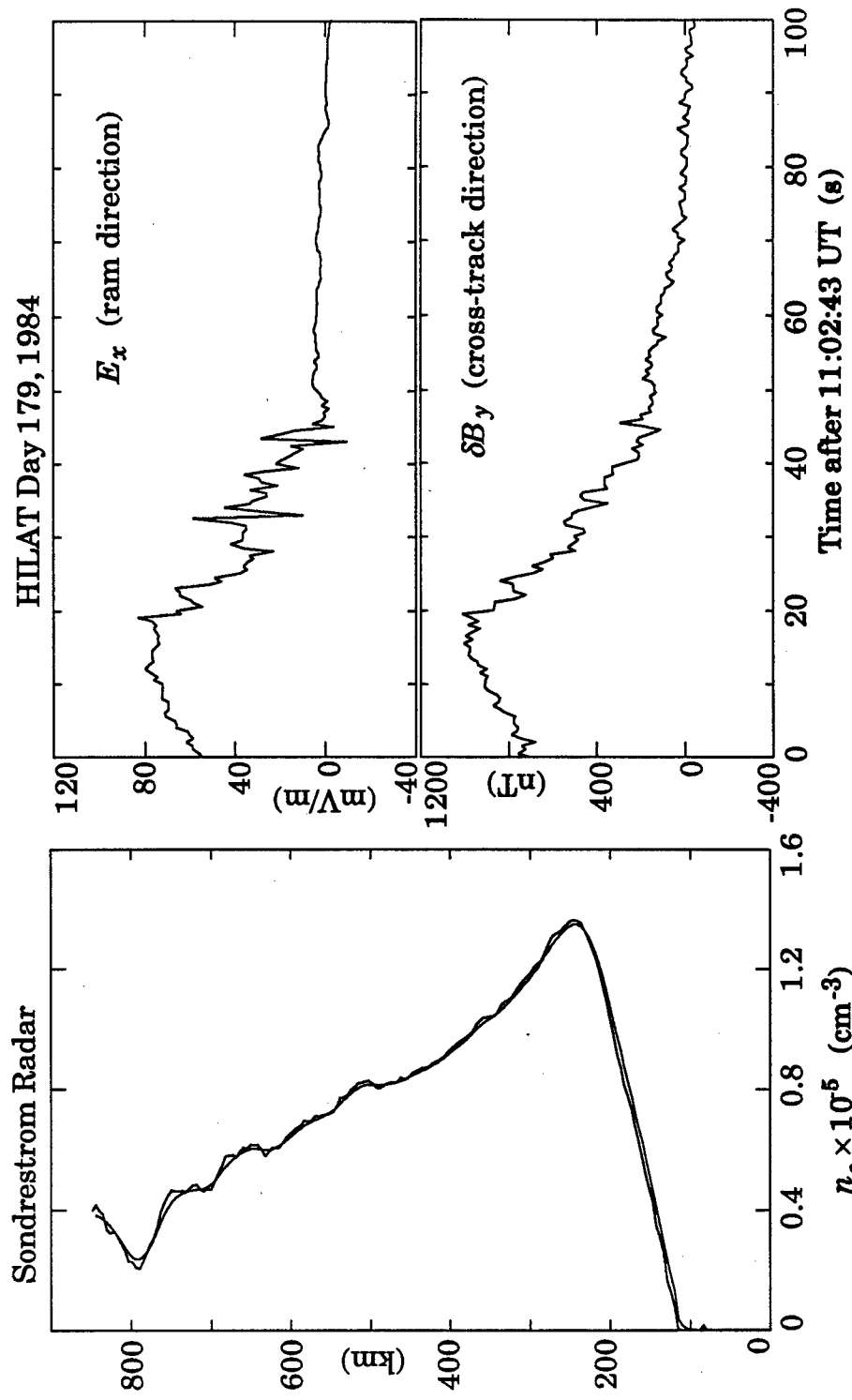


Figure 5.11 Smoothed and unsmoothed density profiles taken by the Sondrestrom radar on 27 June, 1984, and averaged in latitude (left), taken at the same time as the HILAT electric and perturbation magnetic field data shown at right.

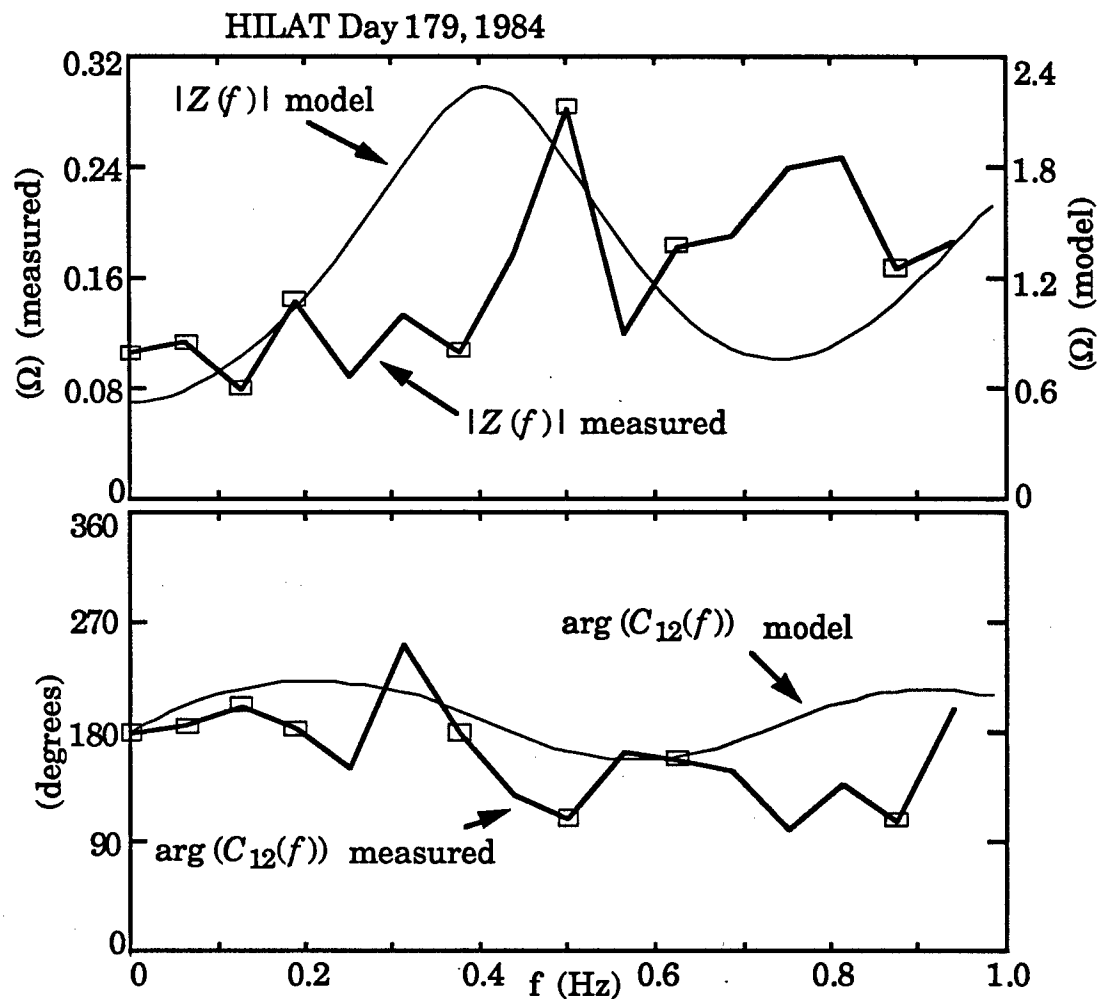


Figure 5.12 Comparison of numerical model and experimental results using the smoothed density profile and electric and magnetic fields shown in Figure 5.11. Ensemble averages were formed from 11 separate 32 point (16 s) intervals overlapping by 16 points each. Boxes indicate a coherency exceeding 0.5.

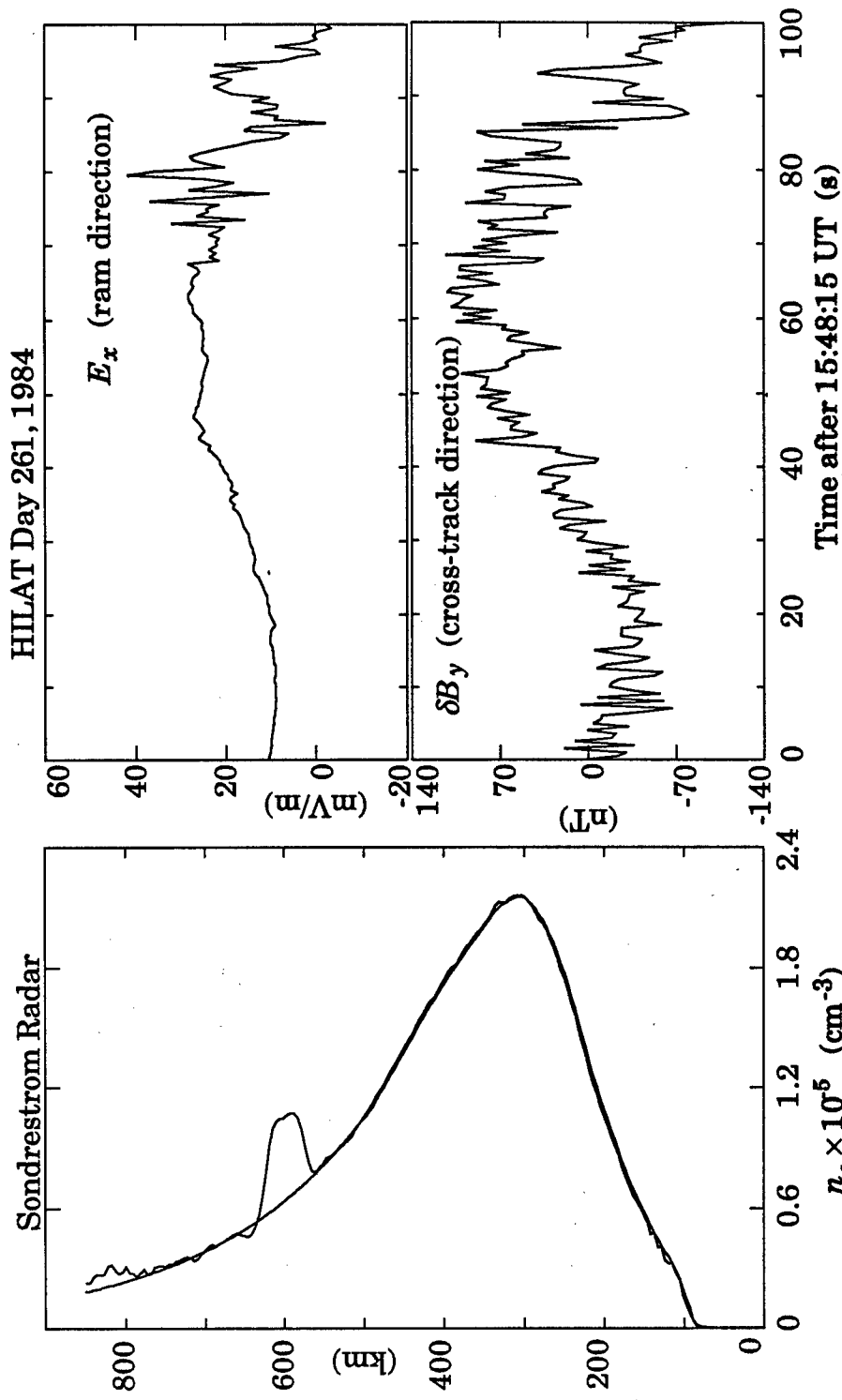


Figure 5.13 Smoothed and unsmoothed density profiles taken by the Sondrestrom radar on 17 September, 1984, and averaged in latitude (left), taken at the same time as the HILAT electric and perturbation magnetic field data shown at right.

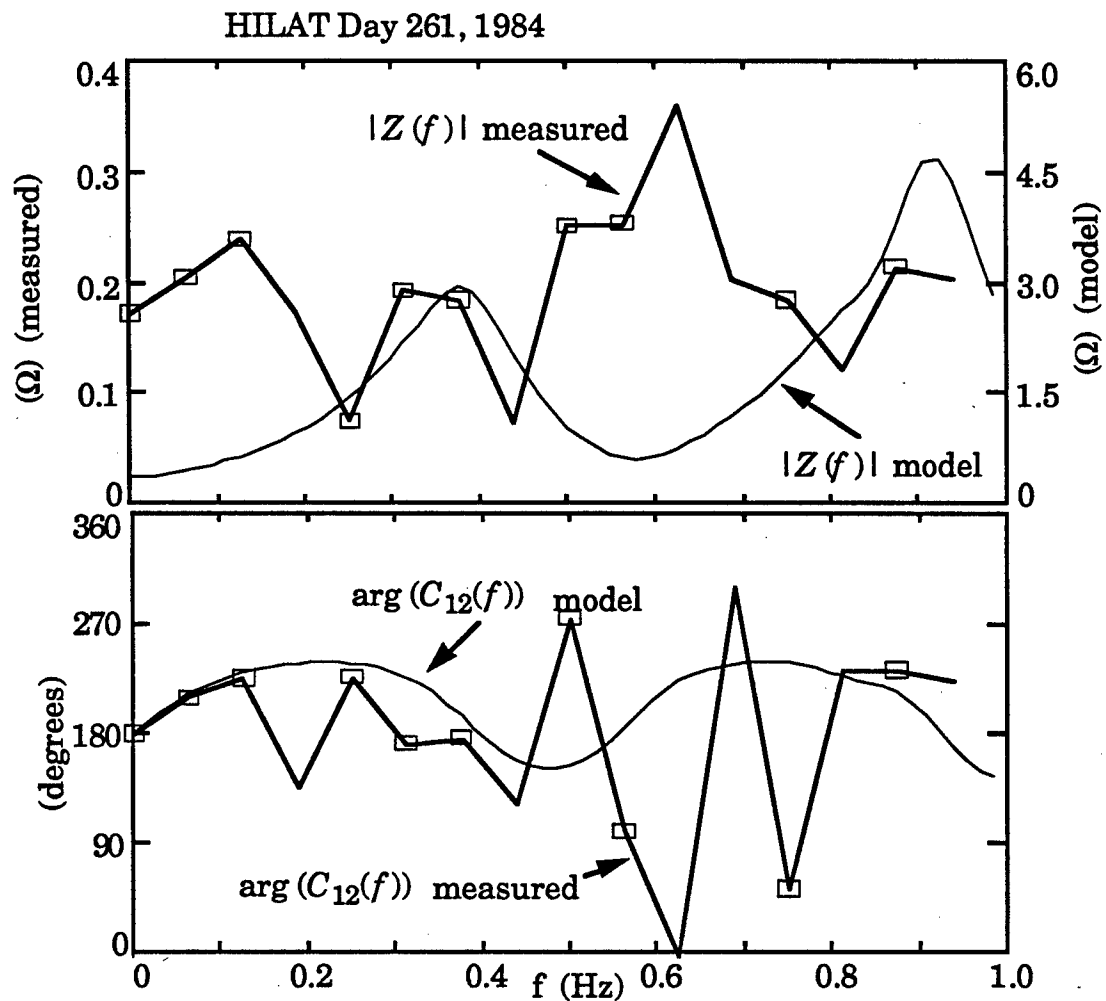


Figure 5.14 Comparison of numerical model and experimental results using the smoothed density profile and electric and magnetic fields shown in Figure 5.13. Ensemble averages were formed from 11 separate 32 point (16 s) intervals overlapping by 16 points each. Boxes indicate a coherency exceeding 0.5.

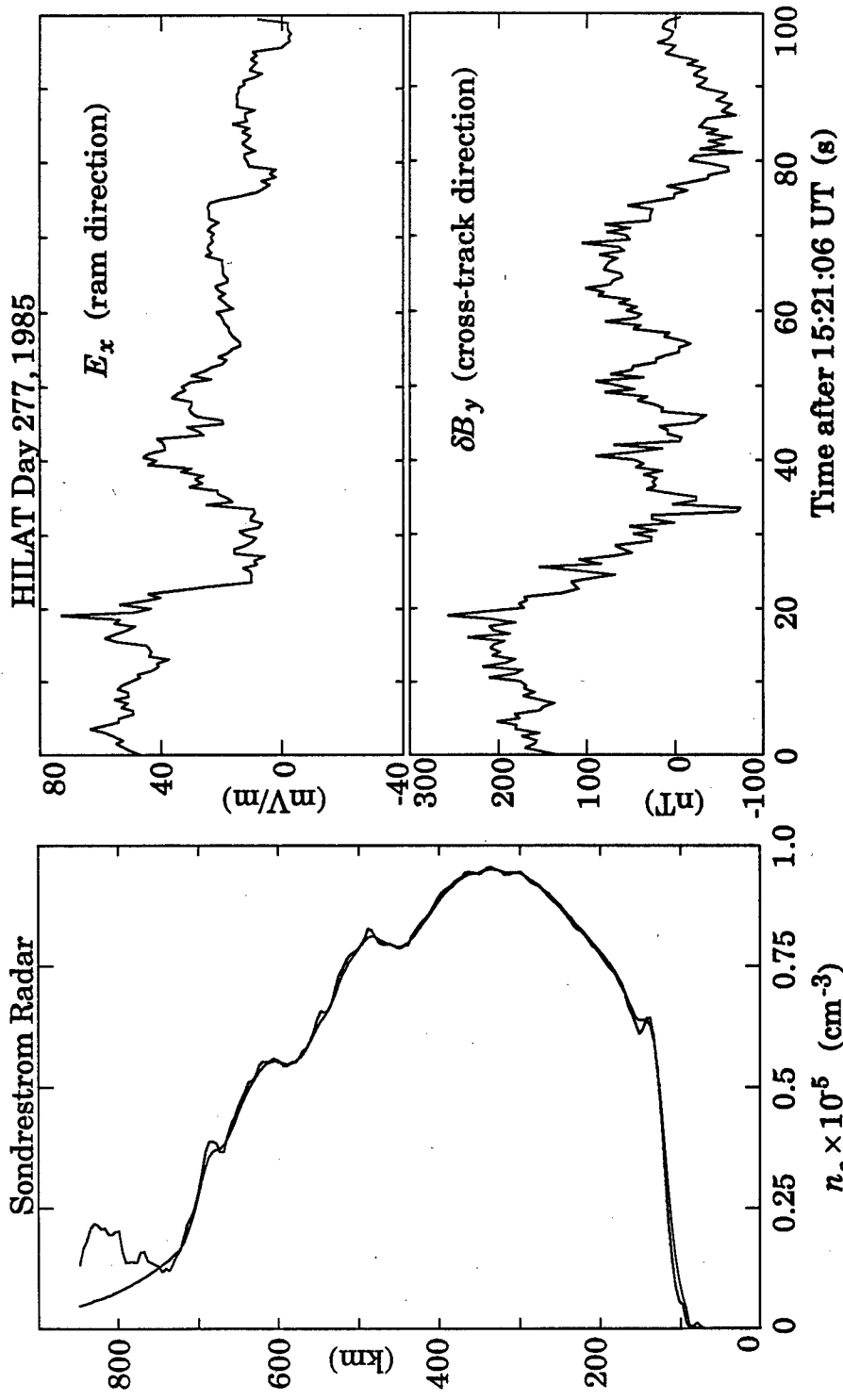


Figure 5.15 Smoothed and unsmoothed density profiles taken by the Sondrestrom radar on 4 October, 1985, and averaged in latitude (left), taken at the same time as the HILAT electric and perturbation magnetic field data shown at right.

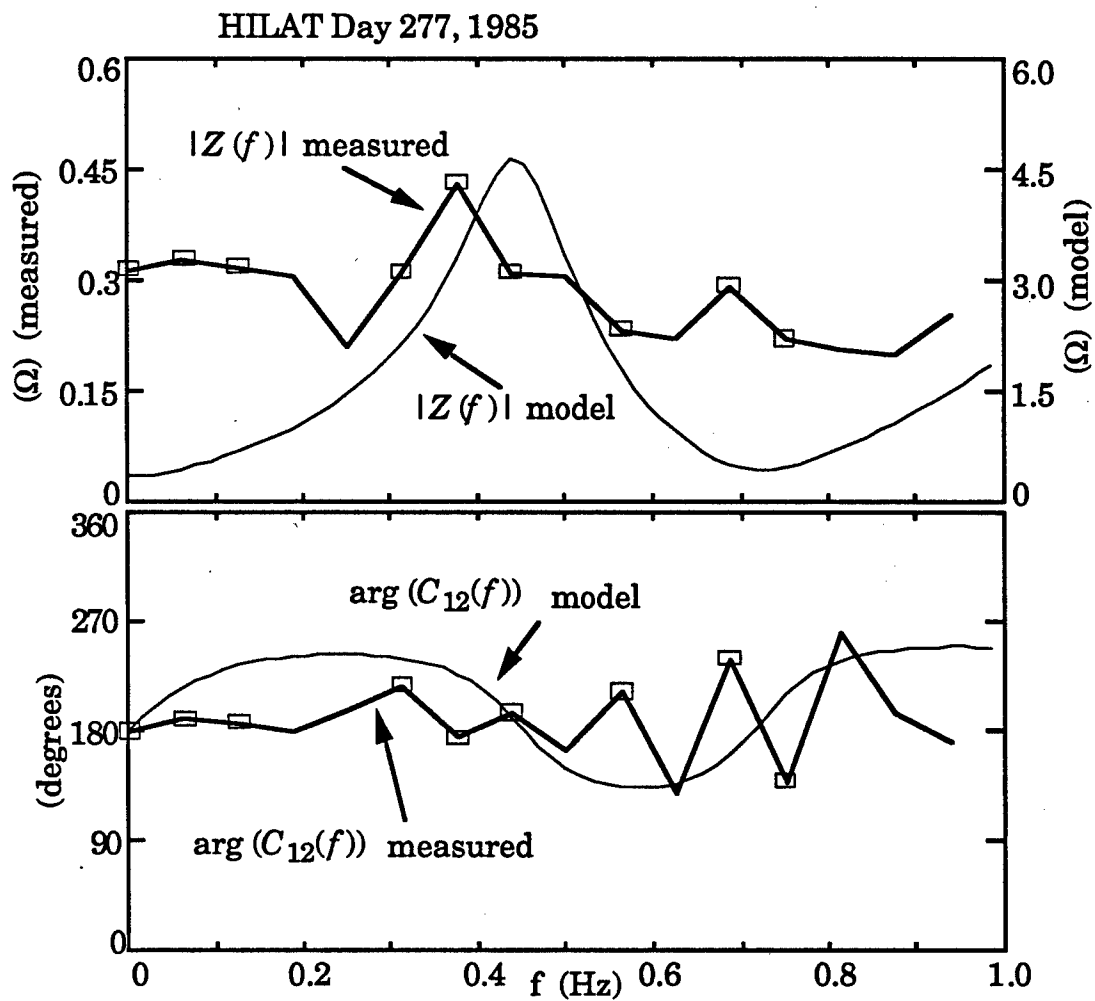


Figure 5.16 Comparison of numerical model and experimental results using the smoothed density profile and electric and magnetic fields shown in Figure 5.15. Ensemble averages were formed from 11 separate 32 point (16 s) intervals overlapping by 16 points each. Boxes indicate a coherency exceeding 0.5.

these cases, the maximum measured impedance value falls within about 15% of the model's prediction. Unfortunately, the peak measured impedance on Day 096, 1984 (Figure 5.10) does not have a coherence above 0.5 associated with it, and therefore the fact that it lies near the modeled peak may be coincidental. On Day 063, 1984 (Figure 5.8), the ionospheric density profile was such that there are two impedance peaks below 1 Hz, and two peaks are clearly visible in the data. However, only the second impedance peak has a coherency above 0.5.

On Day 261, 1984 (Figure 5.14), there is a poor match between the model and experiment, and in fact the peak measured impedance occurs at a frequency for which the modeled impedance is minimum. A possible reason for the poor match is that the average density profile measured by the radar is not representative of the actual ionosphere below HILAT when Alfvén wave energy, if any, was present.

Day 344, 1983 (Figure 5.6) is an especially interesting case. On other passes and in the sounding rocket data the measured impedance function starts near Σ_P^{-1} at zero frequency and tends to increase. This is a consequence of a highly conducting ionosphere with $\Sigma_P^{-1} < Z_A$ where Z_A is the Alfvén impedance at the measurement altitude. One can see from the Day 344 density profile in Figure 5.5 that there is not much density in the E region, which causes a Σ_P^{-1} ($\sim 3 \Omega$) greater than Z_A ($\sim 2 \Omega$). In this case the model standing wave impedance is maximum at 0 Hz and decreases with frequency. While the measured impedance values do not match the modeled values, the low order trend in the measured Z does decrease by a factor of 3 at higher frequencies, presumably because of the low E-region density.

Turning again to the example with two impedance peaks in both the measured and modeled data (Figure 5.8), we find that the frequency of the second measured impedance peak is .2 Hz smaller than predicted by the model. It is interesting to note that in the frequency range of the measured impedance maximum (0.6 - 0.8 Hz), the measured cross-spectrum has a high coherency and the phase is at a minimum, while the modeled phase maximizes. Comparing the measured and modeled phase spectra, one might expect that the input to the numerical model could be adjusted to bring them into agreement. One would have to find a parameter that affects only the higher frequency part of the curve while leaving the agreement between the impedance peaks at 0.3 Hz unaffected. Decreasing the electron density in the E and F regions will move both impedance peaks towards larger frequencies, thus an inaccurate density profile is probably not the cause for the disparity between the data and modeled curves.

In contrast to the electron density profile, the ion collision frequency v_i near 150 km *can* affect only the high frequency part of the impedance and phase spectra. The reason for this is that, roughly speaking, Alfvén waves penetrate down into the ionosphere as long as the wave frequency ω exceeds v_i . This effect is illustrated in Figure 5.17, where we have modeled the meridional electric field magnitude $|E_x|$ for two different frequencies. We have used the "EF" density profile in Figure 4.2 as input to the model. If one defines the Alfvén wave reflection altitude as the altitude near the E region where $|E_x|$ is minimum, then Figure 5.17 shows that a 1.2 Hz Alfvén wave penetrates to about 140 km, whereas a 0.5 Hz wave reflects at 180 km. Decreasing v_i below 150 km could then lower the reflection altitude for waves with frequencies near 1

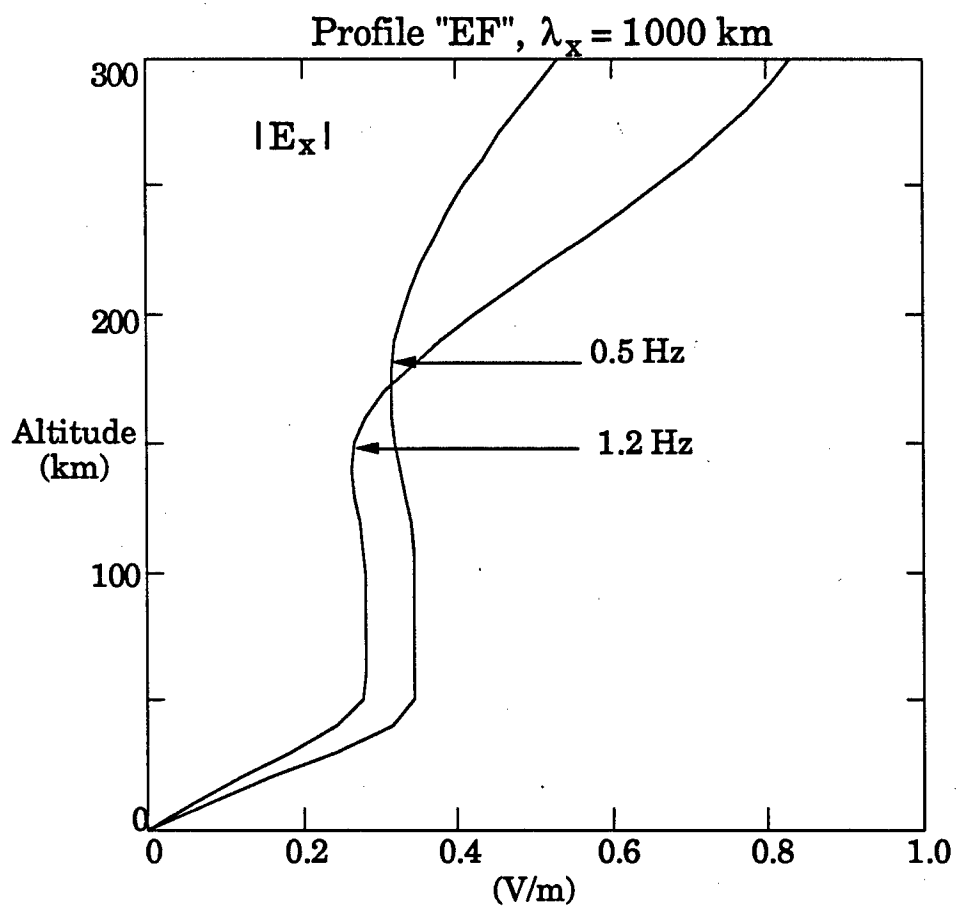


Figure 5.17 Model meridional electric field profiles for two Alfvén waves illustrating the fact that higher frequency waves reflect from lower altitudes.

Hz, which in turn would decrease the frequency of maximum $|Z|$ for those waves. Our modeled profiles of v_i are based on a neutral atmosphere model with an assumed thermospheric temperature of 1000 K. The actual thermospheric temperature can vary widely, and as a result, the neutral atmosphere density and ion-neutral collision frequency can also vary. Thus the lack of agreement between our modeled and measured frequencies of peak $|Z(f)|$ might be explained in part by our poor knowledge of $v_i(z)$.

The frequency dependence of the reflection altitude also explains why the frequency of the second impedance peak in Figure 5.8 (0.8 Hz) is not three times the frequency of the first peak (0.3 Hz). This factor of three relation would hold for a constant reflection altitude because impedance peaks occur when an observer is $\lambda/4$ and $3\lambda/4$ above the reflector. But since higher frequency waves reflect from lower altitudes in the case of ionospheric reflections, the frequency of the second impedance peak is somewhat lower than three times the frequency of the first peak.

While we have found reasonable agreement between measured and modeled frequencies of the frequencies of maximum $|Z(f)|$, in all cases the measured impedance is much smaller than predicted by the standing Alfvén wave model, and in fact it is less than Σ_P^{-1} in most cases, although this also may indicate a problem with the neutral atmosphere or collision frequency models.

We pointed out that the sounding rocket discussed in the previous section traveled mostly parallel to auroral structures and therefore spent a significant amount of time in regions where Alfvén waves seem to occur the most. This could account for the good data/theory match in

that case, especially in the phase spectrum. HILAT flies mostly perpendicular to auroral structures and probably spends less time in regions with Alfvén waves. In the HILAT passes we have analyzed it appears much of the field energy is due to quasi-static fields with an associated impedance function $Z(f) = \Sigma p^{-1}$. Even so, the impedance function in most cases shows a significant increase at frequencies for which it is predicted to be maximum by the standing wave model. Thus HILAT must have flown through regions of Alfvénic fluctuations, and most importantly *the frequencies of detectable Alfvén waves are determined by the standing wave pattern, not the wave source.* That is, in almost all cases there is at least some Alfvén wave energy present at peaks in the standing wave impedance function, thus the magnetosphere is apparently supplying a continuous spectrum of waves, but only at those frequencies corresponding to peaks in $Z(f)$ does the electric field from Alfvén waves constitute a significant fraction of the total electric field spectrum measured across the auroral oval.

5.6 A Quantitative Estimate of the Amount of Alfvén Wave Energy in Electromagnetic Field Data

We have found measured impedances in the sounding rocket and satellite data which fall somewhere between Σp^{-1} and the numerical model's prediction. Roughly speaking, a higher measured impedance means more spectral power due to Alfvén waves and less to Doppler-shifted static structures. We can attempt to state this relationship quantitatively by assuming that there is no smearing in the measured impedance spectrum due to variations in the Pedersen conductivity along the flight path, and that at any given time the measurements are due

completely either to Alfvén waves or to static fields. (The case in which both Alfvén waves and Doppler-shifted static fields are present at the same time almost certainly occurs but is difficult to treat since we have no way of knowing the relative phase between the Fourier components of the two contributions.) Under this last assumption we can conceptually separate the total power spectral density in a time series into 2 parts, i.e. $P_E = P_{E,A} + P_{E,S}$ and $P_B = P_{B,A} + P_{B,S}$, where $P_{E,A}$ and $P_{B,A}$ are the power spectral densities of electric and magnetic fields from sub-intervals containing only Alfvén waves, and $P_{E,S}$ and $P_{B,S}$ are from those sub-intervals containing static structures. The fraction of the electric field spectral power due to Alfvén waves at frequency f is

$$q_E(f) = P_{E,A}/(P_{E,A} + P_{E,S}) \quad (5.6a)$$

and for the magnetic field

$$q_B(f) = P_{B,A}/(P_{B,A} + P_{B,S}) \quad (5.6b)$$

Recognizing that $\mu_0^2 P_{E,S}/P_{B,S} = 1/\Sigma_P^2$ and $\mu_0^2 P_{E,A}/P_{B,A} = Z^2_{model}$ (Z_{model} is the numerical model's prediction of the standing wave impedance at a fixed altitude) leads to

$$q_E(f) = (\Sigma_P^2 - Z^2_{measured}(f)) / (\Sigma_P^2 - Z^2_{model}(f)) \quad (5.7a)$$

$$q_B(f) = (\Sigma_P^2 Z^2_{measured}(f) - 1) / (\Sigma_P^2 Z^2_{model}(f) - 1). \quad (5.7b)$$

We can evaluate the above expressions for rocket data shown in Figure 5.2 by choosing values at the peak in the impedance function, near 0.5 Hz. In this case $\Sigma_P^{-1} = 0.3 \Omega$, $Z_{measured} = 1.5 \Omega$, and $Z_{model} = 3.5 \Omega$. The result is $q_E = 0.96$ and $q_B = 0.18$, i.e. Alfvén waves are responsible for 96% of the measured electric field power and 18% of the magnetic field power at 0.5 Hz. We expect the Alfvén wave magnetic field contribution to

be small since the numbers were taken from the peak in $Z(f)$ which corresponds to a magnetic field node in the standing wave pattern. For the Day 063 HILAT data in Figure 5.8 the relevant numbers near the peak at 0.3 Hz are $\Sigma_P^{-1} = 0.12 \Omega$, $Z_{measured} = 0.18 \Omega$, $Z_{model} = 3.0 \Omega$, $q_E = 0.55$ and $q_B = 0.002$. Thus half of the electric field energy and almost none of the magnetic energy measured by HILAT during this particular pass is attributable to Alfvén waves.

At this point we must issue a note of caution concerning these estimates. The quantity q_E increases very rapidly with $Z_{measured}$, and quickly reaches a value above 90%. Thus any anomalous increases in the measured impedance will cause q_E to fall in the 90% range. For this reason, estimates of q_E may be biased towards large values. Another potential source of error is our assumption of horizontal spatial homogeneity in the ionosphere. However, at first guess it would seem that this effect would smear the impedance function and *decrease* the peak impedance measurement, causing a decrease in the q_E estimate.

5.7 Discussion

The impedance function measured with the Black Brant X sounding rocket flying nearly parallel to auroral structures (i.e. eastward) indicates that the electric and magnetic field fluctuations above 0.1 Hz in the spacecraft frame are due mainly to standing Alfvén waves rather than Doppler-shifted spatial structures. In contrast, spectral energy from static structures plays a more important role in the HILAT measurements, but some Alfvén wave electric field energy is clearly present in most passes at frequencies where the electric field standing wave pattern is predicted to be maximum. A plausible reason

for the fact that HILAT measured less Alfvén wave energy than the sounding rocket is that HILAT's velocity is perpendicular to most of the auroral structure, and most of the Alfvén wave energy seems to be localized at latitudes near auroral arcs. These findings argue for the importance of Alfvén waves in the electromagnetic structure of the disturbed auroral oval, and they lend credence to the idea that at the scale size of auroral arcs, magnetosphere-ionosphere coupling is influenced by Alfvén waves as suggested, for example, by *Hasegawa [1976], Goertz and Boswell [1979], Haerendel [1983], Lysak and Carlson [1983], and Seyler [1988]*.

While we have concluded that the measured structure in the impedance function is due to standing Alfvén waves, we must also consider a few other explanations. For example, it is possible that the value of Σ_P associated with small scale static electric and magnetic fields is different than the Σ_P relating large scale fields, since small scale structures in the aurora, such as arcs, are associated with density enhancements. As a result, a spacecraft measuring Doppler-shifted static structures might find $Z(f)$ at low frequencies (i.e. large scales) to be larger than at high frequencies (small scales) since the Σ_P relating small scale fields would be higher. This mechanism is not the cause for the structure we observe in $Z(f)$ because 1) it predicts a decrease in Z rather than the observed increase, and 2) it cannot account for the phase spectrum measured by the sounding rocket.

In addition to standing waves, kinetic Alfvén waves (i.e. $k_x c / \omega_{pe} \sim 1$) can also increase the field impedance measured above the ionosphere above Σ_P^{-1} , as we can see from Faraday's Law, which tells us that $k_x E_z - k_z E_x = \omega B_y$. Eliminating E_z with Equation (2.17) and k_z with (2.15) gives

$$\mu_0 \frac{E_x}{B_y} = \mu_0 V_A \sqrt{1 + k_x^2 c^2 / \omega_{pe}^2} \quad (5.8)$$

The correction term $k_x^2 c^2 / \omega_{pe}^2$ is small for the HILAT data because spatial scales on the order of c/ω_{pe} transform to several Hz in the satellite frame, but the peaks we measure in $Z(f)$ occur between 0 and 1 Hz. On the other hand, since the sounding rocket was traveling nearly parallel to auroral structures and in the same direction as the plasma flow, it is possible that the Doppler-shifted frequencies corresponding to auroral structures could fall into the tenths of Hz range, and kinetic Alfvén waves could possibly cause higher impedances in the rocket data. Again, (5.8) does not predict the phase spectrum shown in Figure 5.2, while the standing wave model does make such a prediction. We conclude that small horizontal wavelengths are not responsible for the structure in the rocket-measured $Z(f)$.

Another complication can arise if a spatially localized Alfvén wave in a drifting plasma reflects from the ionosphere, but the reflected part of the wave convects away from the incident part. This can happen if $d/l_x > V_A/V_{drift}$, where d is the distance of the measuring platform from the reflection point, l_x is the spatial scale of the Alfvén wave, and V_{drift} is the plasma drift velocity. A spacecraft above the ionosphere would then measure the local Alfvén wave impedance rather than the standing wave impedance. This scenario was discussed by *Mallinckrodt and Carlson [1978]*, but is not relevant to the data discussed in this chapter since incident and reflected waves are clearly interfering in our data.

Throughout our analysis we have assumed that the field fluctuations we measure at any given time are either purely spatial or

purely temporal. Of course both types can and most likely do occur simultaneously, and incorporating this fact would complicate our analysis considerably. For example, if we measure a spatially modulated Alfvén wave, Doppler shifting of the spatial structure would cause the measured wave frequency to be "mixed" to different frequencies. Future work should attempt to include complications such as this and the ones listed above, but much more detailed information about the 3-dimensional density structure in the ionosphere will be needed, and therefore measurements from a single satellite or rocket alone will not suffice.

To compare our results here with previous work [Sugiura *et al.*, 1982], we performed a statistical analysis on the time-domain rocket data without filtering and we find that the correlation coefficient between the electric and magnetic fields ρ is 0.70, and the rms field fluctuations are related by $\mu_0 E_{rms} / B_{rms} = 0.33 \Omega$. This value is in excellent agreement with the value of Σ_P^{-1} deduced from the Langmuir probe measurements. Since most of the spectral energy in the electric and magnetic fields is at low frequencies, this result gives the same impedance as found in the low frequency limit of $Z(f)$. It is interesting to note that at short time scales Sugiura *et al.* [1982] noticed fine structures in the electric field that were not present in the magnetic field. This corresponds to an increase in $Z(f)$ at higher spatial and/or temporal frequencies, as we have found to occur in the presence of standing Alfvén waves.

To reiterate the findings of this chapter we note that even though the HILAT-measured impedance spectra and the modeled spectra presented in Figures 5.6 - 5.16 do not match well in terms of numerical values, there is reasonable agreement between the measured and

modeled frequencies at which $Z(f)$ maximizes. This fact along with the excellent agreement between the sounding rocket data and the predictions of the numerical model allow us to conclude that Alfvén waves are an important part of the overall electrodynamic coupling between the magnetosphere and auroral ionosphere. Furthermore, the quantitative estimates in Section 5.6 indicate that the electromagnetic field energy carried by Alfvén waves exceeds the energy carried by structured Birkeland currents in the vicinity of auroral arcs.

CHAPTER 6

THE EFFECT OF ALFVEN WAVES ON INCOHERENT SCATTER RADAR MEASUREMENTS

6.1 Introduction

This thesis has helped to establish the importance of Alfvén waves in the high-latitude ionosphere, and we might now ask how the presence of Alfvén waves might affect the interpretation of radar measurements. High-latitude radars play a crucial role in the study of magnetosphere-ionosphere coupling, and rocket or satellite data are often analyzed in the context of supporting radar data since the radar measurements in many ways complement spacecraft measurements. Incoherent scatter radars are especially good at measuring density, temperature, and plasma drift velocity, among other parameters, both as a function of altitude and horizontal distance. Unfortunately the resolution of radar measurements is limited spatially by the antenna beam-width and temporally by the fact that many single measurements must be averaged due to the statistical nature of the returned signal. In practice, integration times are at least a few seconds and usually longer, depending on the ionospheric plasma density. Spacecraft, on the other hand, are able to take measurements of the electric field, for example, with a time resolution many orders of magnitude better than this, albeit only at one point in space per measurement.

The signal analysis which extracts plasma parameters from the returned radar signal usually relies on the assumption that all

macroscopic quantities are homogeneous within a volume defined by the radar beam width and pulse length, and that they are time-stationary during the integration period. However, high resolution satellite measurements have shown that spatial homogeneity at antenna beam-width scales is not always a safe assumption at high latitudes. *Swartz et al.* [1988] gave an example of a Millstone Hill radar measurement which suffered from a breakdown in the assumption of spatial homogeneity by using HILAT data to identify 2 km/s drift velocity variations within the 80 km width through which the antenna beam scanned during the 30 s integration period. By simulating the distortion in a theoretical spectrum which would result from the HILAT-measured velocity shears, the authors showed that a parameter fitting program would erroneously predict ion and electron temperatures of 2705 K and 990 K, while the undistorted spectrum would have indicated 1500 K. They suggested that velocity shears are an alternate explanation for distorted incoherent scatter spectra which had previously been attributed to non-Maxwellian plasmas [*Moorcroft and Schlegel, 1988; Lockwood et al., 1987; and Løvhaug and Flå, 1986*] or ion hot spots [*Kofman and Lathuillere, 1987*].

There is evidence that time-stationarity during the radar integration period can also be violated at high latitudes. From our analysis in Chapter 5 of rocket and satellite data we have established that substantial time-varying electric fields can exist in the ionosphere with periods less than a typical radar integration period of 5 to 10 s. The event near 09:31 UT in Figure 5.1 shows an electric field pulse with an amplitude exceeding 100 mV/m and a characteristic frequency of about 0.3 Hz. The $\mathbf{E} \times \mathbf{B}$ drift velocity resulting from this electric field is over 2 km/s. Clearly

the assumption of time-stationarity would not be valid if radar measurements were taken in the vicinity of such a pulse.

6.2 Incoherent Scatter Spectra with Time-Varying Drifts

The theoretical spectrum received by an incoherent scatter radar was derived by *Dougherty and Farley* [1960, 1963], *Farley et al.* [1961], and *Farley* [1966]. Data processing in an ISR experiment usually involves measuring the spectrum or autocorrelation function at each range for each inter-pulse period (IPP), then averaging over several IPPs. The result is fit to the theoretical curve in a least squares sense.

The theoretical "ion line" or low Doppler shift portion of an incoherent scatter radar spectrum is shown in Figure 6.1 for 2 different plasma densities. The spectra were generated assuming that the transmitter frequency is 1290 MHz (the operating frequency of the Sondrestrom radar), the plasma has O⁺ as its only ion constituent, $T_e = T_i = 1500$ K, and the antenna is directed along \mathbf{B}_0 . The spectrum for $n_e = 10^6$ cm⁻³ is typical for cases in which the radar wavelength is much longer than $4\pi\lambda_D$ where λ_D is the Debye length. With this set of parameters $\lambda_D = 2.3$ mm. The wavelengths of the Sondrestrom and EISCAT (933 MHz) radars are small enough so that λ_{radar} is comparable to $4\pi\lambda_D$ for lower densities, and the measured spectra lose their double-humped appearance as evidenced by the $n_e = 10^4$ cm⁻³ ($\lambda_D = 2.3$ cm) curve in Figure 6.1. The depth of the valley at zero Doppler shift depends not only on the Debye length but also the ratio T_e/T_i and the ion composition.

If the ionospheric plasma has a bulk drift, the entire spectrum is shifted by an amount $\omega_d = \mathbf{k} \cdot \mathbf{V}_d$ where \mathbf{V}_d is the line-of-sight drift velocity and $|\mathbf{k}| = 4\pi/\lambda_{radar}$. If the drift is due to an Alfvén wave, \mathbf{V}_d will change

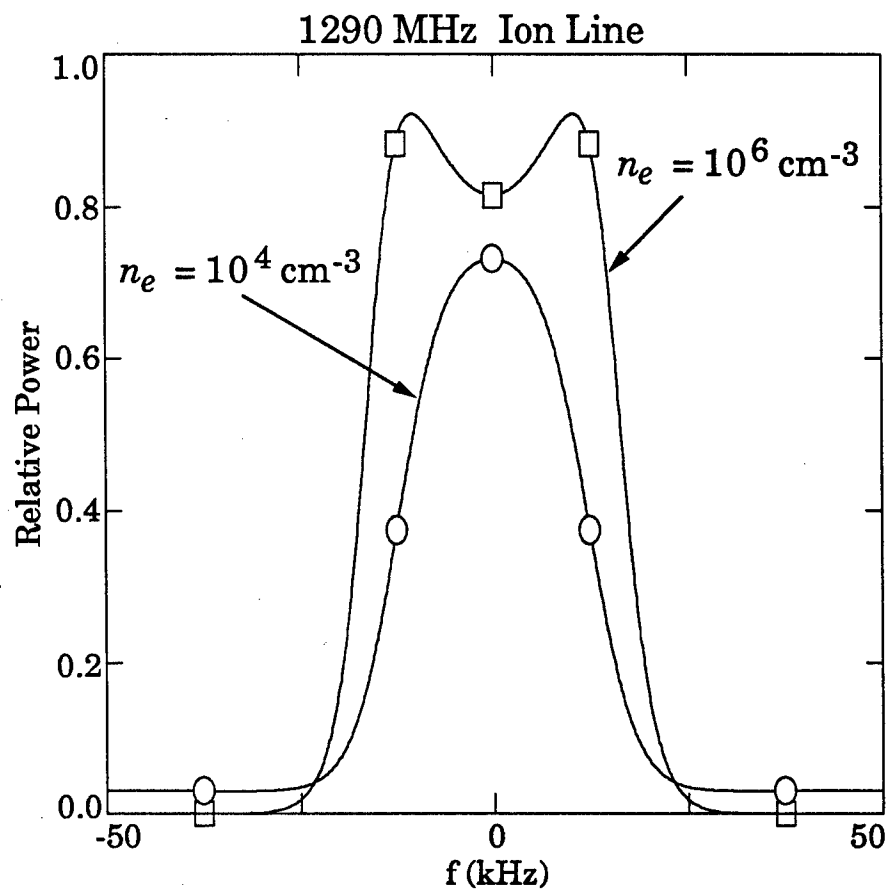


Figure 6.1 Theoretical ion-line spectra at 1290 MHz assuming an O⁺ plasma with two different densities.

from IPP to IPP and the spectrum $S'(\omega)$ resulting from the averaging process will be

$$S'(\omega) = \frac{1}{N} \sum_{i=1}^N S(\omega - \mathbf{k} \cdot \mathbf{V}_{d,i}) \quad (6.1)$$

where i is an IPP index and N is the number of IPPs included in an integration time. We have assumed that the drift velocity does not change substantially during a single IPP, which is typically on the order of 10 ms in duration.

In order to quantify the amount of distortion introduced by an Alfvén wave in a high latitude ISR experiment we distorted several theoretical spectra in the manner indicated by Equation (6.1) assuming that the drift velocity $\mathbf{V}_{d,i}$ varies sinusoidally with i , i.e.

$$|\mathbf{V}_{d,i}| = V_{d,max} \sin(2\pi i/N) \quad (6.2)$$

where we have used $N = 1000$. Figure 6.2 shows the effect of this operation on both spectra in Figure 6.1 for $V_{d,max} = 750$ m/s. The associated electric field amplitude is about 38 mV/m, which is certainly possible at high latitudes. The $n_e = 10^6$ cm⁻³ spectrum appears to be most affected, with its double-humped structure nearly obliterated. Since the peak-to-valley ratio has changed drastically, one would expect a least-squares fitting program to underestimate the temperature ratio T_e/T_i . Distorting the spectrum in the smaller n_e case has widened it, but the fact that there was no pronounced valley in the spectrum to begin with suggests that the T_e/T_i estimate from a fitting program will not suffer from errors as large as those in the high density, small Debye length case.

Figures 6.3a and b show temperature estimates from a least-squares fitting program versus $V_{d,max}$ for the two spectra in Figure 6.1. The

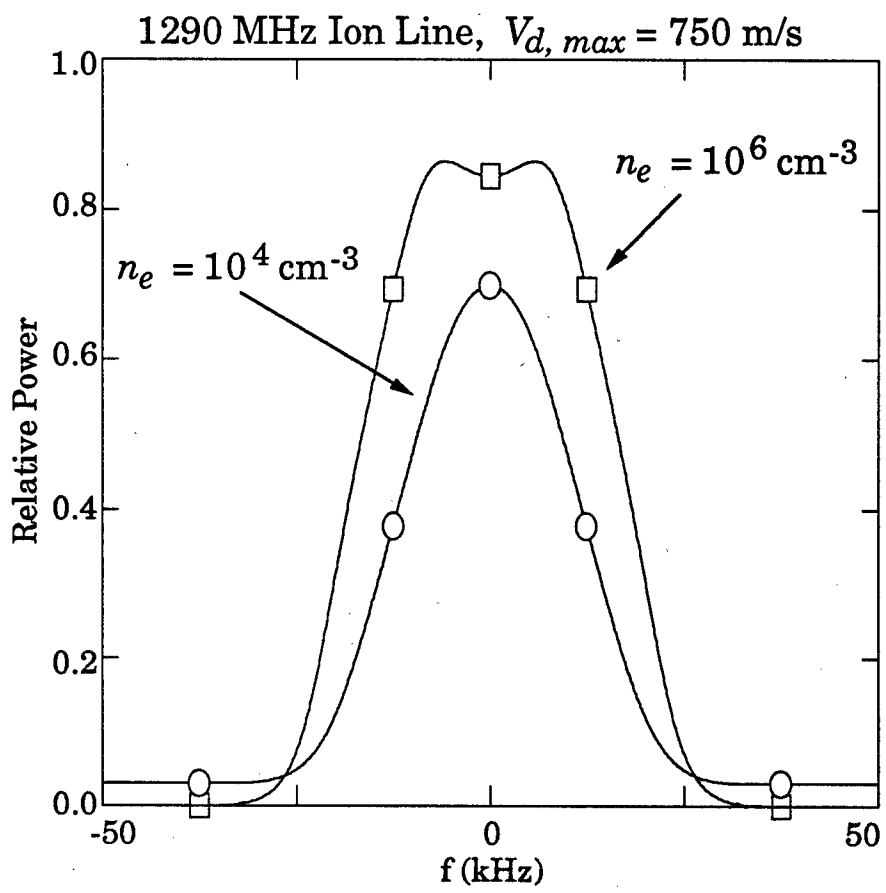


Figure 6.2 Spectra which would result from smearing the spectra in Figure 6.1 with a 750 m/s amplitude sinusoidal drift velocity which has a period less than the radar integration time.

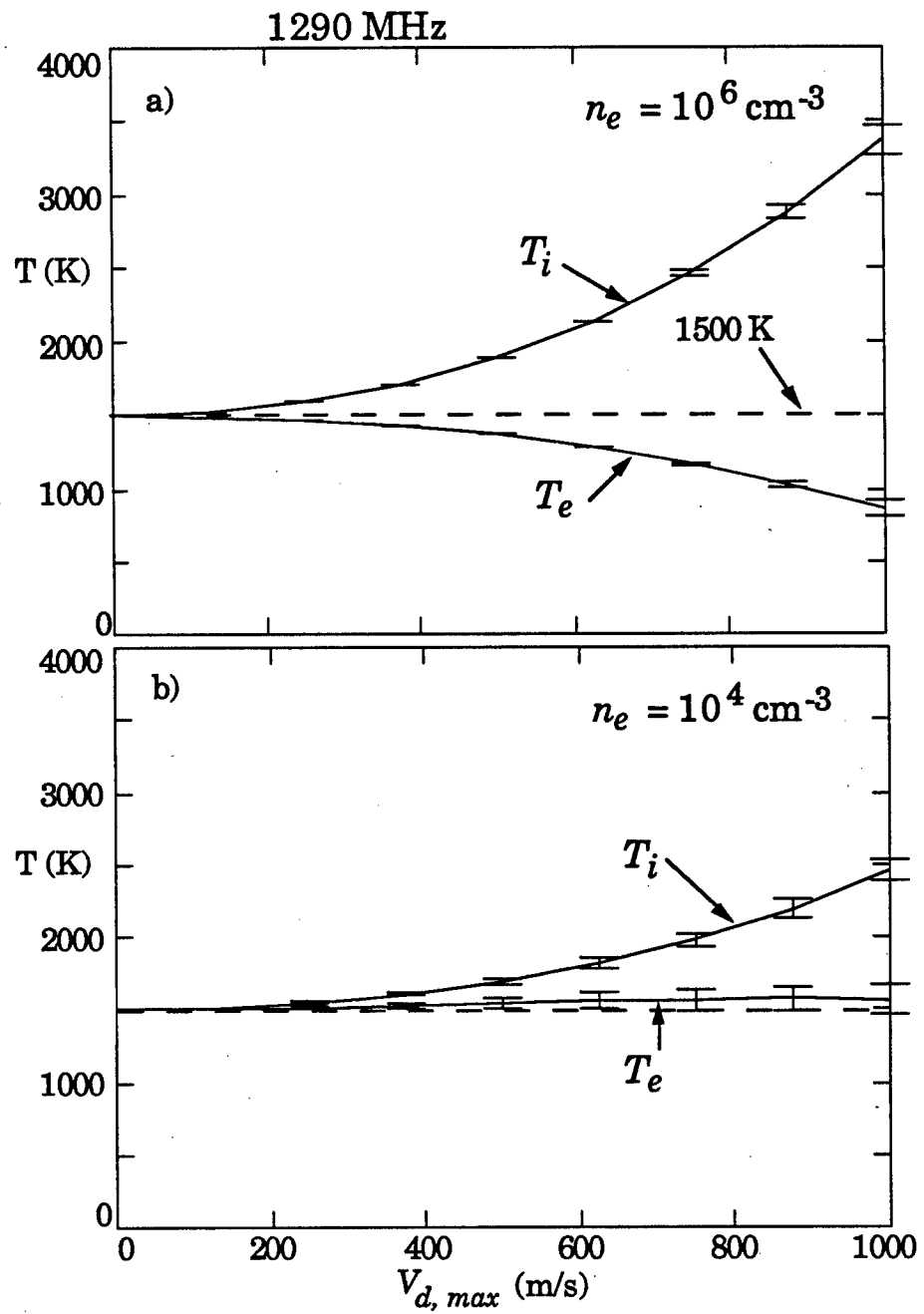


Figure 6.3 Electron and ion temperature fits to ideal 1290 MHz ion-line spectra which have been smeared with a drift velocity of the form $V_d = V_{d,max} \sin(2\pi t/T)$, where T is less than the radar integration time.

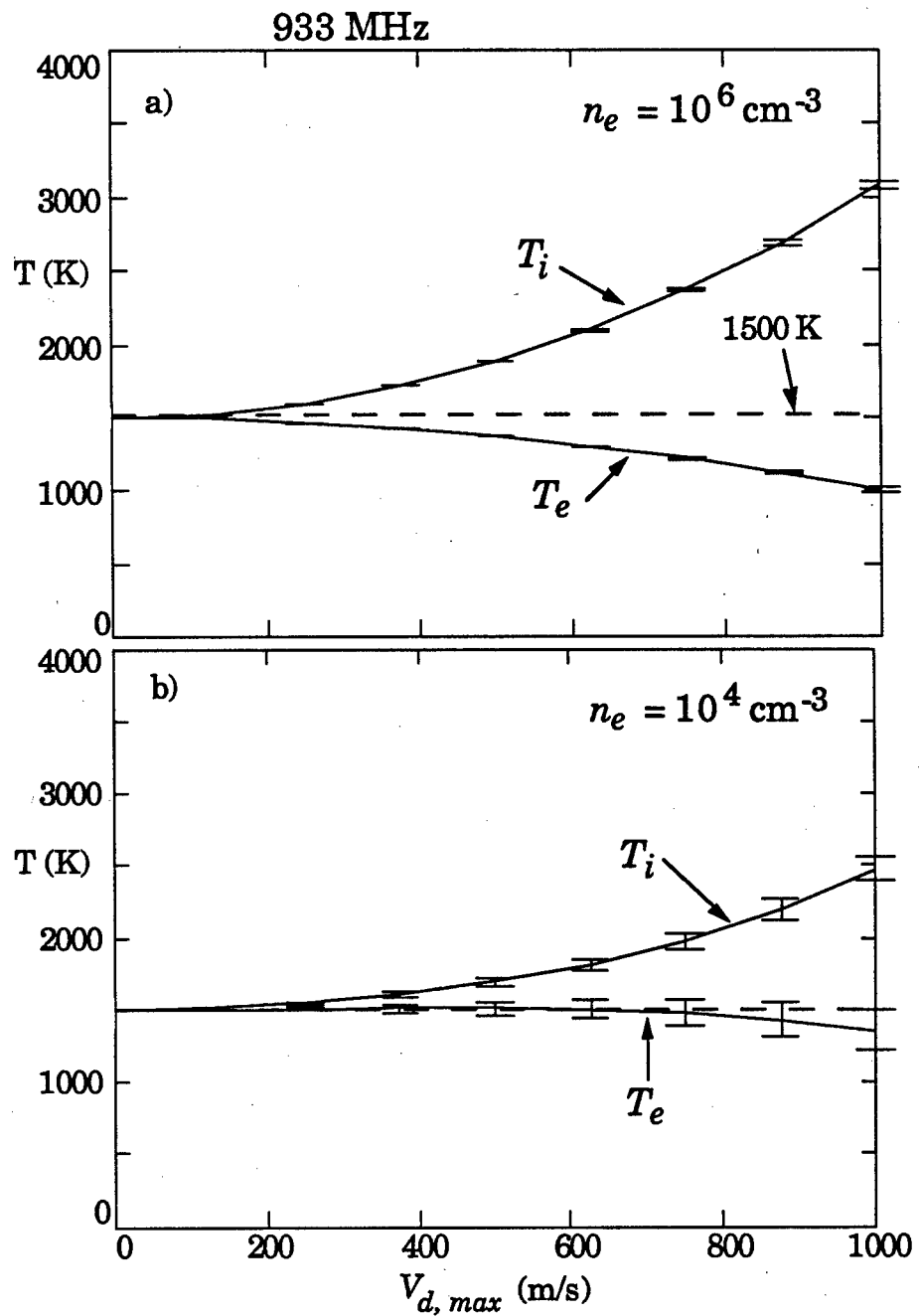


Figure 6.4 Electron and ion temperatures fits to ideal 933 MHz ion-line spectra which have been smeared with a drift velocity of the form $V_d = V_{d, max} \sin(2\pi t/T)$, where T is less than the radar integration time.

codes for generating theoretical spectra and performing the fits were supplied by *P. Erickson and J. Pingree* [personal communication, 1990]. Figures 6.4a and b show curves generated using parameters identical to those in Figure 6.3 except for the transmitter frequency, which has been changed to the EISCAT UHF frequency of 933 MHz.

According to Figure 6.3a, velocity fluctuations with amplitudes of 250 m/s, which are quite common in the auroral zone, can generate an anomalous increase in T_i of almost 100 K and an associated decrease in T_e of about 30 K. In the lower density case (Figure 6.3b) the temperature estimate errors are less than half of these values. Unfortunately, although the errors are smaller, lower density plasmas require longer radar integration times and thus it is more likely that time-stationarity will be violated. A 1 km/s sinusoidal drift can cause an erroneous T_i of nearly 3500 K and T_e of about 850 K in the $n_e = 10^6 \text{ cm}^{-3}$ case. But while fluctuations of this magnitude certainly occur in the auroral ionosphere, the event shown in the Black Brant data in Chapter 5 lasts only a few seconds. In this case a longer integration time might serve to reduce the error in the T_i estimate from what it would be if the Alfvén wave lasted the entire integration period.

At 933 MHz with $n_e = 10^6 \text{ cm}^{-3}$ (Figure 6.4) the temperature estimate errors are slightly less than in the 1290 MHz case. For $n_e = 10^4 \text{ cm}^{-3}$, errors in the estimated T_i are about the same at both transmitter frequencies, while T_e estimates are in greater error at 933 MHz, although only by 150 K with a 1 km/s drift.

6.3 Conclusions

Swartz et al. [1988] have shown that spatial velocity shears at middle and high latitudes can violate the assumption of spatial homogeneity with ISR antenna beams, and can cause anomalously large ion temperature estimates. This phenomenon can mimic the effect of ion hot spots or non-Maxwellian plasma distributions.

We have shown that similar errors in temperature fits can occur in the presence of Alfvén waves. In the case where $\lambda_{radar} \gg 4\pi\lambda_D$ the increased ion temperature estimates are accompanied by a marked decreases in T_e estimates. If observed over a period of several minutes, this signature might help to distinguish anomalously large ion temperatures due to Alfvén waves from actual occurrences of ion hot spots since the latter would not likely occur simultaneously with decreases in the electron temperature.

Ground-based magnetometers might also be used to identify ISR spectra distorted by Alfvén waves, although these instruments tend to average over a vast portion of the sky. An event like the one shown in Chapter 5 (Figure 5.1) near 09:31:30 UT might have a magnetic signature on the ground known as a "giant pulsation", and simultaneous measurement of such a magnetic pulsation with distorted ISR spectra would be a useful demonstration of the effect of Alfvén waves on radar measurements.

Optical data from image intensified TV images might prove more useful in identifying causes of distorted spectra since rapid motion of auroral forms would be a good indication of Alfvén wave activity. The amount of spectral distortion could be compared inside and outside of such regions, for example.

CHAPTER 7

CONCLUSIONS AND SUGGESTIONS

FOR FUTURE RESEARCH

7.1 Summary of Results

The electric and magnetic fields which couple the magnetosphere and ionosphere carry a wealth of information regarding the amount and direction of energy flow, the characteristics of energy dissipation in the ionosphere, the temporal and spatial structure of magnetospheric energy sources, and the presence of neutral winds in the ionosphere. Since there are many physical processes which create and modify them, *in-situ* measurements of these fields can be difficult to interpret. In this thesis we have taken existing analysis techniques, e.g. spectral and cross-spectral analysis, and applied them in new ways to auroral electric and magnetic field data. We will now summarize the main results presented in this dissertation. Since Chapter 5 contains the bulk of the results, we begin there.

In-situ measurements of magnetosphere-ionosphere coupling via Alfvén waves. Chapter 5 contains data from two different experiments: 1) a sounding rocket launch into the dayside auroral oval, and 2) several oval crossings by the HILAT satellite. The results of these two experiments are similar in that at frequencies below about 0.1 Hz (as measured in the spacecraft frame) the meridional electric to zonal magnetic field ratio $Z(f) = \mu_0 E_x(f)/\delta B_y(f)$ is equal or nearly equal to the inverse of the height-integrated Pedersen conductivity of the ionosphere

Σ_P^{-1} , and the cross-product of the fields indicates a downward Poynting vector. These measurements are consistent with energy flow directed from the magnetosphere toward the ionosphere in the form of quasi-static electric fields and field-aligned currents. This energy is dissipated in the conducting part of the ionosphere. The measurements in Chapter 5 are also consistent with earlier findings from *Sugiura et al.* [1982], *Sugiura* [1984], and *Smiddy et al.* [1984].

For time scales shorter than 10 s the results from the rocket and satellite experiments differ. The rocket-measured $Z(f)$ increases smoothly to a peak value of about $4\Sigma_P^{-1}$ at 0.3 Hz and above. This value is near the Alfvén impedance $\mu_0 V_A$, which indicates that the fields are due to Alfvén waves and the fluctuations are therefore temporal rather than spatial structures which have been Doppler-shifted from the rocket motion. Furthermore, the shape of $Z(f)$ and the phase relation between E_\perp and δB_\perp indicate a standing Alfvén wave pattern due to reflections from the ionosphere.

The satellite data consist of six passes for which the frequency-averaged coherency spectra were significantly larger than could be expected from random noise. The measured impedance spectra fall near Σ_P^{-1} over most of the spectrum and do not vary as much as in the sounding rocket case. However, in most cases the frequency of the maximum measured impedance falls within 10-15% of the frequency predicted from the standing Alfvén wave model. A plausible explanation for this is that most of the field energy measured by HILAT is from structured quasi-static fields, but occasionally there are Alfvén waves present. Alfvén waves can be identified in the impedance spectra by their increased impedance, and we find that the frequency of the resulting

electric field enhancement is determined by the electrical length of the satellite above the reflecting part of the ionosphere. That is, HILAT measures increased impedances at frequencies for which its orbital altitude is at the peak of the electric field standing wave pattern. If the frequencies of detectable Alfvén waves were determined by the wave source, one would expect increased impedances at frequencies which bear no relation to those predicted by the standing wave model. This is apparently not the case. Unfortunately the variances of the satellite-measured phase spectra were too large to predict the phase shift between the meridional electric and zonal magnetic fields.

We found two pieces of evidence which suggest that the measured Alfvén wave energy is concentrated near auroral arcs. The first is from the rocket data in Figures 5.1c and d, which shows that increases in electric field energy in the 0.25-0.35 Hz range are correlated with enhancements in precipitating electron energy flux. The second is indirect, and follows from the observation that based on the measured impedance spectra a much larger fraction of the electromagnetic field energy measured from the sounding rocket is due to Alfvén waves than in any of the 6 HILAT passes. Since the sounding rocket velocity was eastward, it is likely that it spent much more time in the vicinity of auroral arcs than HILAT, which moves mostly perpendicular to auroral structures. Consequently, HILAT spends less time near individual arcs and this may explain the diminished evidence for Alfvén waves in HILAT data.

Again, the major points from Chapter 5 are:

- The frequency-dependent relations between amplitudes and phases of the meridional electric and zonal perturbation magnetic field

data from the Greenland II Black Brant sounding rocket are in excellent agreement with a standing Alfvén wave model.

- The values of the impedance function measured by HILAT are much lower than those predicted by the numerical Alfvén waves model, indicating that much of the spectral energy is dominated by quasi-static structures Doppler-shifted by the spacecraft velocity.
- HILAT does detect some Alfvén wave energy at frequencies for which the satellite is at a peak in the electric field standing wave pattern, indicating that the shape of the Alfvén wave frequency spectrum near the ionosphere is determined by wave interference, not the magnetospheric wave source.
- Alfvén waves appear to be localized in latitude near auroral arcs.

It is not clear from this study if the spatial coincidence of Alfvén waves and arcs is due to a causal link between the two, as suggested by previous authors (see Chapter 5). Hopefully, future studies can help to establish such a link by adding to the amount of low-frequency data taken by spacecraft traveling parallel to the auroral oval. These studies will have to be carried out either with sounding rockets or satellites in a somewhat lower inclination orbit than HILAT (81°), closer to 70° . Successful experiments in the future will need to include many different instruments, as in the upcoming Auroral Turbulence campaign. High time resolution ground-based auroral imaging will be especially helpful in determining the amount of spatial structuring and dynamic activity characterizing the environment in which *in-situ* measurements are taken.

Numerical model of Alfvén wave reflections in the ionosphere. A model similar to the one presented in Chapter 4 is a very useful tool in interpreting the data. Future models can be improved by relaxing the assumption of spatial homogeneity in horizontal directions, although this will greatly complicate the code. However, we have been able to explain several features in the data without taking into account auroral density structuring. Although we have used the numerical model mainly as an aid in interpreting experimental data, in Chapter 4 we showed that it is also a useful tool for understanding the general reflection and absorption properties of the ionosphere. A summary of these properties is as follows:

- The meridional electric field reflection coefficient $|\Gamma|$ for Alfvén waves with periods greater than 10 s is close to $(\Sigma_p^{-1} - \mu_0 V_A) / (\Sigma_p^{-1} + \mu_0 V_A)$ where the Alfvén velocity is taken above but close to the ionosphere. This can be interpreted as meaning that the ionosphere behaves as a thin conducting slab on these time scales.
- For time scales shorter than 10 s, $|\Gamma|$ decreases. In model ionospheres with an F region, $|\Gamma|$ experiences sharp nulls separated by a few tenths of Hz. These nulls correspond to resonances which increase the electric field amplitude (and thus the Joule heating) above the E region. Thus as a general rule, it appears that more E-region ionization increases $|\Gamma|$, and F-region ionization tends to decrease $|\Gamma|$.
- Electron collisions have little effect on the reflection coefficient, nor do the density and ionization scale heights in the lower atmosphere. Therefore the ion collision and plasma density profiles above 100 km are mainly responsible for the behavior of $|\Gamma(f)|$.

- The horizontal spatial scale of the Alfvén wave has a negligible effect on $|\Gamma|$ for $\lambda_x > 10$ km, and $|\Gamma|$ decreases somewhat as λ_x approaches 1 km.

Energy flow into and out of the upper atmosphere. Many parameters of the solar-terrestrial system (e. g. solar sunspot number and geomagnetic activity indices) are continuously monitored from ground-based and orbiting instruments. The total low-frequency electromagnetic energy flux into the polar cap and auroral oval is not currently monitored in this way, yet it is potentially an important factor in characterizing the energetics of the upper atmosphere.

In Chapter 3 we compare two quantities which are useful for measuring EM energy input into the ionosphere, Joule dissipation and Poynting flux. They have been used by previous authors who have made case studies of individual events, but they are not routinely monitored. The first quantity relies on electric field measurements and assumed or derived ionospheric density and collision frequency profiles. Satellites which can measure both electric and perturbation magnetic fields can determine the Poynting vector and thereby circumvent the potential errors in Joule dissipation measurements arising from incorrect ionospheric models. Another advantage of using Poynting flux is that it is a signed quantity, thus upward Poynting flux can be used to indicate areas in which the neutral wind is acting as an electrical dynamo and supplying energy to the magnetosphere.

Effects of Alfvén waves on incoherent scatter radar spectra. Finally, in Chapter 6 we have argued that Alfvén waves can occur in the auroral oval with amplitudes and frequencies sufficient to severely distort

incoherent scatter radar spectra. The plasma drifts from a 20 mV/m wave with a period much less than the radar integration period tend to cause significant increases in apparent ion temperature as estimated from least-squares fitting programs. When the plasma Debye length is much less than the radar wavelength, the programs erroneously predict decreased electron temperatures as well.

7.2 Future Research: Quasi-Static Fields and Neutral Winds

In Chapter 3 we established that in many ways, satellite measurements of the DC Poynting vector $\mathbf{E} \times \mathbf{H}$ are superior to Joule heating estimates. Hopefully, satellite Poynting flux measurements will be part of future synoptic studies of the high-latitude ionosphere.

An especially interesting application of Poynting flux measurements is in the area of ionosphere-thermosphere interactions. In Section 3.3 we calculated electric fields and currents generated by neutral winds in the ionosphere for two different electrical loads, and we showed that neutral wind dynamos give rise to an upward Poynting vector above the ionosphere. While detections of upward Poynting flux by satellite can reveal much about the ionosphere and winds below, altitude profiles of $E_{\perp}(z)$ and $\delta B_{\perp}(z)$ (which must be measured with sounding rockets instead of satellites) would be of more use in a detailed study of wind-driven dynamos. A reason that altitude profiles are necessary is that, contrary to our assumption in the Section 3.3 examples, thermospheric neutral winds can vary in altitude as a result of tides and gravity waves. The height variation of the winds causes associated changes in perturbation magnetic fields, as we shall show later in this section.

At middle and low latitudes, global scale electric fields and currents in the ionosphere are controlled mainly by tidal modes in the thermosphere, especially during the daytime, as discussed by *Richmond et al.* [1976] and *Richmond and Roble* [1987]. The thermosphere-ionosphere interaction is important at smaller scales as well, where neutral atmosphere dynamics are driven by gravity waves. For example, *Röttger* [1973] and *Kelley et al.* [1981] showed that gravity waves can cause structuring of equatorial spread-F irregularities.

During magnetically quiet periods the neutral wind is an important source of electric fields and currents at high latitudes as well, as has been measured with the Chatanika radar by *Brekke et al.* [1974]. Even during magnetically active times the neutral wind can be important. As we discussed in Chapter 3, the effective conductivity of the ionosphere is modified by neutral winds, so even if the neutral winds are not driving dynamo fields, the load characteristics of the ionosphere are affected by winds. Another neutral wind effect was considered by *Forbes and Harel* [1989], who showed that a magnetospheric disturbance can accelerate the neutral wind in such a way that the net magnetic perturbation decreases after some time even though the driving electric field remains constant.

Vertical variation of wind velocities on scales of tens to hundreds of km in the thermosphere can occur as a result of upwardly propagating gravity waves and tides, and the correlation of these winds with ionospheric electric fields has been measured using chemical tracers released by sounding rockets [*Mikkelsen et al.*, 1981, 1987] and modeled numerically by *Pereira* [1979], among others. *Earle and Kelley* [1988] compared Chatanika-measured electric fields with mesospheric gravity waves and found similar spectral characteristics, suggesting that during

quiet times, thermospheric winds and electric fields are strongly coupled.

While gravity waves can create dynamo electric fields in the thermosphere, it is difficult to show experimentally that a particular spacecraft or radar electric field measurement is due to gravity waves. For example, one might try to show that the electric field \mathbf{E} and neutral wind \mathbf{U} vary together in time, but the minimum wave period for gravity waves is on the order of five minutes. Of course, spacecraft are unable to make measurements at a single point in space for this long. Ground-based radars can be used for the electric field measurement, but the problem of measuring the neutral wind above 100 km for tens of minutes remains.

A second way one might study the gravity wave-electric field interaction is to correlate the variations of \mathbf{U} and \mathbf{E} as a function of altitude. But, as we showed in Chapter 4, electric fields with time scales of over 10 s map along geomagnetic field lines, so \mathbf{U} may vary but \mathbf{E} will not. However, since the horizontal current in the ionosphere can be driven by both electric fields and winds, it so happens that $\delta\mathbf{B}_\perp$ does vary with altitude in the presence of gravity waves. We suggest that simultaneous rocket measurements of $\delta\mathbf{B}_\perp$ and \mathbf{U} might be a useful way to study the interaction between gravity waves and the ionosphere.

To obtain some idea of the magnetic field magnitudes one can expect from gravity waves, we will now calculate some wind-driven magnetic field profiles for the simplified case in which \mathbf{B}_0 is vertical, $\partial/\partial y = 0$ (no variation in the zonal direction), and \mathbf{U} , \mathbf{E} , and $\delta\mathbf{B}$ vary as $\exp(ik_x)$. Furthermore, we will allow only a zonal wind U_y and a meridional electric field E_x .

In general, the current \mathbf{J} is given by

$$\mathbf{J} = \sigma(\mathbf{E} + \mathbf{U} \times \mathbf{B}_0) \quad (7.1)$$

where σ is given by Equation (3.3). As we discussed in Chapter 3, (7.1) can be found by transforming $\mathbf{J}' = \sigma' \mathbf{E}'$ from the neutral wind frame into the Earth-fixed frame. The \hat{x} and \hat{y} components of Ampere's law, $\nabla \times \mathbf{B} = \mu_0 \mathbf{J}$, can now be written:

$$\hat{x}: \frac{\partial B_y}{\partial z} = -\mu_0 \sigma_P (E_x + U_y B_0) \quad (7.2a)$$

$$\hat{y}: \frac{\partial B_x}{\partial z} - \frac{\partial B_z}{\partial x} = -\mu_0 \sigma_H (E_x + U_y B_0) \quad (7.2b)$$

Thus, given $E_x(z)$ (which is constant), $U_y(z)$, and a boundary condition for B_y , we can integrate (7.2a) to find $B_y(z)$. We can find both E_x and a boundary value for B_y above the ionosphere from current continuity and the fact that $J_x = \sigma_P(E_x + U_y B_0)$:

$$J_z = ik_x \int_{ionosphere} \sigma_P (E_x + U_y B_0) dz \quad (7.3)$$

We can eliminate J_z with Ampere's Law, $\mu_0 J_z = -ik_x B_y$. Since E_x is constant in altitude, (7.3) can be written

$$-B_y = \mu_0 \Sigma_P E_x + \mu_0 \int_{ionosphere} \sigma_P U_y B_0 dz \quad (7.4)$$

Notice that we have divided all quantities by k_x . This is of course only valid for $k_x \neq 0$, and the physical reason for this is that we must have at least some variation in x to have electric and magnetic fields above the ionosphere. If there is no structure in the \hat{x} direction, the neutral wind would still drive currents but there would be no divergence of currents, no charge buildup, and consequently no electric fields.

To completely solve for E_x and B_y above the ionosphere we need an additional relation between them, but this is dependent on the "load" which is receiving energy from the wind dynamo. In Chapter 3 we used the conjugate ionosphere with a neutral wind as a load. This assumes that the two ionospheres have been electrically connected for a long time compared to the time it takes an Alfvén wave to propagate between hemispheres so that a steady state has been reached, and the example is probably more useful as an illustrative tool than as a geophysical model.

A more appropriate load model in the auroral oval and especially in the polar cap is simply an outward-traveling Alfvén wave which does not reflect and never returns to the ionosphere. In the oval, field lines may be closed but they are very elongated, and an Alfvén wave would likely convect away from its region of origin even if it did reflect from the conjugate ionosphere. In the polar cap with southward IMF the field lines are open, so unless a neutral wind-driven Alfvén wave reflects from some magnetospheric turbulence or boundary, the neutral wind sees only an Alfvén wave load. This means that we relate the fields at the top of the ionosphere with the Alfvén impedance, $\mu_0 E_x/B_y = \mu_0 V_A = Z_A$. From (7.4), the neutral wind-driven electric field in and above the ionosphere is then

$$E_x = - \left(\frac{\mu_0 V_A}{1 + \mu_0 V_A \Sigma_P} \right) \int_{ionosphere} \sigma_P U_y B_0 dz \quad (7.5)$$

In most cases $\mu_0 V_A \Sigma_P > 1$. For a neutral wind which is constant in altitude we can put $U_y B_0$ outside of the integral in (7.4), and the resulting electric field will be slightly less than $U_y B_0$. This can be understood as follows. Currents in the \hat{x} direction are driven by U_y , and charges build up where this is a divergence of current, creating electric

fields which oppose the current. If there were no load, the electric field would drive a current exactly opposing the wind-driven current and we would find the electric field $E_x = -U_y B_0$. Alfvén waves act as a high (but not infinite) impedance load and carry away some of the charge, making the electric field magnitude $|E_x| < |-U_y B_0|$. For any high impedance load, the electric field will give a fairly accurate measure of U_y in the ionosphere, although it is difficult to assure in any given high-latitude measurement that no electric fields applied in the magnetosphere are present. This should be less of a problem in the dayside mid-latitude zone and a study of such regions might be very interesting. Fields with an outward Poynting flux and which are related by the Alfvén impedance might be a useful indication of fields produced solely by neutral winds

We are now ready to investigate the altitude dependence of the zonal magnetic field B_y by integrating Equation (7.2a). We will not plot the electric field since it is constant in altitude, but we will note the value of E_x in each of the figures. Figure 7.1a shows $cB_y(z)$ for $U_y B_0(z) = 1$ with the "EF" model density profile (Figure 4.2a). There is not much difference between this and the field profile due to magnetospheric forcing shown in Figure 4.7c. The relation between E_x and B_y is quite different in the two cases, however, since in the wind-driven case the Poynting vector is away from the ionosphere and the field impedance is Z_A instead of Σ_P^{-1} .

Altitude-dependent winds complicate $B_y(z)$. Thermospheric winds with amplitudes of 100-200 m/s and wind shears with vertical wavelengths of tens to hundreds of km can be caused by the vertical propagation of gravity waves and tides [Mikkelsen *et al.*, 1987]. Figures 7.1b-d show $cB_y(z)$ for altitude-dependent winds of the form $U_y(z) =$

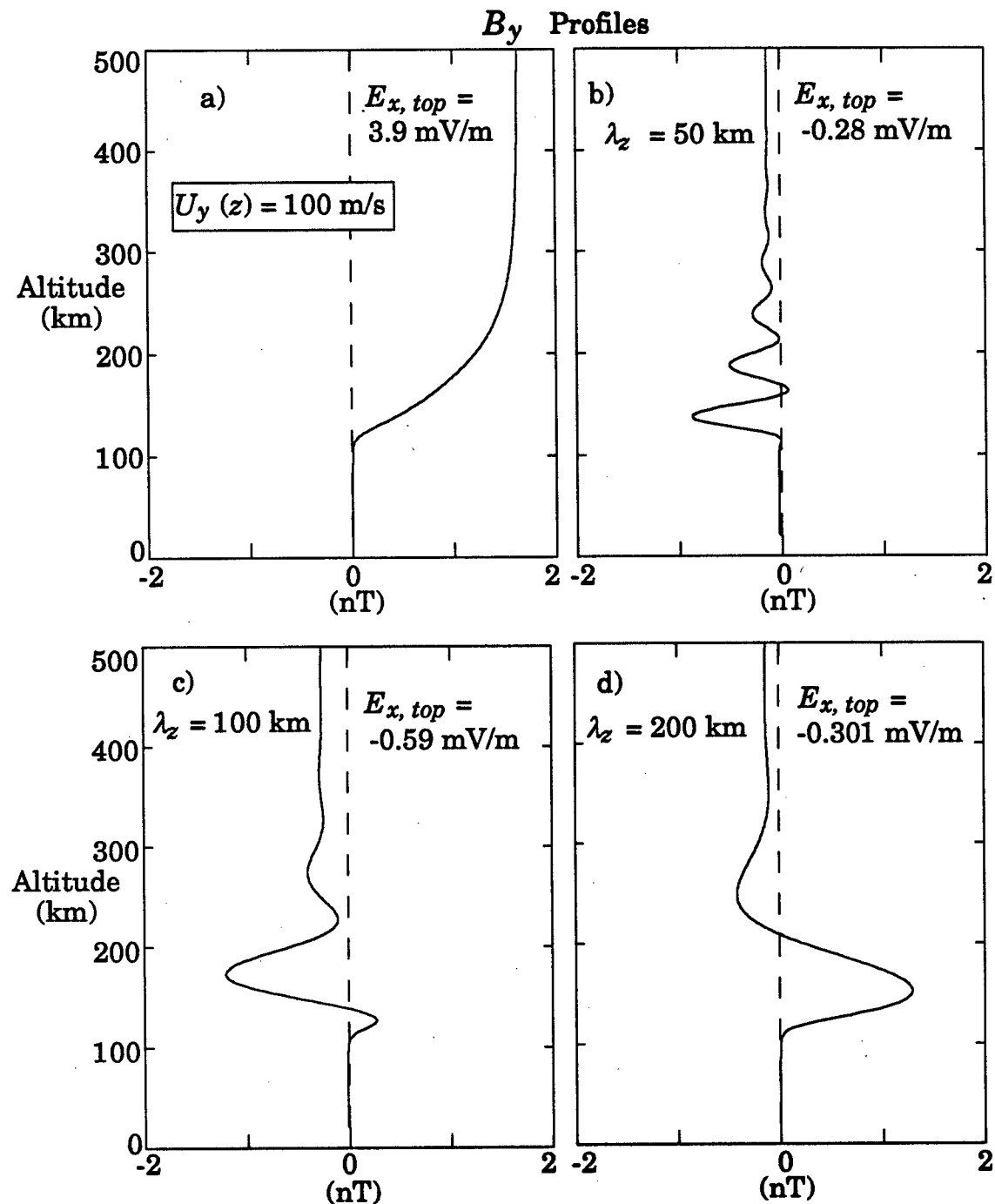


Figure 7.1 a) Zonal magnetic field perturbation due to a 100 m/s neutral wind which is constant in altitude. b-d) Magnetic perturbations due to zonal neutral winds of the form $U_y(z) = 100\cos(2\pi(z - 100 \text{ km})/\lambda_z)$. All four profiles were calculated using Profile "EF" shown in Figure 4.2, and the upper boundary condition demands that $E_x/\delta B_y = V_A$.

$U_{max} \cos(2\pi(z - 100 \text{ km})/\lambda_z)$ with $U_{max} = 100 \text{ m/s}$ and $\lambda_z = 50, 100, \text{ and } 200 \text{ km}$.

At wavelengths for which the integral in Equation (7.5) is zero, E_x and B_y above the ionosphere vanish but there can still be horizontal currents and perturbation magnetic fields in the ionosphere. This suggests a way in which sounding rockets might identify gravity wave-driven magnetic fields: the zonal magnetic field due to gravity waves can be stronger in the E region than above, whereas static B -fields driven by the magnetosphere increase monotonically with height. This distinction is true only in the DC limit, thus such an experiment would have to be carried out during low magnetic activity. Although neutral winds at ionospheric heights are difficult to measure, an experiment which correlates the neutral wind altitude profile with $B_y(z)$ would be very useful in demonstrating the existence of a gravity wave-driven dynamo. From (7.5) we see that in the northern hemisphere one would look for magnetic perturbations in the same direction as Uy (since $B_0 < 0$) while in the southern hemisphere the two quantities would have opposite signs.

Unfortunately, the magnetic fields generated by gravity waves shown in Figure 7.1 are quite small, i.e. 1-2 nT. Winds on the order of 300 m/s could create magnetic fields of about 5 nT, but the measurement would still be difficult to make. One would probably have to perform the experiment at sub-auroral latitudes to minimize magnetospheric sources of electric and magnetic fields.

7.3 Future Research: Spacecraft Measurements of Alfvén Waves

The comparison of spacecraft measurements and numerical model predictions presented in Chapter 5 has proven to be a fruitful method for

studying Alfvén waves. Continued studies along these same lines may help to reveal the nature of the relationship we observed between Alfvén waves and auroral arcs. A two dimensional (i.e. vertical and meridional) model of the Alfvén wave-ionosphere interaction might be necessary to understand the latitudinal dependence of Alfvén wave occurrences.

Although we have searched roughly 25 satellite passes for evidence of Alfvén waves, we have only a few cases for which there is strong evidence for waves. Satellites with more sensitive instruments and lower inclination orbits than HILAT can possibly help to increase the number of observations of Alfvén wave associated with auroral arcs. *M. C. Kelley* [personal communication, 1990] has suggested that a statistical study of field fluctuations could help to quantify the relative importance of Alfvén waves in the auroral ionosphere. This study would be carried out with data from an extended satellite mission by calculating E_{\perp} and δB_{\perp} fluctuation amplitudes within a few wide frequency intervals between 0 and 1 Hz. Fluctuation amplitudes exceeding some minimum value (to ensure the presence of geophysical signals) would contribute to an overall average, and the resulting electric and magnetic field averages at each frequency would be divided to form impedance estimates. The amount of any increase in field impedances with increasing frequency could be used to make a numerical estimate, as described in Section 5.6, of the relative importance of Alfvén waves and quasi-static fields in auroral electrodynamics.

7.4 Future Research: Incoherent Scatter Radar Measurements of the Aurora

Spatially sheared and time-varying plasma drifts can hinder attempts to measure ionospheric plasma temperatures with incoherent scatter radars, as discussed in Chapter 6. But the same fluctuations responsible for the errors are worthy of study in themselves. A joint radar-optical experiment is presently being planned for the EISCAT radar which will seek to identify ISR spectra distorted by spatial and temporal electric field variations.

The EISCAT radar is a tri-static system with a transmitter in Trömsø, Norway and receivers in Norway, Sweden, and Finland. The antenna beam widths for the UHF system are all 0.6° , thus the width of the Trömsø beam at, say 100, 200 and 300 km above Kiruna, Sweden is 2.3, 3.0, and 3.3 km respectively. (The distance between Trömsø and Kiruna is roughly 200 km.) The beam width of the Kiruna receiving antenna in the same regions is 1.1, 1.2, and 3.1 km. Thus velocity shears in the common volume of the two antenna beams are less likely to affect the received spectrum at Kiruna than at Trömsø, especially at lower altitudes. An enhanced ion temperature or non-Maxwellian velocity distribution, on the other hand, would affect spectra at both receivers equally. Comparing the spectra from both locations is a good way to determine the relative importance of shears, ion hot spots, and non-Maxwellian plasmas.

The radar measurements will be taken with a high time resolution (tens of ms per frame) all-sky TV camera situated below the common volume in Kiruna. The optical data will provide valuable information concerning the spatial and temporal structure of electric fields in the

radar scattering region. Although the camera cannot measure electric fields directly, it can record the optical signature of auroral arcs, which are known to be associated with large velocity shears. Thus one would expect the velocity shears in a stable, quiescent arc within the common volume to broaden the backscattered spectrum in Trömsø and have a smaller effect on the Kiruna measurement, due to the smaller receiving antenna beam width. When interpreting distorted spectra measured at both receiver sites and in the absence of auroral arcs, one could probably rule out spectral contamination from velocity shears.

The all-sky TV camera can also be useful for identifying conditions conducive to Alfvén waves. In at least one example, namely the Black Brant rocket flight we analyzed in Chapter 5, the very presence of auroral precipitation was an indication of Alfvén waves. At this point we do not know if all arcs have associated Alfvén waves, but optical evidence of fast time variations such as perturbations propagating along arcs or pulsating auroras would most likely be a telltale sign of Alfvén wave electric fields. As we suggested in Chapter 6, ground-based magnetometer data might also be used to verify the presence of temporal fluctuations. If, based on measurements from several instruments, one is fairly confident that Alfvén waves and spatial velocity shears are not present in the radar scattering volume, the ion hot spot or non-Maxwellian interpretation of distorted ISR spectra can be applied with some confidence.

An important part of the experiment we have outlined here is the fact that many instruments will be used simultaneously. There will be simultaneous data from the radar, an optical camera, a ground-based magnetometer, and possibly a satellite, if there happens to be a coincident

pass. Multiple diagnostics are necessary because although the visible part of the aurora lies in a relatively confined region, i.e. in the auroral oval between 100 and 1000 km in altitude, the keV electron energy source is thousands of km above the ionosphere, and the source of plasma is probably much farther away still. The structure of the visible aurora is thought to be imposed in the acceleration region, thus optical images provide information from a part of the auroral system which is quite removed from the E- and F-region radar measurements.

Unfortunately, the regions of the auroral system which lie beyond the acceleration zone are accessible only to satellites, and it is next to impossible to coordinate measurements in those regions with ionospheric measurements of the aurora, in large part because of the fact that one cannot know exactly how geomagnetic field lines map from the ionosphere to the magnetotail. Numerical simulations can help to piece together an understanding of the different parts of the auroral system, but of course simulations require accurate information concerning boundary conditions, and this information must be supplied with experimental data.

APPENDIX A

POYNTING'S THEOREM

A formal derivation of Poynting's theorem begins with consideration of the total magnetic energy in some volume,

$$\epsilon_B = \left(\frac{1}{2\mu_0}\right) \iiint B^2 dV \quad (A1)$$

The time rate of change of this quantity can be written

$$\frac{\partial \epsilon_B}{\partial t} = \left(\frac{1}{\mu_0}\right) \iiint \mathbf{B} \cdot \frac{\partial \mathbf{B}}{\partial t} dV \quad (A2)$$

Using $\partial \mathbf{B} / \partial t = -\nabla \times \mathbf{E}$ and the vector identity $\nabla \cdot (\mathbf{E} \times \mathbf{B}) = \mathbf{B} \cdot \nabla \times \mathbf{E} - \mathbf{E} \cdot \nabla \times \mathbf{B}$ we have

$$\frac{\partial \epsilon_B}{\partial t} = -\frac{1}{\mu_0} \iiint \nabla \cdot (\mathbf{E} \times \mathbf{B}) dV - \frac{1}{\mu_0} \iiint \mathbf{E} \cdot (\nabla \times \mathbf{B}) dV \quad (A3)$$

If we consider the static case $\partial \epsilon_B / \partial t = 0$ and furthermore, that $\nabla \times \mathbf{B} = \mu_0 \mathbf{J}$, we can write

$$\frac{1}{\mu_0} \iiint \nabla \cdot (\mathbf{E} \times \mathbf{B}) dV = - \iiint \mathbf{E} \cdot \mathbf{J} dV \quad (A4)$$

Finally, from Gauss' Theorem

$$\iint \mathbf{P} \cdot d\hat{s} = \iiint \mathbf{E} \cdot \mathbf{J} dV \quad (A5)$$

where $\mathbf{P} = (\mathbf{E} \times \mathbf{B}) / \mu_0$ and the vector $d\hat{s}$ is pointed into the volume everywhere.

A classic example of this result is that of a long thin wire of resistance R carrying a current I across a voltage V . Since the magnetic field in this case is given by $B = \mu_0 I / 2\pi a$ and $E = V/L$ where a is the wire radius and L is its length, the total energy flux into the wire is the surface integral of \mathbf{P} ,

$$W = \iint \mathbf{P} \cdot d\hat{s} = \frac{1}{\mu_0} \left(\frac{V}{L} \right) \left(\frac{\mu_0 I}{2\pi a} \right) (2\pi a L) = VI \quad (\text{A6})$$

which yields the total energy dissipated per unit time in the volume. Obviously, in deriving this result we have ignored the fringing fields and the contributions at the ends of the thin wire.

APPENDIX B

STATIC MAGNETIC FIELDS FROM AN IDEALIZED AURORAL ARC

Figure B1 shows an idealized auroral arc which is constructed of 3 infinite sheet currents with current density \mathbf{K} (Amps/(unit length)). The field-aligned current sheet at $x = -d/2$ has a downward current in the $-z$ direction, and the parallel sheet at $x = +d/2$ consists of upward current. Connecting the 2 sheets at $z = 0$ is a sheet of x -directed current with width d which models the layer of Pedersen current in an auroral arc. To find the magnetic field vector \mathbf{H} due to the current sheets we can use the Biot-Savart law:

$$\mathbf{H} = \frac{1}{4\pi} \int_{A'} \frac{\mathbf{K} \times \hat{\mathbf{a}}_R}{R^2} dA'. \quad (\text{B1})$$

$\hat{\mathbf{a}}_R$ is a unit vector from the current sheets (at primed coordinates) to an observation point (at unprimed coordinates), and for the z -directed sheet at $x = d/2$ it is given by

$$\hat{\mathbf{a}}_R = \frac{(x - d/2)\hat{x} - y'\hat{y} + (z - z')\hat{z}}{\sqrt{(x - d/2)^2 + y'^2 + (z - z')^2}}. \quad (\text{A2})$$

We have assumed that we are observing in the $y = 0$ plane. Using this with $\mathbf{K} = K\hat{z}$ in (B1) leads to

Ideal Auroral Arc

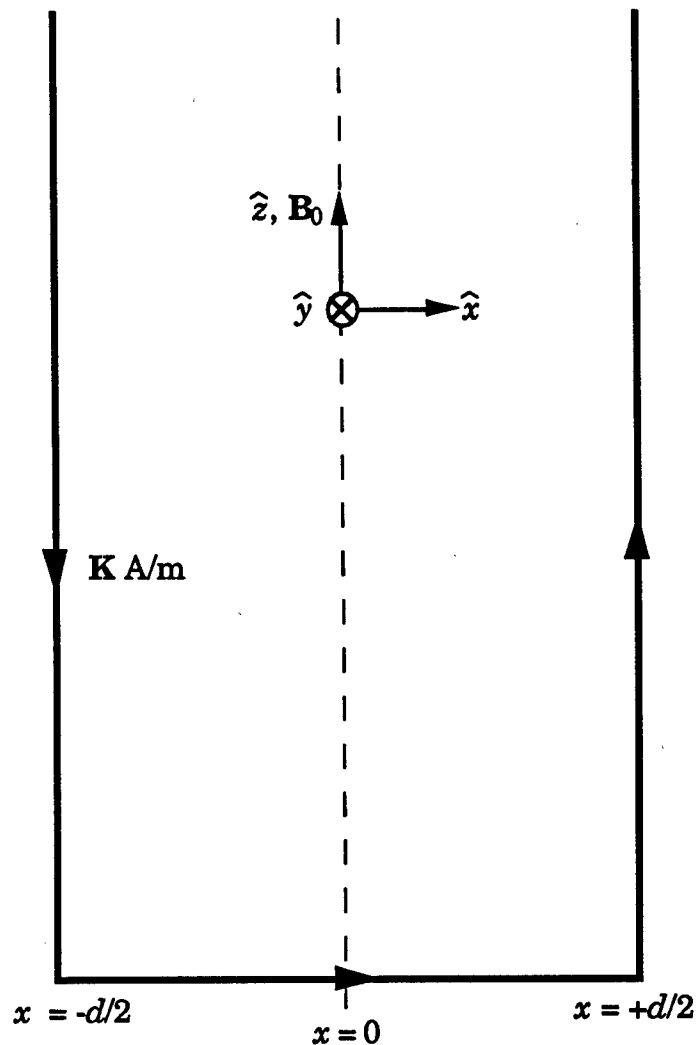


Fig. B1.

Figure B1 Geometry used to calculate magnetic fields due to an ideal auroral arc which produces no Hall current and which has an infinitely thin Pedersen current layer at $z = 0$.

$$\mathbf{H}_1 = \frac{K}{4\pi} \iint_{A'} \frac{y' \hat{x} + (x - d/2) \hat{y}}{(x - d/2)^2 + y'^2 + (z - z')^2} dy' dz'. \quad (\text{B3})$$

We use the subscript "1" to denote the magnetic field due only to the current sheet at $x = +d/2$. The \hat{x} component in (B3) vanishes because the integrand is an odd function of y' . Integration of the remaining term over y' can be carried out with the aid of the following integral:

$$\int \frac{dw}{(w^2 + a^2)^{3/2}} = \frac{w}{a^2(w^2 + a^2)^{1/2}}. \quad (\text{B4})$$

The result is

$$\mathbf{H}_1 = \frac{K}{2\pi} \int_0^\infty \frac{(x - d/2) \hat{y}}{(x - d/2)^2 + (z - z')^2} dz'. \quad (\text{B5})$$

Another integral identity helps at this stage:

$$\int \frac{dw}{w^2 + a^2} = \frac{1}{a} \tan^{-1}\left(\frac{w}{a}\right). \quad (\text{B6})$$

Note that in applying (B6) to (B5) a sign change is introduced because $dw = -dz'$. The result of this integration gives the contribution to the magnetic field \mathbf{H}_1 from the field-aligned current sheet at $x = +d/2$:

$$\mathbf{H}_1 = \frac{-Ky}{2\pi} \left(\frac{\pi}{2} \operatorname{sgn}(d/2 - x) - \tan^{-1}\left(\frac{z}{x - d/2}\right) \right). \quad (\text{B7})$$

The $\operatorname{sgn}(w)$ function is +1 for $w > 0$ and -1 for $w < 0$. The contribution \mathbf{H}_2 from the current sheet at $x = -d/2$ can be found by changing the sign of d and K in (B7):

$$\mathbf{H}_2 = \frac{-Ky}{2\pi} \left(\frac{\pi}{2} \operatorname{sgn}(x + d/2) + \tan^{-1}\left(\frac{z}{x + d/2}\right) \right). \quad (\text{B8})$$

Next we will calculate the magnetic field \mathbf{H}_3 due to the \hat{x} -directed current sheet at $z = 0$. The unit vector from the current sheet to an observer is

$$\hat{a}_R = \frac{(x - x')\hat{x} - y'\hat{y} + z\hat{z}}{\sqrt{(x - x')^2 + y'^2 + z^2}}. \quad (\text{B9})$$

This combined with the fact that $\mathbf{K} = K\hat{x}$ yields

$$\mathbf{H}_3 = \frac{K}{4\pi} \iint_{A'} \frac{z\hat{y} + y'\hat{z}}{\left((x - x')^2 + y'^2 + z^2\right)^{3/2}} dy'dx'. \quad (\text{B10})$$

With the aid of (B4) and (B6) the result of the integration is

$$\mathbf{H}_3 = \frac{-Ky}{2\pi} \left(\tan^{-1}\left(\frac{x+d/2}{z}\right) - \tan^{-1}\left(\frac{x-d/2}{z}\right) \right). \quad (\text{B11})$$

Finally we are ready to sum the 3 contributions \mathbf{H}_1 , \mathbf{H}_2 , and \mathbf{H}_3 to find the total magnetic field \mathbf{H} with the aid of the identity

$$\tan^{-1}(w) + \tan^{-1}(1/w) = \frac{\pi}{2} \text{sgn}(w). \quad (\text{B12})$$

The result is

$$\mathbf{H} = \frac{-Ky}{4} \left(\text{sgn}(x+d/2) - \text{sgn}(x-d/2) + \text{sgn}\left(\frac{x+d/2}{z}\right) - \text{sgn}\left(\frac{x-d/2}{z}\right) \right). \quad (\text{B13})$$

Thus for all points "inside" the ideal arc, i.e. $z > 0$ and $-d/2 < x < d/2$, $\mathbf{H} = -Ky\hat{y}$. Outside and below the arc, \mathbf{H} is identically zero. The Pedersen current sheet exactly cancels the magnetic fields from field-aligned currents in an ideal arc, and therefore a ground-based magnetometer would not measure a zonal magnetic field under such an arc. However, we have neglected the Hall current associated with auroral arcs, and this current *will* produce a magnetic perturbation on the ground in the meridional (cross-arc) direction.

REFERENCES

Akasofu, S.-I., Auroral arcs and auroral potential structure, in *Physics of Auroral Arc Formation*, edited by S.-I. Akasofu and J. R. Kan, pp. 1-14, American Geophysical Union, Washington, D. C., 1981.

Alfvén, H., *Cosmical Electrodynamics*, Oxford University Press, New York, 1950.

Allen, J., Sauer, H., Frank, L., and Reiff, P., Effects of the March 1989 solar activity, *EOS Trans., AGU*, 70, 1479, 1989.

Banks, P. M., and G. Kockarts, *Aeronomy, Part A*, Academic Press, New York, 1973.

Banks, P. M., and G. Kockarts, *Aeronomy, Part B*, Academic Press, New York, 1973.

Berthelier, A., J.-C. Cerisier, J.-J. Berthelier, J.-M. Bosqued, and R. A. Kovrazkhin, The electrodynamic signature of short scale field aligned currents, and associated turbulence in the cusp and dayside auroral zone, *Electromagnetic Coupling in the Polar Clefts and Caps*, P. E. Sandholz and A. Egeland (eds.), 299, Kluwer Academic Publishers, 1989.

Birkeland, K., *Norwegian Aurora Polaris Expedition, 1902-3 Part 1*, H. Aschehoug and Company, Christiania, 1908.

Boehm, M. H., C. W. Carlson, J. P. McFadden, J. H. Clemmons, and F. S. Mozer, High resolution sounding rocket observations of large amplitude Alfvén waves, *J. Geophys. Res.*, in press, 1990.

Boström, R., G. Gustafsson, G. Holback, G. Holmgren, H. Koskinen, and P. Kintner, Characteristics of solitary waves and weak double layers in the magnetospheric plasma, *Phys. Rev. Lett.*, 61, 82, 1988.

Brekke, A., J. R. Doupnik, and P. M. Banks, Incoherent scatter measurements of E region conductivities and currents in the auroral zone, *J. Geophys. Res.*, 79, 3773, 1974.

Budden, K. G., *The Propagation of Radio Waves*, 669 pp., Cambridge University Press, 1985.

Chmyrev, V. M., V. N. Oraevsky, S. V. Bilichenko, N. V. Isaev, G. A. Stanev, D. K. Teodosiev, and S. I. Shkolnikova, The fine structure of intensive small-scale electric and magnetic fields in the high-latitude ionosphere as observed by *Intercosmos-Bulgaria 1300* satellite, *Planet. Space Sci.*, 33, 1383, 1985.

Cummings, W. D., and A. J. Dessler, Field-aligned currents in the magnetosphere, *J. Geophys. Res.*, 72, 1007, 1967.

Dougherty, J. P., and D. T. Farley, A theory of incoherent scattering of radio waves by a plasma, *Proc. Roy. Soc.*, A259, 79, 1960.

Dougherty, J. P., and D. T. Farley, A theory of incoherent scattering of radio waves by a plasma, 3, Scattering in a partly ionized gas, *J. Geophys. Res.*, 63, 5473, 1963.

Dubinin, E. M., P. L. Israelevich, N. S. Nikolaeva, I. Kutiev, and I. M. Podgorny, Localized auroral disturbance in the morning sector of topside ionosphere as a standing electromagnetic wave, *Planet. Space Sci.*, 33, 597, 1985.

Earle, G. D., Electrostatic plasma waves and turbulence near auroral arcs, Ph. D Thesis, Cornell University, Ithaca, New York, 1988.

Earle, G., and M. C. Kelley, Spectral studies of the sources of ionospheric electric fields, *J. Geophys. Res.*, 92, 213, 1987.

Eather, R. H., *Majestic Lights, The Aurora in Science, History, and the Arts*, American Geophysical Union, Washington, D. C., 1980.

Erlandson, R. E., L. J. Zanetti, T. A. Potemra, L. P. Block, and G. Holmgren, Viking magnetic and electric field observations of Pc 1 waves at high latitudes, *J. Geophys. Res.*, 95, 5941, 1990.

Farley, D. T., Jr., A theory of electrostatic fields in the ionosphere at nonpolar geomagnetic latitudes, *J. Geophys. Res.*, 65, 869, 1960.

Farley, D. T., A theory of incoherent scattering of radio waves by a plasma, 4, The effect of unequal ion and electron temperatures, *J. Geophys. Res.*, 71, 4091, 1966.

Farley, D. T., J. P. Dougherty, and D. W. Barron, A theory of incoherent scattering of radio waves by a plasma, 2, Scattering in a magnetic field, *Proc. Roy. Soc.*, A263, 238, 1961.

Farley, D. T., Jr., H. M. Ierkic, and B. G. Fejer, Radar interferometry: a new technique for studying plasma turbulence in the ionosphere, *J. Geophys. Res.*, 86, 1467, 1981.

Fejer, B. G., Larsen, M. F., and D. T. Farley, Equatorial disturbance dynamo electric fields, *Geophys. Res. Lett.*, 10, 537, 1983.

Feynman, R. P., Leighton, R. B., and M. Sands, *The Feynman Lectures on Physics, Vol. II*, Addison-Wesley, Reading, Mass., 1964.

Foster, J. C., J. P. St. Maurice, and V. J. Abreu, Joule heating at high latitudes, *J. Geophys. Res.*, 88, 4885, 1983.

Forbes, J. M., and M. Harel, Magnetosphere-thermosphere coupling: An experiment in interactive modeling, *J. Geophys. Res.*, 94, 2631, 1989.

Francis, W. E. and R. Karplus, Hydromagnetic waves in the ionosphere, *J. Geophys. Res.*, 65, 3593, 1960.

Goertz, C. K., and R. W. Boswell, Magnetosphere-ionosphere coupling, *J. Geophys. Res.*, 84, 7239, 1979.

Greifinger, P., Ionospheric propagation of oblique hydromagnetic plane waves at micropulsation frequencies, *J. Geophys. Res.*, 77, 2377, 1972.

Gurnett, D. A., R. L. Huff, J. D. Menietti, J. L. Burch, J. D. Winningham, and S. D. Shawhan, Correlated low-frequency electric and magnetic noise along the auroral field lines, *J. Geophys. Res.*, 89, 8971, 1984.

Haerendel, G., An Alfvén wave model of auroral arcs, in *High-Latitude Space Plasma Physics*, edited by B. Hultqvist and T. Hagfors, 543 pp., Plenum Press, New York, 1983.

Hallinan, T. J., and T. N. Davis, Small-scale auroral arc distortions, *Planet. Space Sci.*, 18, 1735, 1970.

Hargreaves, J. K., *The Upper Atmosphere and Solar-Terrestrial Relations*, 298 pp., Van Nostrand Reinhold Company, New York, 1979.

Hasegawa, A., Particle acceleration by MHD surface wave and formation of aurora, *J. Geophys. Res.*, 81, 5083, 1976.

Hasegawa, A., Kinetic properties of Alfvén waves, *Proc. Indian Acad. Sci.*, 86 A, 151, 1977.

Hughes, W. J., The effect of the atmosphere and ionosphere on long period magnetospheric micropulsations, *Planet. Space Sci.*, 22, 1157, 1974.

Hughes, W. J., Pulsation research during the IMS, *Rev. Geophys.*, 20, 641, 1982.

Hughes, W. J., and Southwood, D. J., The screening of micropulsation signals by the atmosphere and ionosphere, *J. Geophys. Res.*, 81, 3234, 1976.

Iijima, T. and T. A. Potemra, Field-aligned currents in the dayside cusp observed by Triad, *J. Geophys. Res.*, 81, 5971-5979, 1976.

Inoue, Y., Wave polarizations of geomagnetic pulsations observed in high latitudes on the Earth's surface, *J. Geophys. Res.*, 78, 2959, 1973.

Iyemori, T., and K. Hayashi, PC 1 micropulsations observed by MAGSAT in the ionospheric F region, *J. Geophys. Res.*, 94, 93, 1989.

Jaccia, L. G., Static diffusion models of the upper ionosphere above the E-layer, *Res. Space Sci., Smith. Inst. Astrophys. Obs., Spec Rep.*, 332, 1971.

Jenkins, G. M., and D. G. Watts, *Spectral Analysis and Its Applications*, Holden-Day, San Francisco, 1968.

Kelley, M. C., *The Earth's Ionosphere, Plasma Physics and Electrodynamics*, Academic Press, Inc., San Diego, 1989.

Kelley, M. C., M. F. Larsen, C. LaHoz, and J. P. McClure, Gravity wave initiation of equatorial spread F: A case study, *J. Geophys. Res.*, 86, 9087, 1981.

Kelley, M. C., D. J. Knudsen, and J. F. Vickrey, Quasi-DC Poynting flux measurements on a satellite: A diagnostic tool for space research, *J. Geophys. Res.* in press, 1990.

Knudsen, D. J., M. C. Kelley, G. D. Earle, C. Carlson, M. Boehm, and B. McFadden, Scale size dependence of auroral field impedances and Poynting flows, *EOS Trans. AGU*, 69, 432, 1988

Knudsen, D. J., Distinguishing Alfvén waves from quasi-static field structures associated with discrete aurora: Sounding rocket and HILAT satellite measurements, *Geophys. Res. Lett.*, in press, 1990.

Kofman, D., and C. Lathuillere, Observations by incoherent scatter technique of the hot spots in the auroral zone ionosphere, *Geophys. Res. Lett.*, 11, 1158, 1987.

Koskinen, H., R. Bostrom, and B. Holback, Viking observations of solitary waves and weak double layers on auroral field lines, in *Ionosphere-Magnetosphere-Solar Wind Coupling Processes*, edited by T. Chang, G. B. Crew, and J. R. Jasperse, p. 147, Scientific, Cambridge, Mass., 1989.

Kudeki, E., Plasma turbulence in the equatorial electrojet, Ph. D Thesis, Cornell University, Ithaca, New York, 1983.

Labelle, J. W., Ionospheric turbulence: Case studies in equatorial spread F and development of a rocket-borne interferometer, Ph. D Thesis, Cornell University, Ithaca, New York, 1985.

Lockwood, M., B. J. I. Bromage, R. B. Horne, J. P. St-Maurice, D. M. Willis, and S. W. H. Cowley, Non-Maxwellian ion velocity distributions observed using EISCAT, *Geophys. Res. Lett.*, 14, 111, 1987.

Løvhaug, U. P., and T. Flå, Ion temperature anisotropy in the auroral F-region as measured with EISCAT, *J. Atmos. Terr. Phys.*, 48, 959, 1986.

Lysak, R. L., and C. W. Carlson, The effect of microscopic turbulence on magnetosphere-ionosphere coupling, *Geophys. Res. Lett.*, 8, 269, 1981.

Lysak, R. L., and C. T. Dum, Dynamics of magnetosphere-ionosphere coupling including turbulent transport, *J. Geophys. Res.*, 88, 365, 1983.

Lysak, R. L., Auroral electrodynamics with current and voltage generators, *J. Geophys. Res.*, 90, 4178, 1985.

Lysak, R. L., Coupling of the dynamic ionosphere to auroral flux tubes, *J. Geophys. Res.*, 91, 7047, 1986.

Lysak, R. L., Theory of auroral zone PiB pulsation spectra, *J. Geophys. Res.*, 93, 5942, 1988.

Mallinckrodt, A. J., and C. W. Carlson, Relations between transverse electric fields and field-aligned currents, *J. Geophys. Res.*, 83, 1426, 1978.

McPherron, R. L., Magnetospheric substorms, *Reviews of Geophysics and Space Physics*, 17, 657, 1979.

Melrose, D. B., *Instabilities in Space and Laboratory Plasmas*, 280 pp., Cambridge University Press, Cambridge, 1986.

Mikkelsen, I. S., T. S. Jørgensen, M. C. Kelley, M. F. Larsen, E. Pereira, and J. Vickrey, Neutral winds and electric fields in the dusk auroral oval 1. Measurements, *J. Geophys. Res.*, 86, 1513, 1981.

Mikkelsen, I. S., M. F. Larsen, M. C. Kelley, J. Vickrey, E. Friis-Christensen, J. Meriwether, and P. Shih, Simultaneous measurements of the thermospheric wind profile at three separate positions in the dusk auroral oval, *J. Geophys. Res.*, 92, 4639, 1987.

Moorcroft, D. R., and K. Schlegel, Evidence for non-Maxwellian ion velocity distributions in the F-region, *J. Atmos. Terr. Phys.*, 48, 455, 1988.

Mozer, F. S. and R. H. Manka, Magnetospheric electric field properties deduced from simultaneous balloon flights, *J. Geophys. Res.*, 76 (7), 1697, 1971.

Mozer, F. S. and R. Serlin, Magnetospheric electric field measurements with balloons, *J. Geophys. Res.*, 74 (19), 4739, 1969.

Nicholson, D. R., *Introduction to Plasma Theory*, 292 pp., John Wiley & Sons, New York, 1983.

Papoulis, A., *Probability, Random Variables, and Stochastic Processes*, McGraw-Hill, New York, 1965.

Paul, C. R., and S. A. Nasar, *Introduction to Electromagnetic Fields*, 742 pp., McGraw-Hill Book Company, New York, 1987.

Pereira, A. E. C., Numerical modeling of high latitude winds in the upper atmosphere, Ph.D Thesis, Cornell University, 1979.

Poole, A. W. V., P. R. Sutcliffe and A. D. M. Walker, The relationship between ULF geomagnetic pulsations and ionospheric Doppler oscillations: Derivation of a model, *J. Geophys. Res.*, 93, 14656, 1988.

Potemra, T. A., Bythrow, P. F., Zanetti, L. J., Mobley, F. F., and W. L. Scheer, The HILAT magnetic field experiment, *Johns Hopkins APL Technical Digest*, 5, 120-124, 1984.

Providakes, J., Radar interferometer observations and theory of plasma irregularities in the auroral ionosphere, Ph. D Thesis, Cornell University, 1985.

Press, W. H., B. P. Flannery, S. A. Teukolsky, and W. T. Vetterling, *Numerical Recipes: The Art of Scientific Computing*, 818 pp., Cambridge University Press, Cambridge, 1986.

Prince, C. E., Jr. and F. X. Bostick, Jr., Ionospheric transmission of transversely propagated plane waves at micropulsation frequencies and theoretical power spectrums, *J. Geophys. Res.*, 69, 3213, 1964.

Ramo, S., J. R. Whinnery, and T. Van Duzer, *Fields and Waves in Communication Electronics*, John Wiley & Sons, New York, 1965.

Rich, F. J., Heelis, R. A., Hanson, W. B., Anderson, P. B., Holt, B. J., Harmon, L. L., Zuccaro, D. R., Lippincott, C. R., Girouard, D., and W. P. Sullivan, Cold plasma measurements on HILAT, *Johns Hopkins APL Technical Digest*, 5, 114-119, 1984.

Richmond, A. D., S. Matsushita, and J. D. Tarpley, On the production mechanism of electric currents and fields in the ionosphere, *J. Geophys. Res.*, 81, 547, 1976.

Richmond, A. D., and R. G. Roble, Electrodynamic effects of thermospheric winds from the NCAR thermospheric general circulation model, *J. Geophys. Res.*, 92, 12365, 1987.

Robinson, R. M., and R. R. Vondrak, Measurements of E region ionization and conductivity produced by solar illumination at high latitudes, *J. Geophys. Res.*, 89, 3951, 1984.

Röttger, J., Wave-like structures of large-scale equatorial spread-F irregularities, *J. Atmos. and Terr. Phys.*, 35, 1195, 1973.

Sagalyn, R. C., and H. K. Burke, Atmospheric electricity, in *Handbook of Geophysics and the Space Environment*, edited by A. S. Jursa, p. 20-1, National Technical Information Service, Springfield, VA, 1985.

Sahr, J. D., Observation and theory of the radar aurora, Ph. D Thesis, Cornell University, Ithaca, New York , 1990.

Seyler, C. E., Nonlinear 3-D evolution of bounded kinetic Alfvén waves due to shear flow and collisionless tearing instability, *Geophys. Res. Lett.*, 15, 756, 1988.

Schunk, R. W., and G. C. G. Walker, Theoretical ion densities in the lower thermosphere, *Planet. Space Sci.*, 21, pp. 1875-1896, 1973.

Siefring, C. L., and M. C. Kelley, Analysis of standing wave patterns in VLF transmitter signals: Effects of sporadic-E layers and *in-situ* measurements of low electron densities, *J. Geophys. Res.*, in press, 1990.

Smiddy, M., Burke, W. J., Kelley, M. C., Saflekos, N. A., Gussenhoven, M. S., Hardy, D. A. and F. J. Rich, Effects of high-latitude conductivity on observed convection electric fields and Birkeland currents, *J. Geophys. Res.*, 85, 6811-6818, 1980.

Stern, D. P., Large-scale electric fields in the Earth's magnetosphere, *Reviews of Geophysics and Space Physics*, 15, 156, 1977.

Stix, T. H., *The Theory of Plasma Waves*, 283 pp., McGraw-Hill, New York, 1962.

Sugiura, M., N. C. Maynard, W. H. Farthing, J. P. Heppner, and B. G. Ledley, Initial results on the correlation between the magnetic and electric fields observed from the DE-2 satellite in the field-aligned current regions, *Geophys. Res. Lett.*, 9, 985, 1982.

Sugiura, M., A fundamental magnetosphere-ionosphere coupling mode involving field-aligned currents as deduced from DE-2 observations, *Geophys. Res. Lett.*, 11, 877, 1984.

Swartz, W. E., J. F. Providakes, M. C. Kelley, and J. F. Vickrey, The effect of strong velocity shears on incoherent scatter spectra: a new interpretation of unusual high-latitude spectra, *Geophys. Res. Lett.*, 15, 1341, 1988.

Takahashi, K. S. Kokubun, T. Sakurai, R. W. McEntire, T. A. Potemra, and R. E. Lopez, AMPTE/CCE observations of substorm-associated standing Alfvén waves in the midnight sector, *Geophys. Res. Lett.*, 15, 1287, 1988.

Temerin, M., K. Cerny, W. Lotko, and F. S. Mozer, Observations of double layers and solitary waves in the auroral plasma, *Phys. Rev. Lett.*, 48, 1175, 1982.

Vickrey, J. F., Vondrak, R. R., and S. J. Matthews, Energy deposition by precipitating particles and Joule dissipation in the auroral ionosphere, *J. Geophys. Res.*, 87, 5184-5196, 1982.

Vickrey, J. F., R. C. Livingston, N. B. Walker, T. A. Potemra, R. A. Heelis, M. C. Kelley, and F. J. Rich, On the current-voltage relationship of the magnetospheric generator at intermediate spatial scales, *Geophys. Res. Lett.*, 13, 495, 1986.

Weimer, D. R., C. K. Goertz, D. A. Gurnett, N. C. Maynard, and J. L. Burch, Auroral zone electric fields from DE 1 and 2 at magnetic conjugations, *J. Geophys. Res.*, 90, 7479, 1985.

Zmuda, A. J., J. H. Martin, and F. T. Heuring, Transverse magnetic disturbances at 1100 kilometers in the auroral region, *J. Geophys. Res.*, 71, 5033, 1966.